ABSTRACT

Title of Dissertation: RETRIEVALS OF ANTARCTIC SEA ICE PHYSICAL PROPERTIES FROM SATELLITE RADAR ALTIMETRY

Steven William Fons
Doctor of Philosophy, 2021

Dissertation Directed by: Professor James Carton
Dept. of Atmospheric and Oceanic Science
Dr. Nathan Kurtz
NASA Goddard Space Flight Center

Satellite observations have been used in sea ice research throughout the last 40+ years and have brought to light substantial changes in the global sea ice coverage. More recently, satellite altimetry has become a valuable tool to estimate the thickness of sea ice - a parameter that plays an important role in the Earth System by moderating heat and moisture fluxes between the polar ocean and atmosphere. While radar altimetry has been effective in providing estimates of Arctic sea ice thickness, the complex snow stratigraphy and uncertain snow depth on Antarctic sea ice have precluded sea ice thickness retrievals in the Southern Ocean, leading to a decade-long gap in the thickness record spanning the lifetime of ESA's CryoSat-2 satellite. This dissertation will address the need for Antarctic sea ice thickness estimates from CryoSat-2 through the development and assessment of new retrievals of sea ice physical properties that enable the estimation of sea ice thickness.

The first part of this dissertation is aimed at developing a CryoSat-2 retrieval

algorithm that is less dependent on uncertain returns from the snow-ice interface of Antarctic sea ice. This method exploits observed scattering of Ku-band radar pulses from the snow surface and snow volume atop sea ice and uses a physical waveform model and optimization approach to retrieve the air-snow interface elevation and snow freeboard. Building off the initial development, the second part of this work offers improvements to – and assessments of – the retrieval process though comparisons with coincident snow freeboard measurements from NASA's ICESat-2 laser altimeter. The final part of this dissertation uses the retrieval process to estimate snow depth and ice freeboard, enabling first estimates of Antarctic sea ice thickness that span the CryoSat-2 mission. Potential applications for use of this method over Arctic sea ice are also explored.

The studies within this dissertation represent new possibilities for CryoSat-2 data and lay a foundation for the development of a combined laser-radar altimetric record of Antarctic sea ice thickness.

RETRIEVALS OF ANTARCTIC SEA ICE PHYSICAL PROPERTIES FROM SATELLITE RADAR ALTIMETRY

by

Steven William Fons

Dissertation submitted to the Faculty of the Graduate School of the
University of Maryland, College Park in partial fulfillment
of the requirements for the degree of
Doctor of Philosophy
2021

Advisory Committee:
Professor James Carton, Chair/Advisor
Dr. Nathan Kurtz, Advisor
Professor Sinéad Farrell
Dr. Thorsten Markus
Professor Rachel Pinker
Professor Laurent Montési, Dean's Representative

Acknowledgments

I owe a great debt of gratitude to the many people who helped me get to where I am today.

First and foremost, I would like to thank my research advisor, Dr. Nathan Kurtz, for giving me the opportunity to work on such an exciting project and teaching me everything I could hope to learn (and more!) about sea ice and altimetry. I'm exceptionally grateful for the guidance and support, as well as for all the opportunities this research has provided. I remember meeting with him for the first time (having never heard of "freeboard" before) and leaving with an excitement about Antarctic sea ice that stayed with me throughout my time as a graduate student. My thanks go out to my academic advisor, Dr. Jim Carton, for putting me in touch with the "NASA guys" and for all his help in preparing for this dissertation and its defense. Also, I sincerely appreciate my committee members for their constructive feedback on this work over the past few months and years, namely: Drs. Sinead Farrell, Thorsten Markus, Laurent Montesi, Rachel Pinker, and Alek Petty.

My academic career truly began as an undergraduate at the University of Wisconsin, where I was so privileged to be surrounded by many inspirational instructors and researchers; especially Drs. Jon Martin, Grant Petty, Ankur Desai, Mark Kulie, Zak Handlos, Melissa Breeden, and many others who instilled in me a curiosity to

better understand the Earth System. Additionally, I would not be studying what I am today without the AMRC team led by Dr. Matthew Lazzara, whose passion for Antarctic science clearly steered me poleward.

I was fortunate to join a fantastic AOSC department at the University of Maryland in 2016. Thanks to so many great professors (especially Tim Canty), fellow students, and staff members (especially Tammy Hendershot) for helping to make my time at UMD both productive and enjoyable. I'm particularly grateful to the group of classmates-turned-friends (Shaun, Casey, Dylan, and Niko) who – between the late-night grading sessions and cramming for exams – still found time for office basketball, Friendsgiving dinners, and DJ Bird Karaoke at Town Hall.

I also would like to thank the entire Cryospheric Sciences Lab at NASA Goddard, from whom I learned so much over the past 4+ years. Special thanks go out to Jeremy Harbeck, Adam Greeley, and Marissa Dattler for being great officemates; to Claire Parkinson, Rachel Tilling, Marco Bagnardi, Chelsea Parker, Linette Boisvert and the sea ice tea(m) for the weekly tag-ups; to Tyler Sutterley for his python CryoSat-2 readers that saved me countless hours of coding; and to Kelly Brunt, Tom Neumann, Brooke Medley, Isabel Nias, Denis Felikson, Thomas Overly, and so many others for being exemplar scientists and even better human beings.

Almost 10% of my PhD was spent at sea as part of the MOSAiC Expedition, and I'm so appreciative to Nathan Kurtz and Melinda Webster for the incredible opportunity. Thanks to Steffi Arndt for her superb ICE team leadership; to the FYI coring team for some of the longest yet most rewarding days on the ice; to Gina, Amy, David, and Elena for the coffee clubs, Zillertals, and the overall friendship;

and to the entire PS122/3 expedition team for helping make an amazing experience even more enjoyable.

Last but not least, I would like to acknowledge my family for all the love and encouragement they have provided during (and long before) my PhD. To my parents, Terry and Laura – thank you for the unwavering support in everything that I do. To my siblings, Nathan, Lindsay, and Allie – thank you for being the best role models in all aspects of life. And finally, to my fiancée Kaitlyn – thank you for being the best partner, proofreader, and friend that I could ask for.

To all these folks and so many more, thank you!

Table of Contents

List of Tables

List of Figures

List of Abbreviations

AIDJEX	Arctic Ice Dynamics Joint Experiment
Am-Bel	Amundsen and Bellingshausen
AR5	Fifth Assessment Report
ATM	Airborne Topographic Mapper
AWI	Alfred Wegener Institute
BAS	British Antarctic Survey
BGEP	Beaufort Gyre Exploration Project
CAMBOT	Continuous Airborne Mapping By Optical Translator
CCI	Climate Change Initiative
CDR	Climate Data Record
CPOM	Centre for Polar Observation and Modelling
CryoVex	CryoSat Validation Experiment
DMS	Digital Mapping System
DMSP	Defense Meteorological Satellite Program
DTC	Dry Tropospheric Correction
ECMWF	European Centre for Medium-Range Weather Forecasts
EM	Electromagnetic
ERS	European Remote Sensing Satellite
ESA	European Space Agency
FDR	False Discovery Rate
FES2004	Finite Element Solution 2004
FYI	First Year Ice
GIM	Global Ionosphere Map
GPT	Geocentric Polar Tide
IBC	Inverse Barometric Correction
IC	Ionosphere Correction
ICESat	Ice, Cloud, and land Elevation Satellite
ICESat-2	Ice, Cloud, and land Elevation Satellite-2
IPCC	Intergovernmental Panel on Climate Change
IQR	Interquartile Range

KK20	Kacimi and Kwok (2020)
Lidar	Light Detection and Ranging
LPET	Long Period Equilibrium Tide
LRM	Low Resolution Mode
MOSAiC	Multidisciplinary Drifting Observatory for the Study of Arctic Climate
MYI	Multi-Year Ice
MSS	Mean Sea Surface
NASA	National Aeronautics and Space Administration
NESOSIM	NASA Eulerian Snow On Sea Ice Model
NRT	Near Real Time
NSIDC	National Snow and Ice Data Center
OCOG	Offset Center Of Gravity
OIB	Operation IceBridge
OLT	Ocean Loading Tide
OT	Ocean Tide
P18	Paul et al. (2018)
PDF	Probability Density Function
PP	Pulse Peakiness
Radar	Radio Detection and Ranging
Resnorm	Squared Norm of the Residual
SAMOSA	Synthetic Aperture Radar Altimetry Model Studies and Applications
SAR	Synthetic Aperture Radar
SARIn	Synthetic Aperture Radar Interferometry
SET	Solid Earth Tide
SHEBA	Surface Heat Budget of the Arctic Ocean
SIPEX	Sea Ice Physics and Ecosystem Experiment
SIRAL	Synthetic Aperture Interferometric Radar Altimeter
SMMR	Scanning Multichannel Microwave Radiometer
SSALTO	Multi-mission ground segment of Altimetry, Orbitography and precise localization
SSA	Sea Surface Anomaly
SSD	Stack Standard Deviation
SSH	Sea Surface Height
SSM/I	Special Sensor Microwave Imager
SSMIS	Special Sensor Microwave Imager/Sounder
SYI	Second Year Ice

TFMRA	Threshold First Maximum Retracker Algorithm
V1(2)	Version 1 (2)
WGS84	World Geodetic System 1984
WHOI	Woods Hole Oceanographic Institution
WTC	Wet Tropospheric Correction

Chapter 1: Introduction

This chapter provides a brief introduction into sea ice - including its formation, characteristics, and role in the climate system - and gives the overall objectives and outline of this dissertation.

1.1 Sea ice and the earth system

Sea ice plays a complex yet integral role in the earth system processes of the polar latitudes. It interacts with every component of the climate system, and, by floating at the interface between the atmosphere and ocean, has the unique function of regulating exchanges of heat, moisture, and salinity between these media. The importance of sea ice can be seen across scales, as it acts simultaneously as a habitat for tiny microfauna and as an expansive regulator of Earth's global energy budget. Sea ice had long been in the eyes of early polar explorers, however, recent large changes in the ice cover has brought it back into the spotlight of scientists, policymakers, and the public alike.

Sea ice is perhaps best known for its bright, high-albedo surface that reflects a majority of incoming solar radiation back to space. At any given time, roughly 12 - 18 km^2 (about 4%) of the earth's surface is covered in sea ice (Cavalieri et al., 2003),

with albedos ranging between about 0.6 (bare ice) and upward of 0.9 (snow-covered) (Allison et al., 1993; Massom et al., 2001; Perovich and Polashenski, 2012). This vast area of highly-reflective surface tends to result in net hemispheric cooling, as the incoming radiation that would otherwise be absorbed by the ocean (albedo $<$ 0.1) and emitted as heat is instead reflected away (Payne, 1972; Pinker et al., 2014). There are huge climate implications brought on by the effect of sea ice albedo, most notably the initiation of competing feedback loops: a positive ice-albedo feedback and negative feedback involving thermodynamic ice growth (Budyko, 1969; Curry et al., 1995; Holland et al., 2006).

The ice-albedo feedback arises due to the large difference in albedo between sea ice and the surrounding ocean (Curry et al., 1995). As ice melts, more of the ocean surface is exposed to the incoming radiation, resulting in enhanced heating, melting of sea ice, further absorption of radiation by the ocean, and so on. This process is considered a large contributing factor to the polar amplification of climate signals (Dai et al., 2019; Holland and Bitz, 2003). A negative feedback also can arise, however, from a warming world. As sea ice thins, it tends to act as less of an insulator between the ocean and atmosphere, resulting in enhanced thermodynamic ice production in winter months (Ebert and Curry, 1993; Holland et al., 2006). These competing feedbacks add to the complexity and sensitivity of sea ice in the climate system.

Another notable contribution of sea ice to the earth system comes from its salinity. Sea ice forms through a process of brine rejection, which means that as ocean surface-layer temperatures drop and water begins to freeze, brine is pushed

out of the forming ice and down into the ocean below (Aagaard and Carmack, 1989; Petrich and Eicken, 2016). This brine rejection increases the salinity - and therefore the density - of the surrounding water, which causes that water to sink. As this process occurs across the polar oceans, large quantities of water are set into downward motion, forming deepwater and contributing to the global thermohaline circulation (Cottier et al., 2016; Meredith and Brandon, 2016; Yang and Neelin, 1993). The inverse is true when sea ice melts: since most of the salt was rejected during formation, the melting of sea ice contributes a net freshwater flux into the surrounding ocean. This melting leads to generally less-saline and less-dense water, which can slow down the thermohaline circulation (Cottier et al., 2016; Stouffer et al., 2006). Since sea ice is made of ocean water, the freezing and melting of sea ice does not contribute to changes in the global sea level whereas ice from land that calves or melts into the sea surely does (Alley et al., 2005).

The impact of sea ice extends far beyond the polar regions, justifying the need to understand and observe sea ice and the processes that drive its growth, development, and melt.

1.1.1 Sea ice growth processes

Sea ice can develop following multiple pathways depending on its local environment (Fig. 1.1). As ocean water begins freezing at about -1.8°C (due to its salt content) it first forms either in a granular congelation of ice crystals or as frazil ice, which appear similarly as aggregates of ice crystals (Petrich and Eicken, 2016).

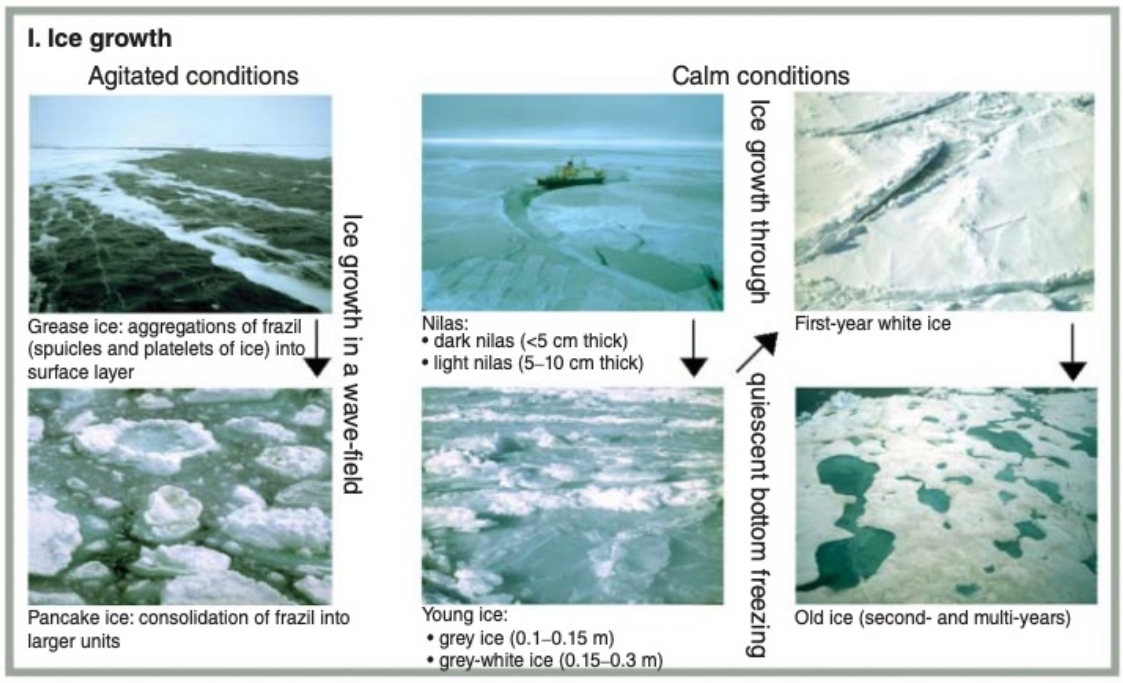

Figure 1.1: Sea ice growth pathways under calm (right) and agitated (left) conditions. Adapted from Thomas (2017).

From there, continued growth follows one of two pathways depending on the conditions of the ocean. Under calm conditions, congelation ice typically forms first and coalesces into a surface layer of nilas that is darker (lighter) when it is <5 cm (5-10 cm) thick. This nilas can continue to freeze from the bottom-down, becoming classified as young grey ice (0.1-0.15 m), young grey-white ice (0.15-0.3 m), and eventually white first-year ice (FYI). FYI that survives a summer melt season and continues growing the next winter becomes classified as second-year ice (SYI) or multi-year ice (MYI).

Under rougher, more agitated ocean conditions, sea ice takes a different growth path. Frazil is more likely to form first, and will instead aggregate into a sheet of grease ice that is generally thin (<5 cm) and sits atop the surface of the water. These aggregates are "flexible" when grouped together, and therefore do not immediately

break apart in the waves. As the grease ice gets thicker, however, it eventually breaks apart into round disks known as pancake ice (Fig. 1.1). These pancakes can continue to grow thermodynamically, but also can break apart dynamically as the pancakes clash together. If the ocean calms or the temperature drops further, the water surrounding the pancakes freezes and forms larger sea ice floes made up of the individual pancakes.

1.1.2 Hemispheric asymmetries in sea ice coverage

The geographic differences that determine the growth pathway of sea ice stem from larger hemispheric differences in sea ice properties. While they may look similar, Arctic sea ice is in fact very different than sea ice that forms in the Southern Ocean. These differences are largely driven by the geographical dissimilarities in the land masses at both poles (Simmonds, 2015). In the Northern Hemisphere, the location of the geographic North Pole is in the central Arctic Ocean, a large basin bounded on all sides by the land masses that make up Canada, Greenland, Scandinavia, Siberia, and Alaska. Ocean water in this basin is comparatively calm, so sea ice mostly forms first as nilas before continuing quiescent bottom-growth (Petrich and Eicken, 2016). At its larger extents, Arctic sea ice can spread out enough to completely cover the basin in ice (Fig. 1.2). However, its growth is restricted by these geographic bounds. In the Antarctic, the opposite is true: the geographic South Pole is found high atop the Antarctic Plateau, well over 1000 km from the nearest ocean. Sea ice in the Southern Ocean forms around the continent,

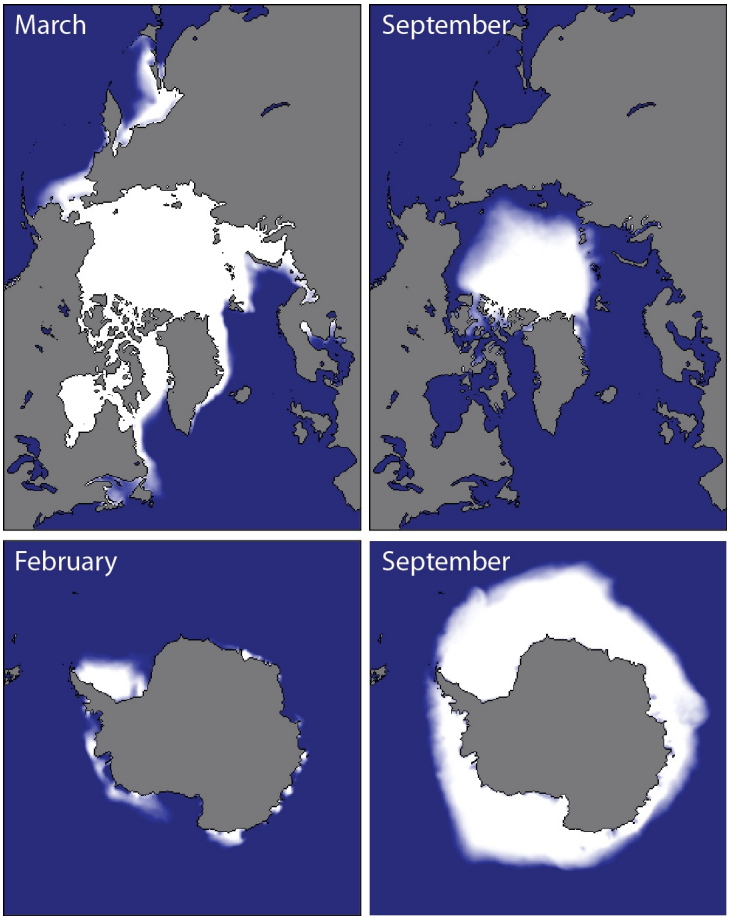

Figure 1.2: Typical sea ice coverage in the Northern and Southern Hemispheres (top and bottom, respectively) for the respective seasonal maximum and minimum sea ice extents. Data shown are sea ice concentration climatologies from 1981-2010. From NSIDC (2020).

which is encircled entirely in water. The ice is able to grow in extent as far as possible, until it reaches waters too warm to freeze or currents too strong to permit sustained growth (Meredith and Brandon, 2016). Due to this lack of constraint, Antarctic sea ice typically forms following the pancake-ice pathway (Fig. 1.1, Petrich and Eicken 2016).

Due to these geographic bounds, it is no surprise that the maximum extent of Antarctic sea ice is typically greater than that in the Arctic (Fig. 1.2). At its peak, Antarctic sea ice can cover around 20 million km^2 - which it usually reaches

in late September - compared to about 16 million km^2 in the Arctic, which is generally reached in early March (Fetterer et al., 2017). Arctic sea ice has recently seen minimum extents around 4.5 million km^2, which has decreased substantially from the $\sim$7 million km^2 minimum extents typically experienced between 1979-1990 (Fetterer et al., 2017). Antarctic sea ice on the other hand has remained mostly constant in extent since 1979, showing only slight increases over this time before recent large interannual variability resulted in its smallest minimum extent of the satellite record of about 2.1 million km^2 in 2017 (Fetterer et al., 2017; Parkinson, 2019). The minimum sea ice extent is an important climate indicator (EPA, 2016) and is monitored closely each year.

A final impact of the geographic constraints on sea ice relates to its thickness. Since Arctic sea ice can only grow so far in extent, it tends to grow vertically and be thicker on average than Antarctic sea ice, which is able to continuously expand outwards and is thinner on average. The thickness of the snow layer atop sea ice also comes into play: the wealth of available moisture in the Southern Ocean leads to more precipitation and thicker snow layers on sea ice, while the Arctic tends to have less snowfall and comparatively thinner snow depths (Giovinetto et al., 1992; Massom et al., 2001). While the dynamic range of sea ice thickness and snow depths on sea ice are orders of magnitude smaller than the ranges of observed sea ice extents, they still have important implications for the polar environments in which they exist as well as the global climate system as a whole.

1.2 Sea ice thickness

The thickness of sea ice is defined as the height of the ice layer floating on the ocean, from the bottom of the ice below the waterline to the top of the ice above it. Sea ice thickness can vary substantially over relatively small length scales, however, thickness tends to spatially correlate over larger areas (Eicken et al., 1991; Ponsoni et al., 2019). In the Arctic, wintertime sea ice thickness typically ranges between 2-3 m while in the Antarctic, thicknesses are generally thinner, between 1-2 m (NSIDC, 2020). As mentioned above, this quantity is an important control on the regulation of heat and moisture fluxes between the ocean and atmosphere (Persson and Vihma, 2016). In the wintertime, Arctic near-surface temperatures can get below -30°C within 1m of the sea ice, while the oceans stay at a constant -1.8°C (Fig. 1.3). This strong temperature gradient (around 0.16°C / cm) would typically result in very large positive heat fluxes from the ocean to the atmosphere, however, the sea ice and snow cover reduces this substantially (Persson and Vihma, 2016; Steffen and Demaria, 1996).

The earliest information on the basin-scale thickness distributions come from measurements collected on ships and submarines in the mid 20th century. In the Arctic, military submarines collected data on sea ice draft throughout the 20th century, with data from 1958 onwards being declassified for scientific research (Bourke and Garrett, 1987; Kwok and Rothrock, 2009; Rothrock et al., 1999). Bourke and Garrett (1987) combined these measurements to produce a climatology of sea ice thickness in the Arctic ocean (Fig. 1.4). They found the thickest ice to be located

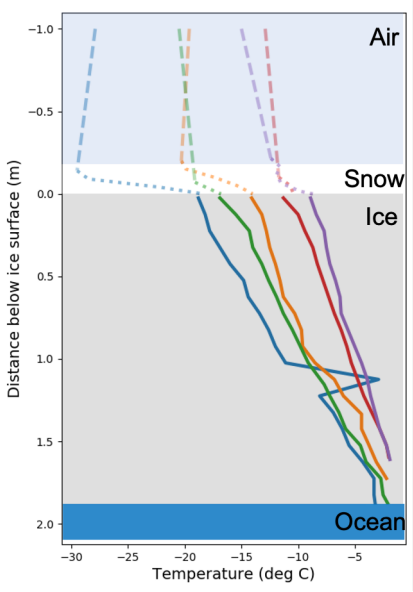

Figure 1.3: Profiles of temperature between the atmosphere, snow layer, sea ice, and ocean taken from manual measurements during the MOSAiC Expedition. Each line represents a different measurement date between March and May 2020. More info on the data collection is found in Chapter 6.

along the Canadian Archipelago, with regions as thick as 8 m nearest to the coast. Outwards into the Arctic basin, they found a gradient of decreasing thickness, with around 3.5 m at the North Pole and less than 2 m nearer to Siberia. Almost everywhere in the Arctic had climatological winter sea ice thickness values greater than 1 m (Fig. 1.4). In the Antarctic, Worby et al. (2008) pulled together reports from scientific and resupply cruises from 1981-2005 to develop a sea ice thickness climatology based on the ship observations. They found the thickest ice in the western Weddell Sea (near the Antarctic Peninsula) as well as in the near-coastal Ross Sea. Thinner ice was typically found in the Indian and Pacific Ocean sectors, as well as in the eastern Weddell Sea. (Fig. 1.4).

The thickness distribution of sea ice can be determined by a variety of factors. The most obvious is the contribution from thermodynamic growth. As ice freezes

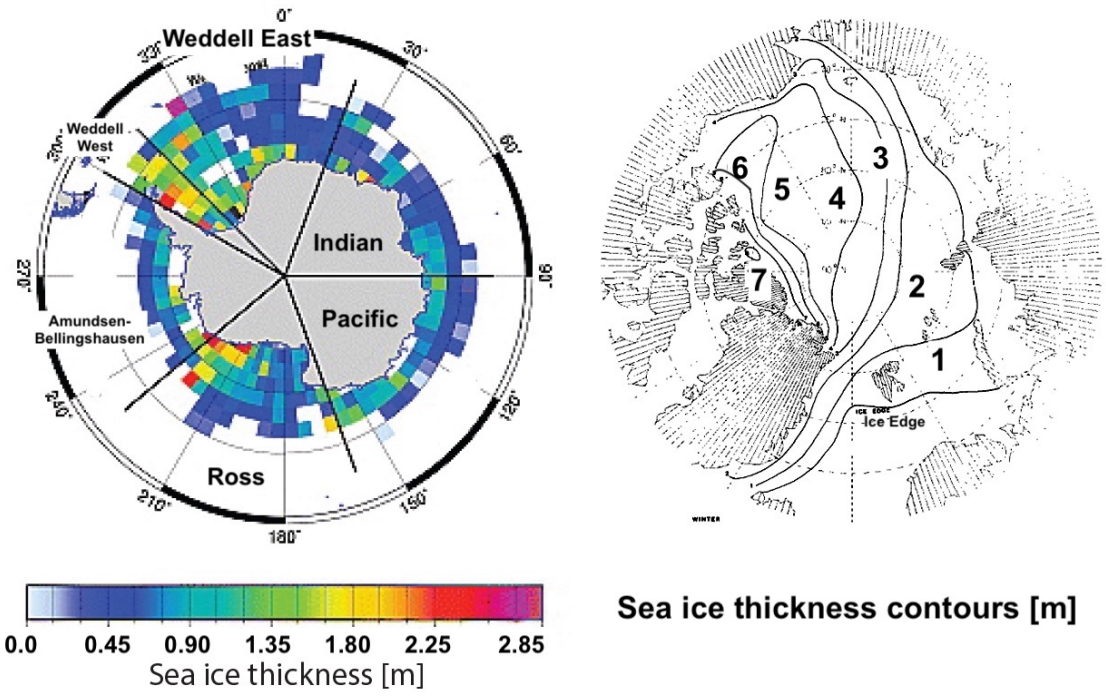

Figure 1.4: Early sea ice thickness maps derived from ship-based observations in the Antarctic (left) and submarine-based observations in the Arctic (right). Contours in Arctic plot are drawn for every 1 m of thickness. Adapted from Worby et al. (2008) and Bourke and Garrett (1987).

and continues to freeze, it tends to get thicker. However, dynamic processes also can contribute. Advection and divergence of sea ice by external forces - mainly wind and currents - can cause cracks (or leads) in the sea ice, which exposes open water. These leads can freeze and form new, thin ice, reducing the local thickness (Haas, 2016). As the winds and currents move ice floes around, these floes often converge, forming pressure ridges or rafted ice. These features deform the surfaces of ice floes and can lead to considerably thicker and rougher ice than the surroundings, which adds to the observed thickness distribution. Typically, the mean value of a thickness distribution refers to the average value of all ice in the region of interest, while the modal value of a thickness distribution is said to represent the average thickness of just the level (i.e. non-deformed) ice (Haas, 2016). Knowledge of the sea ice thickness distribution gained through observations is important for earth system modeling (Allard et al., 2018; Schröder et al., 2019).

1.2.1 Sea ice thickness observations

While the developed climatologies (Fig. 1.4) provide a basic understanding of how sea ice thickness is distributed at both poles, they provide little information on the geographic variability and the basin-scale interannual variability of sea ice thickness - both of which are important characteristics of thickness representations within climate models (Holland et al., 2006; Stroeve et al., 2014). For this, both ground-based and remotely-sensed measurements are extremely useful.

Data collected from the ground provide the most detailed - and simple - thick-

ness measurements, at the cost of covering only a small spatial and temporal range. Many of these data are collected during campaigns that involve a ship - usually an icebreaker - and work out on an ice floe. The first drifting expedition is thought to be Fridtjof Nansen's Fram expedition of 1893-1896 (Hunkins et al., 1979), but the first scientific expedition designed for studying the Arctic was likely in the 1930's with the Soviet North Pole drifting station (Shirshov and Fedorov, 1938). More recently, dedicated international teams of scientists have coordinated campaigns to study Arctic sea ice properties and processes. These expeditions include the Arctic Ice Dynamics Joint Experiment (AIDJEX, Evans 1972) in the 1970's, the Surface Heat Budget of the Arctic Ocean (SHEBA, Perovich et al. 1999) in the 1990's, the Multidisciplinary drifting Observatory for the Study of Arctic Climate (MOSAiC, Rex et al. 2019) in 2019, and many other smaller campaigns. While working on an ice floe, holes can be drilled through the ice and a simple thickness gauge can be used to find its thickness at a given point location (Fig. 1.5). Automated buoys or installed hot-wire stakes can cover a longer time series (Polashenski et al., 2011), but still offer thickness information only at a single point. More recently, electromagnetic (EM) thickness profilers towed on sleds have been used to provide transects of thickness measurements along an ice floe (Haas, 2016).

Fewer large field campaigns have occurred in the Antarctic due to the ice being mostly annual and tougher to access. However, some, like the East and West Antarctic Sea Ice Campaigns (Allison et al., 1993) and near-annual campaigns from the Alfred Wegener Institute (AWI) and the British Antarctic Survey (BAS) have worked on the Antarctic sea ice and collected thickness information using the

methods above. Since icebreakers often resupply the permanent research stations around the Antarctic continent, these ships can be used to deploy buoys which collect snow and ice thickness information at a point and continue recording as the ice moves (Fromm et al., 2020).

Figure 1.5: Sea ice thickness measurement techniques. Clockwise from top left: manual drillings (photo by: Laura Wischnewski), automated thermistor buoys (photo by: Steven Fons), airbourne (helicopter) EM soundings (photo by: Steven Fons), and airborne (fixed-wing) laser/radar instruments (photo by: Jeremy Harbeck).

To increase the spatial coverage of thickness observations over the ground-based measurements, aircraft are often employed. Both fixed-wing planes and helicopters can be mounted with instruments that aid in retrieving ice thickness. Radars and laser scanners can provide elevation estimates of the sea ice and sea surface, which can be combined to estimate thickness (discussed in next chapter). This tech-

nique is used commonly on airborne campaigns, most notably on NASA's Operation IceBridge (OIB) campaign. OIB was a 10-year aircraft mission to survey the land and sea ice at both poles. In total, it flew over 900 flights and collected measurements over both Arctic and Antarctic sea ice (Farrell et al., 2012; Kurtz et al., 2013; Merzdorf, 2020). Another measurement technique involves towing an EM instrument above the ice, which exploits the EM conductive differences between ice and water to estimate the thickness of the ice. This technique has been used recently at both poles, and has shown good agreement with ground-based measurements (Haas et al., 2009).

Airborne thickness measurements represent a big step above ground-based measurements in terms of spatial coverage. However, the polar regions are difficult locations in which to work and access, rendering many missions too costly to routinely fly. Additionally, airborne measurements still do not provide basin-scale estimates of thickness. For this, satellite platforms have been used. Scientific satellites have been in orbit for dozens of years and used for sea ice research for about the last 40 (Parkinson, 2019). These early instruments consisted of passive sensors, meaning they detect reflected sunlight and emitted radiation from the surface. For sea ice research, passive sensors typically are used for monitoring sea ice extent (Comiso et al., 1997; Parkinson, 2014; Spreen and Kern, 2016) though studies have been able to estimate snow depth on sea ice under certain conditions (Markus and Cavalieri, 1998). To measure sea ice thickness from space, active sensors - namely altimeters - need to be used. Satellite altimetry has been employed for sea ice research since the 1990's and has continued, virtually uninterrupted, into 2021 (Fig.

1.6).

Altimetric retrievals of sea ice thickness have primarily focused on Arctic sea ice, since more snow depth on sea ice information exists (Petty et al., 2017). These estimates have come from both laser and radar altimeters (discussed in Chapter 2) and have been successfully used to initialize sea ice models/forecasts and to evaluate climate model simulations (Allard et al., 2018; Blockley and Andrew Peterson, 2018; Mu et al., 2018; Schröder et al., 2019; Stroeve et al., 2014). In the Antarctic, there is a substantial lack of basin-scale sea ice thickness observations mainly due to the lack of available snow depth information (Petty et al., 2017; Price et al., 2019). While techniques involving laser altimetry have been able to provide some estimate of thickness using assumptions or parameterizations of the snow cover (Kern et al., 2016; Kurtz and Markus, 2012; Li et al., 2018), the uncertainty surrounding radar penetration has precluded any Antarctic sea ice thickness estimates from satellite radar altimetry (Paul et al., 2018; Schwegmann et al., 2016). This deficiency in radar-derived thickness estimates is problematic for validating sea ice and climate models in the Southern Ocean (Massonnet et al., 2013; Petty et al., 2017). More discussion on satellite altimetry is provided in subsequent chapters.

1.2.2 Past trends in sea ice thickness

Trends in sea ice thickness have been uncovered utilizing early submarine and more recent satellite data. Kwok and Rothrock (2009) combined submarine data with thickness estimates from NASA's Ice, Cloud, and land Elevation Satellite

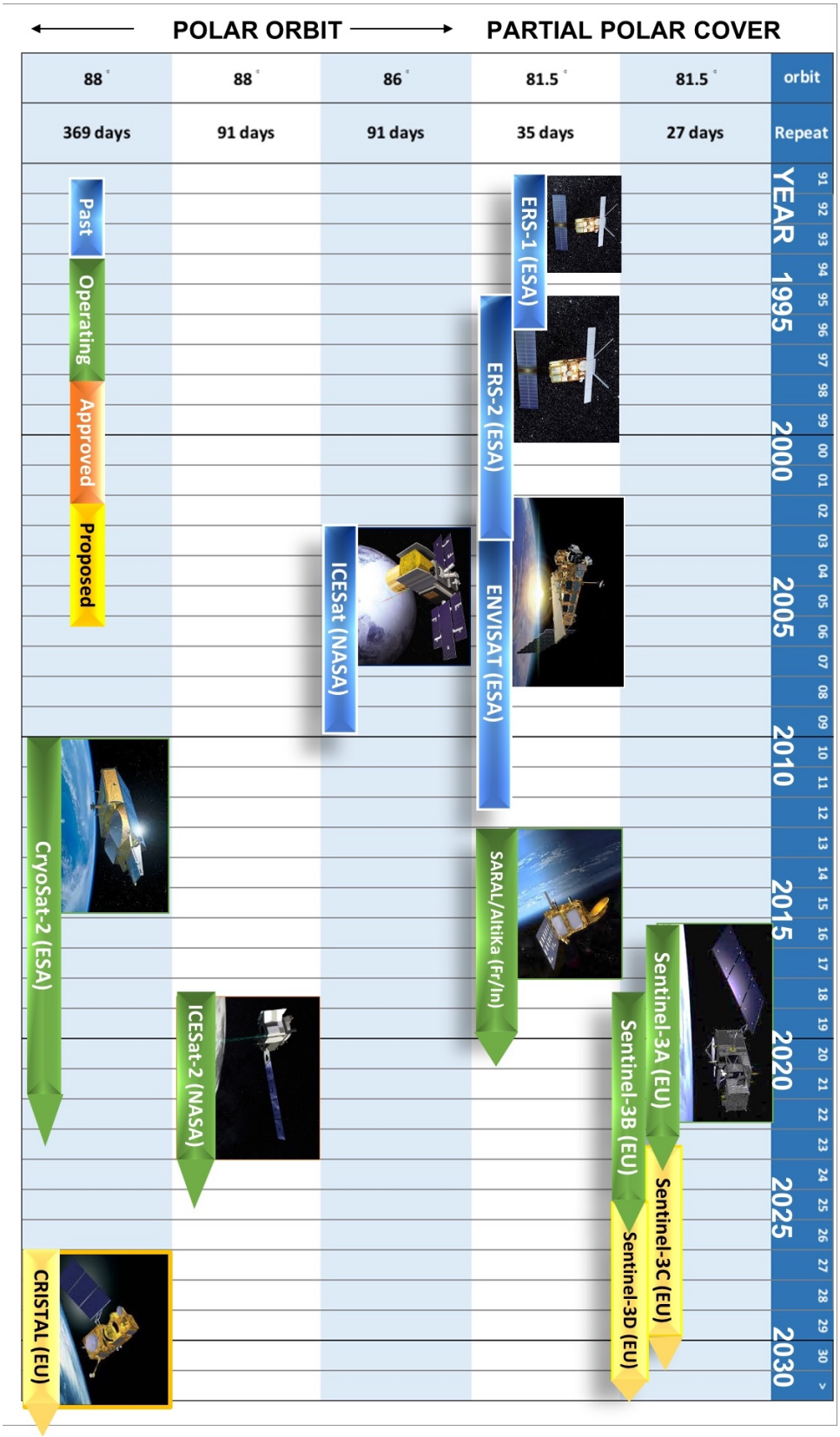

Figure 1.6: Timeline of past and proposed satellite altimeters. From NOAA Laboratory for Satellite Altimetry.

(ICESat) to find a thinning of the Arctic sea ice cover of 1.75 m from 1980 to 2008 - an "astonishing" rate of over 6 cm per year over that span (Fig. 1.7). Other works have deduced thickness from ice age data derived from passive sensors, and have found that the Arctic is, in general, getting younger (Fowler et al., 2004; Maslanik et al., 2007). This means that more of the older, thicker, MYI is melting while less of the thinner ice is surviving melt seasons to become MYI. Overall, this leads to more of the Arctic being covered with thinner ice, which leads to a thinner thickness distribution on average.

In the Antarctic, the substantial lack in basin-scale sea ice thickness observations discussed above has prevented long-term trends from being uncovered. Nevertheless, Kurtz and Markus (2012) used all available data from ICESat, along with an assumption of the snow cover, to find a slight thinning of around 0.02 m between 2003 and 2008, with some regions thinning more and others thickening (Fig. 1.7). With the launch of ICESat-2 in October 2018, a new altimetry time series has begun from which further change can be detected (Abdalati et al., 2010; Markus et al., 2017).

Despite the short trends in Antarctic sea ice thickness from altimetry, models have been successfully used to recreate past thickness distributions and interannual change. Holland (2014) used a model of the Southern Ocean forced by reanalysis to assess trends in thickness and volume between 1992 and 2010. They found an overall thickening of the Antarctic ice pack at the rate of 1.2 mm / year over that 18 year range, that was caused in part by wind-driven dynamics (Holland, 2014). Similarly, Massonnet et al. (2013) found a modeled increase in sea ice volume between 1980-

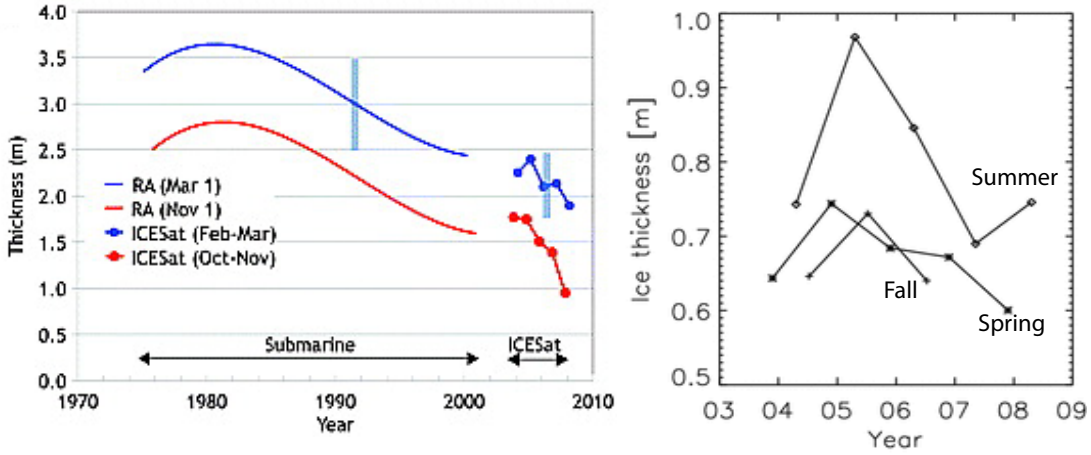

Figure 1.7: Past trends in (left) Arctic and (right) Antarctic sea ice thickness. Adapted from Kwok and Rothrock (2009) and Kurtz and Markus (2012).

2008 by using a data assimilation approach and a coupled ocean-sea ice model. Both of these trends in thickness and volume followed similar, small positive trend in sea ice extent. While these modelling works proved to be useful, they would sill benefit from a longer time series of observations from which to better validate the results.

1.2.3 Future projections of sea ice thickness

Based off the observed past trends in sea ice thickness, it is perhaps no surprise that similar trends are likely to continue in the future. Arctic sea ice is projected to continue a decline in sea ice age, which would translate to a thinner overall ice pack (Hunke and Bitz, 2009). While the Intergovernmental Panel on Climate Change (IPCC) Fifth Assessment Report (AR5) states that there is high confidence for a decline in Arctic sea ice extent, it does recognize that there is a range in the ability to simulate observed thickness patterns, reducing confidence in modeled thickness estimates (IPCC, 2014). Nevertheless, Holland et al. (2006) found a future decline in

modeled Arctic sea ice thickness of around 1 m by 2100, the likelihood and severity of which, they argued, could be mitigated through a reduction in greenhouse gas emissions.

In the Antarctic, projections are even more so complicated by the lack of available knowledge on past and current sea ice thickness trends. Holland (2014) found links between Antarctic sea ice extent and thickness over their study period, suggesting future trends in extent could give some idea into the changes in thickness. However, the IPCC AR5 asserts low confidence in Antarctic-wide sea ice extent projections given offsetting regional trends - that current models are not able to replicate - and lack of available validation data (IPCC, 2014). Sadai et al. (2020) studied climate effects of a melting Antarctic ice sheet to the year 2250, and found that a large influx of freshwater into the Southern Ocean could raise the ocean freezing point, which in turn would stratify the water column, reduce convection, and result in a substantial thickening of sea ice along the coast. These findings (along with other modeled studies of Antarctic sea ice thickness), however, use models that once again lack calibration and validation data in the Southern Ocean and therefore exhibit lower confidence in the resulting thickness distribution (Petty et al., 2017; Williams et al., 2015).

For Antarctic sea ice especially, it is clear that the current lack of available basin-scale sea ice thickness data is limiting not just our understanding of the current thickness distributions or observed trends, but is also limiting our ability to model future projections of thickness.

1.3 Dissertation goals and overview

Given the importance of Antarctic sea ice and the current lack in knowledge of its basin-wide thickness, it is evident that new estimates of pan-Antarctic sea ice thickness are needed to better detect and understand recent changes in the Southern Hemisphere sea ice cover. This dissertation will address the above need through the development and assessment of new retrievals of Antarctic sea ice physical properties from satellite radar altimetry. The overarching goal of this work is to provide estimates of Antarctic sea ice thickness from CryoSat-2 for the decade-long mission, which do not currently exist. In order to achieve this goal, this work will undertake the following:

- Develop a new technique to retrieve Antarctic sea ice snow freeboard utilizing a physical model and waveform fitting technique
- Assess the retrieved snow freeboards using coincident data from satellite laser altimetry
- Estimate the snow depth on sea ice from the retrieved parameters and use the snow depths in calculations of sea ice thickness

The subsequent chapters of this dissertation are organized as follows:

- Chapter 2 provides background on satellite altimetry, methods to retrieve sea ice properties, and covers the current state of radar altimetry (specifically CryoSat-2) algorithms for retrieving sea ice freeboard and thickness. Also, further motivation for the dissertation is provided.

- Chapter 3 focuses on the development of a physical model and retrieval algorithm that incorporates the scattering impacts of the snow layer on retrieving sea ice properties. Independent airborne data showcasing scattering effects from the air-snow interface are also shown, as are independent comparisons of sea ice elevation. This chapter was originally published in *The Cryosphere* (Fons and Kurtz, 2019).

- Chapter 4 concerns freeboard retrievals using this method, and discusses improvements made to the original algorithm from Chapter 3. A more thorough validation is shown using along-track and basin-scale comparisons to ICESat-2. This chapter covers work submitted to *Earth and Space Science* (Fons et al., 2021).

- Chapter 5 covers ice freeboard and snow depth retrievals using this algorithm, and combines information from previous chapters to estimate Antarctic sea ice thickness and volume. A 10+ year time series of Antarctic sea ice thickness from CryoSat-2 is shown, along with observed trends in the data.

- Chapter 6 explores the potential to apply this algorithm to Arctic sea ice, and compares retrieved properties to airborne and ground-based measurements. Potential applications for Arctic snow depth retrievals are also discussed.

- Chapter 7 concludes this dissertation by providing summaries from each chapter, as well as potential avenues for future research.

Chapter 2: Background and Motivation

This chapter provides a background into satellite altimetry and its use in sea ice research. Current methods for retrieving sea ice properties using CryoSat-2 are discussed, along with their shortcomings. This chapter concludes with motivation for the work covered in the remainder of the dissertation.

2.1 Satellite altimetry

Satellite altimetry has been used since the 1970's as a method to measure the height of the earth surface (Haas, 2016; Mcgoogan et al., 1974). The concept of space-borne altimetry is simple: an instrument in low-earth orbit emits a pulse of radiation towards the earth and measures the time it takes for that pulse to return to a detector on the instrument. Combining that time with the speed of the wave through the atmosphere, one can calculate the range from the surface to the spacecraft, and, combining that range with a precise knowledge of the spacecraft's altitude above some reference surface, a useful quantity of surface elevation can be deduced (Carton, 1989). In reality, the process of determining surface elevation to a high degree of accuracy and fidelity from hundreds of kilometers away can be more nuanced and difficult. This process varies depending on the type of altime-

ter, the wavelength utilized, and many internal (instrument impacts) and external (atmosphere and geophysical impacts) factors.

Earth-observing satellite altimeters are typically designed to operate in two different wavelength groups: radar (radio detection and ranging), which includes microwave radiation ranging from about 3 to 35 GHz, and lidar (light detection and ranging, hereafter referred to as 'laser'), which includes visible and near-infrared wavelengths ranging from about 400 to over 1000 nm (Rosmorduc et al., 2016). These subsets differ in scattering and absorption properties, and therefore have different information encapsulated in their returns. The longer-wavelength radar pulses tend not to be affected by atmospheric conditions while the shorter-wavelength laser pulses tend to be scattered away by the presence of thick clouds (Brenner et al., 2007). Wavelength differences are important over sea ice, where Ku-band radar pulses tend to penetrate into snow layers while laser pulses tend to scatter predominantly from the snow surface (Fig. 2.1, Giles et al. 2007). The focus of this work is on radar altimetry and specifically the CryoSat-2 radar altimeter, which operates in the Ku-band frequency at 13.6 GHz (Wingham et al., 2006). ICESat-2 data are also used throughout, which is a laser operating in the visible part of the spectrum with a 532 nm wavelength (Markus et al., 2017; Neumann et al., 2019). Unless otherwise noted, mentions in this work of 'radar altimetry' will refer to Ku-band altimetry, while 'laser altimetry' will typically reference visible wavelengths.

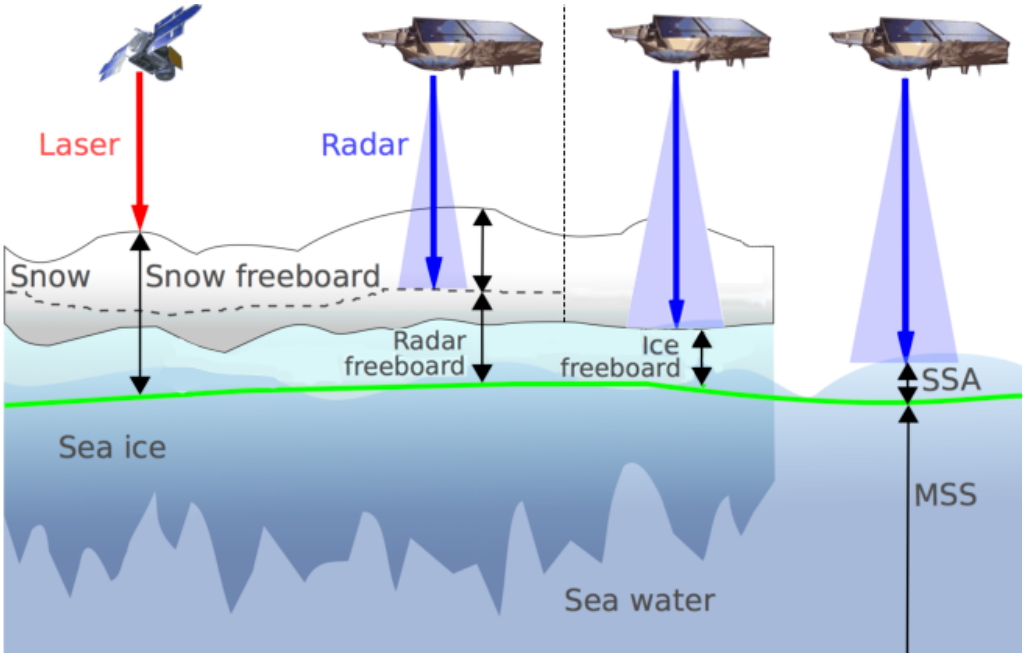

Figure 2.1: Penetration depths and subsequent sea ice freeboards retrieved from laser altimetry (left) and radar altimetry (under different snow layer conditions/assumptions, middle left and right). Retrieval of the sea surface anomaly (SSA) from the mean sea surface (MSS) is given on the right. Adapted from Ricker et al. (2014).

2.2 Radar altimetry and CryoSat-2

Radar altimeters typically operate by sending a pulse or burst of pulses of microwave radiation down to the surface and detecting the return power spectrum (Rosmorduc et al., 2016). These return pulses are also called echoes, returns, and waveforms, and represent spectra of return power over time that differ in shape depending on the type of the altimeter. Radar altimeters typically come in one of two types: beam-limited or pulse-limited. Both of these designations refer to the limiting factor of the radar return. For beam-limited altimeters, the shape of the return pulse is determined by the width of the beam, while for pulse-limited altimeters the shape of the return pulse is determined by the length of the emitted

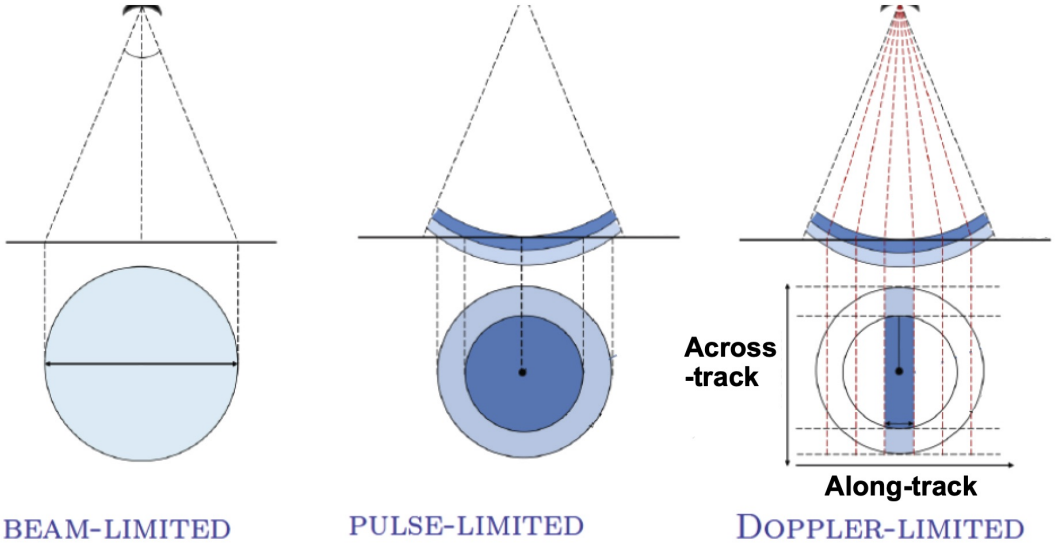

Figure 2.2: Differences in radar footprints between beam-limited (left), pulse-limited (middle) and SAR (Doppler-limited, right) altimeters. Adapted from Sørensen (2016).

pulse (Fig. 2.2, Martin et al. 1983; Rosmorduc et al. 2016). To have a reasonably-sized footprint from a radar instrument, a beam-limited altimeter would need to have a very large antenna that is impractical for spacecraft. Therefore, most radar altimeters use a pulse-limited platform (Cipollini and Snaith, 2013).

Outside of the traditional beam- and pulse-limited altimeters, there exists another class of altimetry referred to as Synthetic Aperture Radar (SAR) altimetry, or delay-Doppler altimetry. SAR altimetry utilizes the along-track motion of the spacecraft to create a synthetically-large antenna and coherently processes groups of return echoes based on their polarization (Drinkwater et al., 2004; Raney, 1998; Wingham et al., 2006). This processing effectively creates strips of footprints within the area illuminated by the radar pulse on the surface (Fig. 2.2). SAR processing is used by the satellite altimeter CryoSat-2.

As mentioned, CryoSat-2 is a Ku-band radar altimeter launched by the European Space Agency (ESA) in April of 2010. It is the successor of CryoSat, which attempted launch in 2006 but failed to reach orbit (Wingham et al., 2006). Since launch, CryoSat-2 has provided consistent sampling of Earth's surface with a focus on land and sea ice in the polar regions, recording 10 years on orbit in April of 2020 and continuing to record data at the time of this writing. CryoSat-2 operates in three distinct modes: Low resolution mode (LRM), Synthetic Aperture (SAR) mode, and Synthetic Aperture - Interferometric (SARIn) mode (Drinkwater et al., 2004; Wingham et al., 2006). LRM is a traditional pulse-limited mode that is used over ice sheets where large changes in topography are not expected. The pulse-limited footprint has an area of around 2.15 km^2 (Scagliola, 2013). SAR mode is used primarily over sea ice zones in both hemispheres. SAR processing results in an along-track footprint that is pulse-Doppler-limited, while maintaining a footprint that is pulse-limited in the across-track direction. The resulting footprint is approximately 1.65 km across-track and 360 m along-track, though strong-scattering returns can come from the much larger beam-limited footprint (Scagliola, 2013). The same pulse-Doppler-limited footprint is present in the SARIn mode, which additionally utilizes the interferometric capabilities of the instrument to record the phase and arrival angle of the return pulse. SARIn data are typically collected along the coastlines and in mountainous regions (Wingham et al., 2006). More information on the CryoSat-2 data is given in Chapter 3.

In each mode, CryoSat-2 can only detect elevations from within a given "window" of where the surface is expected to be. This window is 60 m in LRM and

SAR modes and 240 m in SARIn mode to handle the larger changes in surface slope (European Space Agency, 2019a). The received echo falls somewhere within the window depending on the surface height. In order to retrieve surface elevation from the CryoSat-2 echoes, one must find the location of the surface (as a function of the return time) along the waveform. This surface finding is done through a process called 'retracking'. Retracking is the method of picking out the surface along a radar altimeter waveform, and many different retracking methods exist depending on the surface or parameter being studied (Garcia et al., 2014; Ricker et al., 2014; Rosmorduc et al., 2016). CryoSat-2 retracking is done to retrieve sea surface heights (Jain et al., 2015), wind and significant wave heights (Abdalla et al., 2018), and elevations of inland water, ice sheets, and sea ice (Helm et al., 2014; Laxon et al., 2013; Nielsen et al., 2015). The retracking process provides the retracking correction, discussed in the next section.

2.3 Sea ice freeboard and thickness from CryoSat-2

CryoSat-2 data have been used over sea ice primarily to enable estimation of its thickness. As noted in Chapter 1, sea ice thickness is defined as the height of the sea ice both below and above the water level. This quantity cannot be directly measured from space (Kwok, 2011) but instead must be deduced from other quantities and mathematical relationships. Typically, radar altimetry-derived sea ice thickness is given by:

$$h_i = \left(\frac{\rho_w}{\rho_w - \rho_i}\right) h_{fi} + \left(\frac{\rho_s}{\rho_w - \rho_i}\right) h_s, \tag{2.1}$$

where h_i is the sea ice thickness, $h_{f\,i}$ is the ice freeboard, h_s is the snow depth, ρ_w is the density of seawater, ρ_i is the density of sea ice, and ρ_s is the density of snow. This equation is derived from the assumption of hydrostatic equilibrium (given in Appendix A).

In Equation 2.1, freeboard is the quantity that is able to be retrieved from altimetry, and therefore is the necessary first step in estimating thickness. Freeboard is defined as the height of the ice above the water level. There are two distinct types of freeboard: the "snow" (or "total") freeboard, which is the height of the snow and ice above the local sea surface, and the "ice" freeboard, which is defined as the height of just the ice above the local sea surface. Snow freeboard is typically retrieved from a laser altimeter, while the ice freeboard is commonly retrieved from a radar altimeter such as CryoSat-2. Studies that do not account for radar wave speed slowdown within the snowpack retrieve what is known as "radar freeboard", which is so named to acknowledge the non-physical "interface" that is retrieved. The retrieved height from radar freeboards is typically located within the snow layer at a level higher than the snow-ice interface. Figure 2.1 shows examples of the sea ice freeboard measured from different satellite altimeters. The following sections step through the process of retrieving sea ice freeboard and estimating thickness from CryoSat-2.

2.3.1 Elevation retrieval

The first step in retrieving sea ice freeboard and thus the sea ice thickness is to retrieve the elevation of the sea ice and local sea surface. Elevation (h_e) of the surface is given by:

$$h_e = A - R_0 \tag{2.2}$$

where A is the altitude of the satellite center of gravity above the World Geodetic System 1984 (WGS84) ellipsoid andR_n is the range from the satellite to the surface, given by:

$$R_0 = R_n + c_r + c_g \tag{2.3}$$

where R_n is the raw range computed from the time delay to a reference point of the range window, c_r is the retracking correction, and c_g is the geophysical correction. Both A and R_n are given in the CryoSat-2 data products (European Space Agency, 2019a). Through Equations 2.2 and 2.3, the raw range is converted to a more useful unit of measure, which is elevation of the surface above the WGS84 ellipsoid (European Space Agency, 2019a). This is done by accounting for geophysical impacts to the radar pulse (geophysical correction) the location of the surface along the waveform (retracking correction). A summary of these terms is provided in Fig. 2.3.

2.3.2 Geophysical corrections

Geophysical corrections are values added to the ranges to account for the effects of physical phenomena on the radar pulse as well as on the surface of interest (Rosmorduc et al., 2016). For sea ice, they include effects from the ocean surface, the atmosphere, and tides. The individual corrections applied to SAR / SARIn data over sea ice typically are derived from models and are discussed in this section.

The ocean surface correction includes the Inverse Barometric correction (IBC). The IBC accounts for variations in the sea surface height due to atmospheric pressure variations (European Space Agency, 2019a). Values come from the Meteo-France Multi-mission ground segment of Altimetry, Orbitography and precise localization (SSALTO) (Carrère and Lyard, 2003) and range from -15 cm to +15 cm.

The atmospheric propagation corrections include the Dry Tropospheric correction (DTC), the Wet Tropospheric correction (WTC), and the Ionosphere correction (IC). The DTC and WTC are corrections for refraction and path delay of the radar beam due to the dry gas (DTC) and water vapor (WTC) respectively. The DTC is computed by the CryoSat-2 processors using dynamic mean surface pressure values from the European Center for Medium-Range Weather Forecasts (ECMWF) model, and ranges in value from 1.7 to 2.5 m (European Space Agency, 2019a). The WTC is sourced from Meteo-France SSALTO and is based on the ECMWF model, with a range between 0 to 50 cm. The IC accounts for the path delay brought on by the free electron content of the ionosphere and also ranges between 0 and 50 cm. The IC is calculated from both the Global Ionosphere Map (GIM) and the Bent model; the

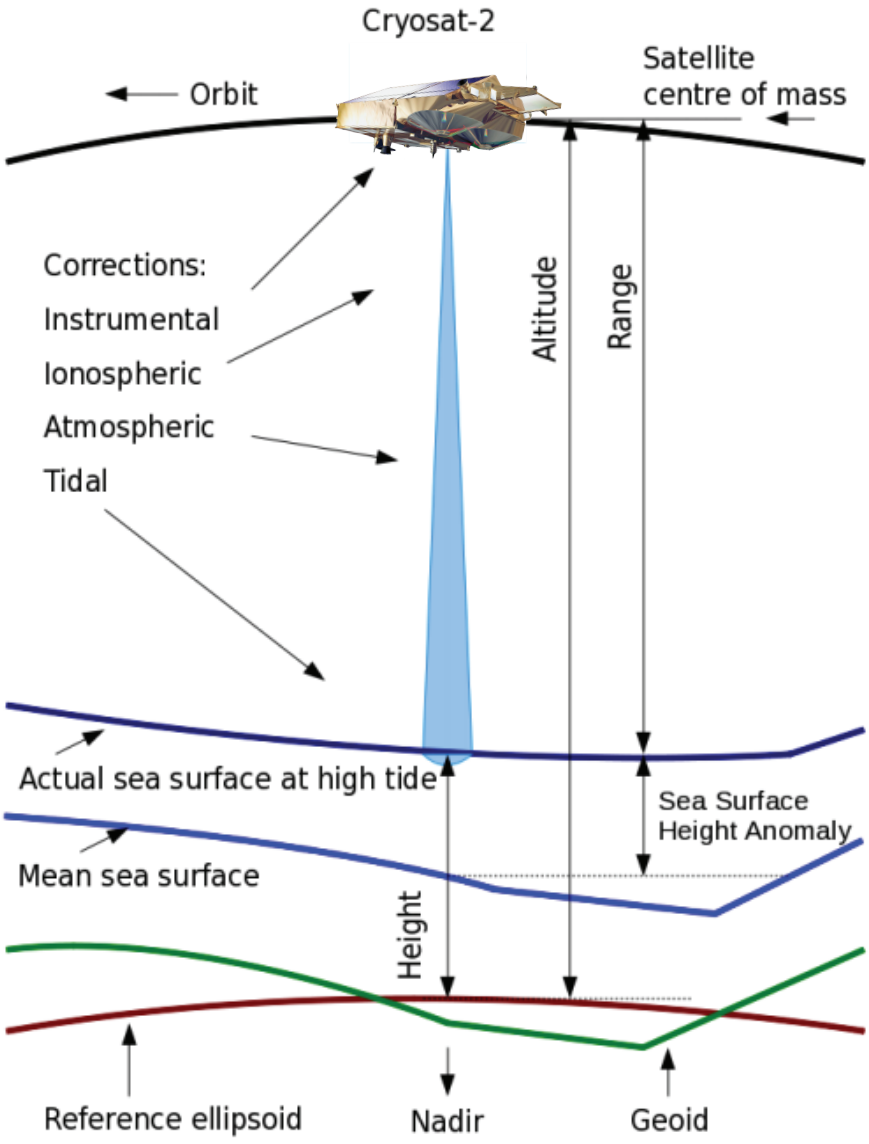

Figure 2.3: Geophysical corrections and reference surfaces applied to CryoSat-2 data (Eqns. 2.2 and 2.3) to retrieve elevation. From European Space Agency (2019a).

Bent model is only applied when the GIM data are not available (European Space Agency, 2019a).

The tidal corrections are used to adjust the range to appear as if it originated from a mean-tide or tide-free sea surface (CryoSat-2 data are provided in the mean-tide system; European Space Agency 2019a). They include the Ocean Tide (OT), Long Period Equilibrium Tide (LPET), Ocean Loading Tide (OLT), Solid Earth Tide (SET), and Geocentric Polar Tide (GPT). The OT removes the effect of local tides on the elevations, and ranges from -50 cm to +50 cm (European Space Agency, 2019a). It is derived from the Finite Element Solution 2004 (FES2004) tide model (Lyard et al., 2006). The LPET takes into account the low-frequency tidal effects brought on by gravitational attraction, and is typical small (<1 cm, European Space Agency 2019a). The OLT ranges from -2 cm to +2 cm and accounts for the deformation of the Earth's crust due to the weight of the ocean (European Space Agency, 2019a). The OLT is also computed using the FES2004 model. The SET removes deformation of the earth due to tidal forces from the sun and moon, and is derived from the Cartwright tide model (Cartwright and Edden, 1973) ranging from -30 cm to +30 cm (European Space Agency, 2019a). Finally, the GPT accounts for the low-frequency distortion of the Earth due to variations in the centrifugal force, which induces perturbations in the Earth's rotational axis. This correction is small, ranging from -2 cm to +2 cm and is derived using polar location files sourced from SSALTO (European Space Agency, 2019a).

2.3.3 Retracking correction

The last step in computing absolute elevation is determining the retracking correction. As mentioned above, retracking is the process of finding the location of the surface along the waveform. The retracking point over sea ice is most often found on the leading edge of the waveform, and is given as a function of time. The retracking correction, then, is given as an offset value – also in units of time – from the reference point of the range window (Fig. 2.4). While geophysical corrections remain mostly constant across all different methods of retrieving sea ice elevation and freeboard using CryoSat-2, the retracking correction is where the retrievals differ. Each method uses a slightly different retracking technique and therefore end up with slightly different elevation and freeboard distributions. The two most common retracking methods include empirical retrackers, which find the retracking point using power threshold values verified by field and airborne measurements, and physical retrackers, which find the retracking point using a physically-based model of the waveform and fitting the model to the CryoSat-2 waveform. These techniques and associated publications are reviewed in Section 2.4.

2.3.4 Surface type discrimination

Once all the components of Equations 2.2 and 2.3 are found and the elevation is computed, the next step in calculating the freeboard is to classify the CryoSat-2 waveforms into their respective surface types, so that the elevations of the sea surface and ice surface can be differentiated. It has been found that radar returns

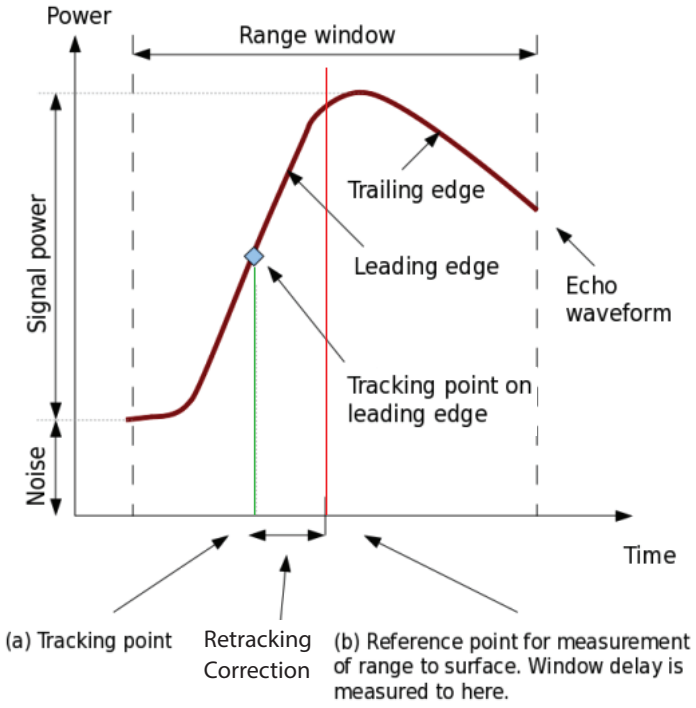

Figure 2.4: An idealized CryoSat-2 waveform with characteristics labeled that are used to determine the retracking correction. From European Space Agency (2019a).

from sea ice are typically diffuse, with a relatively low return power value (10-30 dBf, Kwok and Cunningham 2015). This shape is brought on by the roughness of the surface as well as the volume scattering from the snow and ice layers. On the other hand, returns from sea ice leads typically have much greater return power values (>40 dBf) and are much more specular in shape (Fig. 2.5). These scattering characteristics can be used to classify each waveform into groups relating to their surface type.

Like with retracking, the surface type discrimination procedure is often done in different ways. However, almost all methods use some combination of waveform characteristics to distinguish between surface types. Possible surface types include sea ice/floe-type waveforms, lead-type waveforms, ocean-type waveforms,

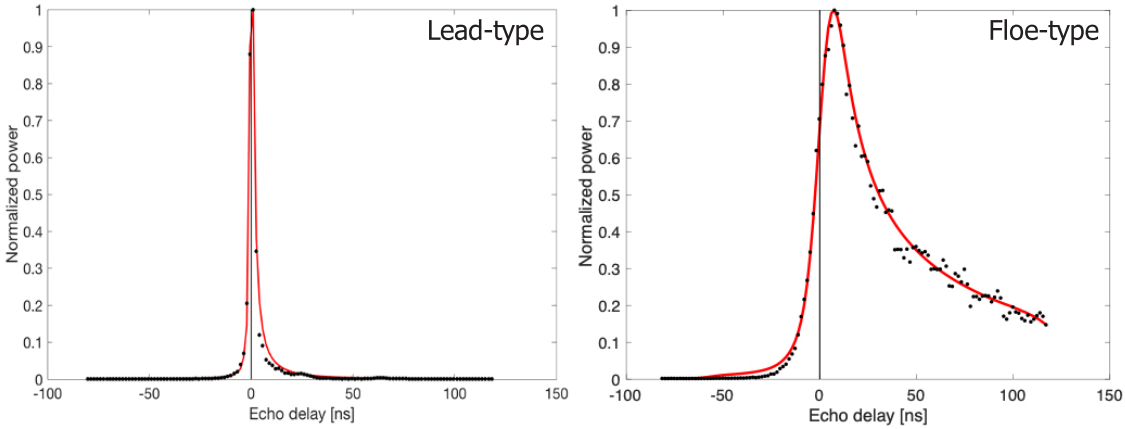

Figure 2.5: CryoSat-2 waveforms classified as lead-type (left) and floe-type (right) using the process from Kurtz et al. (2014). Black points represent actual CryoSat-2 data, while red lines show a best-fit modeled waveform (discussed in Chapter 3).

and mixed/ambiguous waveforms. Laxon et al. (2013) used the parameters of pulse peakiness (PP) and stack standard deviation (SSD) to distinguish between lead and floe waveforms. Most methods used these parameters as well (Guerreiro et al., 2017; Kurtz et al., 2014; Landy et al., 2020; Tilling et al., 2018), with others also incorporating parameters of kurtosis and offset center of gravity (OCOG) width (Ricker et al., 2014) as well as machine learning methods (Lee et al., 2016). While the thresholds vary between methods, in general, the specular lead-type waveforms have a larger PP and a smaller SSD, while floe-type waveforms have a smaller PP and larger SSD. Figure 2.5 shows examples of lead and floe-type waveforms distinguished by the classification scheme in Kurtz et al. (2014).

2.3.5 Freeboard calculation

Following the surface type discrimination and elevation retrieval, the classified waveforms and their respective elevations are combined to compute the sea ice

freeboard. Very simply, the freeboard is defined as:

$$h_f = h_e - ssh, \tag{2.4}$$

where h_f is the freeboard, h_e is the elevation of the ice surface and ssh is the elevation of the local sea surface (sea surface height, hereafter SSH). From altimetry, SSH is generally found by averaging the elevations of lead-type points within a segment ranging from 10-25 km (Kwok and Cunningham, 2015) or by interpolating between lead points on either side of floe-type returns (Tilling et al., 2018). Each SSH segment or interpolated value is subtracted from the individual sea ice elevation measurements, resulting in an individual freeboard measurement for each floe-type waveform.

Since Ku-band radar pulses typically penetrate the snow layer, it is important to account for the speed of the radar wave in the snowpack when calculating freeboard, which slows down due to the different dielectric constants of air and snow (Mallett et al., 2020). As mentioned above, studies that neglect corrections for wave speeds tend to retrieve surfaces higher than what is assumed, resulting in radar freeboards, while those who correct for this effect are said to retrieve their respective assumed surface (usually assumed as the snow-ice interface) which leads to ice freeboard. This corrections requires a knowledge of the snow depth, discussed in the next section.

2.3.6 Sea ice thickness estimation

Once ice freeboard is retrieved from the CryoSat-2 data, it can be combined with other datasets and assumptions to estimate the sea ice thickness. As shown in Equation 2.1, the densities of the sea ice, snow cover, and seawater are needed to find thickness under the hydrostatic assumption. Studies of Arctic sea ice thickness typically utilize a single value for seawater density - usually 1024 kg/m^3 (Wadhams et al., 1992) - and ice density based on ice type - around 916 kg/m^3 for FYI and 882 kg/m^3 for MYI (Alexandrov et al., 2010). Snow density values in the Arctic typically come from a climatology of density values that vary between ∼200 to ∼350 kg/m^3 (Warren et al., 1999). Even less is known about the distribution of sea ice and snow density in the Antarctic, but similar values are currently used (Table 2.1). All of these values can vary over small length scales, and therefore some uncertainty exists in using these single parameterizations (Kurtz and Markus, 2012; Landy et al., 2020; Mallett et al., 2020). Figure 2.6 shows sea ice density profiles for sea ice cores collected during the MOSAiC expedition between March and May 2020 in the Arctic Ocean. While the bulk density value is near the expected value of 916 kg/m^3, one can see the small-scale variability in the vertical density profile - especially in the SYI cores - brought on partially by the presence of snow-ice (near the top of the core profiles) and porous skeletal layers at the very bottom of the ice cores.

A primary difficulty of estimating sea ice thickness from satellite comes from the snow depth parameter (h_s) and the lack of widely available basin-scale snow depth measurements. Currently, the most commonly-used methods to incorporate

Study	**Seawater density** [kg / m^3]	**Ice density** [kg / m^3]	**Snow density** [kg / m^3]
Kurtz and Markus (2012)	1024	900 ± 20 (Spring) 875 ± 20 (Summer) 900 ± 20 (Fall)	320 ± 50 (Spring) 350 ± 50 (Summer) 340 ± 50 (Fall)
Kern et al. (2016)	1023.9	915 ± 20	300
Li et al. (2018)	1023.9	915	300
Kacimi and Kwok (2020)	1024	917	320 ± 70
This study	1024	917± 20	320± 50

Table 2.1: Density values of snow, ice, and seawater used in previous studies of satellite laser altimeter-derived Antarctic sea ice thickness. Values used in Chapter 5 are also given.

snow depth in CryoSat-2 thickness estimates include utilizing snow depth climatologies (such as from Warren et al. (1999)) or models (such as from Petty et al. (2018); Liston et al. (2018), and others), while other methods have attempted to use snow depth data derived from satellite sensors alone (such as from Kacimi and Kwok (2020); Kwok et al. (2020c); Lawrence et al. (2018); Markus and Cavalieri (1998)). In addition to being a necessary component in the thickness equation, the snow layer and its scattering properties can also impact the freeboard retrievals themselves, and is therefore an important component of this dissertation and is discussed thoroughly in subsequent sections and chapters.

2.4 Current state of CryoSat-2 sea ice freeboard retrievals

The previous section outlined the basic formula for retrieving sea ice freeboard from satellite altimetry and using these retrievals to estimate thickness. Most studies using CryoSat-2 for this purpose follow that general outline, with slight differences in the elevation retrievals as well as the freeboard and thickness cal-

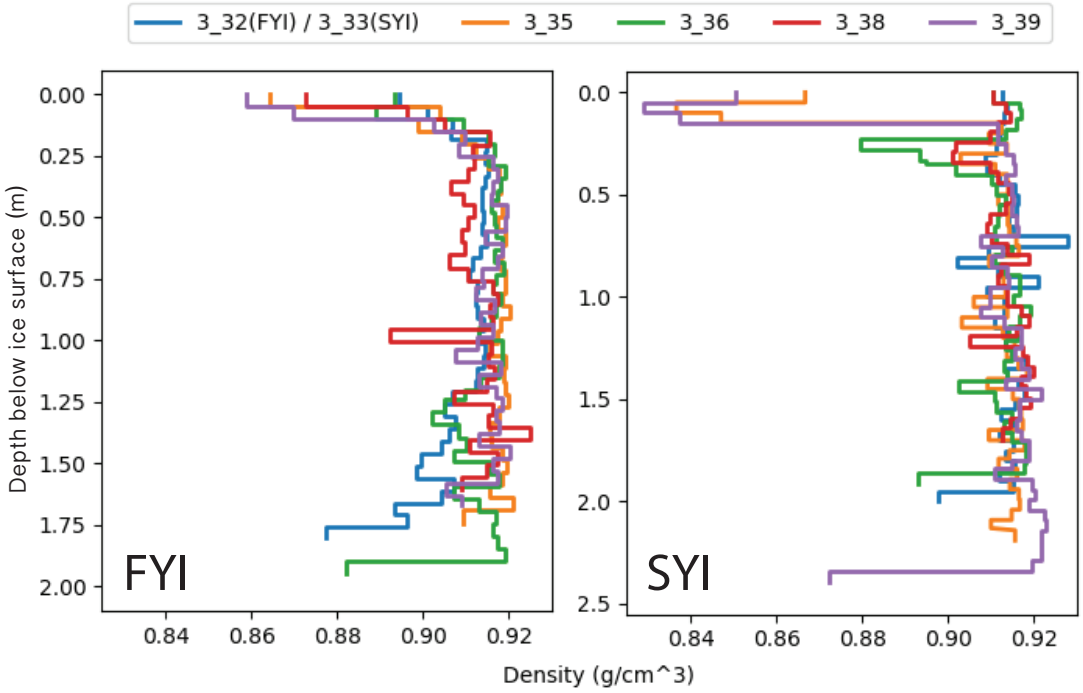

Figure 2.6: Ice core density profiles from FYI (left) and SYI (right) sites collected from Arctic sea ice in 2020 during the MOSAiC Expedition. Each color line represents a different ice core, where 3_XX refers to the week of the MOSAiC expedition in which the core was collected. Data are recorded in 5 cm sections.

culations. Geophysical corrections are generally consistent between retrievals and therefore differences in elevation stem largely from the choice of retracking method. As mentioned above, there are typically two main retracking techniques used in CryoSat-2 retrievals: empirical and physical.

2.4.1 Empirical retracking

Empirical retrackers are the most prevalent type of retracking method due to their simplicity and computational efficiency. Laxon et al. (2013) was the first to show Arctic sea ice thickness retrievals from CryoSat-2, and, in the process, set the standard for empirical retracking. In this work, they modified a retracker designed for the European Remote Sensing satellite (ERS-1) (Giles et al., 2008; Laxon et al., 2003) for use with the CryoSat-2 SAR waveforms. They deduced empirically that the return time at which the waveform leading edge reached 70% of the maximum power level provided a good estimate of surface location. From there, the retracking correction could be found and elevation computed (Fig. 2.4). For lead elevations, they found that the specular return was easier to model and could be fit with a combined Gaussian-exponential function to enable the surface retracking. Tilling et al. (2018) used this retracker to estimate Arctic sea ice thickness and volume, creating an operational product put out by the Centre for Polar Observation and Modelling (CPOM).

Ricker et al. (2014) experimented with different power threshold values in their threshold first-maximum retracker algorithm (TFMRA) and showed that the

retrieved mean Arctic freeboard values can vary as much as 10 cm (17 cm) for FYI (MYI) between 40% and 80% thresholds. Their comparison to laser altimeter measurements showed that the radar was penetrating the snow surface with all thresholds used, but that they varied in terms of elevation. No direct in-situ measurements of snow-ice interface elevations were available, and thus they could not definitively say which threshold was most accurate. Since Ricker et al. (2014), others (e.g. Hendricks et al. 2016) have used a variation of the TFMRA to retrieve sea ice freeboard and thickness, including Lee et al. (2016), who used a 40% threshold for their retrievals and combined it with a machine learning approach for surface-type classification.

Kwok and Cunningham (2015) used a slightly different empirical approach to retrieve sea ice elevation from CryoSat-2, electing to utilize the variables P_c and W_c, the peak power and the width of the centroid relative to the peak, respectively, to find the retracking point. This method, known as an OCOG-style retracker (Rosmorduc et al., 2016), has been used in other studies to investigate temporal changes in thickness and volume and compare to other satellite and in situ measurements of thickness (Kwok and Cunningham, 2015; Kwok and Kacimi, 2018; Kwok and Markus, 2018).

The empirical retracking algorithms discussed above all are focused on Arctic sea ice. While no dedicated empirical retracking algorithms have been designed exclusively for Antarctic sea ice, some studies have applied the techniques above to sea ice in the Southern Ocean. The TFMRA algorithm was used as part of the ESA Climate Change Initiative (CCI) sea ice project to retrieve global sea ice freeboard

and thickness. Schwegmann et al. (2016) and Paul et al. (2018) used the TFMRA to retrieve Antarctic sea ice elevation and freeboard to be able to reconcile with Envisat. Schwegmann et al. (2016) did not correct for wave speed propagation through snow, and therefore retrieved the radar freeboard, while Paul et al. (2018) attempted to use passive microwave-derived snow depths to correct for this effect and estimate the ice freeboard. Other studies using this retracker compared CryoSat-2 retrievals with EM measurements of sea ice thickness in certain areas such as the Ross sea (Price et al., 2015). The OCOG-style retracker put forth in Kwok and Cunningham (2015) was also used to estimate thickness in certain locations, focusing mainly on the Weddell sea (Kwok and Kacimi, 2018). The potential for basin-scale estimates of Antarctic sea ice freeboard was also explored with this method, both stand-alone with CryoSat-2 and in combination with ICESat-2 for snow depth retrievals (Kacimi and Kwok, 2020; Kwok and Kacimi, 2018).

2.4.2 Physical retracking

While empirical retracking typically relies on a fixed waveform power threshold to pick out the surface, physical retrackers use a different technique altogether. Instead, physical retrackers estimate the range by constructing a modeled waveform based on the physics of the EM interaction between the transmitted pulse and the scattering surface (Quartly et al., 2019) and fitting the modeled waveform to the CryoSat-2 data. In minimizing the difference between the modeled waveform and the data, one can estimate certain physical quantities that comprise the model. One

such quantity is usually the surface location as a function of radar return time, from which the retracking correction can be found (Kurtz et al., 2014).

Though equations to model received radar waveforms have existed in literature prior (Brown, 1977; Galin et al., 2013; Raney, 1998; Wingham et al., 2004), Kurtz et al. (2014) were the first to fully utilize them for CryoSat-2 retracking and retrieval purposes. They built on past works by including a backscatter coefficient that varies with incidence angle, which they showed to be necessary when using a physical model with CryoSat-2 data. Kurtz et al. (2014) compared freeboard retrievals using both their physical approach and a threshold approach to independent data from OIB, and found improvements over the empirical method when using consistent physical assumptions inherent in the model.

Since Kurtz et al. (2014), other physical retracking methods have been employed to retrieve sea ice properties. The SAR Altimetry MOde Studies and Applications (SAMOSA) method (Ray et al., 2015) was originally used for ocean height retrievals, but has since been explored for sea ice freeboard retrievals (SAMOSA+, Laforge et al. 2020). Landy et al. (2019) used a physical facet-based model to construct CryoSat-2 echoes based on topography from OIB, and has later used this model to retrieve sea ice freeboard and assess the uncertainty that sea ice roughness can have on freeboard retrievals (Landy et al., 2020). As available computational power continues to grow, the potential for more - and more complex - physical retracking methods grows with it.

So far, most studies using physical retrackers have been focused on Arctic sea ice. However, their physical nature could prove to be useful over Antarctic sea ice

where uncertainties brought on by the snow layer typically are large (Paul et al., 2018; Willatt et al., 2010). The rest of this dissertation focuses on utilizing a physical retracking algorithm to retrieve Antarctic sea ice freeboard and thickness, which was first proposed in Fons and Kurtz (2019).

2.5 Shortcomings of current CryoSat-2 retrievals

The most commonly-used CryoSat-2 retrieval methods discussed above have provided a substantial framework for estimating sea ice freeboard. However, certain assumptions made in the retrieval processes limit the confidence that can be placed in their estimates. Particularly, some shortcomings exist that stem primarily from the assumptions involving the snow layer on top of sea ice and the location of the dominant scattering return within the sea ice-snow system. Many of the current retrievals (Kurtz et al., 2014; Kwok and Cunningham, 2015; Laxon et al., 2013; Lee et al., 2016; Tilling et al., 2018) assume that the radar pulse penetrates the snow layer and that the dominant scattering surface at Ku-band frequencies is located at the snow-ice interface. This assumption was first made for CryoSat-2 data in Laxon et al. (2013) who acknowledged that scattering from the snow layer may introduce errors and bias thickness measurements. This assumption primarily comes from laboratory measurements that showed that for a cold, dry snow cover on sea ice, a Ku-band pulse at nadir will result in a return originating from the snow-ice interface (Beaven et al., 1995). Others followed in this assumption for Arctic freeboard retrievals, noting that it may be more valid over Arctic sea ice where there

are fewer morphological features in the snow layer than in the Antarctic (Willatt et al., 2011).

As CryoSat-2 continued to collect data, much work went into trying to better understand the scattering effects of the snow on Ku-band radar pulses. It was found that the inside of the snow layer can exhibit a complex stratigraphy brought on by a variety of external processes. Nandan et al. (2017) found that brine wicked from the ice up into the snowpack can influence the salinity of the snow layer and strongly attenuate radar returns. In fact, this process can create a saline snow/non-saline snow interface (Fig. 2.7) that is higher than the snow-ice interface, which can appear as the dominant scattering horizon in CryoSat-2 waveforms and bias freeboard retrievals (Nandan et al., 2017). Additionally, studies of passive microwave data have shown that the microwave properties of snow can change with snow temperatures (Howell et al., 2008; Markus et al., 2009), meaning that CryoSat-2 returns could be complicated by the presence of liquid water within the snow layer during time periods of sea ice melt.

The potential for complex snow stratigraphies is enhanced over Antarctic sea ice. The wealth of available moisture from the surrounding ocean leads to enhanced precipitation and generally thicker snow depths than in the Arctic (Giovinetto et al., 1992; Maksym et al., 2012). These thicker snow depths can depress the ice surface down to - or below - the sea surface, leading to negative ice freeboard values (Maksym and Jeffries, 2000). At the edges of ice floes and through cracks in the ice, seawater can then infiltrate the snow layer and create a high-salinity slushy layer near the snow-ice interface (Massom et al., 1997). Like the conclusions found in Nandan et al.

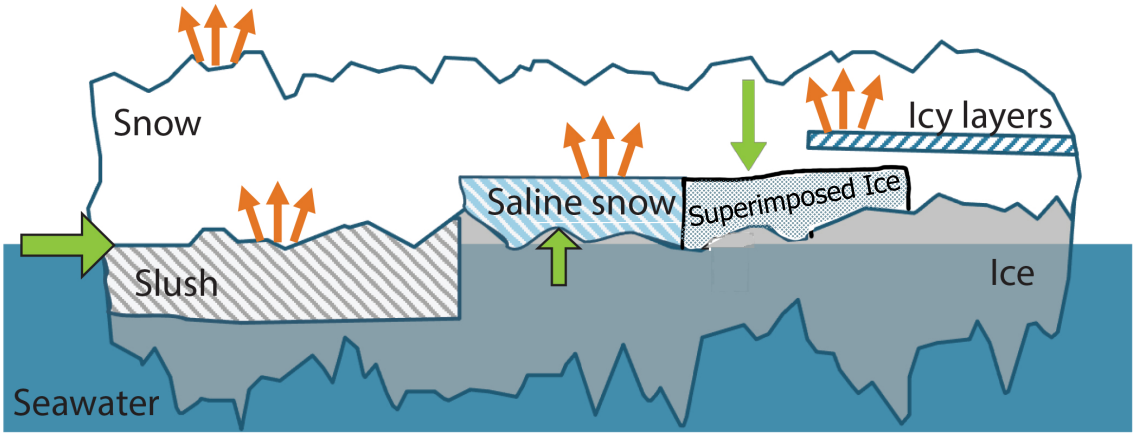

Figure 2.7: Schematic of potential scattering locations present from various stratigraphic features of Antarctic sea ice. Green arrows represent movement of water or salt, while red arrows represent potential scattering horizons from each feature.

(2017), this slush layer can act as the dominant scattering horizon from CryoSat-2 returns and bias the freeboard retrievals. Additionally, melted snow and slush can re-freeze, leading to the formation of superimposed ice and snow-ice, respectively, produce more potential imitation snow-ice interfaces for Ku-band pulses (Fig. 2.7, Maksym and Jeffries 2000).

In addition to the effects of snow stratigraphy on CryoSat-2 returns, the snow depth also can impact sea ice freeboard and ice thickness estimates from empirical retrackers especially when the depth is not known. For one (as mentioned above), the lack of knowledge of the snow depth can preclude the correction for radar wave speed through the snow layer, resulting in the retrieval of radar freeboard instead of ice freeboard (Ricker et al., 2014; Schwegmann et al., 2016). Secondly, thicker snow layers can contribute more volume scattering of the radar pulse, which can impact the waveform shape and make threshold retracking more uncertain (when snow layer scattering is assumed to be negligible, Fons and Kurtz 2019; Kurtz et al. 2014). Finally, unknown snow depths prevent the calculation of sea ice thickness

through the hydrostatic assumption (Eqn. 2.1).

While physical retrackers attempt to improve upon empirical retrackers by accounting for variable CryoSat-2 surface returns, they still include assumptions of the snowpack that contribute to observed uncertainties. Kurtz et al. (2014) assumes that the snow layer is transparent to Ku-band radar pulses, following the experiments of Beaven et al. (1995), and do not include the scattering impacts of the snow layer within their physical model. They compute a radar penetration error that increases with snow depth, ranging from 0 to 15 cm for snow depths under 50 cm (Kurtz et al., 2014). Landy et al. (2020) also assume that the dominant scattering comes from the snow-ice interface, and compute a bias brought on by the occurrence of partial (as opposed to full) penetration into the snowpack. They find that the partial penetration impact can contribute the largest bias to their overall thickness retrievals, accounting for 24% of the potential bias over MYI (Landy et al., 2020). Clearly, there is a need for better representation of the snow layer in physical retracking models to improve sea ice freeboard estimates.

In summary, two primary aspects of the snow layer on sea ice substantially impact currently-used CryoSat-2 retrieval methods and cause shortcomings in estimates of freeboard and thickness:

1. Snow depth: Uncertain snow depths can (a) prevent the correction of radar wave speeds through snow and (b) complicate (or prevent) calculations of sea ice thickness using Equation 2.1.

2. Snow stratigraphy: Complex and highly-variable snow stratigraphies can cause

the dominant scattering horizon to be located at a level above the often-assumed snow-ice interface, especially for Antarctic sea ice.

Not knowing (or not accounting for) the above effects of the snow layer can introduce errors in retrieved elevations that can propagate to the estimation of freeboard and thickness.

2.6 Motivation for dissertation

The above shortcomings in current CryoSat-2 retrievals of sea ice freeboard clearly motivate the need for an improved method of addressing the snow layer-induced uncertainty in the retrievals. But without current basin-scale measurements of snow depth/morphology or knowledge of the dominant scattering surface within the snowpack, how can this be done?

One method to improve retrievals is to question the assumptions of radar propagation through snow. While many of the studies above acknowledged that dominant scattering horizon can change based on the stratigraphy present, they also assumed that the snow cover was mostly transparent to Ku-band radar pulses. Instead of focusing on the snow layer's potential to transmit radar pulses, one could focus on the opposite, or the snow layer's potential to reflect radar pulses.

Willatt et al. (2010) used a sled-mounted altimeter to characterize the returns of Ku-band frequencies from Antarctic sea ice. These measurements were recorded during the Sea Ice Physics and Ecosystem eXperiment (SIPEX) cruise on board the Australian icebreaker *Aurora Australis* in 2007. By recording radar returns

over snow-covered sea ice with a known stratigraphy, they found that only 30% originated from the snow-ice interface, while 23% originated from within the snow layer and 43% from the air-snow interface. With these results (Fig. 2.8) they concluded that the assumption of a Ku-band radar pulse scattering predominantly from the snow-ice interface is not always valid for Antarctic sea ice (Willatt et al., 2010). Perhaps more importantly, they showed actual examples of Ku-band pulses scattering from the air-snow interface and snow volume, proving that the snow layer is not completely transparent at this frequency.

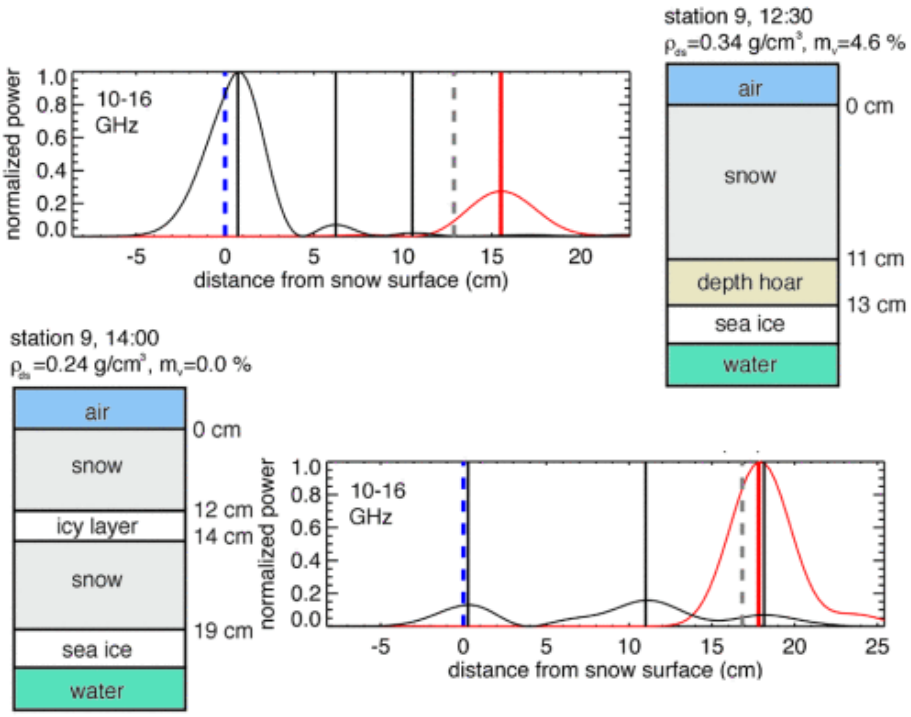

Figure 2.8: Example air-snow-ice-water profiles found from Antarctic sea ice and corresponding 10-16 GHz radar returns. Black lines represent returns with snow cover, while red lines represent returns after the snow is removed. Vertical lines show locations of peaks. Adapted from Willatt et al. (2010).

This work was corroborated from airborne data over Arctic sea ice. Simi-

lar variable penetration depths to those shown in Willatt et al. (2010) were found in airborne data collected during CryoSat validation Experiments, (CryoVex, Hendricks et al. 2010; Willatt et al. 2011). Kwok (2014) used multiple radars aboard OIB flights in the Arctic ocean to estimate the effects that the snow layer has on CryoSat-2 sea ice freeboard retrievals. He found that the air-snow interface of Arctic sea ice clearly contributes to the return at Ku-band frequencies, even if the impact is comparatively small (Kwok, 2014).

While a snow layer still may transmit a majority of the incoming Ku-band pulse under cold and dry conditions, these studies have shown that some of the received power can originate from the air-snow interface and snow volume atop sea ice.

This dissertation is motivated primarily by the above finding. This work exploits the fact that scattering at Ku-band frequencies can originate from the air-snow interface, and aims to retrieve the elevation of this interface from CryoSat-2 returns. In doing so, the goal is to limit the reliance on uncertain returns from the snow-ice interface using threshold retracking methods. By accounting for scattering that occurs from the snow surface and snow layer through the use of a physical waveform model, this work will show the ability to retrieve the air-snow interface elevation (resulting in snow freeboard estimates) as well as an improved tracking of the snow-ice interface (resulting in estimates of snow depth and ice freeboard). This work will focus on Antarctic sea ice retrievals for two reasons: 1) the impacts of the snow layer on Ku-band scattering is enhanced over Antarctic sea ice compared to Arctic sea ice and 2) no basin-scale estimates of Antarctic sea ice thickness from CryoSat-2

currently exist.

The following chapters use this motivation in the development and assessment of a CryoSat-2 retrieval algorithm that enables the estimation of snow freeboard, ice freeboard, snow depth on sea ice, and sea ice thickness.

Chapter 3: Retrieval of Snow Freeboard of Antarctic Sea Ice using Waveform Fitting of CryoSat-2 Returns

In this chapter, a CryoSat-2 algorithm to retrieve the surface elevation of the air-snow interface over Antarctic sea ice is presented. This algorithm utilizes a two-layer physical model that accounts for scattering from a snow layer atop sea ice as well as scattering from below the snow surface. The model produces waveforms that are fit to CryoSat-2 level 1B data through a bounded trust region least squares fitting process. These fit waveforms are then used to track the air-snow interface and retrieve the surface elevation at each point along the CryoSat-2 ground track, from which the snow freeboard is computed. To validate this algorithm, retrieved surface elevation measurements and snow surface radar return power levels are compared with those from Operation IceBridge (OIB), which flew along a contemporaneous CryoSat-2 orbit in October 2011 and November 2012. Monthly average pan-Antarctic maps of snow freeboard show a spatial pattern similar to that found a decade earlier with ICESat, but highlight the need for comparisons with temporally coincident snow freeboard data (shown in Chapter 4). The basis of this chapter can be found in Fons and Kurtz (2019), published in *The Cryosphere*.

3.1 Introduction

As discussed in previous chapters, radar altimetry has been used in recent years to estimate Arctic sea ice elevation, freeboard, and thickness. Most radar altimeters operate in the Ku-band at around 13.6 GHz, a frequency that has been shown to produce a dominant backscatter from the snow-ice interface (Beaven et al., 1995). The retrieved freeboard from radar altimetry, therefore, is generally assumed to be the ice freeboard especially when the snow is relatively dry and thin. Ku-band retrievals of ice freeboard have been employed in the Arctic (Giles et al., 2008; Laxon et al., 2003, 2013), where thinner and drier snow conditions tend to exist (Webster et al., 2018). In the Antarctic, radar freeboard calculations (and subsequent thickness calculations) are complicated substantially by the depth and variable vertical structure of the snow on top of the sea ice (Kwok, 2014; Price et al., 2015; Willatt et al., 2010). Due to the wealth of available moisture from the surrounding ocean, Antarctic sea ice experiences more frequent precipitation – and therefore greater snow depths – than that of the Arctic (Giovinetto et al., 1992; Maksym et al., 2012; Massom et al., 2001). The deep snow can be heavy enough to depress the sea ice surface down near or even below the sea surface, leading to flooding and wicking of the seawater within the snowpack (Massom et al., 2001; Willatt et al., 2010) that can act to obscure returns from radar altimeters. Additionally, dense, warm and/or moist snow can cause the dominant scattering surface to be located within the snowpack at a level that is higher than the snow-ice interface (Giles et al., 2008; Willatt et al., 2011, 2010).

Freeboard retrievals that neglect range corrections for radar propagation through a snow layer are referred to as "radar freeboards" . Radar freeboard was calculated in the Antarctic by Schwegmann et al. (2016), who used data from CryoSat-2 and Envisat to retrieve freeboard with the eventual aim to create a joined Envisat-CryoSat-2 sea ice thickness record. To counteract the effects of the snow layer on electromagnetic wave propagation, Paul et al. (2018) included a snow layer range correction to radar freeboards computed using CryoSat-2 and Envisat to retrieve ice freeboard over both Arctic and Antarctic sea ice. While the method put forth by Paul et al. (2018) demonstrates usefulness in reconciling thickness between Envisat and CryoSat-2, there still exist uncertainties in the sea ice thickness retrievals brought on by the validity of the snow depth climatology used in the corrections.

When using Ku-band altimetry for retrievals of freeboard and thickness, the largest source of uncertainty comes from the snow on sea ice. Uncertainty in the depth, salinity, and vertical structure can impact ranging and freeboard calculation (Armitage and Ridout, 2015; Nandan et al., 2017; Ricker et al., 2015). In order to counteract this uncertainty and improve the knowledge of the scattering effects of a snow layer on sea ice, this work aims to utilize Ku-band altimetry from CryoSat-2 to retrieve the elevation of the air-snow interface and subsequently the snow freeboard. While it is true that Ku-band radar pulses generally penetrate the snow surface on sea ice and have a dominant scattering layer beneath, what is often not included in freeboard retrieval algorithms, especially those depending on an empirical waveform evaluation, is the fact that there are physical and dielectric differences between air and snow (Hallikainen and Winebrenner, 1992; Stiles and Ulaby, 1981) that

results in scattering – albeit comparatively weaker – from the air-snow interface (discussed in Section. 3.3). Though this scattering is not typically the dominant return from radar pulses, it has been shown that it can be detected from airborne as well as ground-based sensors (Kurtz et al., 2013; Kwok, 2014; Willatt et al., 2010). Satellite radar returns of the air-snow interface elevation would be important in the Antarctic where snow-ice interface returns are complex and uncertain, and provide the possibility for snow depth estimations from radar altimetry. Knowledge of the snow depth in the Antarctic would enable more accurate sea ice thickness calculations, given that recent studies of Antarctic sea ice thickness rely on passive microwave snow depth data (Kern et al., 2016), assumptions of snow depth being equal to snow freeboard (Kurtz and Markus, 2012), parameterizations of snow depth from both snow freeboard (Li et al., 2018) and multi-year ice fraction (Hendricks et al., 2018), or even treatment of the snow and ice layers as a single layer with a modified density (Kern et al., 2016).

Typically, CryoSat-2 pulses are limited by the receive bandwidth (320 MHz, corresponding to a vertical resolution of 0.234 m) and therefore not able to resolve the air-snow interface explicitly (Kwok, 2014). In this chapter, it is shown that a two-layer physical model that accounts for the scattering effects of a snow layer on top of sea ice can be used to retrack the air-snow interface from CryoSat-2 radar waveforms, compute the surface elevation, and calculate snow freeboard. This two-layer model builds on the single-layer method developed in Kurtz et al. (2014). This study begins by explaining the datasets that are used (Section 3.2), discussing the physical rationale (Section 3.3) and method (Section 3.4) of retrieving snow

freeboard from CryoSat-2, and showing initial validation of the approach (Sections 3.5 and 3.6). Then, the freeboard calculation, results, and comparisons are discussed in Section 3.7. Finally, a discussion on the application to snow depth retrievals and possibility for future work is provided in Sections 3.8 and 3.9.

3.2 Data

Data for this study primarily come from ESA's CryoSat-2 satellite, launched in 2010. The principal payload aboard CryoSat-2 is SIRAL, a Synthetic Aperture Interferometric Radar Altimeter, which has a frequency in the Ku-band at 13.575 GHz and a receive bandwidth of 320 MHz (Wingham et al., 2006). SIRAL operates in one of three modes: "low resolution" mode (LRM), "synthetic aperture" (SAR) mode, and "synthetic aperture interferometric" (SARin) mode. In the Southern Hemisphere, LRM is used over the Antarctic continent and areas of open ocean and therefore is not considered in this study (Wingham et al., 2006). SAR and SARin data, which are taken over the sea ice zone and the Antarctic coastal regions, respectively, are both utilized in this work. Specifically, level 1B data from both of these operating modes are used. SAR level 1B data consist of 256 samples per echo while SARin data contain 512 samples per echo (Wingham et al., 2006). In order to maintain consistency between the two modes, both SAR and SARin data are here truncated to 128 samples per echo.

CryoSat-2 level 1B data utilize "multi-looking" to provide an average echo waveform for each point along the ground track. These multi-looked echoes corre-

spond to an approximate footprint of 360 m along track and 1.65 km across track (Scagliola, 2013; Wingham et al., 2006). Within the level 1B data, the one-way travel time from the center range gate to the satellite center of mass is provided. This information is used to retrieve elevation above the WGS84 ellipsoid. To do so, first the one-way travel time is multiplied by the speed of light in a vacuum. Then, geophysical and retracking corrections are applied following Kurtz et al. (2014). Geophysical corrections are applied by using the CryoSat-2 data products, which include the ionospheric delay, dry and wet tropospheric delay, oscillator drift, dynamic atmosphere correction (which includes the inverse barometer effect), pole tide, load tide, solid Earth tide, ocean equilibrium tide, and long period ocean tide. The retracking corrections are obtained through the waveform fitting method, discussed in Section 3.4. Adding the corrections to the raw range provides the surface elevation.

For this study, CryoSat-2 data from October 2011-2017 are utilized. October was chosen so that a substantial sea ice extent is present in each year of data and also so there is overlap with the spring ICESat campaigns, which ran roughly from October to November 2003-2009. Seven years of data allows for a longer-term average to be computed and facilitates better comparison with the ICESat spring seasonal average (Section 3.7).

Data from NASA's OIB airborne campaign are used in multiple capacities throughout this study. First, OIB 2-8 GHz Snow Radar (Leuschen et al., 2014) and 13-17 GHz Ku-band radar altimeter (Leuschen et al., 2014) data are used to confirm the presence of scattering of the radar beam from the air-snow interface (Section

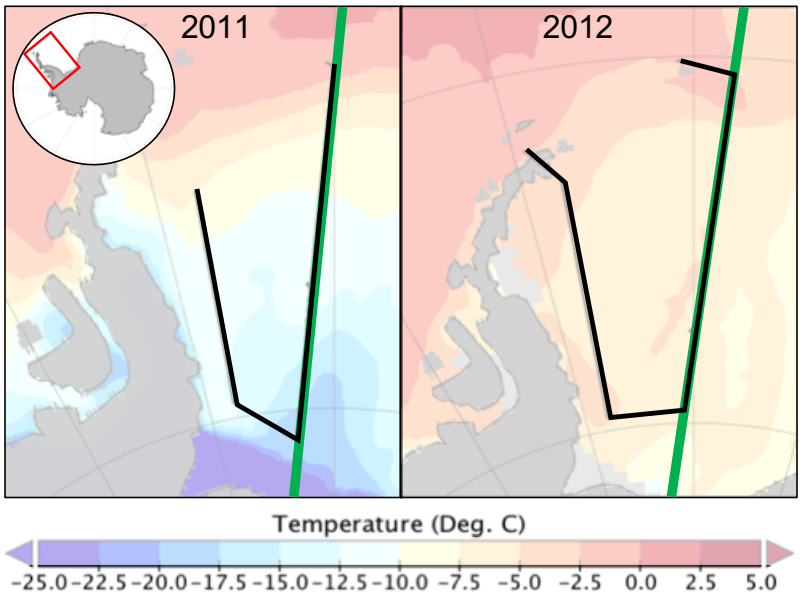

Figure 3.1: Maps of the Operation IceBridge 13 October 2011 (left) and 07 November 2012 (right) Sea Ice Endurance campaign flight paths (in black) along with the contemporaneous CryoSat-2 ground track (in green). Flight paths are overlaid on hourly average sea ice surface temperatures from MERRA-2 at the midpoint time of the OIB flight (Global Modeling and Assimilation Office (GMAO), 2015).

3.3). These data are taken from flights over the Weddell Sea on 13 October 2011 and 7 November 2012, which correspond to planned underflights of a contemporaneous CryoSat-2 orbit. This flight line is known as the "Sea Ice–Endurance" mission and is shown in Fig. 3.1. Second, these coincident observations are used in Section 3.6 for direct comparisons of elevations found between OIB and CryoSat-2, in order to validate this CryoSat-2 algorithm. Specifically, Airborne Topographic Mapper (ATM) elevation data (Studinger, 2014) are used and compared against that of CryoSat-2.

Sea ice freeboard data taken from ICESat between 2003-2007 (Kurtz and Markus, 2012) are used primarily as a comparative measure in this chapter. This product is gridded to 25 km and uses a distance weighted Gaussian function to

fill gaps in the gridded data. Specifically, seasonal average freeboard values from the various ICESat campaigns are compared with CryoSat-2 monthly average freeboard data obtained using this algorithm. The austral spring ICESat freeboard dataset consists of measurements made from October and November 2003-2007 (Fig. 3.2). These ICESat freeboard and thickness data are publicly available online at https://earth.gsfc.nasa.gov/cryo/data/antarctic-sea-ice-thickness.

Lastly, sea ice concentration data are used to filter out grid boxes that are largely uncovered with ice. The Version 3 Bootstrap monthly average product provides sea ice concentration on a 25 km polar stereographic grid. Grid boxes with monthly average concentrations less than 50% are removed. This product is derived using brightness temperatures from Nimbus-7 Scanning Multichannel Microwave Radiometer (SMMR) and Defense Meteorological Satellite Program (DMSP) Special Sensor Microwave Imager / Sounder (SSM/I-SSMIS) passive microwave data (Comiso, 2017).

3.3 Observed Ku-band scattering of radar from Antarctic sea ice

While more recent studies have shown the effects that a snow layer can have on Ku-band ranging and freeboard retrievals (Armitage and Ridout, 2015; Nandan et al., 2017; Ricker et al., 2015), past works that utilize Ku-band altimetry for ice freeboard retrieval tend to neglect scattering that occurs from the snow surface and volume, and assume that the dominant return occurs from the snow-ice interface (Beaven et al., 1995; Kurtz et al., 2014; Laxon et al., 2013). For most cases, especially

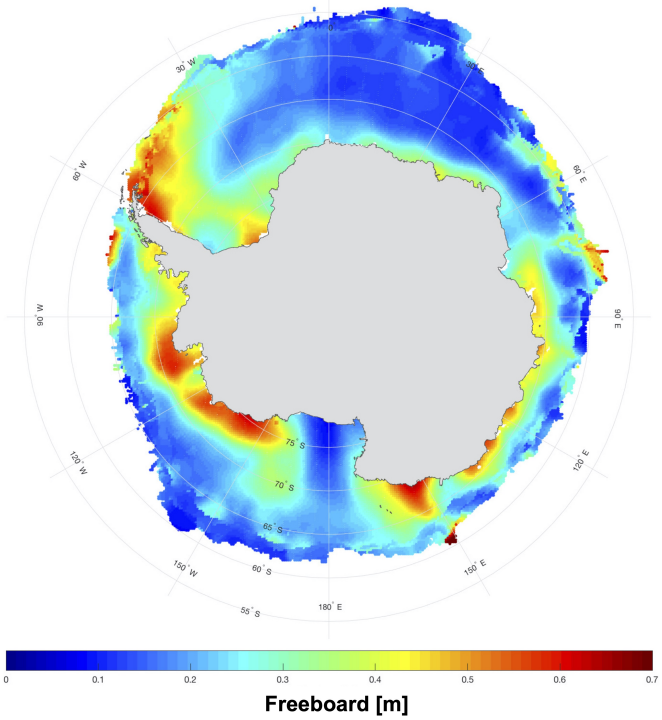

Figure 3.2: ICESat austral spring mean freeboard, consisting of measurements taken in October and November 2003-2007.

in the Arctic where the snow cover is relatively thin and dry, this assumption is generally valid (Armitage and Ridout, 2015; Willatt et al., 2011). However, the physical differences between air and snow indicate that scattering can occur from the air-snow interface as well (Hallikainen and Winebrenner, 1992; Willatt et al., 2010). This air-snow interface scattering is the fundamental basis for measuring snow freeboard using radar altimetry. Kwok (2014) used OIB data to find that scattering from the air-snow interface does contribute to the return at Ku-band frequencies. To further prove this fact, OIB echograms from the Ku-band and snow radars (Fig. 3.3) are utilized. These echograms provide a vertical profile of the radar backscatter along the flight path displayed in Fig. 3.1, and come from the November 2012 campaign. Comparing the lower-frequency snow radar, which is

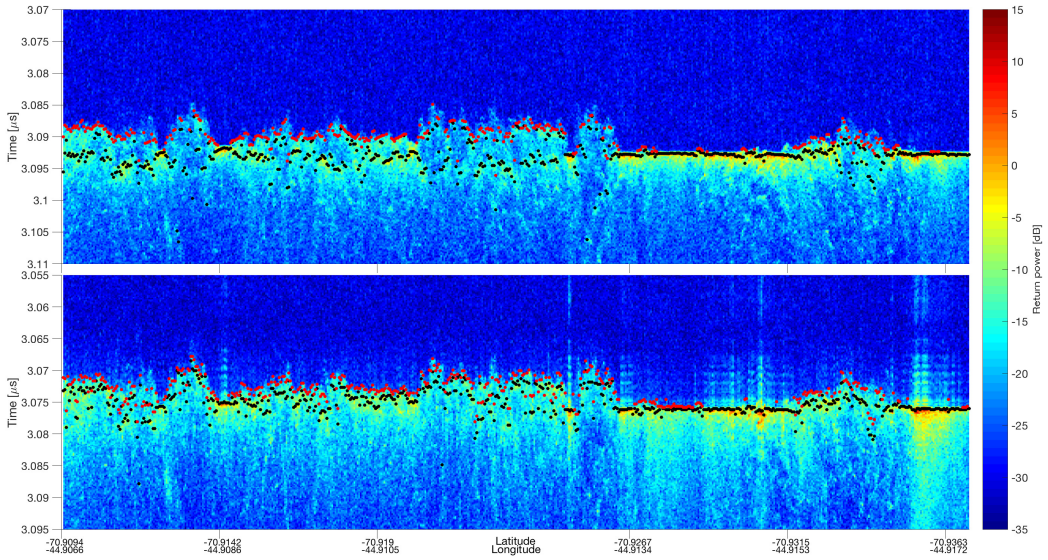

Figure 3.3: Example echograms from OIB snow radar (top) and Ku-band radar (bottom) taken from the November 2012 Sea Ice Endurance campaign. Black points denote locations of maximum power and red points denote the first location where the power rises 10 dB above the noise level, both found from the peak-picking algorithm discussed in text. The length of the transect covered in this echogram is 3.02 km. The mean (standard deviation) noise level for the snow radar is found to be -29.1 dB (1.39 dB) while the signal level at the air-snow interface is found to be -16.8 dB (1.47 dB). For the Ku-band altimeter, the noise level is found to be -30.3 dB (1.32 dB) while the air-snow interface signal level is found to be -17.9 dB (2.09 dB), showing the surface return is well above the noise for both instruments.

known to detect the air-snow interface, with the higher frequency Ku-band radar altimeter, one can see the difference in scattering between the snow-covered floe points and the leads in both radar profiles.

In this study, a simple "peak picking" algorithm is employed to mark the vertical locations of both the maximum backscatter and the first point that rises 10 dB above the noise level for each horizontal point along the flight line. While not explicitly extracting layers from the IceBridge data, these points are used as initial guesses of the air-snow and snow-ice interfaces into the model (Section 3.4.3). These initial guesses are not exactly the expected backscatter coefficients from the

two layers, but instead a rough approximation from their peak powers. The peak-picked air-snow interface power is compared to that of the maximum (assumed snow-ice interface) power, as displayed in Fig. 3.4. This frequency distribution shows that for the 2012 IceBridge campaign over Antarctic sea ice, the difference of the air-snow interface power from the maximum power is smaller for the snow radar, with a mean of 12.94 dB, than for the Ku-band altimeter, which has a mean difference of 14.00 dB. This result is expected, as it means that the scattering power from the air-snow interface is closer in magnitude to that of the snow-ice interface in snow radar returns. However, the curves have a similar distribution and mean, indicating that the Ku-band radar return likely consists of scattering from the air-snow interface as well. Overall, a comparison of the OIB radars provides further evidence that scattering of Ku-band radar pulses can occur at the air-snow interface. The following sections utilize this notion to retrieve snow freeboard from CryoSat-2 returns.

3.4 Surface elevation retrieval methodology

This section introduces a new two-layer retrieval method that expands on the single layer method employed by Kurtz et al. (2014). Following Kurtz et al. (2014), this study retrieves surface elevation from CryoSat-2 data by first using a physical model to simulate return waveforms from sea ice. Then, a least-squares fitting routine is used to fit the simulated waveform to the CryoSat-2 level 1B data. Sea ice parameters, including the surface elevation, can then be computed from the

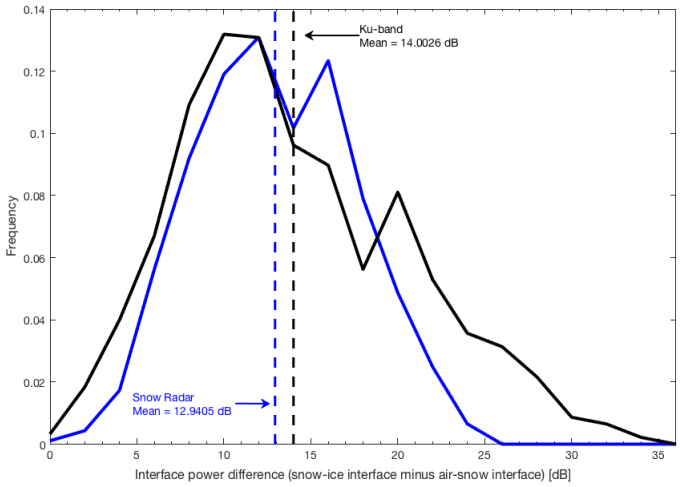

Figure 3.4: Frequency distributions of the difference in air-snow interface power from snow-ice interface power taken from the November 2012 IceBridge Sea Ice Endurance campaign. The blue curve represents the snow radar, while the black curve represents the Ku-band radar. Note that the locations of the air-snow and snow-ice interfaces are approximations found from the peak-picking algorithm (Fig. 3) and are not exactly the expected backscatter coefficients from the two layers.

fit waveform. The following section describes this process. For a more detailed derivation of the theoretical basis surrounding the physical model and waveform fitting routine, see Kurtz et al. (2014).

3.4.1 Physical waveform model

When assuming a uniformly backscattering surface, Kurtz et al. (2014) expressed the received radar echo, $\Psi(\tau)$, as

$$\Psi(\tau) = P_t(\tau) \otimes I(\tau) \otimes p(\tau) \tag{3.1}$$

where τ is the echo delay time relative to the time of scattering from the mean scattering surface and $\otimes$ represents a convolution of the compressed transmit pulse,

$P_t(\tau)$, the rough surface impulse response, $I(\tau)$, and the surface height probability density function, $p(\tau)$ (Brown, 1977; Kurtz et al., 2014). The terms are defined as

$$P_t(\tau) = p_0 sinc^2(B_w \tau), \tag{3.2}$$

where p_0 is the peak power of the pulse and B_w is the received bandwidth,

$$p(\tau) = \frac{1}{\sqrt{2}\pi\sigma_c} exp\left(-\frac{1}{2}\left(\frac{\tau}{\sigma_c}\right)^2\right), \tag{3.3}$$

where $\sigma_c = \frac{2\sigma}{c}$ is the standard deviation of the surface height in the time domain and c is the speed of light in vacuo, and

$$\begin{aligned} I(\tau) = \frac{\lambda^2 G_0^2 D_0 c^0(0^\circ)}{32\pi h^3 \eta} \sum_{k=-\frac{N_b-1}{2}}^{\frac{N_b-1}{2}} H\left(\tau + \frac{\eta h \xi_k^2}{c}\right) \\ \exp\left[\frac{-2\xi_k^2}{\eta^2}\left(\frac{1}{\gamma_1^2}+\frac{1}{\gamma_2^2}\right) + \frac{c\eta}{h\gamma_1^2}\left(\tau + \frac{\eta h(\xi_k^2)}{c}\right)\right] \int_0^{2\pi} d\theta \\ \exp\left[-4\xi_k \sqrt{\frac{c}{h\eta^3}\left(\tau + \frac{\eta h \xi_k^2}{c}\right)} \cos\theta \left(\frac{1}{\gamma_1^2}+\frac{1}{\gamma_2^2}\right) - \frac{2c\cos(2\theta)}{h\eta\xi_2^2}\left(\tau + \frac{\eta h \xi_k^2}{c}\right)\right] \\ \left(1 + \frac{\alpha}{h^2}\left(\left(\frac{h\xi_k}{\eta}\right) + \frac{ch}{\eta}\left(\tau + \frac{\eta h \xi_k^2}{c}\right) + 2\left(\frac{h\xi_k}{\eta}\right) cos\theta \sqrt{\frac{ch}{\eta}\left(\tau + \frac{\eta h \xi_k^2}{c}\right)}\right)\right)^{\frac{-3}{2}} \\ \left(\sum_{n=0}^{N_b}\left(0.54 - 0.46\cos\left(\frac{2\pi n}{N_b} - \pi\right)\right) cos\left(2k_0 \upsilon_s \left(n - \frac{N_b}{2}\right)\sqrt{\frac{c\tau}{\eta h} + \xi_k^2}\cos\theta - \xi_k\right)\right)^2 \end{aligned} \tag{3.4}$$

where the variables (average values , when applicable, following Kurtz et al. 2014) for CryoSat-2 are as follows: λ (0.0221 m) is the center wavelength, G_0 (42 dB) is the one-way antenna gain, D_0 (30.6 dB) is the one-way gain of the synthetic beam, c (299792485 m s^{-1}) is the speed of light in vacuo, $\sigma^0(0^0)$ is the nadir backscatter

coefficient, h (725 km) is the satellite altitude, η (1.113) is a geometric factor, N_b (64) is the number of synthetic beams, τ is the echo delay time, ξ_k is the look angle of the synthetic beam k from nadir, H is a Heaviside step function, γ_1 (6767.6) is the elliptical antenna pattern term 1, γ_2 (664.06) is the elliptical antenna pattern term 2, α is the angular backscattering efficiency, k_0 (284.307 m^{-1}) is the carrier wave number, υ_s (7435 m/s) is the satellite velocity, σ is the standard deviation of surface height, and B_w (320 MHz) is the received bandwidth.

Under the assumption that only surface scattering is present and occurs from the snow-ice interface alone (i.e. no surface scattering from the air-snow interface nor volume scattering from within the snow or ice layers), Equation 3.1 is able to accurately model a received CryoSat-2 echo over the Arctic (Kurtz et al., 2014). However, due to thicker snow depths on Antarctic sea ice as compared to the Arctic, scattering effects from the snow layer cannot be neglected when retrieving surface elevation. Therefore, Equation 3.1 is here modified to become

$$\Psi(\tau) = P_t(\tau) \otimes I(\tau) \otimes p(\tau) \otimes \upsilon(\tau) \tag{3.5}$$

where $\upsilon(\tau)$ is the scattering cross section per unit volume as a function of echo delay time (Kurtz et al., 2014). Following Arthern et al. (2001) and Kurtz et al. (2014), $\upsilon(\tau)$ is defined in terms of physical parameters including the surface backscatter coefficients of snow and ice, ${\sigma^0}_{\text{surf-snow}}$and ${\sigma^0}_{\text{surf-ice}}$, respectively, and the integrated volume backscatter of snow and ice, ${\sigma^0}_{\text{vol-snow}}$and ${\sigma^0}_{\text{vol-ice}}$, respectively. Together,

the total backscatter can be written as

$$\sigma^0 = \sigma^0_{surf-snow} + \sigma^0_{vol-snow} + \sigma^0_{surf-ice} + \sigma^0_{vol-ice} \tag{3.6}$$

For snow on sea ice, $\upsilon(\tau)$ becomes:

$$\upsilon(\tau) = \begin{cases} 0 & \tau < -\frac{2h_s}{c_s now} \\ \sigma^0_{surf-snow}\delta\left(\tau + \frac{2h_s}{c_{snow}}\right) + \sigma^0_{vol-snow}k_{e-snow}\exp & \\ \quad\left[-c_{snow}k_{e-snow}\left(\tau + \frac{2h_s}{c_{snow}}\right)\right] & 0 < \tau \leq -\frac{2h_s}{c_{snow}} \\ \sigma^0_{surf-ice}k^2_{e-snow}\exp\left[-\frac{k_{e-snow}h_s}{2}\right]\delta(\tau) + \sigma^0_{vol-ice}k_{e-ice} & \\ \quad\exp\left[-\frac{k_{e-snow}h_s}{2} - c_{ice}k_{e-ice}\tau\right] & \tau \geq 0 \end{cases} \tag{3.7}$$

which accounts for signal attenuation in the snow and ice layers and loss of power at the air-snow and snow-ice interfaces. Equation 3.7 comes from Kurtz et al. (2014) and uses the form of $\tau = 0$ at the snow-ice interface. In Equation 3.7,

$$\sigma^0_{vol-snow} = \frac{\sigma_{vol-snow}k^2_{t-snow}}{k_{e-snow}} \tag{3.8}$$

and

$$\sigma^0_{vol-ice} = \frac{\sigma_{vol-ice}k^2_{t-snow}k^2_{t-ice}}{k_{e-ice}} \tag{3.9}$$

Static parameters in Equations 3.7 - 3.9 are given values to model a snow layer on sea ice. The two-way extinction coefficients of snow, $k_{e\text{-}snow}$, and sea ice, $k_{e\text{-}ice}$, are assigned to be 0.1 m^{-1} and 5 m^{-1}, respectively, following Ulaby et al. (1982). The speed

of light through snow and ice are c_{snow} and c_{ice}, respectively, where $c_{snow} = \frac{c}{n_{snow}}$ and $c_{ice} = \frac{c}{n_{ice}}$. Here, $n_{snow} = 1.281$ and $n_{ice} = 1.732$, where n_{snow} corresponds to a snow layer with a density of 320 kg/m^3 (Tiuri et al., 1984; Ulaby et al., 1982). A density of 320 kg/m^3 was chosen as an assumption to best represent pan-Antarctic snow on sea ice following results from several in situ surveys (Lewis et al., 2011; Massom et al., 2001; Willatt et al., 2010). Finally, $k_{t\text{-}snow}$ and $k_{t\text{-}ice}$ are the transmission coefficients between the air-snow and snow-ice interfaces, respectively. Both transmission coefficients are generally close to one (Onstott, 2011); this study uses values of $k_{t\text{-}snow}$=0.9849 and $k_{t\text{-}ice} = 0.9775$ as calculated from the Fresnel reflection coefficient using the values of n_{snow} and n_{ice}. The snow depth, h_s, is computed from the echo delay shift of the air-snow and snow-ice interfaces, free parameters t_{snow} and t respectively, which are discussed in Section 3.4.3. The remaining free parameters are given as inputs to the model and are defined in the following section.

The main assumption in this approach is that scattering is expected to come from two defined layers (i.e. the air-snow and snow-ice interfaces) and uniformly throughout the volume. Antarctic sea ice can exhibit complex layer structures that could obscure this simple two-layer method, however, no pan-Antarctic understanding of snow-covered sea ice composition currently exists. Therefore, this two-layer assumption is utilized as an approximation of the broad-scale sea ice cover.

3.4.2 Waveform fitting routine

To fit the modeled waveform to CryoSat-2 data, a bounded trust region Newton least-squares fitting routine (MATLAB function *lsqcurvefit*) is employed. This routine fits the model to the data by iteratively adjusting model input parameters and calculating the difference between the modeled and CryoSat-2 level 1B waveform data, until a minimum solution – or the established maximum number of iterations – is reached. Building off of Kurtz et al. (2014), this process can be shown with the equations

$$P_m(\tau) = A_f L(\tau, \alpha, \sigma) \otimes p(\tau, \sigma) \otimes \upsilon \left(\tau, t_{snow}, \sigma^0_{surf-snow}, \sigma^0_{surf-ice}, \sigma^0_{vol-snow}, \sigma^0_{vol-ice}\right) \tag{3.10}$$

and

$$\min \sum_{i=1}^{128} \left[P_m(\tau_i) - P_r(\tau_i + t)\right]^2, \tag{3.11}$$

where L is a lookup table of $P_t(\tau) \otimes I(\tau)$ as defined in Kurtz et al. (2014), $\mathrm{P_m}$ is the modeled waveform, $\mathrm{P_r}$ is the observed echo waveform, and τ_i is the observed echo power at point i on the waveform. These equations result in nine free parameters: the amplitude scale factor, $\mathrm{A_f}$, the echo delay shift factor at the air-snow and snow-ice interfaces, respectively $\mathrm{t_{snow}}$ and t, the angular backscattering efficiency, α, the standard deviation of surface height, σ, and the terms that together make up the total backscatter, $\sigma^0_{surf-snow}, \sigma^0_{surf-ice}, \sigma^0_{vol-snow}, \sigma^0_{vol-ice}$. These parameters are adjusted with each iteration of the fitting routine and are explained further in Sections 3.4.3. An initial guess for each of the free parameters – in addition to

upper and lower bounds – is provided to the fitting routine. Doing so ensures that the solution reached will closely resemble that of the physical system. Approaches for determining the initial guesses for both lead and floe characterized echoes are outlined in the following section.

This algorithm uses the squared norm of the residual ("resnorm") as a metric for goodness of fit. Modeled waveforms with a resnorm less than or equal to 0.3 are considered to be good fits and have the output parameters used in the retracking correction calculation and surface elevation retrieval. Waveforms with greater fitting error are run again using a different initial guess for α. If the resnorm is still high, the CryoSat-2 echo is not used in the retrieval process. Figure 3.5 shows a spatial distribution of the mean October resnorm values for 2011-2017. The largest residuals are consistently located around the ice edge and near to the continent, while the smallest are collocated with areas of high lead-type fraction (Fig. 3.5), such as the Ross Sea. Since the specular lead waveforms are easily fit with little residual, the overall average distribution shown here is consistently under 0.3 (total mean of 0.13). However, many floe-type points have values closer to the 0.3 threshold. Although a resnorm threshold of 0.3 results in reasonably representative modeled waveforms, it is understood that the use of a single metric can oversimplify the goodness of fit and leaves room for errors in the shape of the modelled waveform.

3.4.3 Lead / floe classification

Prior to constructing a physical model and fitting it to the data, each CryoSat-2 echo is first characterized as either a lead or a floe based on parameters derived from the individual waveform. Specifically, the pulse peakiness (PP) and stack standard deviation (SSD) parameters are used to distinguish between the two surface types, following Laxon et al. (2013). PP is defined as

$$PP = \max(P_r) \sum_{i=1}^{128} \frac{1}{P_{r(i)}} \tag{3.12}$$

from Armitage and Ridout (2015). SSD comes from the CryoSat-2 level 1B data product and is due to the variation in the backscatter as a function of incidence angle Wingham et al. (2006). Figure 3.5 shows average detection rates for lead and floe points using this method, discussed in the following sections.

3.4.3.1 Leads

CryoSat-2 echoes are categorized as leads if the return waveform has a PP > 0.18 and a SSD < 4 (Laxon et al., 2013). Since by definition leads have no snow cover, it is assumed that all scattering of the radar pulse originates from one surface. In this case, that surface is either refrozen new ice or open water. It is also assumed that no volume scattering occurs from leads. Therefore, the volume scattering term in Equation 3.10 goes to a delta function at $\tau = 0$, resulting in four free parameters: the amplitude scale factor, A_f, the echo delay shift factor, t, the

angular backscattering efficiency, α, and the standard deviation of surface height, σ. The initial guess for A_f is set equal to the waveform peak power, with the bounds set to +/- 50% of the peak power. The echo delay shift, t, is given an initial guess equal to the point of maximum power, denoted with t_i. σ is first estimated to be 0.01 for lead points, with bounds taken to be $0 \leq \sigma \leq 0.05$. The initial guess for α, denoted as α_0, is calculated as the ratio of tail to peak power and uses a mean of the 10 ns following the location of peak power. The bounds of α_0 are $\frac{\alpha_0}{100} \leq \alpha_0 \leq 100\alpha_0$. Using the above initial guesses in the fitting routine leads to a modelled waveform that well represents the CryoSat-2 data over leads (Kurtz et al., 2014). The echo delay factor, t, provides the location of the surface as a function of radar return time, which is used in the surface elevation retrieval of each lead-classified echo. The largest fraction of lead-classified points occurs in the Ross Sea, consistent with the location of the Ross Sea Polynya (Fig. 3.5). However, it is also a region known for new-ice formation that could return specular lead-type waveforms, and potentially lead to an overestimation of the sea surface height (discussed in Section 3.7).

3.4.3.2 Floes

Radar echoes with a PP < 0.09 and a SSD > 4 are classified as sea ice floes (Laxon et al., 2013). Due to the presence of a snow layer on top of the sea ice, all nine free parameters (introduced in Section 3.4.1) are employed. These include the four mentioned in the previous section, as well as t_{snow}, the echo delay shift factor of the air-snow interface, $\sigma^0_{surf-snow}$, $\sigma^0_{vol-snow}$, $\sigma^0_{surf-ice}$, and$\sigma^0_{vol-ice}$. The initial guess and

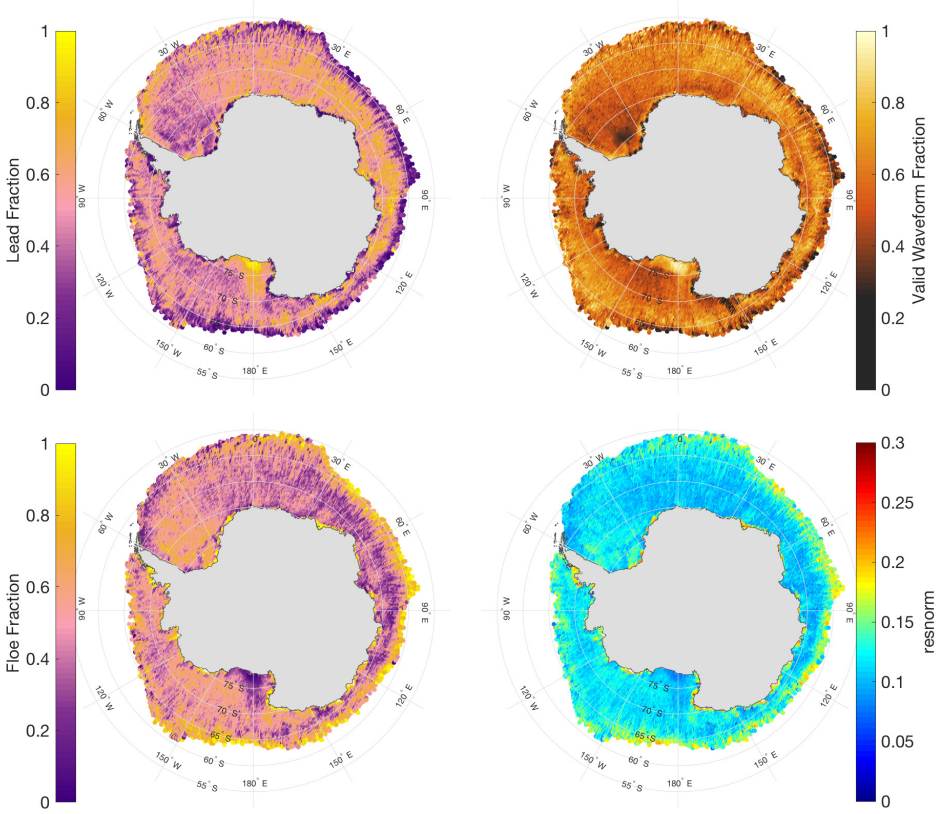

Figure 3.5: October 2011-2017 average maps of lead-type waveform fraction (top-left), floe-type waveform fraction (bottom-left), valid waveform fraction (top-right), and resnorm value (bottom-right).

bounds for A_f is taken to be the same as used for lead points, while the remaining 8 differ from leads. For t_{snow}, the initial guess ($t_{i\text{-}snow}$) comes from the ICESat datasets of the seasonal average total freeboard. The "zero ice freeboard" assumption is employed (Kurtz and Markus, 2012), which assumes that the snow-ice interface is depressed to the sea surface, meaning the ICESat freeboard would be approximately equal to the snow depth. Though this assumption is generally thought to be valid in the Antarctic, it may not hold true in all regions of the Antarctic (Adolphs, 1998; Kwok and Maksym, 2014; Weissling and Ackley, 2011; Xie et al., 2011). Therefore,

this fitting routine attempts to adapt and move away from the zero ice freeboard assumption, with the results being explored in later sections. The ICESat freeboard height at the location of each CryoSat-2 radar pulse is taken and converted in terms of radar return time, which provides a suitable initial guess of the air-snow interface. Bounds of $t_{i\text{-}snow}$ are taken to be +/- 5 ns. The initial guess for t (t_i) is taken to be the first point where the waveform power reaches 70% of the power of the first peak, following Laxon et al. (2013). This is a commonly used threshold retracking method to detect the snow-ice interface from CryoSat-2. Bounds are taken to be +/- 6 ns. σ is first estimated to be 0.15 for floe points, with bounds set to $0 \leq \sigma \leq 1$. The initial guess for α is similar to that in the lead characterization, with the exception that the mean power of points between 90 ns and 120 ns is used in the ratio of tail to peak power. Bounds for α_0 are set as $\frac{\alpha_0}{100} \leq \alpha_0 \leq 100\alpha_0$.

The remaining surface backscatter coefficients and integrated volume backscatter of snow and ice are initially estimated using values taken from OIB Ku-band radar echograms from the Weddell Sea flights. Estimation of the surface backscatter comes from an average of all valid peaks chosen from the echogram peak-picker for the air-snow and snow-ice interfaces of both flights. The snow and ice volume backscatter values are parameterized using average layer backscatter values between the two interfaces and 10 range bins beyond the snow-ice interface, respectively. The initial guesses (bounds) are set to be as follows: $\sigma^0_{surf-snow}$ = -15 dB (+/- 5 dB), $\sigma^0_{vol-snow}$ = -11 dB (+/- 5 dB), $\sigma^0_{surf-ice}$ = -1 dB (+/- 10 dB), and $\sigma^0_{vol-ice}$ = -8 dB (+/- 10 dB). The largest fraction of floe-type points are found in the Weddell Sea and along the ice edge, where older and rougher ice is generally found (Fig.

3.5). These distributions compare qualitatively to that found in Paul et al. (2018), with the exception that this method finds a larger region of lead-type dominant waveforms in the Ross Sea than Paul et al. (2018).

3.5 Waveform model and fitting assessment

This section showcases tests of the sensitivity of different model parameters with respect to the initial guesses provided and to the retrieved freeboard distributions. Additionally, this section assesses the ability of the model and fitting procedure to retrieve known quantities from synthetically-generated data.

3.5.1 Model parameter sensitivity

Figure 3.6 shows a floe waveform sensitivity study looking at a variety of modeled waveforms that differ only in the initial guess for the standard deviation of surface height (σ, top) and the total backscatter coefficient (σ^0, bottom). The range of σ was taken to be between 0.01 (very smooth surface) to 0.4 (rough surface), while σ^0 was varied between three different parameterizations: values from Kurtz et al. (2014), values taken from the OIB Snow Radar data, and from the Ku-band data (above). The resulting freeboard distributions found using an initial guess of $\sigma = 0.35$ and σ^0 taken from Kurtz et al. (2014) are shown as a difference from the values chosen in this study ($\sigma = 0.15$, σ^0 taken from Ku-band radar data) in Fig. 3.6 (C and F). In this case, the effect of altering the backscatter parameterization had a larger effect on freeboard than altering σ. It is evident that physically inconsistent

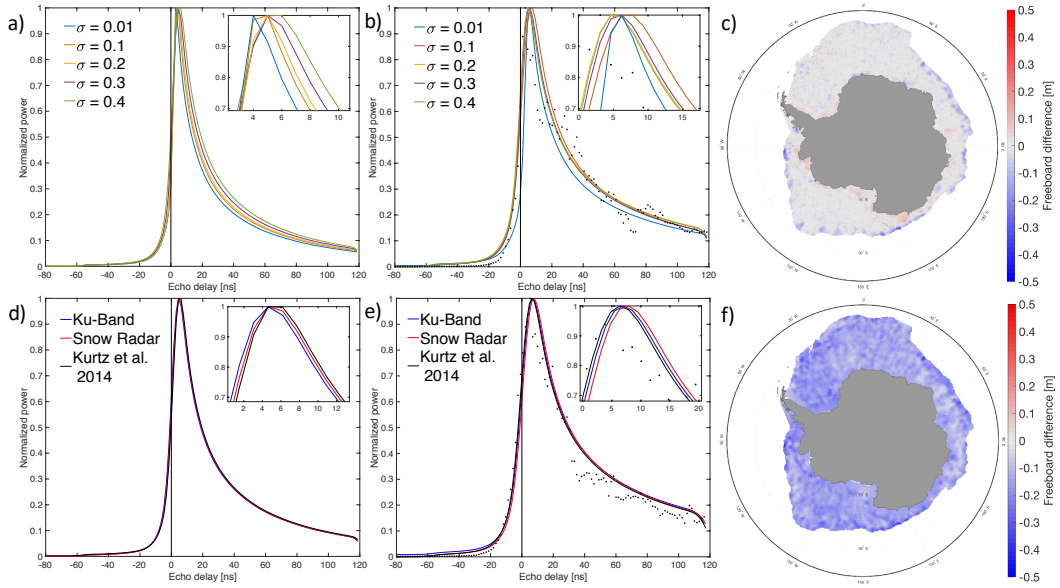

Figure 3.6: A sensitivity study of two initial guess parameters: the standard deviation of surface height, σ, and the total backscatter, σ^0. (a) modeled waveform (before fitting) varying the initial guess value of σ between 0.01 (very smooth surface) and 0.4 (rough surface). (b) waveforms fit to CryoSat-2 data varying the initial guess value of σ between 0.01 and 0.4. (c) October 2016 average freeboard difference: $\sigma = 0.35$ as the initial guess – $\sigma = 0.15$ as the initial guess. (d) as in (a) using three different backscatter parameterizations taken from the OIB Ku-Band radar profile, Snow Radar profile, and Kurtz et al. (2014). (e) as in (b) with the three different backscatter parameterizations. (f) as in (c) showing Kurtz et al. (2014) backscatter as the initial guess – Ku-Band backscatter as the initial guess. Inlaid plots are zoomed in on the waveform peaks. The methodology for freeboard calculations is explained in later sections of the paper.

initial guesses can result in altered freeboard distributions, with the magnitude of the impact potentially being large (broad-scale difference of ∼25 cm in Fig. 3.6(F)). While this uncertainty surely adds to that of the overall results, the use of physically-consistent first guesses acts to reduce the uncertainty as much as possible.

Figure 3.6 shows that the modeled waveform can be sensitive to the initial guess provided, and therefore care is taken to ensure the initial guesses come from physically realistic values.

3.5.2 Assessing the waveform fitting process using synthetic data

While physically-consistent initial guesses are an important part of the waveform-fitting procedure (as discussed in the previous section), it is also important to determine if the model and fitting procedure can retrieve the "correct" result when provided with a good initialization. However, without detailed ground-truth data over the scale of a CryoSat-2 footprint, one cannot know the exact surface parameters from a real waveform. Instead, synthetic waveforms with known physical parameters can be used. This study uses the developed physical model to generate synthetic data and test the ability of this fitting procedure to retrieve the known quantities. This method allows for a quantitative assessment to describe the retrieval's ability, in the form of a coefficient of determination between the retrieved quantity and the prescribed synthetic parameters.

First, 1000 synthetic waveforms are generated using random values of each input parameter. The snow-ice interface tracking point, t, was varied between -100 and -50 ns. The t_{snow} parameter was varied according to a snow depth range from 0 - 60 cm. Roughness (σ) was varied between 0 - 1 m, while α was varied between 0 - 1e6 based on the roughness values (since the two parameters are negatively linked). The amplitude scale factor, A_f, as well as the backscatter coefficients, were held constant since they are not the parameters of interest in this retrieval. After constructing a waveform with the random input values, noise was added to the waveforms. This was done to better simulate real-life waveforms and to ensure the retrieval can still perform in the presence of noise. Both random, multiplicative noise as well as specu-

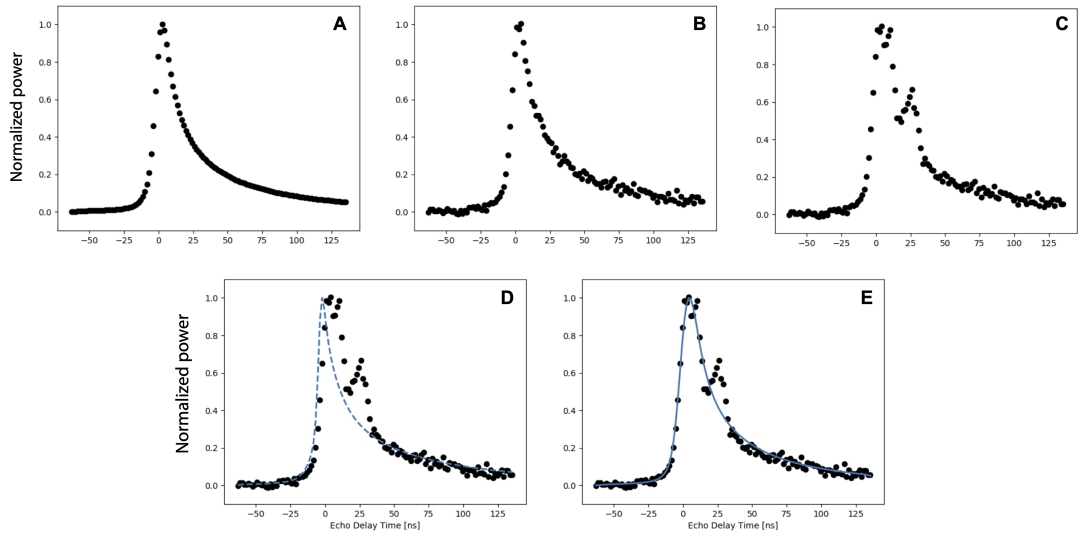

Figure 3.7: Progression of generating and fitting synthetic waveforms. (A) Synthetic waveform generated from model, (B) Waveform from A with random, multiplicative noise added, (C) Waveform from B with off-nadir scattering added, (D) Waveform from C with initial guess waveform (dashed), and (E) Waveform from D with best-fit waveform (dashed).

lar reflections from off-nadir leads were added to the waveforms. Multiplicative noise was added to all waveforms, while off-nadir lead reflections were added randomly to 50% of the generated waveforms. Figure 3.7 shows a progression of generating a realistic synthetic waveform. This process was done for 1000 synthetic waveforms, generating 1000 different tests cases. An example of some synthetic waveforms used in this study are shown in Fig. 3.8.

For each of the 1000 synthetic waveforms, the waveform fitting process described in earlier sections is applied. This process consists of first finding initial guess parameters based on the synthetic waveform characteristics. Since the air-snow interface location initial guess is typically taken from independent data, random values falling in the expected range of t_{snow} were used as this initial guess. All

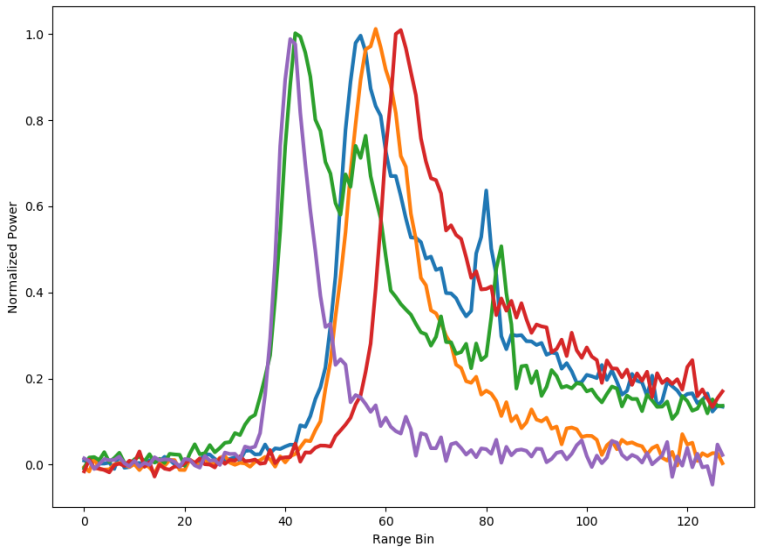

Figure 3.8: Sample synthetic waveforms generated for this assessment.

other parameters' initializations were found using the methods described above. For the air-snow interface case, each waveform was fit three times (in order to counteract the use of a random initial guess), with the output parameters that led to the smallest residual kept as the best fit waveform. All others were fit one time.

Figure 3.9 shows resulting linear regressions for each of the parameters of interest, where the x-axis is the "true value" of a given parameter used in the creation of the synthetic data and the y-axis is the resultant value of that parameter after the waveform fitting processes. As a first-order assessment, one can see the high coefficients of determination (R^2), ranging from 0.80 to 0.99, that signify good ability of this model and fitting procedure to retrieve known quantities. However, some interesting results emerge upon closer assessment. For one, the snow and ice locations tend to have the best results (closest to the 1:1 line) compared to the other two parameters. This is likely due to the fact that these parameters are based off of the leading edge of the waveform, which is less impacted by noise and off-nadir

leads (Fig. 3.8). The t_{snow} parameter seems to have more spread at higher values, which typically corresponds to thicker snow depths. The roughness and angular backscatter terms (Fig. 3.9, bottom) show more spread in these linear regressions. For α, this is expected given the large dynamic range of the parameter and accepted since the R^2 is still high (0.94). The roughness, on the other hand, shows in general good agreement that gets worse at higher values of σ. This could be brought on by the initial guess for σ, which is kept at a constant 0.15 m.

Despite the worse agreement from the roughness term, it is still encouraging to see the percentage of fits that are considered "good" and to see the values that would be rejected by the fitting process. Red points in Fig. 3.9 signify fits that have a resnorm less than 0.3 and therefore would either be re-fit in the retrieval - in hopes that adjusting the initial guess parameters would lead to a better overall fit - or would be discarded all together. Over 90% of the points in all cases would be kept as "good fits". Points that are further from the 1:1 line, especially in the σ and α plots, are generally filtered out. These are likely due to the synthetic off-nadir leads that can complicate the waveforms and the fitting process.

Overall, Fig. 3.9 showcases a general good ability of this model and fitting process to retrieve known parameters in synthetically-generated data. It is acknowledged that actual CryoSat-2 waveforms can be more complex than the synthetic waveforms generated here, however, this analysis provides some confidence in the fitting procedure to improve upon the initial guesses provided. The subsequent sections will look into comparing retrieved elevations and freeboards to actual data collected by independent instruments.

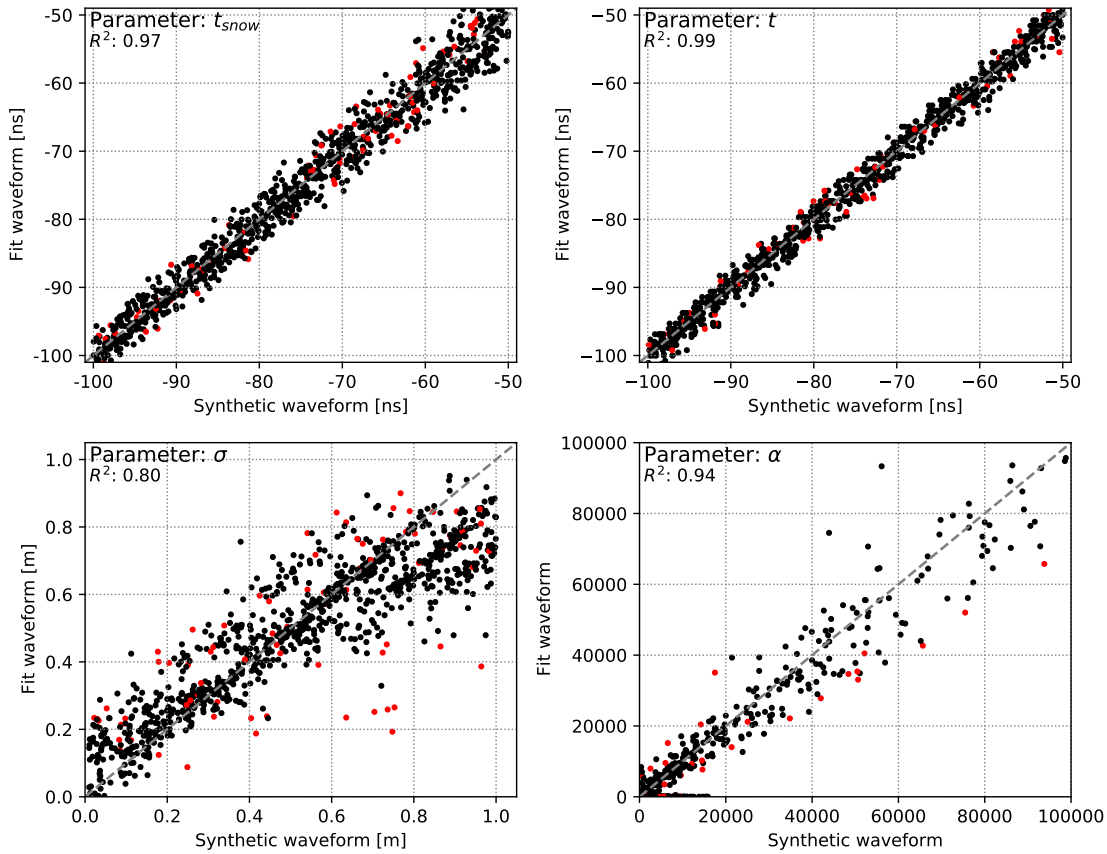

Figure 3.9: Relationships between the synthetic waveform parameters (x-axis) and fit waveform parameters (y-axis) for the four parameters of interest (t_{snow},t,σ,α). Red points indicate poor fits that would be re-processed or filtered out in the retrieval process.

3.6 Initial validation

To evaluate the performance of this algorithm, the returned surface elevation is compared to independent measurements of surface elevation from OIB. Specifically, ATM data taken from the IceBridge underflight of the CryoSat-2 orbit (Fig. 3.1) are compared with retracked CryoSat-2 elevation data derived using this algorithm. The comparison is done between surface elevation measurements before any freeboard calculations are made, ensuring that differences observed are a factor of

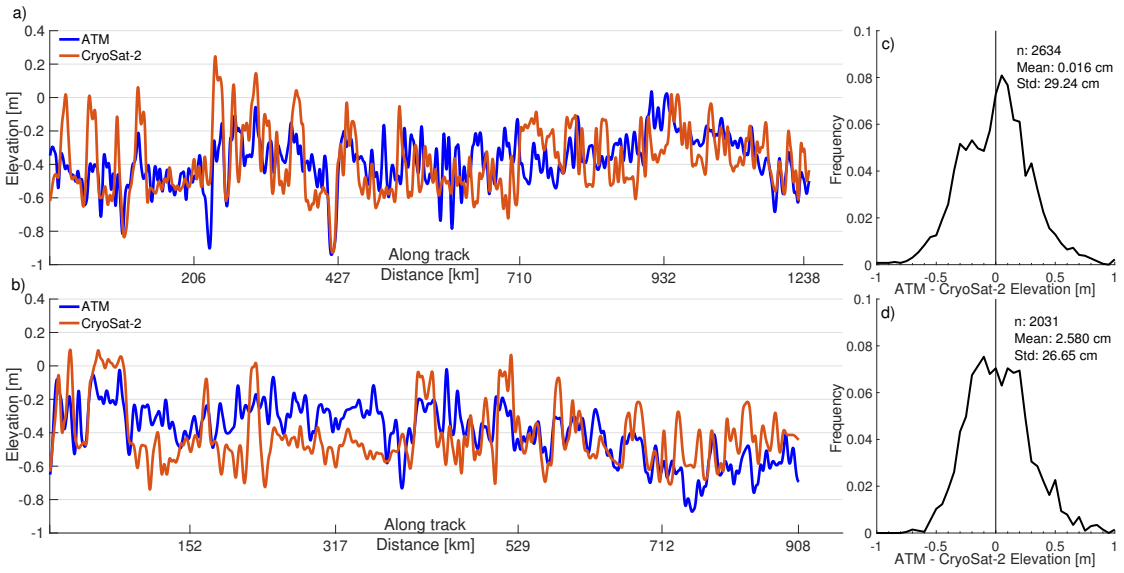

Figure 3.10: Surface (air-snow interface) elevation profiles of OIB ATM (blue) and CryoSat-2 (orange) from the October 2011 (a) and November 2012 (b) campaigns. Frequency distributions of the elevation difference (ATM – CryoSat-2) along the 2011 (c) and 2012 (d) profiles are also shown. The mode of the differences is 0.03 m in 2011 and -0.24 m in 2012. The 2011 profile contains measurements from −63.99° N, −45.11° W to −75.04° N, −49.33° W while the 2012 profile contains measurements from −66.14° N, −43.31° W to −74.25° N, −46.46° W.

the retrieval alone. In order to facilitate a direct comparison, ATM level 2 Icessn elevation data are averaged to the same ground footprint size as a CryoSat-2 echo. Additionally, equivalent geophysical corrections are computed and applied (following Yi et al. 2019) to both the CryoSat-2 and ATM datasets, ensuring that both measurements are in the same frame of reference. These geophysical corrections include effects from tides, which are computed using the TPXO8-Atlas model (Egbert and Erofeeva, 2002), the mean sea-surface height, which are computed using the Technical University of Denmark DTU15MSS dataset (Anderson et al., 2016), and the dynamic atmosphere, which are computed using correction data from the Mog2G model (Carrère and Lyard, 2003).

Surface temperatures from MERRA-2 (Global Modeling and Assimilation Of-

fice (GMAO), 2015) at the midpoint time of both IceBridge flights are found in Fig. 3.1. The 2011 flight had a large (about 20° C) north-south temperature gradient that could result in different snow and ice properties along the flight line, and thus could explain differences observed along the line. In 2012, there was almost no temperature gradient along the flight line. Additionally, surface temperatures remained below freezing for the two weeks prior to both flights, with light snowfall of around 5 mm/day occurring three (four) days prior to the flight in 2011 (2012) but stopping two (three) days before the flight. The time difference between the OIB flight and CryoSat-2 overpass was between 0 and 3.1 hours in 2011 and between 0 and 2.2 hours in 2012.

Figure 3.10 (A and B) shows ATM and CryoSat-2 surface elevation profiles from both the 2011 and 2012 OIB underflights. In these cases, the initial guess for the air-snow interface location in the CryoSat-2 fitting routine comes from the ICESat seasonal average dataset. Overall, the CryoSat-2 retracked elevation profiles capture the general trends found in the ATM profiles. The mean difference in elevation of CryoSat-2 from ATM for the entire flight line is 0.02 cm in 2011 and 2.58 cm in 2012. A frequency distribution of this difference is shown in Fig. 3.10 (C and D). Both years display a Gaussian-like distribution centered near zero (i.e. no difference) with standard deviations of 0.29 m in 2011 and 0.27 m in 2012. It is likely that some of the differences are due to initial temporal and spatial discrepancies between the IceBridge and CryoSat-2 data collections. Correlation coefficients are 0.44 in 2011 and 0.40 in 2012, which, although in the low-to-mid range, is likely brought on by the inherent noise in the data at the shot-to-shot level and non-overlapping

footprints of the two sensors (Yi et al., 2019). Although mean resnorm values from the CryoSat-2 flight lines are 0.11 in 2011 and 0.10 in 2012, signifying good fits, it is still possible that errors in air-snow interface elevation could have arisen from errors in fits that were below the single-metric resnorm threshold but not representative of the actual CryoSat-2 waveform. This resnorm threshold is likely the cause of the "jumps" seen in the CryoSat-2 data, as testing a higher resnorm threshold led to more jumps, while a testing a lower resnorm threshold led to fewer jumps, but worse agreement to ATM. There also appears to be a slight underestimation of ATM by CryoSat-2 in both profiles, which could be brought on by the original footprint sizes, as the smaller ATM footprint is more sensitive to small-scale peaks/ridges than CryoSat-2.

Overall, this initial validation shows the potential of this CryoSat-2 algorithm to retrieve reasonable surface elevation measurements over Antarctic sea ice. This promising result warrants further exploration into freeboard retrieval using this method, discussed in the next section.

3.7 Snow freeboard retrieval

3.7.1 Freeboard calculation

The retrieved elevation of the air-snow interface from this method is used to calculate the snow freeboard of Antarctic sea ice. First, one month of CryoSat-2 data is processed at a time and the outlying data points are filtered out to reduce the inherent noise of the data. The filtering is done by removing any point that

has an output parameter more than three standard deviations away from the mean of the respective parameter. These output parameters include quantities such as the surface elevation, retracking correction, PP, SSD, and τ. Additionally, points with a τ value less than -100 ns were found to produce anomalous surface elevations and therefore are filtered out. Then, surface elevation data consisting only of echo points characterized as leads are gridded to a 25 km polar stereographic grid and averaged over the month. Grid boxes with fewer than five points and/or monthly concentrations less than 50% are ignored. This grid is effectively the mean sea surface elevation. Snow freeboard is calculated by taking each surface elevation point along the CryoSat-2 orbit and subtracting the corresponding mean sea surface elevation value. Any snow freeboard points less than -0.1 m and greater than 2.1 m are filtered out. Between the initial filtering and this freeboard filtering, 41.7% of the total waveforms are filtered out, leaving 58.3% as valid waveforms. This process is done from the entire month of data, and the remaining freeboard values are gridded to 25 km to produce a map of the monthly mean snow freeboard. To study multi-year means for a given month, each monthly snow freeboard grid is averaged over a range of years. In this case, grid boxes with data from fewer than two years are ignored. Both the monthly and multi-year mean snow freeboard grids are smoothed by taking the average of all grid boxes within 2 grid boxes in all directions, which reduces the spatial resolution to 125 km. Smoothing is applied to reduce noise in the CryoSat-2 data and also to fill gaps in the data.

Figure 3.11 shows maps of October monthly averaged snow freeboard values from 2011-2017 as well as the mean of all seven years. The freeboard distribution

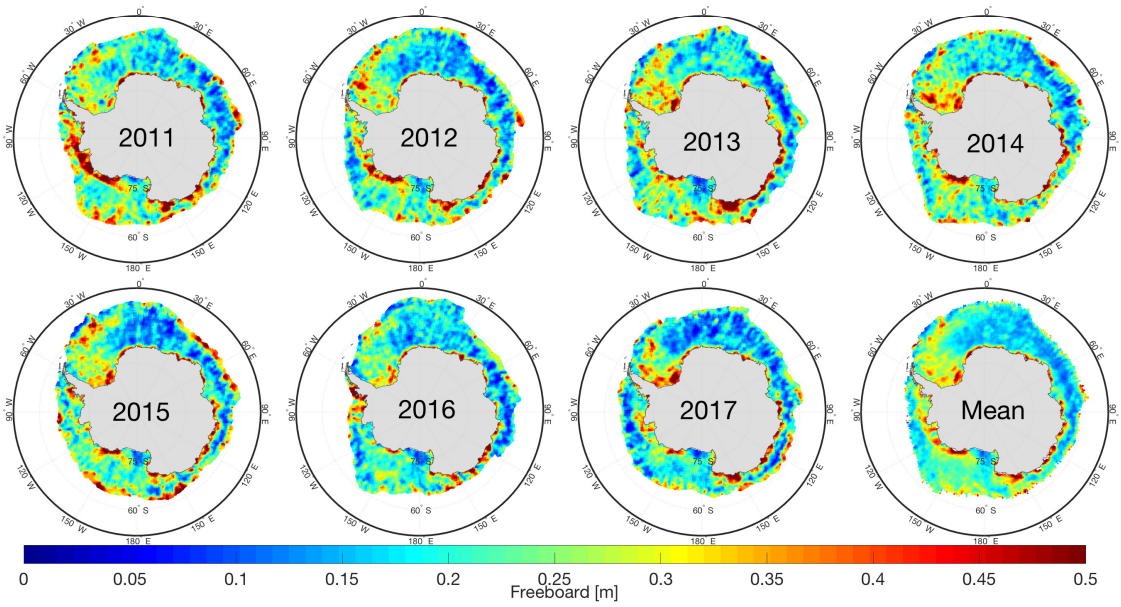

Figure 3.11: October monthly average snow freeboard from 2011-2017, as well as the mean of all years, found using this retrieval method.

corresponds well to what is expected in the Antarctic: the largest values occur in the Weddell and Amundsen seas – where ice production and heavy snow falls are typically prevalent – as well as along the coast of East Antarctica – where snowfall accumulation is also typically large. The smallest values tend to be found off the coast of East Antarctica between 0° and 90° E. Additionally, the region of low freeboard shown in the Ross Sea each year is consistent with the presence of young ice from the Ross Sea Polynya, but could be biased lower due to the large region of lead-type waveforms classified in the area, leading to a higher sea surface height and lower freeboard. While the overall pattern remains similar in each map, there is clear inter-annual variability. For example, the Amundsen Sea region along the Antarctic coastline exhibits a widespread area of very large (over 50 cm) freeboard in 2011, while the same coastal region between 100° W and 150° W shows values between 20 and 35 cm in 2016. Thicker snow freeboard can be found adjacent to the

ice extent edge in each of the years, with the average map clearly showing greater freeboard values along the ice edge in the Western Pacific Ocean (about 90° E to 180° E). This thick freeboard at the ice edge is consistent with the older and thicker ice that has been previously found in the Antarctic frontal ice zone (Nghiem et al., 2016), but could also be due to surface waves penetrating the ice cover, resulting in an altered floe size distribution (Fox and Haskell, 2001) and also a high freeboard bias. Additionally, the high freeboard found here could be a product of the lower CryoSat-2 data density further from the pole as well as the variety of different ice types found in the frontal ice zone.

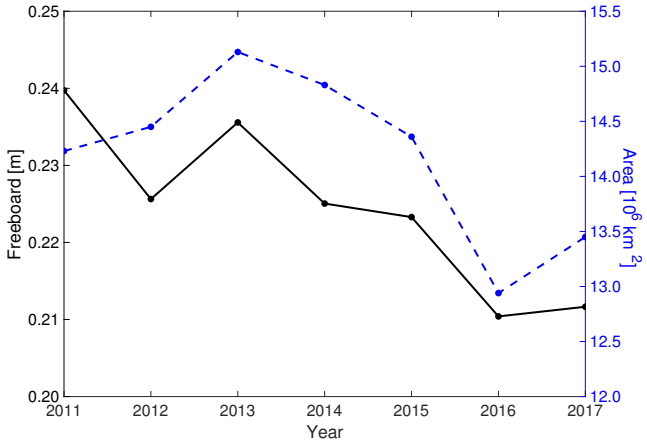

Figure 3.12: October monthly average Antarctic snow freeboard (black) and total sea ice area (blue) for reference. Sea ice area data are gathered from NSIDC (Fetterer et al., 2017).

A time series of mean October snow freeboard from 2011 to 2017 found using this method is shown in Fig. 3.12, with total sea ice area plotted for reference (Fetterer et al., 2017). Apart from slight increases in freeboard from 2012 to 2013 and 2016 to 2017, there is an overall decrease found between 2011 and 2017 of 0.5 cm/yr. The smallest measured freeboard occurred in 2016 (25.8 cm) which is

collocated with a minimum in sea ice area that occurred in the same year. The total average snow freeboard in October from 2011 to 2017 is found to be 27.6 cm with a standard deviation of 13.0 cm. Interestingly, the sea ice area and snow freeboard time series appear highly correlated between 2011 and 2017 (r=0.77) alluding to a potential relationship between freeboard/thickness and area in the Antarctic. This relationship, however, is beyond the scope of this study and should be explored in future work.

3.7.2 Pan-Antarctic freeboard comparisons

To assess the performance of this algorithm on a pan-Antarctic scale, monthly averaged freeboard values from CryoSat-2 are compared with seasonal average freeboard from ICESat. Figure 3.13 shows a difference map between CryoSat-2 and ICESat total freeboard, where positive (negative) values indicate regions where CryoSat-2 measures greater (smaller) freeboard as compared to ICESat. The most notable difference occurs in the Weddell Sea off of the Antarctic Peninsula, where CryoSat-2 records a freeboard value much lower (around 30 cm) than ICESat. A similar region can be found in the Amundsen Sea, where CryoSat-2 measurements are again less than ICESat. CryoSat-2 measures a larger freeboard along most of the sea ice edge, as well as along the Antarctic coast from about 20° W to 60° E. Apart from these areas of noticeable differences between the two datasets, the remainder of the sea ice zone is fairly comparable among both. The total mean difference is only 2.9 cm with a standard deviation of just under 10 cm and a mode difference of

0.8 cm (Fig. 3.13).

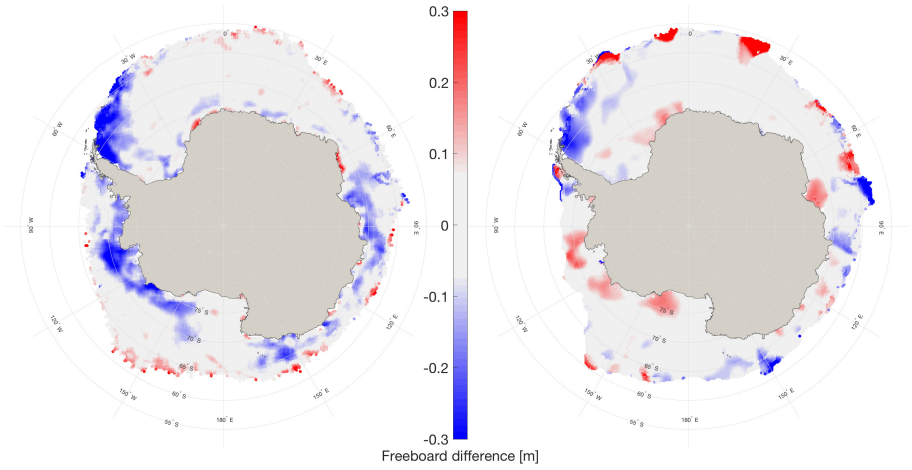

Figure 3.13: Snow freeboard differences showing (left) CryoSat-2 October 2011-2017 average minus ICESat spring 2003-2007 average and (right) ICESat spring 2006 average minus ICESat spring 2003-2007 average. The 2006 data are included as an example year to highlight the interannual variability in the freeboard distribution.

Though this compatibility is encouraging, it is important to note that comparison is indirect in nature. The CryoSat-2 dataset covers October 2011-2017, seven years of data, while this ICESat dataset covers October-November 2003-2007, five years of data. These non-overlapping time periods have different lengths, and the ICESat dataset contains data from October and November in some of the campaigns. Therefore, this comparison shows that this algorithm can produce results similar to the average values found with ICESat, but requires temporally coincident data, such as that forthcoming from ICESat-2, to best assess the accuracy of the retrieval approach (to be discussed in Chapter 4).

Qualitatively, the snow freeboard distribution found in Fig. 3.11 is comparable to that shown in Schwegmann et al. (2016) and Paul et al. (2018). In all studies, the largest freeboard is found along the coast in the Amundsen Sea, East Antarctica,

and in the Weddell Sea, while the smallest freeboard is found in the Ross Sea and off East Antarctic between 0° and 90° E. Similar to what was found in the comparison with ICESat, both Schwegmann et al. (2016) and Paul et al. (2018) find a higher freeboard immediately off the Antarctic Peninsula near the Larson Ice Shelf than is found with this method, which could signal a regional difficulty to retrieve snow freeboard using this algorithm or a complication with the thicker and/or rougher ice that tends to be found in this region. However, these comparisons are still rather indirect, given that the prior works retrieve radar freeboard (Schwegmann et al., 2016) and ice freeboard (Paul et al., 2018) while this method retrieves snow freeboard. Once again, coincident measurements of snow freeboard from ICESat-2 will be invaluable as a comparative tool.

3.8 Application to snow depth retrievals

Given that this algorithm outputs the location of both the air-snow and snow-ice interfaces as a function of radar return time, it seems logical that snow depth could be extracted from these data. Likely, however, the complexities of Antarctic sea ice inhibit this method in tracking the correct snow-ice interface, resulting in a lower-than-expected (judging from passive microwave measurements (Markus and Cavalieri, 1998)) and in-situ surveys (Massom et al., 2001)) snow depth distribution. Figure 3.14 shows a map of the average October 2011-2017 snow depth on sea ice, calculated by subtracting the snow-ice interface elevation from the air-snow interface elevation. It can be seen that for a majority of the Antarctic, a snow depth of around

0.1 m is present. This algorithm appears to be tracking the dominant sub-surface return as a layer within the snowpack as opposed to the ice interface itself, as has been seen in previous studies (e.g. Giles et al. (2008); Willatt et al. (2010)). A potential explanation is that the complex snow stratigraphy found during in situ surveys of the Antarctic sea ice pack (Lewis et al., 2011; Massom et al., 2001; Willatt et al., 2010) and attenuation due to seawater flooding and wicking could be prevalent throughout the Antarctic, and that layers of ice and/or brine could be responsible for an interface return that is higher than the actual snow-ice interface.

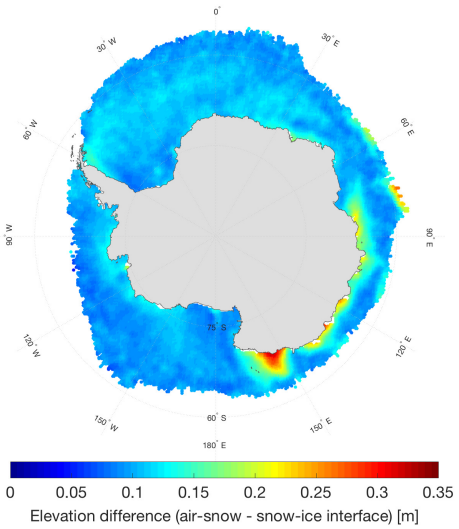

Figure 3.14: October 2011-2017 average difference between the retrieved air-snow and snow-ice interfaces as an exploration into the potential retrieval of snow depth.

A similar result is found when comparing retrieved CryoSat-2 snow depths in the Weddell Sea to that from OIB. Using the peak-picking algorithm on IceBridge data from the 13 October 2011 flight line and converting the distance between peaks to snow depth results in an approximate mean snow depth of 0.26 m. This value is close to the snow depth that was calculated by Kwok and Maksym (2014) for the same flight line (approximately 0.29 m). From CryoSat-2, the mean snow depth

along the flight line is found to be 0.15 m, which is lower than the measured values potentially due to the much larger footprint size and more limited bandwidth from the satellite data.

Despite the widespread small snow depth values, the region off the coast of East Antarctica in Fig. 3.14 (between 90° E and 60° E) exhibits values closer to what is expected. Here, there is a greater snow depth of around 0.3 m. This region is known to have positive ice freeboard values (Maksym and Markus, 2008; Markus et al., 2011; Worby and Wu, 1998), meaning that flooding and saltwater intrusion would play less of a role than in other areas. The near-realistic snow depth measurements here provide evidence that this algorithm could be effective in retrieving snow depth under certain snow conditions, seasons, or locations, but speaks to the inherent complexity and uncertainty associated with Antarctic sea ice. Furthermore, the fact that these snow depth measurements are not higher over other areas of known positive ice freeboard, such as the western Weddell Sea, could signal issues regional issues of the algorithm to retrieve the snow-ice interface. Later chapters of this dissertation explore the improvement of this retrieval algorithm and the resulting snow depths that arise from those improvements.

3.9 Conclusions and future work

In this chapter, a method for retrieving snow freeboard from CryoSat-2 data is developed. It is based off the fundamental idea that scattering of Ku-band radar pulses can originate from the air-snow interface of snow on sea ice. This scattering

is incorporated into a physical waveform model and a least squares fitting routine is used to fit the model to CryoSat-2 level 1B waveforms. The returned fit waveform and associated parameters includes, among others, the location of the air-snow interface as a function of radar return time. That location is then used to retrack the snow surface elevation, and from this, calculate snow freeboard. The performance of this retrieval is evaluated through comparisons with independent measurements. Specifically, surface elevation measurements from OIB ATM, taken in October 2011 and November 2012 along a coincident flight line, help to provide an initial confirmation that the retrieval results were comparable to other data sources. Mean (standard deviation) elevation differences between ATM and CryoSat-2 were found to be just 0.02 cm (29.24 cm) in 2011 and 2.6 cm (26.65 cm) in 2012. Seasonal averaged freeboard data from ICESat allowed for the comparison of the pan-Antarctic freeboard. Though the CryoSat-2 and ICESat freeboard data come from non-overlapping time periods of different lengths and months, there was still general agreement with the freeboard distribution. The mean (standard deviation) difference between CryoSat-2 and ICESat freeboard is 2.9 cm (9.23 cm). The fact that the largest differences between CryoSat-2 and ICESat occur in regions of known thick snow depths could signal a difficulty of the algorithm over the thickest snow, suggesting an area for future improvements to the model. In general, this retrieval algorithm shows promise that snow freeboard can be measured from CryoSat-2 alone.

Though the retrieved air-snow interface elevation and snow freeboard closely resemble that from independent measurements, the retrieved snow-ice interface elevation appears to be larger than expected. Calculated snow depth, therefore, is

lower than typically expected throughout most of the Antarctic sea ice cover as compared to in situ and passive microwave data. Due to strong attenuation of radar returns from brine layers within the snowpack (Nandan et al., 2017), it may not be possible to retrieve the actual snow-ice interface from a Ku-band altimeter in some regions of the Antarctic. However, the region near the Antarctic coast in the western Pacific Ocean (Fig. 3.14) displays snow depths that are much closer to expected, signaling the possibility of snow depth retrieval under certain ice types and conditions. More work is needed to understand why this region shows near-realistic snow depths while other regions with similar ice characteristics (e.g. positive ice freeboard in the western Weddell Sea) do not.

Overall, this study has expanded the functionality of CryoSat-2 as a tool for observing the snow freeboard of Antarctic sea ice, adding to the existing studies retrieving radar freeboard (Schwegmann et al., 2016) and ice freeboard (Paul et al., 2018). In September 2018, CryoSat-2 was joined in space by ICESat-2, NASA's second-generation satellite laser altimeter system (Markus et al., 2017). These coincident altimeters will provide the ability to observe the polar regions like never before. In subsequent chapters, ICESat-2 data will be used as both a comparative measure – for direct monthly comparisons of snow freeboard – as well as an initial guess for the waveform fitting model. These new measurements of air-snow interface elevation and snow freeboard from ICESat-2 help to further validate and improve this retrieval algorithm.

Future work will look into combing these CryoSat-2 snow freeboard measurements with those from laser altimetry to produce an ICESat-CryoSat-2-ICESat-2

time series of snow freeboard in the Antarctic. This reconciled laser-radar altimetric record of snow freeboard would span 15+ years from 2003 throughout the lifetime of ICESat-2, providing a long and robust dataset that could be used in other studies of sea ice. Together with ESA's CCI dataset combing CryoSat-2 and Envisat (Paul et al., 2018; Schwegmann et al., 2016), these long term datasets could lead to improved retrievals of sea ice thickness and an enhanced understanding of sea ice in the Antarctic.

Chapter 4: Assessing CryoSat-2 Antarctic Snow Freeboard Retrievals Using Data from ICESat-2

This chapter utilizes and improves upon the CryoSat-2 retrieval algorithm developed in Chapter 3. Additionally, assessments are made by comparing these CryoSat-2 snow freeboard data to coincident data from ICESat-2. This work was submitted to *Earth and Space Science* and can be found as a preprint on the Earth and Space Science Open Archive (Fons et al., 2021).

4.1 Introduction

ESA's CryoSat-2 radar altimeter has provided a more than 10-year time series of surface elevation data since its launch in 2010 that has been invaluable for cryospheric studies. For sea ice research in particular, CryoSat-2 has enabled basin-scale estimates of Arctic sea ice freeboard and thickness from space, building on the satellite altimeter-based freeboard/thickness time series that began with ERS-1 and -2 (Laxon et al., 2003) and continued with ICESat (Zwally et al., 2008) and Envisat (Connor et al., 2009). Freeboard data from CryoSat-2 have been used to quantify Arctic sea ice thickness and volume over time (Kwok and Cunningham, 2015; Laxon et al., 2013; Tilling et al., 2018), to develop new retrieval algorithms

for sea ice properties (Kurtz et al., 2014; Lee et al., 2016), and to better understand potential bias and uncertainty from radar altimetric studies of sea ice (Kwok, 2014; Landy et al., 2020; Nandan et al., 2017; Ricker et al., 2014).

Despite its widespread use in the Arctic, CryoSat-2 data remain underutilized for sea ice research in the Southern Ocean (Meredith et al., 2019). This is due in part to the lack of available pan-Antarctic snow depth on sea ice information, which contributes to the uncertainty in the dominant scattering horizon from radar returns and limits accurate sea ice freeboard and thickness retrievals (Massom et al., 2001; Paul et al., 2018). Nevertheless, some studies have attempted to provide estimates of freeboard and thickness using different methods and with various caveats. Kwok and Kacimi (2018) calculated ice freeboard and thickness profiles in the Weddell Sea using CryoSat-2 and data from NASA's OIB. Snow depth values were estimated by subtracting the CryoSat-2 freeboards from the ATM laser (total) freeboards. Price et al. (2015) similarly computed thickness from CryoSat-2 in a single region – McMurdo Sound – using snow depth from models, reanalysis, and passive microwave sensors. Work done through ESA's sea ice CCI (Paul et al., 2018; Schwegmann et al., 2016) showcased freeboard retrievals in the Southern Ocean and comparisons between CryoSat-2 and Envisat, but the lack of snow depth data has prevented them from computing sea ice thickness. Fons and Kurtz (2019) put forth a waveform-fitting method that attempted to circumvent the complexities of the effect of the snow layer on radar returns by retrieving the air-snow interface elevation from CryoSat-2. This work - discussed in the previous chapter - exploited the fact that scattering at Ku-band frequencies – though potentially smaller in magnitude

than scattering from the snow-ice interface – does occur from the air-snow interface (Kwok, 2014; Willatt et al., 2010), and incorporated this scattering in a forward waveform model. While the results showed promise, they lacked independent, pan-Antarctic snow freeboard data to validate the retrievals.

While challenges to CryoSat-2-derived Antarctic sea ice freeboard and thickness remain, studies using satellite laser altimetry have proven more successful. Laser altimeters range to the surface of the snow on sea ice and therefore are not impacted by the uncertain scattering horizon within the snow layer. The freeboard retrieved from laser altimeters is therefore the snow freeboard, which can be combined with snow depth information to estimate thickness. NASA's ICESat was the main platform used for laser altimetric studies of sea ice prior to 2019, and studies combined the retrieved snow freeboard with snow depth information from various sources, including passive microwave-derived snow depth (Zwally et al., 2008), a zero ice freeboard assumption (Kurtz and Markus, 2012), and a one-layer modified density model (Kern et al., 2016; Li et al., 2018) to compute thickness. The launch of ICESat-2 in late 2018 has provided an opportunity to advance sea ice research in the Southern Ocean, both in stand-alone studies of Antarctic sea ice and as a unique compliment to CryoSat-2 for combination studies and validation. One such study (Kacimi and Kwok, 2020) combined CryoSat-2 radar freeboards with ICESat-2 snow freeboards to make estimates of snow depth on Antarctic sea ice. They used the resulting snow depth and freeboards to estimate pan-Antarctic thickness and volume for the Austral winter 2019. These results showcase a new thickness dataset but are limited to the years in which both satellites are operating. More combination

studies are possible if the recent CRYO2ICE campaign (European Space Agency, 2018), which better aligned the CryoSat-2 orbit with that of ICESat-2 to improve spatial/temporal coincidence in the Arctic, is altered to optimize the orbital overlaps in the Southern Hemisphere.

Here, this study utilizes ICESat-2 Southern Ocean snow freeboard data to validate the CryoSat-2 snow freeboard retrieval method originally published in Fons and Kurtz (2019). Fons and Kurtz (2019) was a feasibility study that lacked coincident validation data for proper evaluation. Now, with ICESat-2, one is able to better assess and draw conclusions on the CryoSat-2 freeboard retrievals. This work will first discuss improvements made to the CryoSat-2 retrieval algorithm since publication in 2019, which include updates to the model parameters, sea surface height (SSH) determination, the sea ice surface height PDF, and other components of the algorithm (Section 4.3). An estimate of uncertainty in the freeboard retrievals is provided (Section 4.4) prior to showcasing validation of the improved algorithm using data from ICESat-2 both along-track and pan-Antarctic (Section 4.5). This study concludes with a discussion of potential error sources, sampling biases, and difficulties of laser-radar comparisons (Sections 4.6 and 4.7).

4.2 Data

The primary dataset used in this work is the CryoSat-2 baseline-D Level 1-B waveform data (European Space Agency, 2019b,c). These data are acquired by the SIRAL instrument aboard CryoSat-2, which has a frequency in the Ku-

band centered at 13.575 GHz (Wingham et al., 2006). SIRAL operates in three different modes: low resolution mode (LRM), synthetic aperture mode (SAR), and synthetic aperture-interferometric mode (SARIn). Both the SAR and SARIn modes are utilized in this study and provide complete coverage of the Antarctic sea ice pack. The CryoSat-2 echoes in SAR and SARIn modes represent a pulse-doppler-limited footprint of approximately 360 m along track and 1.65 km across track (European Space Agency, 2019a; Scagliola, 2013), however, these echoes can be influenced by off-nadir, specular returns from approximately 15 km across-track (Tilling et al., 2018). For consistency, both SAR and SARIn waveforms are reduced to 128 range bins, with SAR data being truncated and SARIn data being clipped to 128 range bins about the maximum power location. Elevation is computed from these waveforms following the procedure outlined in Fons and Kurtz (2019), which involves retracking the waveforms and applying the geophysical and retracking corrections to the raw ranges.

To assess the retrieved CryoSat-2 snow freeboards, this study utilizes snow freeboard data from ICESat-2, specifically, the release 3 Level 3A sea ice freeboard product ATL10 (Kwok et al., 2020b). ATL10 provides estimates of snow freeboard in both hemispheres for each of the six ICESat-2 beams. The freeboard estimates are computed using the sea ice and sea surface elevations from the ATL07 sea ice height product, which includes variable length segments (ranging from ∼20-200 m) encompassing 150 returned signal photons (Kwok et al., 2020a, 2019). Here, the highest resolution, segment-scale "beam freeboards" are used, which provides a freeboard estimate for each beam and ATL07 segment using only the leads estimated

along the given beam (Kwok et al., 2020a). Unless otherwise noted, mentions of "freeboard" in this chapter refer to the snow freeboard (i.e. the height of the sea ice and snow above the sea surface).

For this study, the CryoSat-2 and ICESat-2 data are analyzed for the coincident ICESat-2 overlap period, ranging from October 2018 until October 2020. Pan-Antarctic maps of freeboard are computed using monthly means and gridded to the NSIDC 25 km x 25 km polar stereographic grid. CryoSat-2 snow freeboards below -0.1 m and above 3.0 m are filtered out prior to gridding, to account for instrument noise and to remove anomalously high freeboard values. Gridded values are only computed if the grid cell contains at least five samples and an ice concentration of at least 50%. Version 3 Bootstrap monthly average ice concentration data (Comiso, 2017) are used for 2018 and 2019 while the NOAA/NSIDC Climate Data Record Near-Real-Time (NRT CDR) monthly sea ice concentration product is used for 2020, when the Bootstrap data are not yet available (Meier et al., 2017). The NRT CDR product essentially takes the higher value from the Bootstrap and NASA Team algorithms (Cavalieri et al., 1996). ICESat freeboard data are used in a limited capacity in this work (described in Section 4.3.1) as part of an initialization of the waveform-fitting model. These data range from 2003-2008, with a description found in Kurtz and Markus (2012).

4.3 Algorithm design and improvements

This section provides a brief overview of the procedure put forth in Fons and Kurtz (2019), which herein will be referred to as Version 1 (V1), but focuses mainly on the improvements that have been made to the algorithm to create Version 2 (V2). The changes were motivated in part by the launch of ICESat-2 in 2018, which provides coincident assessment data that were not yet available for the V1 algorithm. Additionally, lessons learned during the V1 development helped to inform the V2 algorithm. For a more detailed look at the model and waveform-fitting process, see the previous chapter and Fons and Kurtz (2019).

To retrieve sea ice elevation and calculate freeboard from CryoSat-2, this study employs a physical – as opposed to the more commonly used empirical – retracking technique. This technique uses a forward model and waveform-fitting algorithm that constructs a modeled CryoSat-2 waveform from given initial parameters, fits the model to the CryoSat-2 data using an optimization approach, and calculates the retrieved elevation using the best-fit waveform and parameters. The output (free) parameters are given in Table 4.1, where the snow depth and snow-ice interface time delay allow for the calculation of the elevations of both the air-snow and snow-ice interfaces, and from there, an estimation of both the snow freeboard and the ice freeboard. The initial guess parameters in Table 1 are derived from the actual CryoSat-2 waveform and independent measurements. This method was originally put forth in Kurtz et al. (2014), and then was modified to include scattering effects from the snow layer in Fons and Kurtz (2019). In the V1 retrieval, the modeled

waveform was given by:

$$\Psi(\tau) = P_t(\tau) \otimes I(\tau, \alpha) \otimes p(\tau, \sigma) \otimes \upsilon(\tau, h_s) \tag{4.1}$$

where Ψ is the constructed waveform, P_t is the transmit pulse, I is the rough surface impulse response, p is the surface height probability density function, and υ is the scattering cross section per unit volume – all of which are a function of τ, the echo delay time on the waveform, and other parameters given in Table 4.1 (Fons and Kurtz, 2019; Kurtz et al., 2014). Since Fons and Kurtz (2019), a few aspects of the original method have been improved, in order to better model sea ice waveforms and reduce the potential for convergence on local minima, resulting in the V2 algorithm. The main improvements consist of: reducing the number of free parameters in the model, using a new surface height probability density function (PDF), altering the SSH calculation, and a few smaller modifications. These changes are explained in this section.

4.3.1 Free parameters

The V1 algorithm used a model with nine free parameters – a relatively large number that increases the potential for the waveform-fitting optimization procedure to converge on a local, as opposed to global, minimum. In V2, this number is reduced to five parameters and the radar backscatter terms of snow and ice are designated as static. Given the uncertainty associated with these backscatter parameters, this study now relies on values published previously (given in Table 4.1).

The assumption is made that these static terms represent average values across the Antarctic, and it is acknowledged that further study into these quantities could provide useful information on their seasonal and regional variations. V1 retrievals used ICESat data as an initial guess for the air-snow interface location parameter. In V2, this free parameter is updated to be physically quantifiable (snow depth) and is instead estimated using a combined ICESat and ICESat-2 monthly "climatology" as the initial guess. Like in V1, the 'zero ice freeboard' assumption is invoked for this initial guess that assumes the snow depth is equal to the snow freeboard (the implications for this assumption are discussed in Section 4.3.5). Each monthly climatology initialization map (12 in total, one for each month) consists of multiple years of ICESat and ICESat-2 snow freeboard data from the given month averaged together. The ICESat data for a given month comes from the years 2003-2008, while the ICESat-2 data for that month comes from the years 2018-2019. This study adds ICESat-2 data to the initialization to incorporate more – and more recent – data into the initial guess. Additionally, ICESat only collected data during a few months each year while ICESat-2 collects data year round. The added ICESat-2 data therefore provide month-to-month variability in the initial guess. By creating this monthly climatology, the same, independent, consistent initialization is used from year to year. The free parameters used here are given in Table 4.1.

Free Parameters		Initial Value	Bounds	Reference
h_s	Snow depth	ICESat/ICESat-2 monthly "climatology"	± 30 cm	Kurtz and Markus (2012); Kwok et al. (2020b)
t	Snow-ice interface time delay	70% power threshold	± 3 ns	Laxon et al. (2013)
σ	Roughness (std of surface height)	0.15	0-1 m	Fons and Kurtz (2019)
α	Angular backscatter	Lookup table based on waveform characteristics	1.5e1-9e8	Kurtz et al. (2014)
A_f	Amplitude scale factor	1	± 0.5	Kurtz et al. (2014)
Static Parameters				
$\sigma^0_{sfc-snow}$	Snow surface backscatter	0 dB	-	Arthern et al. (2001)
$\sigma^0_{sfc-ice}$	Ice surface backscatter	8 dB	-	Kwok (2014)
$\sigma^0_{vol-snow}$	Snow volume backscatter	-7 dB	-	Beaven et al. (1995)
$\sigma^0_{vol-ice}$	Ice volume backscatter	-17 dB	-	Beaven et al. (1995)
K_{e-snow}	Snow extinction coefficient	0.1 m^{-1}	-	Ulaby et al. (1982)
K_{e-ice}	Ice extinction coefficient	5 m^{-1}	-	Ulaby et al. (1982)

Table 4.1: Free parameters used in the V2 retrieval algorithm and static parameters used in the volume scattering term of the waveform model. Additional static parameters used can be found in Fons and Kurtz (2019) and Kurtz et al. (2014).

4.3.2 Surface height PDF

In the V1 algorithm, a zero-mean Gaussian distribution was used to represent the surface height PDF in the waveform model. Here in V2, the surface height PDF is updated to be a lognormal distribution, which has been shown (over Arctic sea ice) to better represent the sea ice surface PDF over CryoSat-2 footprint scales (Landy et al., 2020). This distribution is given as:

$$p(\tau) = \frac{1}{\tau\sigma_l\sqrt{2\pi}} \exp\left(-\frac{(\ln\tau - \mu)^2}{2\sigma_l^2}\right) \tag{4.2}$$

where μ and σ_l represent the mean and standard deviation, respectively, of the natural logarithm of the surface height. This study assumes a zero-mean distribution and initializes the roughness term (σ) as 0.15, which gets converted to σ_l and adjusted during fitting as a free parameter (Table 4.1). The impact of the lognormal surface height PDF is shown in Fig. 4.1. Modeled waveforms were created with varying roughness values and run using both a lognormal (solid) and normal (dashed) surface height PDF. For small roughness values, the difference in the modeled waveform shape (measured by the squared norm of the residuals) when using the lognormal versus normal distribution is negligible. Conversely, as the roughness increases, these differences increase exponentially. Judging by the example roughness distribution output by this algorithm from September 2020 (Fig. 4.1), most fit waveforms have σ values between 0.1 and 0.45 m and therefore are less sensitive to the modified surface height PDF used. However, there are still waveforms fit with

σ values over 0.5 m which would be more sensitive to the modified surface height PDF and benefit from the more representative lognormal distribution.

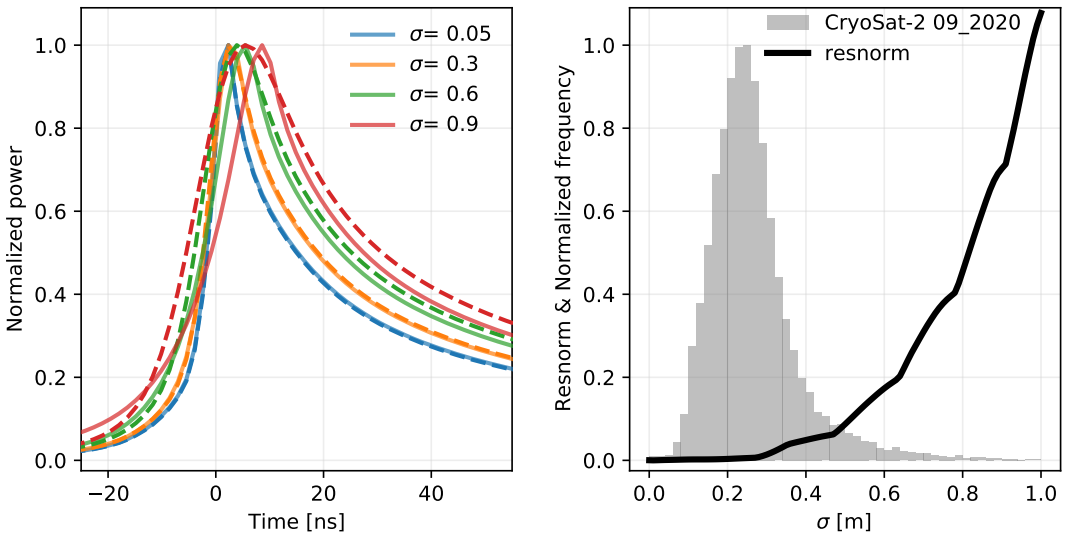

Figure 4.1: Sensitivity of modelled waveform shape to roughness and surface height PDF used. Left: Solid lines show modelled waveforms with varying values of σ created using a lognormal surface height PDF, while dashed lines show the same but using a normal surface height PDF. Right: The difference in shape is quantified using the squared norm of the residual (resnorm, black line) plotted at 1 cm increments from 0 to 1 m roughness. An example normalized histogram of gridded σ values from September 2020 is shown to give its expected range.

4.3.3 Sea surface height

The SSH determined by lead elevations in V1 was, in essence, a 25 km gridded SSH. Though freeboard was computed along-track, the sea surface was averaged for all tracks within the grid cell, and then subtracted from the along-track sea ice elevations. This method overlooked the smaller scale variability in SSH, and therefore potentially biased the retrievals. In V2, SSH is instead calculated along-track. Following Kwok and Cunningham (2015), all the lead-type elevations are averaged together in along-track segments, and any segments where fewer than three

SSH measurements exist are discarded. Given that the lead distribution within the Antarctic sea ice pack is more widespread than that of Arctic sea ice (Reiser et al., 2020), this study uses a segment length of 10 km as opposed to 25 km in Kwok and Cunningham (2015). The 10 km SSH segment length is the same as that used in the ICESat-2 along-track sea ice data products (Kwok et al., 2020a).

4.3.4 Additional modifications

In addition to the improvements mentioned above, a few smaller changes were made to improve on the V1 retrievals and streamline the processing. For one, an "ocean" surface type classification is implemented in V2 using the waveform characteristics of stack standard deviation (SSD, which is the standard deviation of backscatter variation for all waveforms that make up the stack) and skewness (which is a measure of the asymmetry of the waveform). Waveforms with an SSD greater than 50, a skewness less than 0.3, and an along-track rolling average of skewness less than 0.3 are considered ocean points and filtered out before fitting. The rolling average is used to invoke a more conservative filtering scheme, so that single returns with an anomalously low skewness would not be mis-classified as ocean-type and so that the sea ice edge would be preserved for fitting and later potential filtering due to ice concentration (Fig. 4.2).

Another update to V1 was made to the radar propagation correction that accounts for scattering within the snowpack. The V1 algorithm used a typical

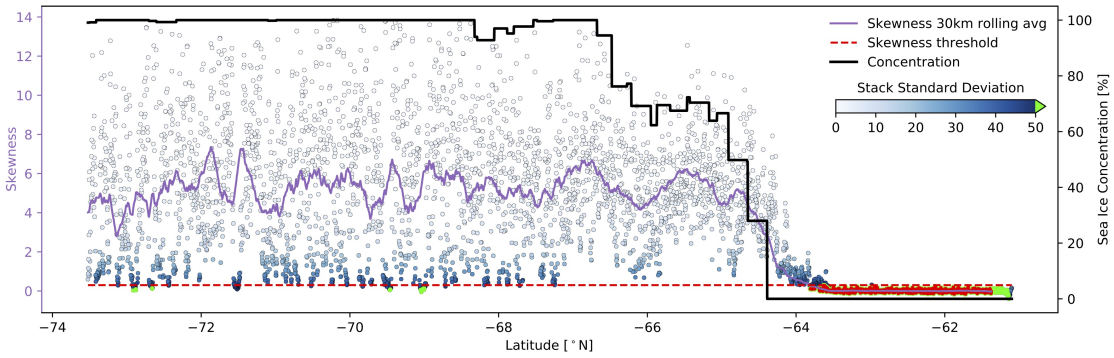

Figure 4.2: Ocean-type waveform filtering for a CryoSat-2 SAR data file. Points are individual waveforms plotted by their skewness (left y-axis) and colored by SSD. The purple line represents the 30 km rolling average of skewness. Dashed red line is the skewness threshold used to filter ocean waveforms, and green points are those above the SSD threshold. Points with red centers are waveforms filtered out along this profile. Solid black line shows the along-track sea ice concentration (right y-axis).

representation of this correction, given by:

$$\delta h = Z_r(1 - c_s/c) \tag{4.3}$$

where δh is the radar range correction, c is the radar wave speed, c_s is the wave speed through snow, and Z_r is the snow depth corrected for wave speed (Mallett et al., 2020). However, the V1 algorithm treated Z_r as the actual snow depth (as it is conventionally interpreted, Mallett et al. 2020) when it should have been corrected for wave speed through snow. Mallett et al. (2020) showed that this interpretation can lead to a bias in the freeboard retrievals through the erroneous reduction by a factor of c_s/c. The V2 algorithm corrects this interpretation and instead uses the wave speed-corrected snow depth in Equation 4.3, given by:

$$Z_r = Z(c/c_s) \tag{4.4}$$

where Z is the real snow depth.

The last update made involved converting the processing from MATLAB to Python programming language. While care was taken to ensure that results were consistent between the two languages, inherent differences in the standard curve fitting toolboxes led to small discrepancies from V1 to V2. For best consistency with the previous processing, this study utilizes the scipy *curve_fit* package (Virtanen et al., 2020) over other fitting packages.

4.3.5 Retrieval assumptions and limitations

Despite the improvements made to create the V2 algorithm, certain assumptions are still inherent within the freeboard retrievals that could impact results. One such assumption is the zero ice freeboard assumption used to initialize the snow depth parameter. V2 invokes this assumption when inputting the snow freeboard climatology as a first guess for snow depth. It is understood that while the zero ice freeboard can be a good assumption is some regions and seasons (Kurtz and Markus, 2012), it is likely not valid for the whole Antarctic sea ice pack (Kwok and Kacimi, 2018) and may lead to biases in the retrievals (discussion in Section 4.6). It is used as a starting point until better snow depth information is available.

Another limitation of the model is its handling of surface roughness. Roughness at different length scales has been shown to significantly impact Ku-band radar returns and bias freeboard retrievals (Landy et al., 2020). V2 attempts to handle this fact by setting σ as a free parameter in the model, with bounds that cover the

expected range of roughness (0-1 m). However, the tracking point on a radar waveform can be influenced by roughness (Fig. 4.1, Landy et al. 2020), and therefore the single-value initialization for snow-ice interface tracking point (t) may introduce a bias. Further work is needed to determine the impacts of a roughness-induced dynamic tracking point initialization on elevation and freeboard retrievals using this method.

4.4 Estimation of uncertainties

The uncertainty in satellite-derived freeboard retrievals comes from a combination of random and systematic uncertainties. The random freeboard uncertainty (σ^2_{fb}) of an individual measurement within a 10 km sea surface segment can be estimated by:

$$\sigma^2_{fb} = \sigma^2_{fh} + \frac{\sigma^2_{lead}}{N} \tag{4.5}$$

where the random uncertainty in the floe height estimates (σ^2_{fh}) is added to that in the SSH estimates ($\frac{\sigma^2_{lead}}{N}$) (Kwok et al., 2020a). Here, the SSH uncertainty is found by calculating the variance in the lead elevations for each 10 km along-track SSH segment and dividing by N, the number of lead points in the segment. Therefore, the uncertainty decreases as the number of leads in a given segment increases. The monthly, basin-scale average of the SSH variance typically ranges from 1 to 1.7 cm, resulting in a small uncertainty contribution of less than 0.2 cm. The floe height uncertainty is calculated over the same 10 km along-track segment, which is estimated as the variance in the floe heights. The standard deviation of floe heights

in a segment tends to be between 12.5 and 14.0 cm, which results in a 1.6 to 2 cm uncertainty for an individual measurement. Combining these two sources results in a random freeboard uncertainty of an individual measurement between ∼1.7 and 2.1 cm. Given the small uncertainty in the SSH measurements, this random freeboard uncertainty is dominated by that in the floe height. It is assumed that this random uncertainty becomes negligible as the number of samples increases through gridding.

The systematic uncertainty in the data is more difficult to estimate given the waveform-fitting procedure applied. There is uncertainty in the input parameters provided to the model, however, it is not initially clear how these uncertainties propagate through the fitting process. In order to provide an estimate of the systematic freeboard uncertainty, a synthetic waveform approach utilizing Monte-Carlo simulation is used. This process is based off of Costa et al. (2011) and is explained in the following paragraphs. A flowchart is provided in Fig. 4.3.

In this retrieval process, it is assumed that a CryoSat-2 waveform can be accurately represented by the waveform model developed, which includes the aforementioned five free parameters. This assumption means that each actual CryoSat-2 waveform (step B in the flowchart, Fig. 4.3) would be therefore be made up of five "true parameters" (A) that represent the actual sea ice surface. These true parameters are obviously not known, which is why the fitting process (C) is used to retrieve the best-guess fit parameters (D) for each CryoSat-2 waveform. This begs the question: how can one tell how well the fit parameters match the true parameters, if the true parameters are not known?

A method to answer this question lies in utilizing synthetic waveforms gener-

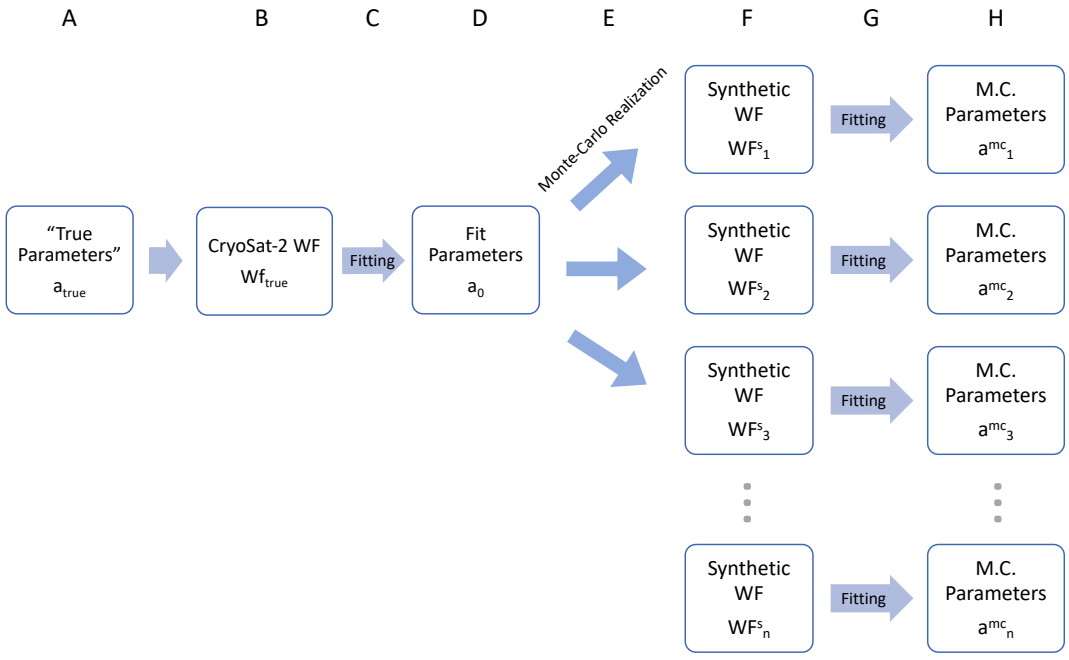

Figure 4.3: Flowchart of the uncertainty estimation process using synthetic waveforms and Monte Carlo realization. Letters refer to the steps in the process and are referenced in text. Adapted from Costa et al. (2011).

ated through Monte-Carlo simulations that draw from the uncertainty in the initial guess parameters. If one assumes a probability distribution for each initial guess parameter governed by the parameter itself (as a mean value) and an estimated uncertainty (as the standard deviation), then a random value can be drawn from each parameter's distribution (E) and used to generate synthetic parameters that cover the range of possible parameters within the uncertainty bounds. This process can be repeated many (n) times to provide many possible parameter combinations within the estimated initial uncertainty (F). These synthetic parameters can be used to generate synthetic waveforms, WF^s_n, which are then treated like CryoSat-2 waveforms: initial guesses are drawn from the waveform, a model is generated from the initial guesses and fit to WF^s_n (step G), and output parameters are retrieved

Parameter	Initial Uncertainty	Reference(s)	Fit Uncertainty
h_s	4.5 cm	Kurtz and Markus (2012), Kacimi and Kwok (2020)	3.0 cm ($0.25 * h_s$)
t	0.41 ns	Ricker et al. (2014)	0.36 ns
σ	4.0 cm	Landy et al. (2020)	2.3 cm
α	$1 * 10^{1.5}$	Kurtz et al. (2014)	$1 * 10^{1.2}$

Table 4.2: Parameters and uncertainty estimates from the Monte Carlo uncertainty estimate. Initial uncertainty values come from references provided, while fit uncertainty values come from the output of the Monte Carlo simulation approach described in text.

(step H) which are here referred to as Monte Carlo parameters, or a_n^{mc}. Under the assumptions provided above, the parameters in H would have the same relationship to the waveforms in F (by way of fitting) as the fit parameters in D have to the true parameters in A. This allows for an error estimate to be computed for each parameter and synthetic waveform, and an estimate of uncertainty to be realized when considering all synthetic waveforms and parameters.

Here, an initial test of n=10000 simulations is run on a CryoSat-2 waveform to provide an estimate of the uncertainty in each fit parameter as well as the resulting freeboard. The initialization parameters and uncertainty ranges (and references) are provided in Table 4.2. It is acknowledged that this is an initial attempt at quantifying uncertainties from this method, and further work is needed to better constrain initial uncertainties.

The two important parameters for computing snow freeboard are the snow depth and the snow-ice interface tracking point. The initial estimated snow depth for this WF_{true} is 12 cm, following the initialization procedure used in the retrievals.

The initial snow depth uncertainty of 4.5 cm comes from an estimated ∼2 cm for the freeboard uncertainty (Kurtz and Markus, 2012; Markus et al., 2011) and 4 cm uncertainty to account for the zero ice freeboard assumption (Kacimi and Kwok, 2020) taken as the average difference between snow depth and snow freeboard over Antarctic sea ice. Through root-sum-square combination (Ku, 1966), this results in 4.5 cm uncertainty in the initial snow depth. The uncertainty in snow-ice interface tracking point is taken to be 6 cm from Ricker et al. (2014), which corresponds to approximately 0.4 ns.

Using the initial uncertainties in Table 4.2, random values were chosen from distributions of each fit parameter in a_0, and synthetic waveforms were created for each combination. The fitting process was applied to all waveforms, and differences in each parameter a_n^{mc} from a_0 were calculated. The mean difference in each parameter from all synthetic waveforms was found, and is used here as the estimate of uncertainty in the respective parameter following the fitting procedure. These values are given in Table 4.2. The fit snow depth uncertainty of 3 cm matches what is found in Spreen et al. (2009) of $0.25 * h_s$ (since h_s in this case is 12 cm). Since only one WF_{true} is utilized in this exploratory analysis, the fit snow depth uncertainty is hereafter taken as $0.25 * h_s$ as a conservative approach to account for both spatial snow depth variation as well as the larger spread in the difference between snow depth and freeboard at thicker snow depths in Kacimi and Kwok (2020) that informed the initial snow depth uncertainty.

The snow freeboard (h_{fs}) found using this retrieval method is given as:

$$h_{fs} = (h_s + h_{s-i}) - h_{ssh} \tag{4.6}$$

where h_{ssh} is the SSH elevation and h_{s-i} is the elevation of the snow-ice interface computed from the parameter t (Table 4.1). With Equation 4.6, the uncertainty in snow freeboard is therefore given by:

$$\sigma_{h_{fs}} = \sqrt{\sigma_{sd}^2 + \sigma_{s-i}^2 + \sigma_{ssh}^2} \tag{4.7}$$

through root-sum-squares error combination. Running the same Monte Carlo procedure as described on a lead-type waveform results in a lead tracking point (i.e. SSH) uncertainty of 0.7 cm. Combining the snow depth (3 cm), ice tracking point (0.36 ns $\approx$ 5 cm) , and SSH (0.7 cm) uncertainties results in a total estimated freeboard uncertainty of 5.9 cm for this assumed snow depth. For varying snow depths, using the equation in Table 4.2, Equation 4.7 can be written as:

$$\sigma_{h_{fs}} = \sqrt{(0.25 * h_s)^2 + \sigma_{s-i}^2 + \sigma_{ssh}^2}, \tag{4.8}$$

which results in $\sigma_{h_{fs}}$ ranging from 5 cm to 16 cm over the range of snow depths observed. These values are reasonable compared to those found in other works (Kern et al., 2016; Tilling et al., 2018). Since this uncertainty is systematic, it typically cannot be reduced by averaging (Ricker et al., 2014), however, it can be influenced by residual bias in the input parameters. The freeboard uncertainty found through

Equation 4.8 is used in Chapter 5 to quantify thickness uncertainty.

Once again, this is provided as a preliminary attempt to estimate uncertainties in the fitting procedure applied. Future work is needed to better constrain the initialization parameter uncertainties that go into this Monte Carlo approach.

4.5 Results

All CryoSat-2 data from October 2018 to October 2020 were processed using the V2 algorithm processing. This section compares the retrieved CryoSat-2 snow freeboards to those from ICESat-2 by examining along-track retrievals using near-contemporaneous overlaps of the two satellites (Section 4.5.1) and comparing pan-Antarctic, monthly gridded freeboard data (Section 4.5.2). Variability in the snow freeboard retrievals is shown in Section 4.5.3.

4.5.1 Along-track comparisons

To compare the freeboard retrieval performance along-track, this study first found near-contemporaneous overlaps in the two satellites' ground tracks that occurred in the sea ice zone with the least possible time difference. An orbital overlap is defined as a CryoSat-2 and ICESat-2 ground track being within 4 km of each other for at least 10 seconds of flight time, which is approximately 70 km along-track. Given the 1.65 km across-track footprint of CryoSat-2 and the 3.3 km spread of the three beam pairs of ICESat-2, 4 km is the maximum separation that could still theoretically result in overlapping footprints. This study finds that the overlap

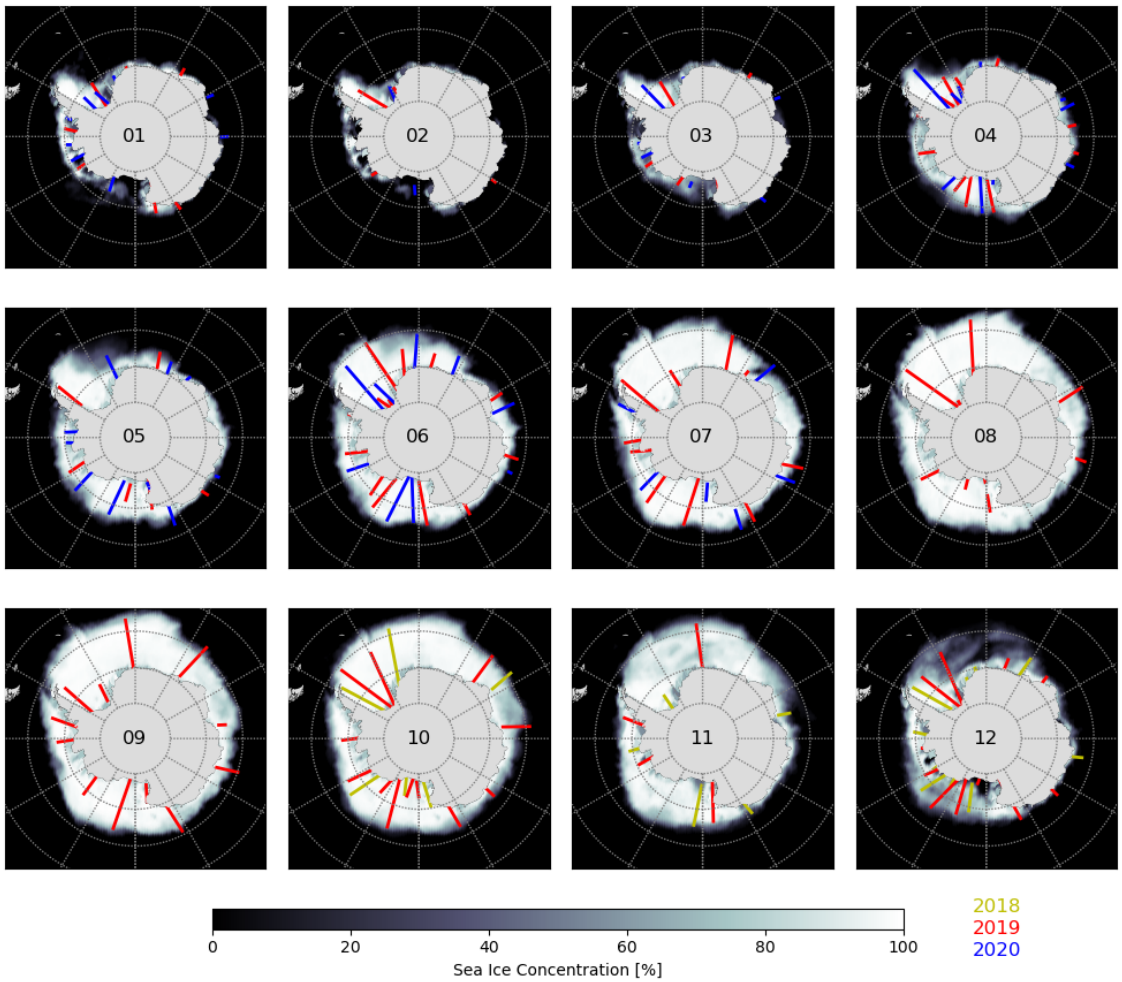

Figure 4.4: CryoSat-2 and ICESat-2 orbit overlaps (defined in text) from October 2018 to December 2020, colored by year. Sea ice concentrations for each month are averages of the years in which there are overlaps present.

definition above results in reasonably overlapping orbital tracks for freeboard comparisons. When the maximum allowable time difference was restricted to 5 hours, 179 such overlaps occurred in various lengths and locations around the Southern Ocean between October 2018 and October 2020 (Fig. 4.4). It is important to note that, with the definition above, no such overlaps have occurred in the Southern Hemisphere sea ice zone since the CRYO2ICE orbit re-configuration – which was optimized for Arctic overlaps – took place in late July 2020.

Due to the orbital alignments and distance of the sea ice pack from the pole (where orbit density is greater), none of the 179 overlaps have occurred with less than three hours of time difference, which is expected for overlaps lasting longer than five seconds (European Space Agency, 2018). All overlaps occurred with between 3.0 and 4.2 hours difference and lasted between ∼70 km and ∼1800 km. These overlaps come from the satellite orbits alone and do not take into account available freeboard data. Therefore, despite the large number of overlaps (Fig. 4.4), many are not ideal for comparisons due to their short length (for those occurring in regions of smaller ice extent) or missing freeboard data (mostly from ICESat-2 missing data due to clouds). Here, two Austral winter overlaps are chosen with many available ICESat-2 data: 27 October 2018, when the satellite ground tracks were approximately 4 hours and 10 minutes apart, and 02 September 2019, when they were about 3 hours and 36 minutes apart (Fig. 4.5). Both overlaps were close to 1015 km long over the sea ice zone, but were trimmed to 1000 km (2018) and 800 km (2019) to remove end sections of the overlaps where significant amounts of ICESat-2 data were missing. Implications of the time differences are discussed in Section 4.6.

Figure 4.5 shows the two along-track comparisons of snow freeboard between CryoSat-2 and ICESat-2. Both the shot-to-shot and 25 km binned average freeboards are shown. In the 2018 (2019) profile, the mean difference is 0.3 cm (7.6 cm) and the standard deviation of differences is 9.3 cm (9.6 cm). Though the 25 km binned correlation is higher in 2019 (0.89) than in 2018 (0.77), the distribution captured by CryoSat-2 in 2018 tends to match ICESat-2 better than in 2019. There is a clear discrepancy in the number of data points from each sensor, with

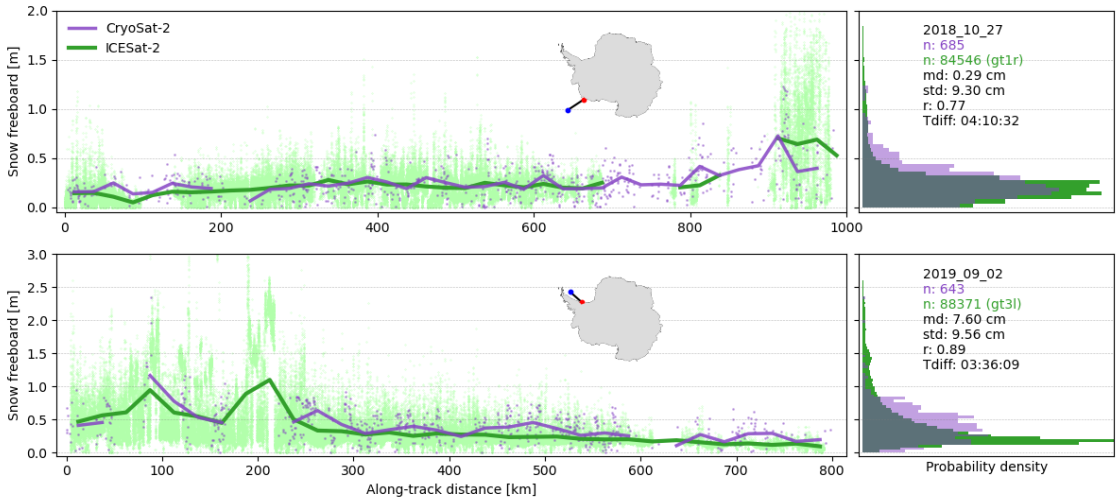

Figure 4.5: Along-track comparisons from two near-coincident overlaps of ICESat-2 (green) and CryoSat-2 (purple). Both profiles showcase data from the CryoSat-2 V2 algorithm. Points show individual measurements while lines give a binned 25 km average. ICESat-2 data come from a single strong beam, given in the right plots. Binned averages are only computed if at least 5% of the possible datapoints for that bin exist. Mean differences (md), standard deviations of differences (std) and correlation coefficients (r) are given in the right plots. Maps show the overlaps used in the profile, with the blue point representing the start and red point representing the end of the profile.

ICESat-2 recording 120-140 times more valid measurements than CryoSat-2. This discrepancy is largely due to the footprint size difference: the smaller footprint of ICESat-2 allows for many more measurements over a given distance than CryoSat-2. Additionally, some CryoSat-2 data are filtered out due to leads (to which CryoSat-2 is more sensitive), mixed surface returns, or poor fitting, which further reduces the number of valid measurements.

4.5.2 Monthly gridded comparisons

The V2 retrieval algorithm was applied to all CryoSat-2 data within the ICESat-2 era, and monthly gridded maps of snow freeboard were created. Figure 4.6 shows an example monthly map (September 2020) of CryoSat-2 V2 data in comparison with that from ICESat-2 and CryoSat-2 V1. As mentioned in Section 4.3.1, only ICESat-2 data from 2018 and 2019 were used in the initialization climatology. Therefore, none of the 2020 ICESat-2 data were included in the initialization of the CryoSat-2 model, allowing for independent monthly comparisons. Snow freeboard values ranged from nearly 0 to over 1.8 m, with a mean (mode) value of 28 cm (21 cm) from CryoSat-2 and 29 cm (23 cm) from ICESat-2. The pan-Antarctic map of freeboard matches well between the two sensors, as the widespread patterns found with ICESat-2 are captured by the CryoSat-2 retrievals with a correlation coefficient of 0.77. A majority of the differences between CryoSat-2 and ICESat-2 are within +/- 10 cm, with larger magnitude differences found along the Amundsen-Bellingshausen coastline and off the peninsula in the western Weddell sea. The mean difference between the two (CryoSat-2 – ICESat-2) is 0.5 cm. While Fig. 4.6 is given to show an example month, this pattern of differences is similar in all months when comparing to ICESat-2.

The original (V1) processing from Fons and Kurtz (2019) was run for this month as well, shown in the top right plot of Fig. 4.6. While a similar spatial pattern of snow freeboard exists, there tend to be thicker freeboards in more of the Weddell Sea and in the Eastern Ross Sea. Additionally, there is more "speckle"

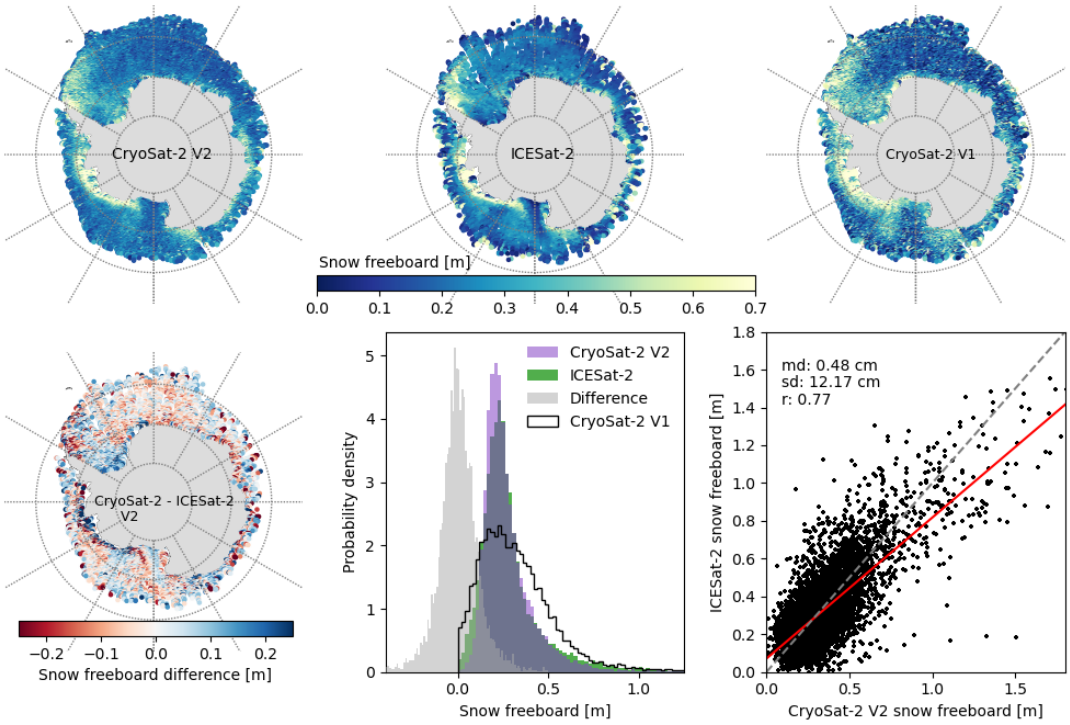

Figure 4.6: An example monthly comparison between CryoSat-2 and ICESat-2 for September 2020. CryoSat-2 V1 is this month computed by the original method put forth in Fons and Kurtz (2019). The distribution from the V1 map is shown in the black line (lower middle). In the lower right, the dashed line is the 1:1 line, while the red line is the linear best fit.

in the freeboard pattern from V1 as compared to V2, as the snow freeboard varies more in V1 over a given area. The V1 distribution is broader with a higher spread than the narrower V2 and ICESat-2 distributions, though the modes of all three are similar. It is clear that the improvements made to create the V2 algorithm have a large impact on the freeboard retrievals, leading to better agreement with ICESat-2.

The freeboard distributions from ICESat-2 (green) and CryoSat-2 V2 (purple) for all months of overlapping operation are given in Fig. 4.7. One can see the seasonal evolution in the freeboard distribution, from the broader distributions of Austral summer, to the narrower distributions skewed to lower freeboards of the

Austral winter. There are consistently more grid cells in the CryoSat-2 data than in the ICESat-2, brought on by data loss due to clouds that attenuate the laser beam but do not impact radar pulses. In general, the distributions given by the two sensors are quite similar, with some systematic differences shown in each month, discussed below. The monthly mean freeboard values given by the vertical lines are overall very similar between CryoSat-2 and ICESat-2, with the exception of larger differences of means in Austral fall months, up to 9 cm in March 2020. The monthly mean differences range from -2.9 to 6.6 cm between CryoSat-2 and ICESat-2, with the standard deviation of differences ranging from 10.8 to 16.8 cm. Correlation coefficients range from 0.57 in January 2020 to 0.80 in September 2019.

In most months shown in Fig. 4.7, ICESat-2 records a greater frequency of thinner (10-15 cm and below) and thicker (50 cm and greater) freeboards. Inversely, CryoSat-2 records a greater probability of "average" (20 to 30 cm) freeboard compared to ICESat-2. In the Austral fall, mainly in March and April 2019 and 2020, the shape of the distributions are most dissimilar, with ICESat-2 skewed to thinner freeboards compared to CryoSat-2. These differences in the freeboard distributions are discussed in Section 4.6.

4.5.3 Snow freeboard variability

Here, this study investigates differences in the monthly mean snow freeboards between CryoSat-2 and ICESat-2 and variability in the measurements. Averaging all years of data for each calendar month yields a mean annual cycle (for the two years

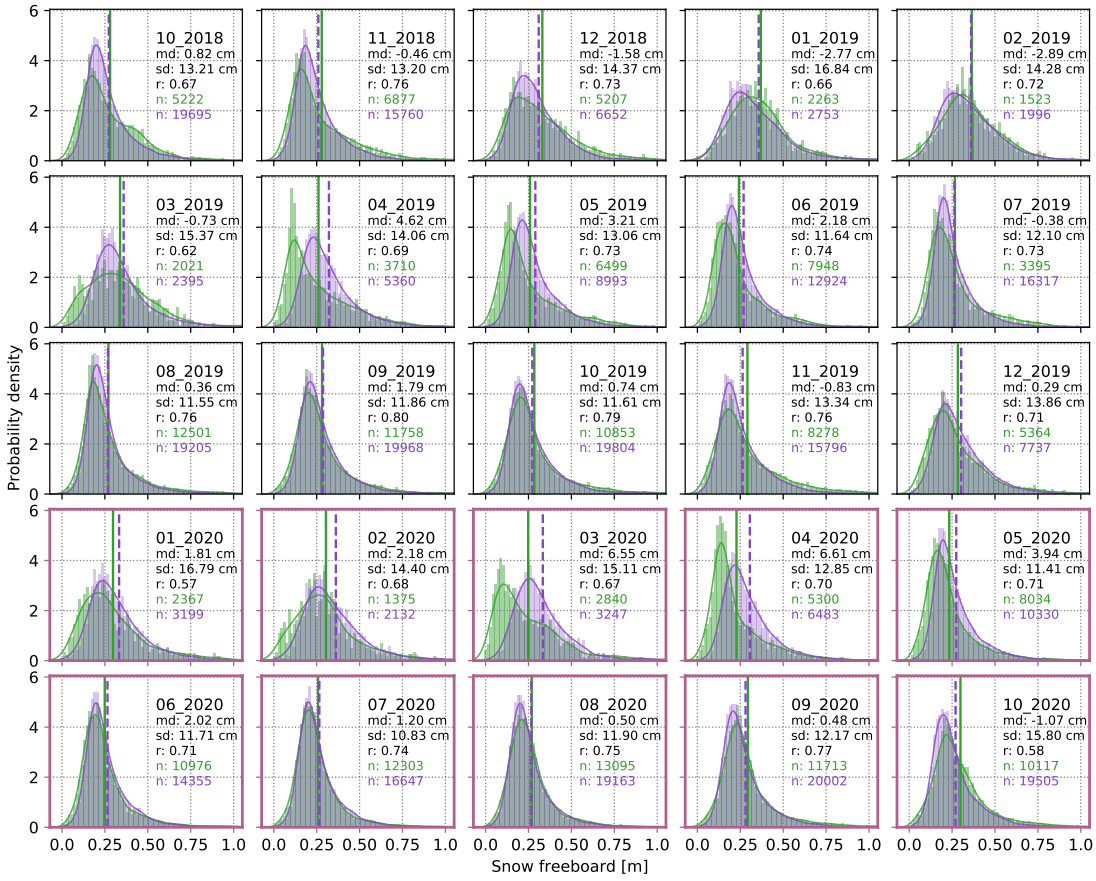

Figure 4.7: Snow freeboard density histograms and PDFs from CryoSat-2 V2 (purple) and ICESat-2 (green) for October 2018 to October 2020. Mean values are shown by the vertical lines. Plots from 2020, where no coincident ICESat-2 data are included in the initialization, are bordered in red.

October 2018-October 2020), given in Fig. 4.8a. Both CryoSat-2 and ICESat-2 exhibit similar shapes in the cycle, with the most notable difference being the more gradual monthly changes in CryoSat-2 freeboards during the Austral fall months compared to ICESat-2. To get a sense of the grid cell variability in the freeboard measurements from both instruments, the standard deviation of all snow freeboard measurements (σ_{fb}) are computed in each 25 km grid cell for a given month. For ICESat-2, σ_{fb} is around 5 cm basin-wide, but ranges monthly from ∼3.4 (June) to ∼7.5 cm (February). For CryoSat-2, σ_{fb} is smaller – around 3 cm basin-wide – and ranges between 2.5 (July) and 3.7 cm (February). These values are given as the shading in Fig. 4.8a.

The monthly mean freeboard differences (CryoSat-2 – ICESat-2) are shown in Fig. 4.8b, where the dashed lines indicate the mean freeboard differences from each year, and the solid black line indicates the 2018-2020 mean freeboard difference for each calendar month. As was also shown in Fig. 4.7, the largest differences occur in Austral fall, with CryoSat-2 recording as much as ∼6 cm thicker snow freeboards compared to ICESat-2. In other months, differences fall between +/- 1 cm, which is mostly in part to offsetting, larger differences in the SSH and floe elevation components. The variability in differences between individual years is largest in January through March (around 5 cm) but is around 2 cm in all other months.

The mean freeboard differences in Fig. 4.8b are broken down into the contributions from the SSH difference and floe height elevation difference. These components are given as bars where each two-colored bar represents a different year (earlier year

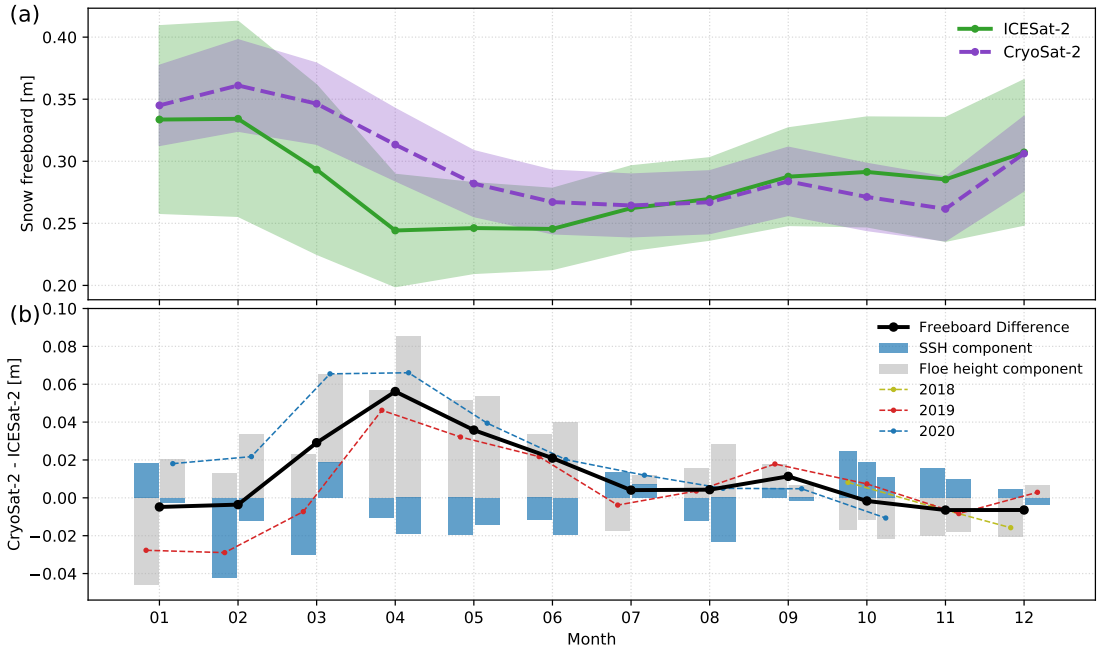

Figure 4.8: (a) Monthly basin-wide mean snow freeboard from ICESat-2 (green) and CryoSat-2 V2 (purple) averaged from October 2018 to October 2020. Shaded region gives the basin-average standard deviation of freeboard measurements in each grid cell, σ_{fb}. (b) Snow freeboard difference (CryoSat-2 V2 minus ICESat-2) for each year 2018 – 2020 and the total average. Freeboard differences are broken into the SSH (blue) and elevation (grey) components (bars) where the left-most bar in each month represents the earlier year of data for that month (2019 in January - September, 2018 in October – December).

of data for a given month is on the left). Since the mean freeboard difference is the sum of the elevation plus the SSH components, the elevation difference can be greater than the freeboard difference when the SSH difference is negative (and vice versa). The SSH difference between CryoSat-2 and ICESat-2 is typically within +/- 2 cm, reaching as much as -4 cm in February 2019. The floe elevation difference is typically largest in Austral fall, where it reaches over 8 cm, and is smaller in later months of the year. The elevation difference dominates the large freeboard differences found in Austral fall. A discussion on potential sources of these differences is given in the following section.

4.6 Discussion

Results from the V2 algorithm show substantial improvement over the V1 algorithm and better agreement with ICESat-2 snow freeboards, especially in the monthly comparisons. This agreement is particularly encouraging for the monthly comparisons in 2020 when no ICESat-2 data were included in the model fitting initialization. The along-track comparisons are promising but stronger conclusions are hard to draw due to the time difference between satellite overlaps. Despite the similarity, there still exist differences in the retrieved freeboards brought on by inherent sampling discrepancies between the satellites, discussed herein.

Comparing the along-track freeboards in Fig. 4.5, it is likely that differences between CryoSat-2 V2 and ICESat-2 arise from two major sources: the time delay between satellite overlaps and the sampling (both geometry and frequency) dif-

ferences between the instruments. As mentioned in Section 4.5.1, the time delay between the satellite overpasses in the Southern Ocean is at minimum three hours. In the locations of the two overlaps in Fig. 4.5, the monthly mean sea ice drift can reach upwards of 10 km per day (Kwok et al., 2017), meaning that the two satellites could be sampling entirely different sea ice. The location of the 2018 overlap in the Amundsen Sea typically experiences faster sea ice drift than the location of the 2019 overlap in the near-coastal Weddell Sea (Kwok et al., 2017), which could explain the higher correlations observed in 2019.

In addition to the time offsets, the large sampling differences – both geometric and frequency-related – likely also contribute to the differences in freeboards observed here. Sea ice surface features can vary greatly over small areas, and the CryoSat-2 SAR/SARIn footprint – with an area over 6,000 times larger than an ICESat-2 footprint – will sample much more of the surface per shot and therefore sample different features with varying elevations and freeboards (Giles et al., 2007). Due to this footprint size difference, the small difference in mean freeboards and similar distributions (especially in 2018) is encouraging, despite the variability in the along-track shot-to-shot freeboard profiles. Additionally, the SAR-processed sampling frequency combined with footprint size limit CryoSat-2 SAR data to approximately 2.6 measurements per along-track kilometer, while ICESat-2 is able to record upwards of $\sim$50 measurements per kilometer, depending on the photon rate and resultant segment length. Additionally, the across-track width of the CryoSat-2 footprint is significantly larger than that from ICESat-2. This higher number of samples and smaller footprint provides an enhanced resolution along the surface

and could allow ICESat-2 to better capture the thickest and thinnest freeboards observed in the profiles.

The mean snow freeboard differences (Fig. 4.8) display an overestimation of the snow freeboard by CryoSat-2 in Austral fall when compared to ICESat-2. Since this discrepancy is dominated more by the elevation retrieval and less from the SSH, this study estimates that this difference is a product of the initial guesses used in the waveform-fitting model. As no reliable, pan-Antarctic measurements of snow depth exist, the snow depth parameter is initialized using snow freeboard data and applying the zero ice freeboard assumption (Kurtz and Markus (2012), Section. 4.3.1). This assumption is likely an overestimate of the snow depth on Antarctic sea ice (Kwok and Kacimi, 2018), and a possible contributor to the positive differences observed here. The fact that the largest differences exist in Austral fall, when snow depth is typically thinnest (i.e. that the zero ice freeboard assumption is least valid), further corroborates this hypothesis. More exploration into the variability in freeboard measurements is needed that could help explain some of the negative differences observed.

The geometric sampling discrepancy discussed above could also contribute to the seasonal freeboard differences observed (Fig. 4.8). Tilling et al. (2019) found that Arctic freeboard data from the larger-footprint Envisat displayed a thick bias compared to the smaller-footprint CryoSat-2, that was attributed to enhanced off-nadir ranging to leads in less-consolidated ice regions. This effect would theoretically be present when comparing CryoSat-2 and ICESat-2, where the difference in footprint size is greater than that of CryoSat-2 and Envisat. Paul et al. (2018) also

compared CryoSat-2 and Envisat freeboards but in the Antarctic, and showed similar differences in freeboard distributions to the ones shown in Fig. 4.7. In both cases, the smaller footprint satellite (CryoSat-2 in Paul et al. (2018) and ICESat-2 here) tended to have broader freeboard distributions while the larger-footprint satellite (Envisat in Paul et al. (2018) and CryoSat-2 here) showed taller, narrower distributions. Even the seasonality of the distribution differences closely aligns between Fig. 4.7 and Paul et al. (2018), where discrepancies are found to be largest in Austral fall. This finding leads us to hypothesize that the differing footprint sizes may contribute to the differences in freeboard distributions shown. More work is needed, however, to quantify the geometric sampling discrepancies and determine the amount that they contribute to the differences in the freeboard distributions.

It is important to note that the comparisons shown in Tilling et al. (2019) and Paul et al. (2018) compare sensors of the same wavelength, while CryoSat-2 and ICESat-2 operate at very different frequencies. It is likely that scattering differences between radar and laser also contribute to the differences observed here. Each radar pulse responds to the sea ice surface differently than that from a laser, which is especially true over mixed sea ice and open water surfaces. In footprints containing both sea ice and leads, a radar pulse can get overwhelmed by the strong specular return from the water while the laser altimeter can either record a drop or a rise in the surface photon rate depending on the roughness of the water surface (Kwok et al., 2020a; Ricker et al., 2014; Tilling et al., 2018). Additionally, the Ku-band backscatter coefficient varies non-linearly across heterogeneous surfaces (Landy et al., 2019), which means that a radar return does not represent an average

of the surfaces in the footprint, but is instead weighted based on the roughness of the surface and features present. More ground-based studies of laser and radar scattering over sea ice, similar to Stroeve et al. (2020), would be useful to better quantify the potential uncertainty brought on by the footprint-scale scattering of these sensors, which could enable better comparisons.

4.7 Conclusions and future work

This chapter has outlined improvements made to the CryoSat-2 waveform-fitting retrieval algorithm put forth in Fons and Kurtz (2019) and showcased first comparisons of the snow freeboard retrievals to ICESat-2 data in the Southern Ocean. Some significant changes were implemented that improved the physical representativeness of the model, reduced the potential for anomalous convergence on local minima, and increased processing efficiency. These V2 improvements were motivated by recent publications (such as Landy et al. (2020) and Mallett et al. (2020)). The improved V2 algorithm was run on all CryoSat-2 data from October 2018 to October 2020 in order to compare with new snow freeboard data obtained from NASA's ICESat-2.

Our results showed 2018-2020 monthly mean differences between these CryoSat-2 snow freeboard retrievals and ICESat-2 ATL10 data ranging seasonally from -0.6 to 5.6 cm; the larger of which hypothesized to be linked to the zero ice freeboard assumption used in our model initialization. When comparing coincident along-track profiles and individual monthly grids, differences ranged from 0.3 to 7.6 cm and -2.9

to 6.6 cm, respectively. This study finds that snow freeboard distributions between the two instruments are comparable in shape, but hypothesize that differences could arise from geometric sampling and sensor frequency discrepancies. These differences are enhanced in Austral fall, matching what was found by Paul et al. (2018) comparing Envisat and CryoSat-2. More work is needed to discern the exact role that the new ice and thin snow depths found during these months play in the differences observed, and how the wavelength discrepancies between these two sensors may also contribute.

In order to more accurately assess the retrievals and compare snow freeboard measurements from these two sensors, more - and longer - orbital overlaps with a time delay closer to zero would be beneficial. These overlaps could also help in estimating systematic uncertainty in the CryoSat-2 retrievals, which is challenging due to a considerable lack in ground truth data from Antarctic sea ice. This idea of generating more overlaps between CryoSat-2 and ICESat-2 is the premise behind the CRYO2ICE campaign, which is currently providing near-coincident overlaps in the Arctic. However, since the orbital realignment in late July 2020, no CryoSat-2 and ICESat-2 overlaps (as defined above) have occurred over sea ice in the Southern Hemisphere as of December 2020. To better facilitate sea ice research in the Southern Ocean, it would be useful to adjust the orbital configuration to optimize for the Southern Hemisphere, as proposed by the CRYO2ICE project (European Space Agency, 2018).

Moving forward, this work will be useful for deriving new estimates of sea ice snow freeboard and thickness in the Southern Ocean for the length of the CryoSat-2

mission, which do not current exist. A CryoSat-2 snow freeboard time series could be reconciled with that from ICESat and ICESat-2 to create a more than 17-year record of Antarctic snow freeboard. Further exploration and validation into the snow depth parameter produced in this forward model output is necessary, but, combined with these or other estimates of freeboard, could enable Antarctic sea ice thickness calculations from CryoSat-2. Snow depth and sea ice thickness retrievals using this algorithm are discussed in the next chapter.

Chapter 5: Ten Years of Antarctic Sea Ice Physical Properties from CryoSat-2

5.1 Introduction

As mentioned in Chapter 1, sea ice thickness is an important parameter in Earth's climate system as it controls fluxes of heat, moisture, and salinity between the ocean and atmosphere (Persson and Vihma, 2016). It also acts as an indicator of climate change and variability (EPA, 2016) due to its intimate relationship with other components of the cryosphere. Knowledge of sea ice thickness has long been important for maritime navigation and continues to be a focus today both for climate studies as well as navigation in icy waters (Bourke and Garrett, 1987; De Silva et al., 2015; Holland et al., 2006). While measuring thickness in situ is a straightforward process - requiring only a hole and a measuring device - the sheer size of the sea ice pack in both hemispheres and the impracticality of routine work in the polar regions limits the ability to manually measure the thickness of the sea ice cover on the basin-scale. Instead, satellite altimeters are typically used.

By measuring the height of the sea ice above the local sea surface (i.e. the freeboard) from altimetry, one can apply assumptions of hydrostatic balance to es-

timate the thickness of the sea ice. As previous chapters have discussed, wavelength differences between the two primary types of altimeters - radar and laser - correspond to varying dominant scattering horizons over sea ice and therefore different retrieved freeboards - ice freeboard and snow freeboard, respectively. These two different freeboard values require different equations for calculating thickness. If the ice freeboard is known, one can use the equation provided in Chapter 2:

$$h_{i-radar} = \left(\frac{\rho_w}{\rho_w - \rho_i}\right) h_{fi} + \left(\frac{\rho_s}{\rho_w - \rho_i}\right) h_s \tag{5.1}$$

to estimate thickness, where $h_{i-radar}$ is the ice thickness computed from the ice freeboard, h_{fi} is the ice freeboard, h_s is the snow depth, and ρ is the density of seawater (ρ_w), ice (ρ_i), and snow (ρ_s). If the snow freeboard is known, then the equation instead becomes:

$$h_{i-total} = \left(\frac{\rho_w}{\rho_w - \rho_i}\right) h_{fs} + \left(\frac{\rho_s - \rho_w}{\rho_w - \rho_i}\right) h_s, \tag{5.2}$$

where $h_{i-total}$ is the ice thickness computed from the snow freeboard, h_{fs} is the snow freeboard, and the snow depth and density are as in Equation 5.1 (Kurtz and Markus, 2012; Kwok, 2011). It is clear from Equations 5.1 and 5.2 that estimates of freeboard and snow depth are the two necessary measurements for deriving thickness from satellite altimetry.

Over Arctic sea ice, altimeter freeboard has been estimated since around 2003 using the ERS-1 and ERS-2 satellites (Laxon et al., 2003). The launch of NASA's

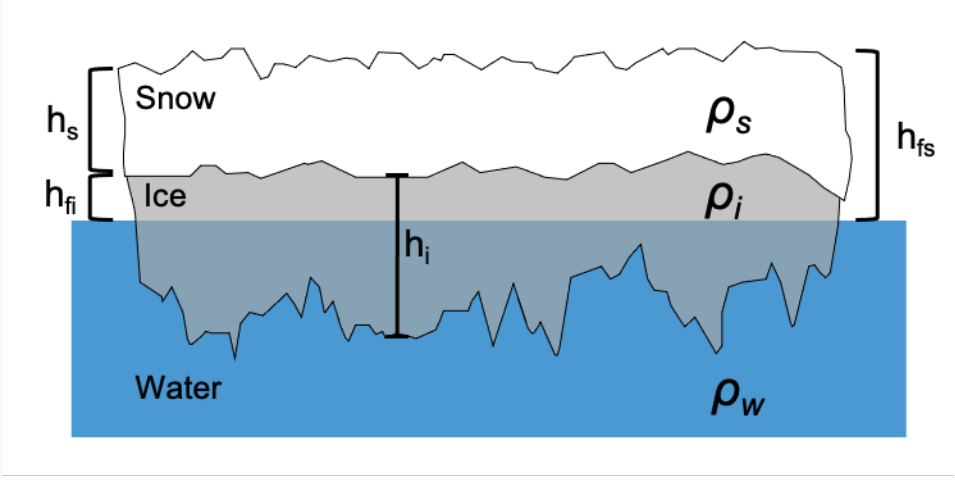

Figure 5.1: Sea ice thickness diagram showing the parameters in Equations 5.1 and 5.2, including snow depth (h_s), ice freeboard (h_{fi}), snow freeboard (h_{fs}), ice thickness (h_i), and the density terms of snow (ρ_s), ice (ρ_i), and seawater (ρ_w).

ICESat in 2003 facilitated sea ice freeboard measurements between 2003-2008 (Farrell et al., 2009; Kurtz et al., 2008; Kwok et al., 2007; Zwally et al., 2002), while ESA's Cryosat-2 satellite has been used extensively to estimate Arctic sea ice freeboard since its launch in 2010 (Kurtz et al., 2014; Kwok and Cunningham, 2015; Landy et al., 2020; Laxon et al., 2013; Ricker et al., 2014; Tilling et al., 2018). In most of these cases, a regional snow depth climatology built from ground-based measurements collected between 1954-1991 are used to convert the freeboard measurements to thickness estimates (Warren et al., 1999). Other studies have employed lower-resolution snow depth data from passive microwave sensors (Kurtz et al., 2009). More recently, NASA's ICESat-2 satellite has been operating, and studies have combined these freeboards with snow depths from models (e.g. Petty et al. 2018) to estimate sea ice thickness (Petty et al., 2020b).

While these studies have found success in estimating sea ice freeboard over Arctic sea ice, few works have done so for Antarctic sea ice. This hemispheric

discrepancy is primarily due to two reasons. First, ice freeboard from radar altimetry is difficult to estimate for Antarctic sea ice. The thicker snow layer on Antarctic sea ice can depress the ice nearer to the ocean surface, leading to flooding, enhanced brine wicking, and other processes that drive complex stratigraphy and complicate returns from Ku-band altimeters (Giovinetto et al., 1992; Maksym and Jeffries, 2000; Willatt et al., 2010). Ground-based studies have shown that assuming a Ku-band radar pulse penetrates to the snow-ice interface is likely incorrect, with dominant returns more likely to originate from within the snow layer or the air-snow interface (Willatt et al., 2010). Second, the snow depth distribution over Antarctic sea ice is not as well known (Giles et al., 2008). Unlike the Arctic, no such ground-based snow depth climatology exists from which thickness can be estimated. Some studies have used passive microwave instruments to derive snow depth, however, these measurements contain large pixel-level uncertainties associated with ice type, sensor footprint size, and a lack of validation data (Kern and Ozsoy-Çiçek, 2016; Maksym and Markus, 2008; Markus and Cavalieri, 1998).

These barriers mean that using radar altimetry, mainly CryoSat-2, over Antarctic sea ice will increase complexity of and uncertainty in the freeboard retrievals. Also, it means that calculating sea ice thickness will require either assumptions about the snow layer or new basin-wide datasets of snow depth on sea ice.

Some works have attempted to retrieve Antarctic sea ice freeboard from CryoSat-2, despite the challenges faced (Fons and Kurtz, 2019; Paul et al., 2018; Schwegmann et al., 2016). Schwegmann et al. (2016) estimated radar freeboard, but the lack of snow depth information prevented the correction for wave speed in snow (in order to

estimate ice freeboard) and the estimation of thickness. Paul et al. (2018) did correct for wave speed using passive microwave snow depths, but did not estimate thickness from the measurements, citing the need for external snow depth data. Fons and Kurtz (2019) estimated snow freeboard from CryoSat-2 using snow scattering information contained in a physical waveform model, but also did not estimate thickness citing a lack of confidence in the snow depth retrievals. As of this writing, no studies of basin-wide Antarctic sea ice thickness derived entirely from CryoSat-2 data exist.

Other studies have been able to estimate Antarctic sea ice thickness from laser altimetry - namely ICESat - through the use of key snow depth assumptions. Kurtz and Markus (2012) applied a "zero ice freeboard" assumption, which assumes that the snow depth depresses the ice down to the water level everywhere, resulting in a snow depth equal to the snow freeboard and an ice freeboard equal to zero. Under this assumption, Equation 5.2 becomes:

$$h_{i-0ifb} = \left(\frac{\rho_s}{\rho_w - \rho_i} \right) h_{fs}. \tag{5.3}$$

Zero ice freeboards have been observed during ground-based measurement campaigns (Willatt et al., 2010) however, this assumption applied basin-wide likely underestimates the actual ice thickness (Kacimi and Kwok, 2020; Kwok and Kacimi, 2018). Other studies have applied a static ratio between freeboard and snow depth derived from passive microwave measurements and assumed a single ice/snow layer in their retrievals (Kern et al., 2016; Li et al., 2018). In each of these studies, the lack of reliable basin-scale snow depth information limited confidence in the

thickness retrievals.

Since the launch of ICESat-2 in 2018, two cryosphere-focused satellite altimeters have been observing sea ice in simultaneous operation (ICESat-2 and CryoSat-2). The contrasting instrument wavelengths provide new potential to estimate snow depth on sea ice by differencing the freeboards retrieved by each sensor, $h_{fs} - h_{fs}$. Kwok et al. (2020c) first showcased this on Arctic sea ice, showing good agreement with snowfall patterns from reanalysis. In the Antarctic, Kacimi and Kwok (2020) used the same technique to derive six months of snow depth on Antarctic sea ice, and used the resulting snow depths along with the retrieved freeboards to provide estimates of sea ice thickness and volume. Their result showed physically-realistic values that provides useful insight into the Antarctic sea ice thickness distribution, however, it relies on the assumption that the Ku-band pulse originates from the snow-ice interface. Additionally, their work is restricted to only time in which both satellites are operating and uses only near-coincident data (time difference <10 days) to estimate snow depth.

While the ICESat and ICESat-2-based studies of Antarctic sea ice provide a good baseline into Antarctic sea ice thickness, they only cover the years 2003-2008 and 2019 onwards. Clearly, there is a large need to utilize CryoSat-2 to fill in the gap between these two measurement periods (Meredith et al., 2019). Additionally, the need to estimate snow depth utilizing large assumptions or external coincident data constrains the current retrievals in terms of confidence as well as temporal coverage.

To address the above needs, this study will utilize a CryoSat-2 waveform-fitting method described in previous chapters to estimate the physical properties

of Antarctic sea ice and generate a 10+ year record of Antarctic sea ice thickness and volume from CryoSat-2. This method relies on a forward waveform model and optimization procedure to assist in retrieving the elevation of both the air-snow and snow-ice interfaces over Antarctic sea ice. While previous chapters have described the algorithm (Chapter 3) and assessed snow freeboard retrievals with independent data (Chapter 4), this chapter will showcase retrievals of snow freeboard, ice freeboard, and snow depth over the entire CryoSat-2 mission, and use the retrieved quantities to estimate the sea ice thickness and volume from 2010-2020.

This chapter is outlined as follows: first, the datasets (Section 5.2) and methods used (5.3) are described. An estimate of uncertainty in the retrievals is also given in Section 5.3. Then, results from the retrieval process are given in Section 5.4 and are broken down by parameter (snow freeboard in 5.4.1, ice freeboard in 5.4.2, snow depth in 5.4.3, and thickness and volume in 5.4.4). Each results subsection contains comparisons to other measurements and showcases monthly and seasonal spatial patterns and distributions. In Section 5.4.5, trends in sea ice thickness and volume are shown. This chapter concludes with a discussion on future work involving the reconciliation of laser-radar altimetry measurements (Section 5.5) and concluding remarks (5.6).

5.2 Data

5.2.1 CryoSat-2

The primary data used in this work come from CryoSat-2, which have been described in previous chapters of this dissertation (Sections 2.2, 3.2, 4.2). This chapter utilizes the same Baseline-D Level 1-B waveform data from both SAR and SARIn modes around the Antarctic continent (European Space Agency, 2019b,c). These data come from footprints that are 1.65 km across-track and 360 m along track, though impacts from off-nadir leads can originate from over 10 km away (European Space Agency, 2019b; Tilling et al., 2018).

In this study, each CryoSat-2 file is processed following the methods outlined in Section 5.3. Focus is given to pan-Antarctic retrievals, so all data are gridded to the NSIDC 25 km polar stereographic grid (EPSG: 3976) to generate monthly and seasonal means.

5.2.2 Ancillary data

Though CryoSat-2 produces the main dataset used in this work, some others are employed in various capacities throughout the study.

Monthly snow freeboard climatology maps from ICESat and ICESat-2 are used as an initialization for this retrieval process. These are monthly mean maps of sea ice snow freeboard (12 in total) consisting of an average of ICESat data from 2003-2008 and ICESat-2 data from 2018-2019 (Chapter 4). These data are collected

using ICESat freeboards from Kurtz and Markus (2012) and using ICESat-2 ATL10 freeboards (Kwok et al., 2020a). Each monthly map is used for initializing the corresponding month of CryoSat-2 data, regardless of the year.

All monthly maps are restricted to grid cells that contain at least 50% ice concentration. To distinguish between lower concentrations, the Bootstrap Version 3 sea ice concentration algorithm is used (Comiso, 2017). This algorithm is based off of brightness temperatures from Nimbus-7 SMMR and DMSP SSM/I and SSMIS instruments, and is provided as daily and monthly averages. The monthly averages are utilized in this study. These data are also used to compute the areal coverage of the sea ice for a given month, where grid cells with concentrations greater than or equal to 50% are used in the area calculation. Area is calculated simply by multiplying the sea ice concentration present in each grid cell by the area of the grid cell, and summing the entire grid or region of interest.

Finally, other datasets are used as comparisons to the retrievals shown. Kacimi and Kwok (2020) collected freeboard data over Antarctic sea ice and estimated snow depth and thickness by combining CryoSat-2 and ICESat-2 freeboard measurements. They showed results from the year 2019 as monthly regional means and standard deviations of each parameter. Results from Kacimi and Kwok (2020) are given here to help validate these CryoSat-2 retrievals. Paul et al. (2018) published CryoSat-2 ice and radar freeboard values over Antarctic sea ice from 2011 - 2017. Again, these data are used as a comparison to the ice freeboard retrievals shown herein.

Two independent data sources are included as an attempt to validate CryoSat-2 snow depth measurements: AWI Snow Buoys and NASA's OIB Snow Radar. The

AWI snow buoys are ground-based instruments that measure the height of the sensor from the air-snow interface of sea ice (Nicolaus et al., 2017). To estimate snow depth, they rely on precise measurements of the initial snow depth and keep track of the accumulation. These provide a first-order estimate of snow depth, however, they do not take into account other processes that can reduce the snow depth but not change the sensor-air-snow interface distance (such as flooding, snow ice formation, refreezing, etc.). The OIB ultra-wide-band Snow Radar is a 2-18 GHz radar that produces along-track echograms of the surface and various layers based on their backscatter characteristics (Leuschen, 2010). No official product of snow depth on Antarctic sea ice from OIB exists, and therefore one must rely on individual algorithms to pick the interfaces and derive snow depth. Here, the *pysnowradar* software package is employed (King et al., 2020), which utilizes a wavelet-transform layer picker (developed in Newman et al. 2014) to derive snow depth. This method has not been extensively validated, and never officially been used over Antarctic sea ice. Both of these datasets exhibit low confidence in their estimates of snow depth, however, they are used here until more validation data from Antarctic sea ice becomes available.

5.3 Methods

This section describes the procedure for retrieving sea ice thickness from CryoSat-2. The procedure is broken down into the elevation retrieval (Section 5.3.1), the freeboard and snow depth estimation (Section 5.3.2), and the calculation

of thickness and volume (Section 5.3.3). Additionally, the method for estimating uncertainty in the retrievals is given (Section 5.3.4). A detailed description of the retrieval methodology can be found in Chapters 3 and 4.

5.3.1 Waveform-fitting and elevation retrieval

The primary methodology for retrieving sea ice properties used in this work is the CryoSat-2 waveform-fitting retrieval algorithm put forth in Fons and Kurtz (2019) and improved in Fons et al. (2021). This process is a physical retracking method that employs a forward waveform model to track the sea ice surfaces on the waveform, which allows for the retrieval of sea ice elevation. The retrieval algorithm is described in previous chapters, however, a broad overview is given in this section.

First, CryoSat-2 level 1B data are ingested. In this method, each individual waveform is classified into its respective surface-type: floe-type (originating from sea ice), lead-type (originating from open water cracks in the ice), ocean-type (originating from the open ocean around the ice pack), and mixed-type (an ambiguous return from mixed-surfaces). This is done by analyzing the PP, SSD, and skewness of each waveform (discussed in Chapters 3 and 4).

After classifying the returns, a physically-modeled waveform is constructed for each individual CryoSat-2 echo. The model is given, generally, by the equation:

$$\Psi(\tau) = P_t(\tau) \otimes I(\tau, \alpha) \otimes p(\tau, \sigma) \otimes \upsilon(\tau, h_{sd}) \tag{5.4}$$

where τ is the echo delay time relative to the time of scattering from the mean

scattering surface and $\otimes$ represents a convolution of the compressed transmit pulse, $P_t(\tau)$, the rough surface impulse response, $I(\tau)$, the surface height probability density function, $p(\tau)$, and the scattering cross section per unit volume, $\upsilon(\tau)$ (Brown, 1977; Fons and Kurtz, 2019; Kurtz et al., 2014). For floe-type waveforms, this model is fed with five different initial parameters: snow depth, snow-ice interface tracking point, roughness, angular backscattering efficiency, and amplitude scale factor (further defined in Table 4.1). Ocean-type and mixed-type waveforms are discarded prior to model creation. Lead-type waveforms have no snow cover (by definition), and therefore the $\upsilon(\tau)$ term goes to a delta function at $\tau = 0$, resulting in four free parameters: snow-ice interface tracking point, roughness, angular backscattering efficiency, and amplitude scale factor. These parameters are derived from waveform characteristics, when applicable, or otherwise from independent datasets (Table 4.1).

The next step involves fitting the modeled waveform to the actual CryoSat-2 waveform through a bounded trust-region Newton least-squares optimization approach. Bounds are provided for each input parameter about the initial guess to constrain the optimization to best-guess physically-realistic values for a given location or waveform shape (Table 4.1). Each function evaluation adjusts the input parameters within the provided bounds, until a minimum residual between the modeled and actual waveforms is found, or until a maximum number of function evaluations (100) is reached. The output "fit parameters" provide estimates of the actual values of each parameter in the waveform model. The large assumptions are that (a) this waveform model accurately can represent a CryoSat-2 return from the sea ice surface and (b) the fitting procedure, when initialized with physically-realistic

inputs and bounds, can find the global minimum optimization result as opposed to getting caught in a local minimum. Fit parameters are discarded if the result is a "poor fit", which is described as having a resnorm (squared norm of the residual) less than 0.3.

The output parameters of snow-ice interface tracking point and snow depth provide the locations of the physical air-snow and snow-ice interfaces on the waveform as a function of radar return time. Retracking corrections are then calculated that relate these locations to the nominal tracking bin provided in the CryoSat-2 data product. Following Equations 2.2 and 2.3, adding the retracking correction and the provided geophysical corrections to the nominal elevations (and accounting for wave speed through the snowpack) results in the elevation of the surface above the WGS84 ellipsoid. These elevations can then be used to estimate freeboard and snow depth.

It must be reiterated that the estimation of ice freeboard and snow depth requires an estimate of the snow-ice interface elevation. As has been previously stated, empirical threshold retrackers typically assume the dominant scattering horizon is always located at the snow-ice interface (and that the snow layer is mostly transparent at Ku-band frequencies), which can lead to an overestimation of the ice freeboard and is a primary reason behind the low confidence in their retrievals of ice freeboard over Antarctic sea ice (Paul et al., 2018; Schwegmann et al., 2016). This physical retracking method does not contain the same assumption and instead uses the physical model and fitting method to estimate the actual snow-ice interface by accounting for attenuation of the signal in snow and ice layers. Therefore, it is hy-

pothesized that this physical method better tracks that snow-ice interface compared to empirical approaches, which motivates the calculation of ice freeboard and snow depth. This is explored further in Section 5.4.2.

5.3.2 Estimating freeboard and snow depth

Once the air-snow and snow-ice interfaces are retrieved using the retracking procedure described above, the freeboard and snow depth can simply be estimated. The first step is determining the sea surface height. The elevation of all lead-type waveforms are averaged in 10 km along-track segments and linearly interpolated, following Kwok et al. (2020a) and Chapter 4. Lead segments are only calculated if at least three lead-type points exist within. This along-track SSH is then subtracted from every floe-type elevation, yielding a freeboard estimate for each floe-type point. Subtracting the SSH from the air-snow interface elevation results in a snow freeboard estimate, while that from the snow-ice interface results in an ice freeboard estimate. Since the effects of the snow layer on radar wave speed propagation is accounted for in the ice freeboard calculation (following Mallett et al. (2020) and Chapter 4), the freeboards can simply be subtracted, snow freeboard - ice freeboard, to get an estimate of snow depth.

Each floe-type waveform with a good fit, therefore, has a snow freeboard, ice freeboard, and snow depth estimate, provided that a co-located 10 km sea surface height segment also exists. Estimates of freeboard and snow depth shown here are gridded onto the NSIDC 25 km polar stereographic grid. To account for instrument

noise and remove potential effects from icebergs, snow freeboards between -0.1 and 3.0 m are kept and gridded. Ice freeboards between -0.25 and 2.25 m and snow depths between 0 and 2 m are included in the gridding.

5.3.3 Calculating sea ice thickness and volume

After obtaining estimates of sea ice freeboard and snow depth on sea ice, the thickness of the sea ice can be calculated by applying the hydrostatic assumption. This assumption follows that an object (in this case, snow-covered sea ice) immersed in a fluid will be buoyed with a force equal to that due to gravity. Combining the thicknesses of the freeboard and snow depth with estimates for the density of seawater, snow, and sea ice (as in Equations 5.1 and 5.2), one can calculate the thickness.

Table 2.1 gives the typical density values used in the above equations by different studies over Antarctic sea ice. This study utilizes the same values given in Kacimi and Kwok (2020) to better enable comparison (Section 5.4.4). They are: $\rho_w = 1024$ kg/m^3, $\rho_i = 917$ kg/m^3, and $\rho_s = 320$ kg/m^3. It is acknowledged that the use of a single, basin-averaged value for density will likely introduce uncertainty in the measurement (Section 5.3.4), as the sea ice density can vary both spatially and temporally (Fig. 2.6, Kurtz and Markus 2012). Future work will aim to better incorporate seasonally-varying density terms. Any interannual variability in the sea ice and snow density terms could also have an impact on observed trends in thickness and volume. To address the spatial variability in density terms, uncertainty

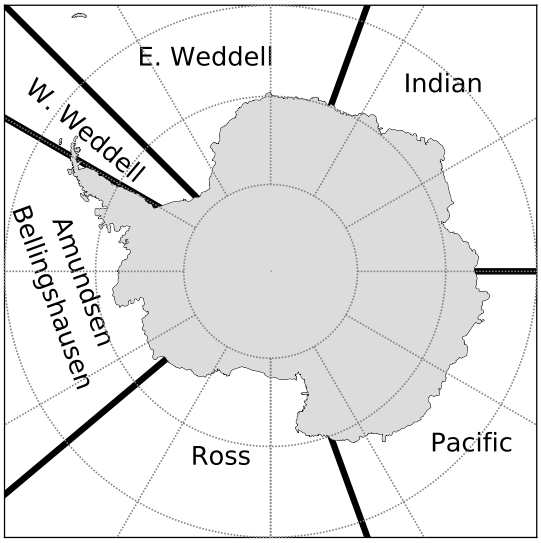

Figure 5.2: Map showing the longitudinally-demarcated regions used in this study. Longitude values are provided in text.

values of 50 and 20 kg/m^3 are assigned to the snow and ice terms, respectively, while the uncertainty in seawater density is taken as negligible (Kurtz and Markus, 2012). The impact of interannual variability in these terms on observed thickness trends is investigated in Section 5.4.5.

Like freeboard and snow depth, thickness is also gridded using the NSIDC polar stereographic projection. Volume is computed simply by multiplying basin-average sea ice thickness by the areal coverage of sea ice. The sea ice area is computed using the Bootstrap sea ice concentration data, where each 25 km grid cell concentration above 50% is multiplied by the area of the grid cell. Then, this total area value can be multiplied by the basin- or region-averaged thickness to compute the volume.

For the freeboard, snow depth, and thickness results given herein, both monthly-

and seasonally-averaged data are shown both for the entire Antarctic basin as well as individual regions. The seasons are broken up as follows: (1) Summer, D-J-F (2) Fall, M-A-M (3) Winter, J-J-A (4) Spring, S-O-N. The regions are longitudinally demarcated as follows: (1) Ross Sea, $160° - 230°$ (2) Amundsen-Bellingshausen Seas (Am-Bel), $230° - 300°$ (3) Western Weddell Sea, $300° - 315°$ (4) Eastern Weddell Sea, $315° - 20°$ (5) Indian Ocean, $20° - 90°$ (6) Pacific Ocean, $90° - 160°$. These regions are shown in Fig. 5.2.

5.3.4 Uncertainty in sea ice thickness retrievals

In this section, an estimate of the uncertainty in the thickness measurements is provided through a Gaussian error propagation method (following Kern and Spreen 2015; Petty et al. 2020b; Spreen et al. 2009). As discussed in the previous chapter, the total uncertainty in a thickness measurement comes from a combination of random and systematic uncertainties. Random uncertainties in thickness measurements can be calculated (Petty et al., 2020b) however, because they are random, we assume they decrease substantially when many individual thickness measurements are averaged together. Since thickness results in this study are shown only at the basin-scale and averaged monthly to a 25 km grid, we assume the random uncertainty becomes negligible basin-wide and do not explicitly calculate it here. Future work involving along-track thickness estimates and validation would necessitate a calculation of random uncertainty.

Instead, an estimate of the systematic uncertainty at the grid cell-scale is

given here. We assume these uncertainties are correlated and represent bias in the measurement, and therefore cannot be reduced through averaging (Ricker et al., 2014). Here, the systematic uncertainty is estimated following Petty et al. (2020b) where:

$$\sigma^2_{hi,s} = \sigma^2_{hs}\left(\frac{\rho_s}{(\rho_w-\rho_i)} - \frac{\rho_w}{(\rho_w-\rho_i)}\right)^2 + \sigma^2_{\rho s}\left(\frac{h_s}{(\rho_w-\rho_i)}\right)^2 + \sigma^2_{\rho i}\left(\frac{h_f\rho_w}{(\rho_w-\rho_i)^2} + \frac{h_s\rho_s}{(\rho_w-\rho_i)^2} - \frac{h_s\rho_w}{(\rho_w-\rho_i)^2}\right)^2. \quad (5.5)$$

In Equation 5.5, $\sigma_{hi,s}$ is the uncertainty in sea ice thickness estimated using snow freeboard (Eqn. 5.1), h_s is the snow depth, h_f is the snow freeboard, and s, w, i represent the density (ρ) and uncertainty (σ) of snow, seawater, and sea ice, respectively. The snow depth uncertainty σ_{hs} is taken from Chapter 4 and is (conservatively) set to 0.25 * h_s (Spreen et al., 2009). Densities of snow (ρ_s), ice (ρ_i), and water (ρ_w) are set to the values given in Section 5.3.3, with the uncertainty in the snow density ($\sigma_{\rho s}$) taken as 50 kg/m^3 and the uncertainty in the ice density ($\sigma_{\rho i}$) taken as 20 kg/m^3, following Kurtz and Markus (2012). The uncertainty in the seawater density is assumed to be negligible and is not included in this calculation (Kern et al., 2016; Kurtz and Markus, 2012; Li et al., 2018). Monthly average 25 km grids of snow depth (h_s) and snow freeboard (h_f) are used in the uncertainty calculation, and therefore uncertainty estimates are provided for each grid cell basin-wide. Monthly average thickness uncertainty values range from around 20 to 40 cm, and are given (basin-wide) in Table 5.1.

An estimate of the volume uncertainty is also provided, but done so in a sim-

Month	$\sigma_{hi}[m]$	$\delta h_i/h_i[\%]$	$\sigma_V[km^3]$	$\delta V/V[\%]$
Jan.	0.26	23	394	12
Feb.	0.33	26	340	14
Mar.	0.29	22	435	13
Apr.	0.26	21	788	12
May.	0.18	15	1097	11
Jun.	0.19	16	1345	10
Jul.	0.19	16	1818	11
Aug.	0.18	16	2044	11
Sep.	0.21	18	2520	13
Oct.	0.20	18	2054	12
Nov.	0.21	21	1617	13
Dec.	0.22	21	900	13

Table 5.1: Monthly pan-Antarctic sea ice thickness (h_i) and volume (V) uncertainty found in this study (Section 5.4.4), shown both as absolute (σ) and fractional (δ) values. All values come from 2010 - 2020.

plistic way compared to some other methods over Arctic sea ice (Tilling et al., 2018). Here, a Gaussian error propagation approach is used to combine the uncertainty due to sea ice thickness and sea ice area, the two components that make up the volume calculation. This is provided as an initial volume uncertainty estimate until more information on the uncertainty relating to snow depth and snow/ice density from Antarctic sea ice is known.

This estimated volume uncertainty is given by:

$$\frac{\delta V}{|V|} = \sqrt{\left(\frac{\delta h_i}{h_i}\right)^2 + \left(\frac{\delta A}{A}\right)^2}, \tag{5.6}$$

where $\delta V/|V|$ is the monthly average sea ice volume fractional uncertainty, $\delta h_i/h_i$ is the sea ice thickness fractional uncertainty, and $\delta A/A$ is the fractional uncertainty in sea ice area. In this study, a conservative fractional uncertainty value for sea ice area of 5% is used (Spreen et al., 2009). The fractional uncertainty in thickness ($\delta h_i/h_i$)

is found by dividing the thickness uncertainty grid by the mean thickness grid and computing the basin-wide average. The right-hand side of Equation 5.6 provides a fractional combined uncertainty in sea ice volume. Multiplying this fractional uncertainty with the mean volume estimate (Section 5.4.4) yields a quantitative sea ice volume uncertainty. This uncertainty ranges generally between 10-14% of the total sea ice volume (Table 5.1). Once again, these values are simply first estimates used to constrain the volume estimates in the context of the observed interannual variability (Section 5.4.5). They are provided (basin-wide) in Table 5.1.

5.4 Results and discussion

The methodology described in Section 5.3 was applied to all CryoSat-2 data collected over the Southern Ocean from the beginning of the mission in July 2010 until October 2020, resulting in over 10 years of data. This time period is hereafter referred to as the "CryoSat-2 period", and results using this methodology are referred to as "CryoSat-2 results" (as comparison datasets that use CryoSat-2 data are named corresponding to their author). In this section, results from the processed data are shown as well as a discussion on comparisons with other datasets and observed trends in the data. Each of the following sections cover a retrieved variable: snow freeboard, ice freeboard, snow depth, and thickness and volume. A summary table with monthly mean values and standard deviations of each variable, from 2010-2020, is provided as Table 5.2.

5.4.1 Snow freeboard

The previous chapter showcased results and validation of these CryoSat-2 snow freeboard retrievals using data from ICESat-2. Details on comparisons and algorithm performance can be found therein. Here, monthly mean freeboard maps and seasonal distributions from the entire CryoSat-2 period are given.

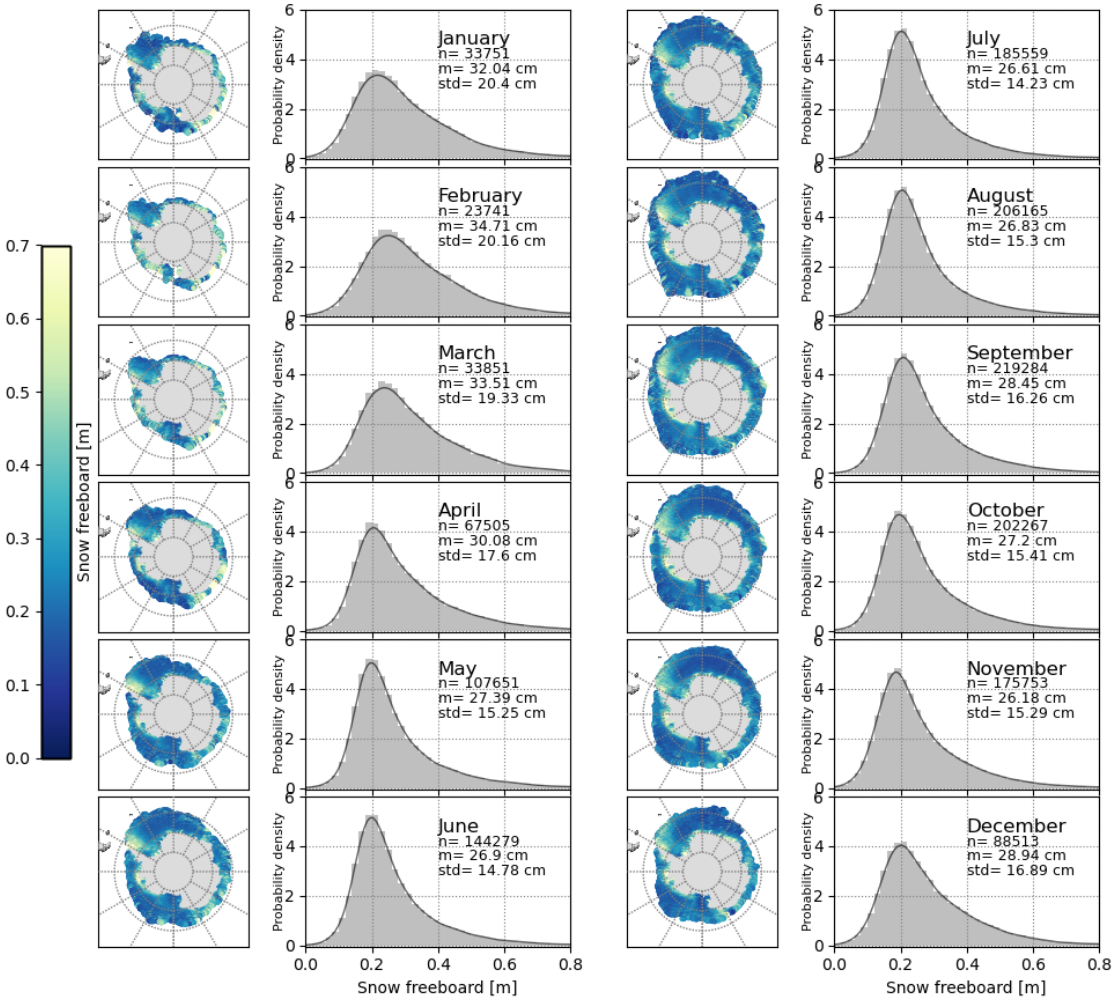

Figure 5.3: Monthly average (July 2010 - October 2020) maps and distributions of snow freeboard from CryoSat-2. Histogram bin sizes are 2 cm. The total number of grid cells included in the distribution (n), the mean (m), and the standard deviation (std) are also given.

Figure 5.3 shows the snow freeboard distributions and spatial patterns for

each calendar month averaged over the CryoSat-2 period. On average, the basin-mean snow freeboard of Antarctic sea ice ranges between 26 (November) and 35 cm (February). The distributions are as expected: broad and shorter in Austral summer and fall - corresponding to the high percentage of thicker freeboards - and narrow and slightly skewed thin in Austral winter and spring - owing to the large areal coverage of thin freeboards primarily in the Indian Ocean and Ross Sea sectors. These shapes echo what was found in Chapter 4 (with ∼one year of data) and compare to that shown with ICESat-2. The spatial maps show thickest snow freeboards in the Western Weddell Sea off the Antarctic Peninsula, as well as along the coastline in the Amundsen-Bellingshausen Seas, while the thinnest freeboards are found in the Ross Sea and Indian Ocean sectors. Some sectors show more seasonality than others, such as the coastal Pacific sector, in which thick freeboards are found in Austral winter that thin on average by the winter and spring.

Though the variability between successive months appears low (i.e. the shapes of the distribution change slowly), one can see more pronounced changes in individual regions and seasons. Figure 5.4 shows histograms of snow freeboard for each region (individual plot) and season (each line) taken from all grid cells between 2010 and 2020. Bin sizes of the histograms are 2 cm. The Pacific, Indian Ocean, and Western Weddell sectors demonstrate the largest seasonality, with mean freeboard seasonal ranges of around 17.5, 10, and 9 cm, respectively. The other sectors show smaller mean snow freeboard seasonal ranges of 4 cm (Am-Bel), 3 cm (Ross), and 2 cm (Eastern Weddell). The Indian, Pacific, and Ross sectors, in which sea ice extent is heavily influenced by the season, show the thickest freeboards in Austral

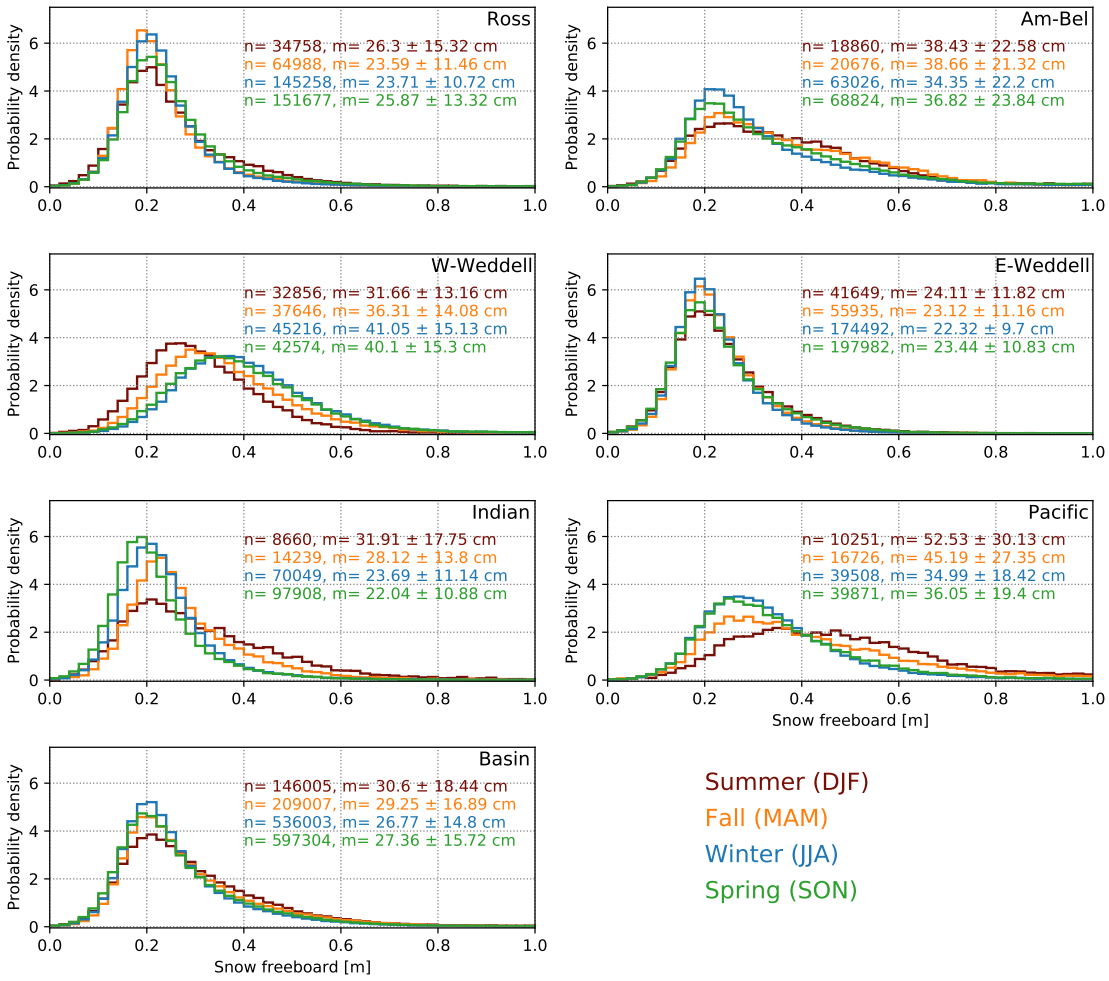

Figure 5.4: Snow freeboard distributions broken down by region (from Fig. 5.2) and season (colors) using CryoSat-2 data from July 2010 to October 2020. The number of grid cells, means, and standard deviations are given. Bin sizes are 2 cm.

summer and fall. This result makes sense as the thin ice typically melts during these seasons, leaving only the thickest freeboards behind. The Western Weddell sector, on the other hand, which varies less in extent throughout the year, shows thickest freeboard in Austral winter. One hypothesis is that the accumulation of snow and basal growth affect the mean snow freeboard in this region more that than the impact of seasonal ice area. Additionally, the ice drift in this region tends to generally flow along and away from the Antarctic Peninsula (Kwok et al., 2017; Paul

et al., 2018), which would oppose any potential dynamic thickening brought on by sea ice drift moving towards the coast. However, more studies on sea ice drift in the Austral summer are needed to further investigate this potential impact on the snow freeboard distribution.

5.4.2 Ice freeboard

While the CryoSat-2 snow freeboard retrievals could be compared with ICESat-2 (in Chapter 4), the ice freeboard retrievals from CryoSat-2 are more difficult to validate given the lack of in situ data and complexity surrounding radar penetration into the snow cover on Antarctic sea ice. Here, other CryoSat-2 retrievals of Antarctic ice freeboard are used as points of comparison, before showcasing results from the CryoSat-2 period.

5.4.2.1 Comparisons with other CryoSat-2 retrievals

Figure 5.5 shows these CryoSat-2 ice freeboard retrievals compared with two other datasets for seven months of the year 2019, broken down by region. Green points (lines) indicate the mean (standard deviation) ice freeboard for a given month and region from Kacimi and Kwok (2020), hereafter referred to as KK20. The basin values from KK20 are averages from all regional means and not the average of the entire basin, and therefore, no standard deviations are provided. Grey points come from Paul et al. (2018), hereafter referred to as P18, and represent regional and monthly means from the years 2011-2017 and therefore are not direct comparisons.

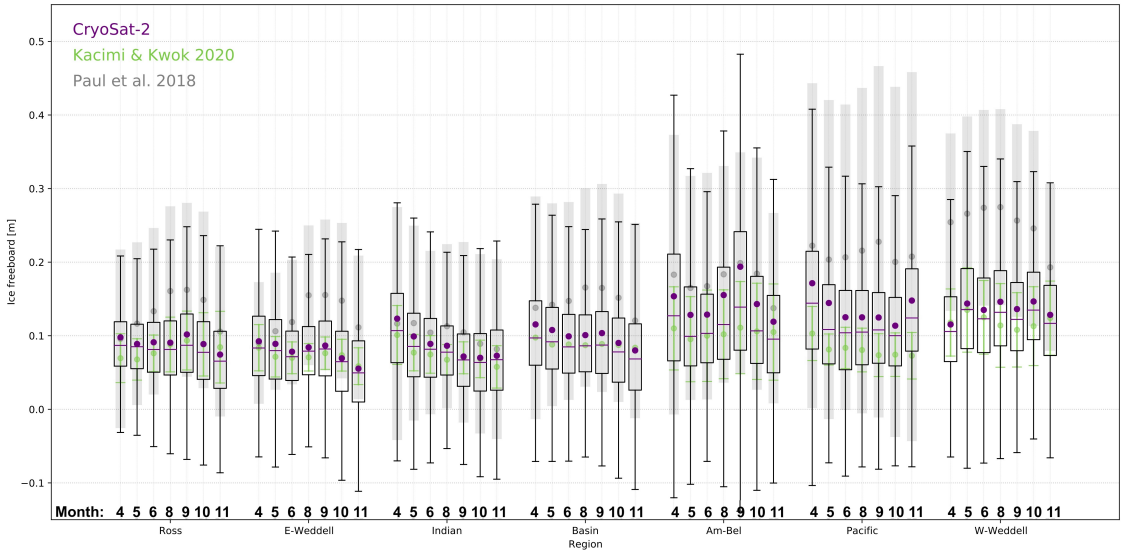

Figure 5.5: Comparison of the retrieved ice freeboard to that from Kacimi and Kwok (2020) for the year 2019. Boxplots (purple) are from the CryoSat-2 data for each region and month, where the boxes show the inter-quartile range (IQR), horizontal lines are the medians, and dots are the mean values. Green points and whiskers represent the mean value and standard deviation from KK20. Data from Paul et al. (2018) from 2011-2017 are also shown as a point of reference, and represent the mean (grey points) and standard deviations (grey shading).

These points (and grey shading representing the standard deviation of the data) are simply given as a reference. Box plots are CryoSat-2 data from 2019, where the points represent the mean value, horizontal lines indicate the median, and the box and whiskers represent the Interquartile Range (IQR) and maximum/minimum of the data, respectively. Data from July 2019 are not included in KK20 and therefore not included here.

These comparisons show a small (1 - 2 cm basin-wide) overestimation of the CryoSat-2 ice freeboard compared to KK20, that is more pronounced over areas of thicker freeboard (Am-Bel and Pacific sectors). However, a similar monthly trend is found in both the CryoSat-2 data and KK20 that is especially apparent basin-wide. KK20 ice freeboards are typically less than 10 cm, while CryoSat-2 ice freeboards

are around 10 cm on average. While the approach outlined here and KK20 use the same instrument and time range to calculate ice freeboard, they differ in their retracking procedure. KK20 uses an empirical retracker developed by Kwok and Cunningham (2015) for Arctic sea ice, while the retrieved CryoSat-2 data come from the physical retracking technique described in this dissertation. Despite the small differences, almost every KK20 data point falls within the CryoSat-2 IQR, signaling good agreement overall.

Ice freeboards from P18 are significantly thicker than these CryoSat-2 and KK20's retrieved ice freeboards. Most months in the Ross, Pacific, and Western Weddell sectors - along with basin-wide - show P18 ice freeboards outside the IQR of the CryoSat-2 data, sometimes greater than 15 cm thicker than CryoSat-2 and/or KK20. Again, since CryoSat-2 is used for the P18 retrievals, these differences likely arise from the different retracking techniques used. P18 uses a 50% power threshold as the tracking point location of the snow-ice interface on the waveform. To further investigate the retracking-induced differences, the total average ice freeboard from the same time period (2011 to 2017) is shown in Fig. 5.6. The middle panels give the CryoSat-2 and P18 ice freeboard spatial distributions and the difference CryoSat-2 - P18. The top and bottom plots show linear regressions of ice freeboard from each sector.

The results in Fig. 5.6 echo what is shown in Fig. 5.5: P18 ice freeboards tend to be thicker than those from this CryoSat-2 method, especially in regions of thicker ice. In the Western Weddell sector, for example, P18 records almost 10 cm thicker ice freeboards on average than this CryoSat-2 method, coming from

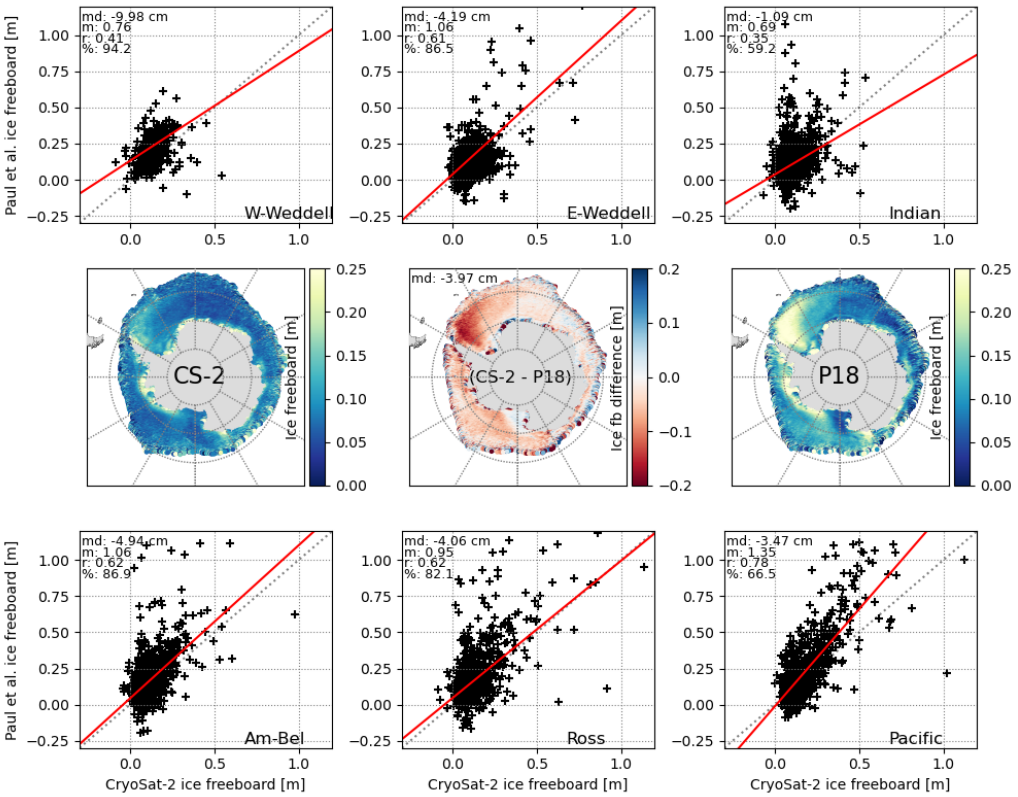

Figure 5.6: Comparison of 2011-2017 average ice freeboard between this method and Paul et al. (2018). Scatter plots show linear regressions for each region, and note the mean difference (md), slope of the regression line (m), correlation (r), and % of grid cells that are larger in P18 compared to this method.

over 94% more grid cells with thicker freeboards in P18 than in CryoSat-2. This is similar in every other sector, as P18 records 1 to 5 cm thicker freeboards and more than 60% to 87% of grid cells thicker than CryoSat-2. It is hypothesized here that this discrepancy comes from the use of a fixed retracking threshold in P18. As mentioned in previous chapters, field campaigns from Antarctic sea ice have found dominant scattering horizons at Ku-band frequencies to be located higher than the actual snow-ice interface (Willatt et al., 2010). When a fixed retracking threshold is used in combination with the assumption that the dominant scattering

originates from the snow-ice interface, this would lead to an over-estimation of the ice freeboard, similar to what is shown in Fig. 5.6. Following this hypothesis and the assumption that the use of the physical retracker more accurately tracks the snow-ice interface, the difference plot in Fig. 5.6 would therefore be analogous to the height of the dominant scattering horizon (when using a 50% threshold retracker) above the actual snow-ice interface, and provide justification for the use of physical retrackers over Antarctic sea ice. More validation is needed to verify the actual location of the snow-ice interface (and therefore the accuracy of the CryoSat-2 retrievals from this method) as well as to determine the effects of surface type classification and sea surface height differences between the two retrievals on the ice freeboard distribution. However, this comparison still provides some confidence that this physical retracker could better retrieve the snow-ice interface compared to empirical methods, which motivates retrievals of ice freeboard and snow depth.

5.4.2.2 Monthly and seasonal ice freeboard from CryoSat-2: 2010-2020

Figure 5.7 shows monthly average ice freeboard distributions and spatial patterns for each calendar month between 2010 and 2020. Ice freeboards range between 8 and 12 cm on average, which monthly standard deviations ranging from ∼9.5 to 13 cm. The spatial patterns resemble the snow freeboard maps, where the thickest freeboards are typically found in the Western Weddell Sea and along the Am-Bel coast. Thinnest ice freeboards are found away from coasts, especially in the Eastern

Weddell, Indian, and Ross sectors.

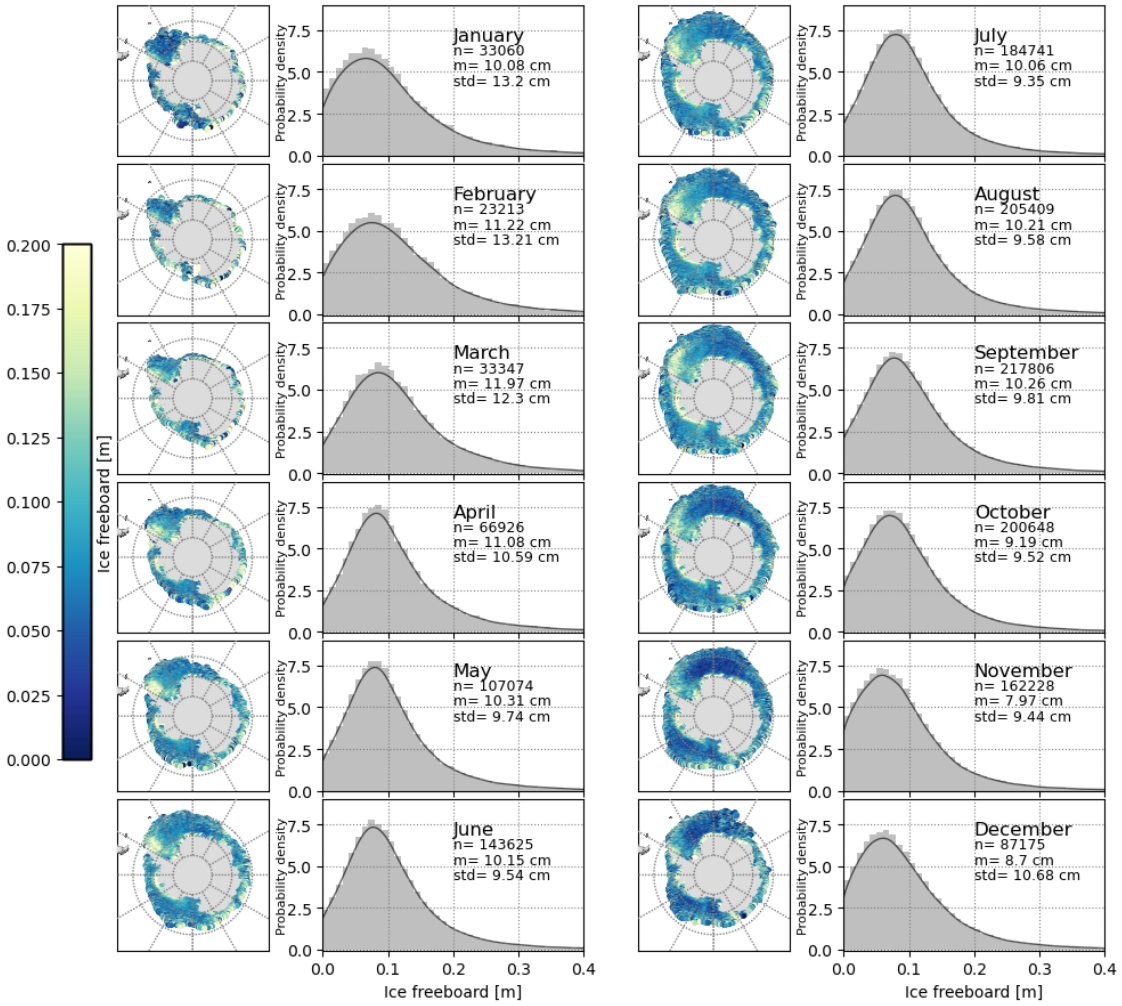

Figure 5.7: As in Fig. 5.3 but for ice freeboard. Bin sizes are 1 cm.

The ice freeboard maps here highlight an interesting seasonality in the presence of zero ice freeboards. As the ice cover expands beginning in March, most of the ice pack shows an ice freeboard greater than ∼5 cm (i.e. there is relatively little spatial area found to have ice freeboards close to zero). This is confirmed by the lower probabilities of zero freeboards in the histograms that continues through the winter season (until August). However, as the season transitions to Austral spring, the presence of zero ice freeboards starts to increase, becoming especially apparent in

November in the Eastern Weddell, Indian, and off-shore Am-Bel sectors (Fig. 5.7). A larger percentage of the basin-wide ice freeboard in these months is zero, as shown by the distributions. This follows the conventional "zero ice freeboard" assumption (Kurtz and Markus, 2012) for Antarctic sea ice. It is possible that these zero ice freeboards in Austral spring are due to increasing snowfall and zero/negative sea ice growth rates. As the ice stops growing but snow continues to accumulate, the ice will get pushed further down to the water level, resulting in zero or near-zero ice freeboards. Despite the presence of some zero ice freeboards in all months, these results suggest that a basin-wide zero ice freeboard assumption for all regions is not representative of the true distribution.

The presence of near-zero ice freeboards in the Weddell Sea in January is possibly due to the same concept as described above, however, the thin freeboards in the Western part of the sector in January is puzzling, given the assumed perennially-thick ice in this region. This is more apparent in Fig. 5.8, which shows seasonal distributions of ice freeboard for each sector. The summer ice freeboard distribution in the Western Weddell sector is substantially lower than in other seasons. One potential explanation is the presence of sea ice submergence that was noted in this region by Haas et al. (2001). In the summer months, ice can submerge further due to changes in isostatic equilibrium, brought on by the combination of basal melting and accumulation of mass in the form of snow and rain on the ice surface (which can be high in this region, Haas et al. 2001). Additionally, internal melting in these months can lead to increases in bulk density, which further submerge the ice. As found in Haas et al. (2001), this combination of processes can lead to greater than 10

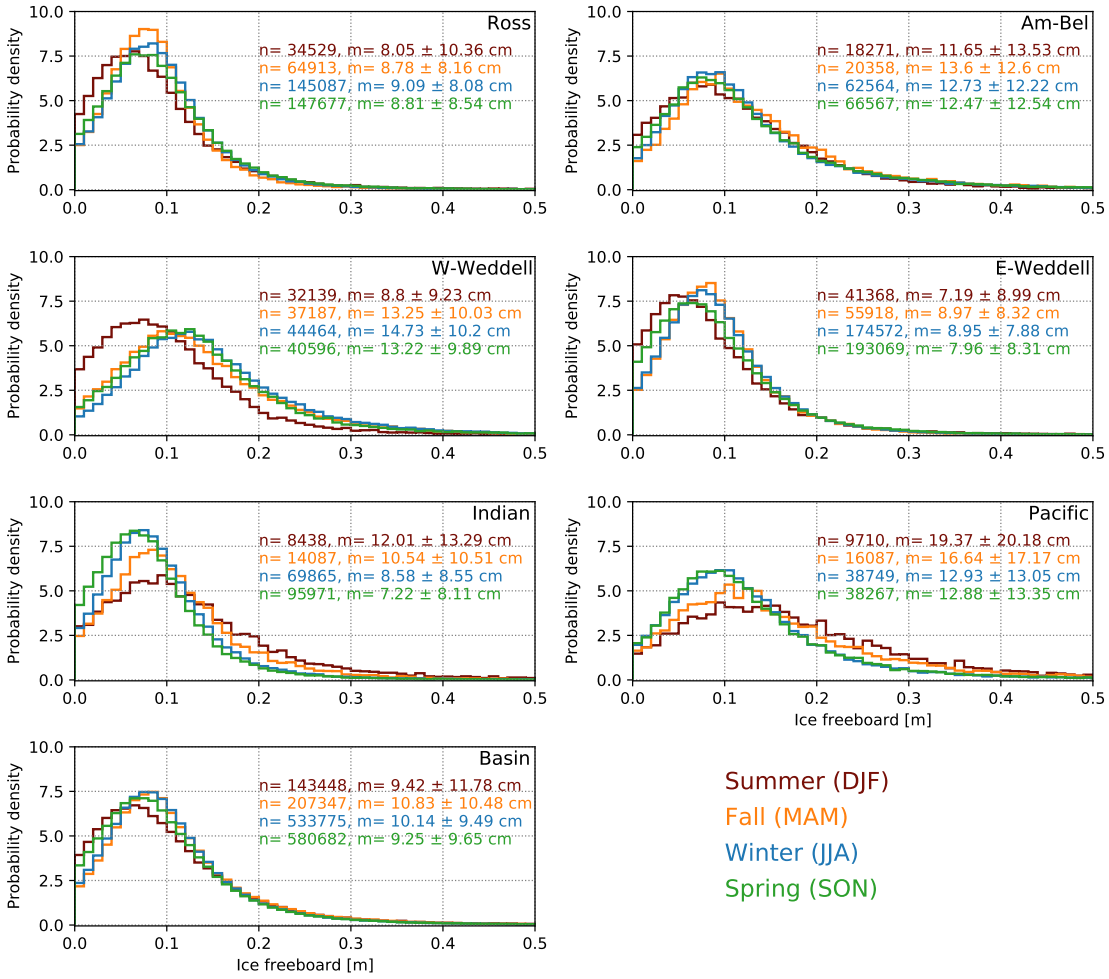

Figure 5.8: As in Fig. 5.4 but for ice freeboard. Bin sizes are 1 cm.

cm of submergence in summer months and contribute to the thinner ice (and snow) freeboards observed. Similar summer seasonal minima in ice freeboard are found, to a lesser extent, in the Eastern Weddell and Ross sectors, where the distributions tend to be narrower and more skewed thin than the Western Weddell. In the Indian and Pacific sectors the opposite is true, as the thickest ice freeboards are found in the summer months and the distributions are broad overall. More summer validation data would be useful - both in terms of physical ice freeboard measurements as well as Ku-band radar scattering over sea ice - to better understand the summer ice

freeboard distributions and how they vary around the continent.

5.4.3 Snow depth on sea ice

The retrieved ice freeboard estimates are subtracted from the snow freeboard estimates, providing along-track snow depth on sea ice for the duration of the CryoSat-2 period. This sections showcases attempts at validation as well as monthly and seasonal patterns in the snow depth distribution.

5.4.3.1 Snow depth comparisons

Much like with ice freeboard measurements, the lack of reliable in situ data involving snow depth on Antarctic sea ice poses a challenge when attempting to validate snow depth retrievals from CryoSat-2. Here, snow depth estimates from KK20 are used as a point of comparison for large-scale (basin wide) snow depth retrievals from CryoSat-2. Additionally, two independent, in situ datasets are also compared with CryoSat-2, highlighting difficulties when relating ground-based and satellite measurements.

Figure 5.9 shows a comparison between CryoSat-2 and KK20 in the same way as Fig. 5.5. Monthly differences in basin-mean snow depth (CryoSat-2 - KK20) range from 1.5 cm in August to 4.6 cm in April. As seen above, differences are largest in regions where snow (and ice) thickness is typically greatest including the Am-Bel, Pacific, and Western Weddell sectors. However, in the Am-Bel and Pacific sectors, the KK20 snow depths fall within the CryoSat-2 IQR, which is not always

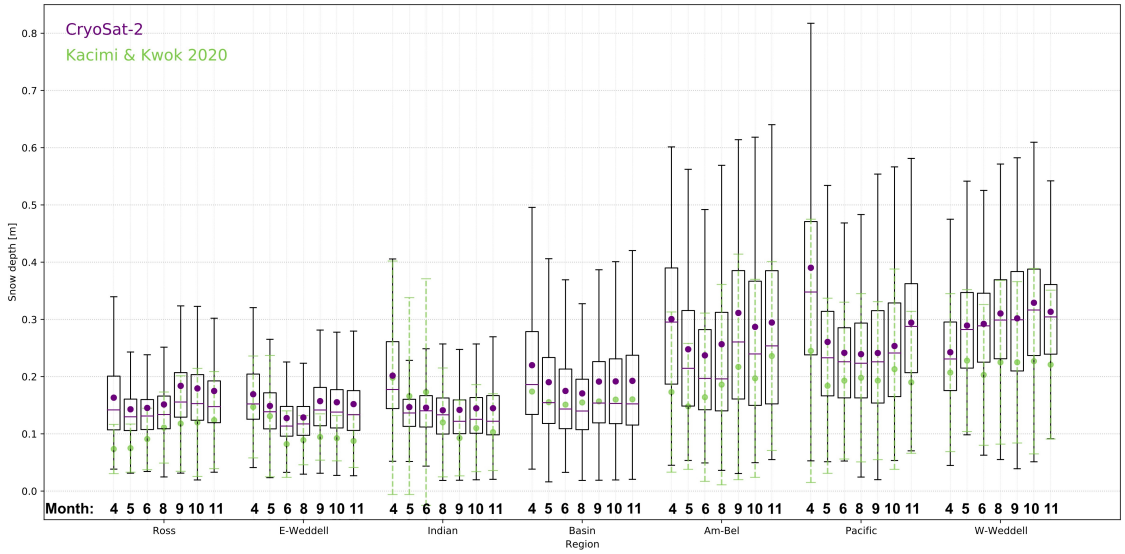

Figure 5.9: As in Fig. 5.5 but for snow depth comparing this method and KK20.

the case for sectors in which the mean differences are smaller (Ross and Eastern Weddell sectors). Overall, the agreement between CryoSat-2 and KK20 is not as good as is seen in the ice freeboard results (Fig. 5.5). While these measurements both use CryoSat-2 data to estimate ice freeboard, KK20 also uses ICESat-2 data and only collects snow depths within +/- 10 days from a valid ICESat-2 freeboard measurement. Therefore, it must be noted that each month in this comparison involves different amounts of data between the two methods which could explain some of the differences observed. The observed similar seasonality in the basin-wide snow depth between both datasets is nevertheless encouraging, despite the bias that exists.

An attempt to compare the retrieved CryoSat-2 snow depths to entirely independent datasets is shown in Fig. 5.10. Here, data from the AWI snow buoys (top plots) and OIB Snow Radar (bottom plots) are used to provide an estimate of snow depth. In both cases, trying to utilize the small spatial scale of the ground measure-

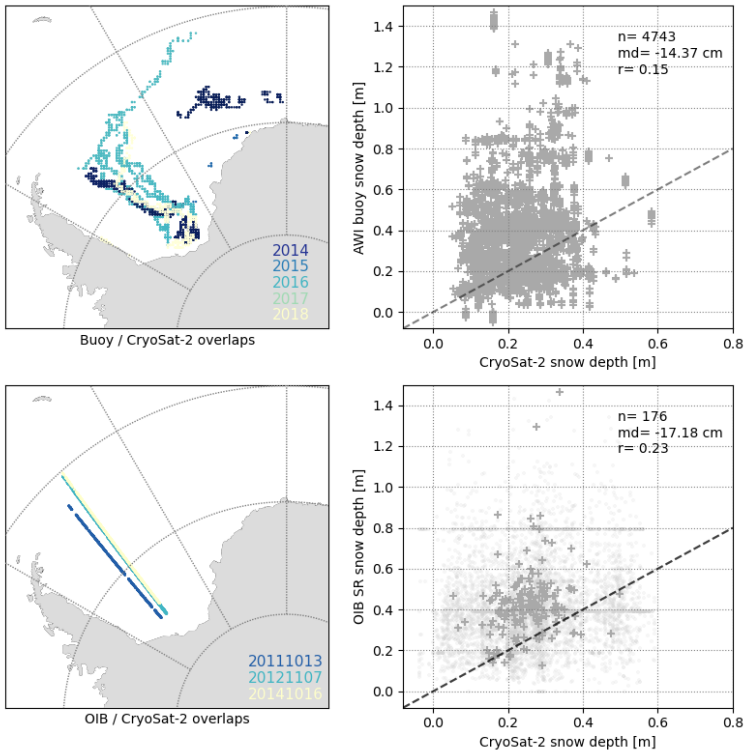

Figure 5.10: Comparisons of the retrieved CryoSat-2 snow depth to that from the AWI snow buoys (top) and OIB snow radar (bottom). Left maps show coincident grid cells with CryoSat-2 while right plots show linear regressions of the coincident data. Each grey point represents one coincident 25x25 km grid cell, while each light grey point represents a CryoSat-2 footprint and the corresponding average snow radar snow depth.

ment leads to issues in the comparisons. For the buoys, overlapping CryoSat-2 orbits with a single buoy are rare, and even so, would only allow for a single CryoSat-2 shot to compare with the buoy data. The Snow Radar data, when averaged slightly to the footprint size of CryoSat-2, display artifacts in the data likely caused by thresholds in the Snow Radar layer picker. To account for these issues and better enable comparisons with CryoSat-2, these data have been gridded into 25 km daily grid cells for comparisons with Snow Radar and monthly grid cells (as few daily gridded overlaps occurred) for comparisons with the AWI buoys.

One can see that there is weak agreement between the CryoSat-2 data and

either of the independent measurements. There are low correlation coefficients and large mean differences, greater than 14 cm, in both cases. There are, however, large assumptions made with each of the independent datasets that suggest high uncertainty in their snow depth estimates. In the case of the buoys, the assumption is that the buoy data provide the physical snow depth. As mentioned above, these buoys record the height of the sensors from the air-snow interface, and therefore they (a) rely on precise initial snow depth measurements in order to accurately record snow depth and (b) do not take into account effects of slush layers, refreezing, snow-ice formation, or other processes that are known to occur on Antarctic sea ice (Willatt et al., 2010). Therefore, the snow buoy data provide potentially biased snow depths (Nicolaus et al. 2016; S. Arndt, personal communication, May 2020). Additionally, the buoy data provide a single Lagrangian measurement through time, while CryoSat-2 provides a larger-footprint Eulerian view of the snow cover, which could further contribute to differences.

In the case of the Snow Radar data, the assumption is that the correct interfaces are being tracked, so that when differenced, the snow depth is obtained. The wavelet algorithm used in *pysnowradar* to derive snow depth from the OIB Snow Radar data is not validated (especially over Antarctic sea ice), and is simply one method to pick interfaces from the radar echograms (King et al., 2020; Newman et al., 2014). The artifacts that exist in the scatter plot of Fig. 5.10 (horizontal lines at 0.8, 0.4, and 0.2 m) could suggest that thresholds used in the algorithm tend to "snag" many points and further reduce the confidence in these data. These independent snow depth measurements could potentially be useful as tools for future

validation, however, more work is needed to better validate their estimates before using them to validate CryoSat-2.

5.4.3.2 Monthly and seasonal snow depth on sea ice from CryoSat-2: 2010-2020

Much like what was shown in Sections 5.4.1 and 5.4.2, the 2010-2020 mean snow depth on Antarctic sea ice for each calendar month is given in Fig. 5.11, along with the basin-wide snow depth distribution for all grid cells between 2010 and 2020. Most notably, these spatial patterns and distributions appear more realistic (based off of other estimates from Markus and Cavalieri 1998 and Kacimi and Kwok 2020) than what was attempted in Chapter 3, signalling that the improvements made in Chapter 4 had a substantial - and beneficial - effect on the ice freeboard and snow depth retrievals. Snow depths range between 17 and 26 cm on average, with the largest basin-wide snow depth occurring in February. Standard deviations of snow depth range between 9.7 and 13 cm. The most notable difference in these distributions from the snow and ice freeboards is the presence of multiple modes in each month. These modes occur at approximately 10, 25, and 30 cm, but vary drastically in the relative magnitudes. The Austral winter and spring distributions have one dominant peak at 10 cm, with much smaller peaks elsewhere. In the Austral summer, these peaks are much closer in magnitude, corresponding to a thicker mean snow depth. These trimodal distributions are apparent in the maps, as there are sharper transitions between thick and thin snow depths than was seen in

the freeboard spatial patterns. The multi-mode distribution is also found on Arctic sea ice (Kwok et al., 2020c; Petty et al., 2020b) where different modes come from different ice types (FYI or MYI). Since most Antarctic sea ice is annual apart from small amounts of perennial ice very near the coast, the different modes observed in Fig. 5.11 likely come from the regional differences in the snow depth distribution, as shown in Fig. 5.12.

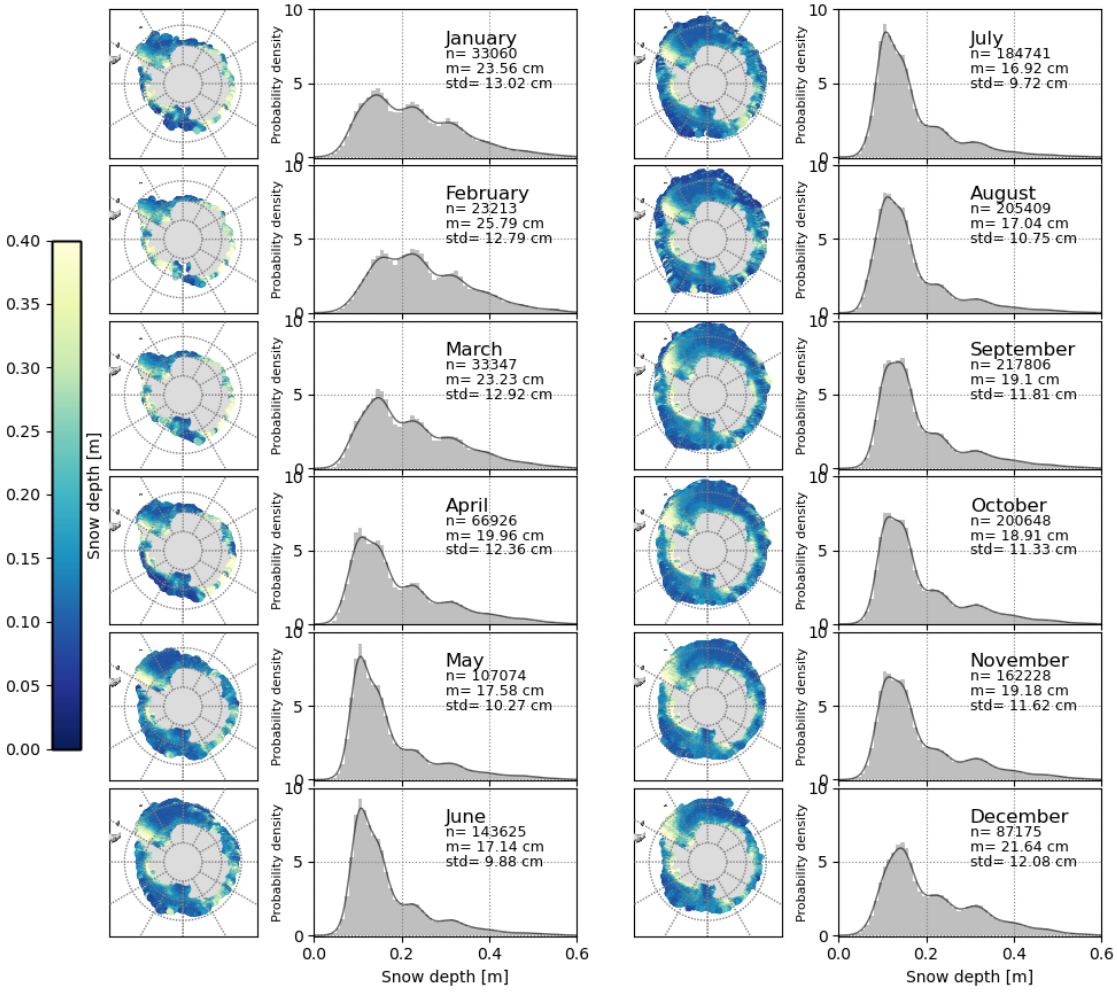

Figure 5.11: As in Fig. 5.3 but for snow depth. Bin sizes are 1 cm.

The seasonal average CryoSat-2 snow depths broken down by sector (Fig. 5.12) showcase a large regional variability that exists in the data. The Western Weddell,

Pacific, and Am-Bel sectors have very broad distributions with thick means (>23 cm), large spreads, and multiple modes, while the other regions have means closer to 15 cm, and are skewed thin with a smaller spread and a single dominant mode. These distributions tend to match those in Markus and Cavalieri (1998), where some regions - such as the Western Weddell - show broader snow depth distributions while other regions - like the Indian Ocean - tend to show distributions with a single mode and a thinner mean snow depth.

In all sectors except the Western Weddell, the thickest average snow depths are found to occur in summer. Following previous discussion, this makes intuitive sense as it is the season in which only the thickest ice remains, allowing for thicker snow loads to accumulate. This finding is especially pronounced in the Pacific and Indian sectors, which have very little ice coverage (low n values) in summer months. In the Western Weddell, the thinnest average snow depths of any season occurs in the summer. This finding is counter-intuitive given the low ice freeboards present there thought to be from ice submergence and generally thicker snow. One possible explanation could be due to the presence of surface melting of the snow layer that can act to reduce snow depths and/or potentially impact retrievals in this region and season. Markus and Cavalieri (1998) found that surface melt in summer months in this region can occur - due in part to the more-northern location compared to other regions - and found that this melt can complicate passive microwave returns. Here, it is possible that surface melt could lead not just to thinner snow depths, but could lead to erroneous CryoSat-2 waveform classification, as melt-affected floe-points may appear more specular in radar returns. This could cause mis-classification of sea ice

returns, which could impact the SSH and retrieved snow-ice interface elevations, potentially leading to anomalous snow depth and/or freeboard values.

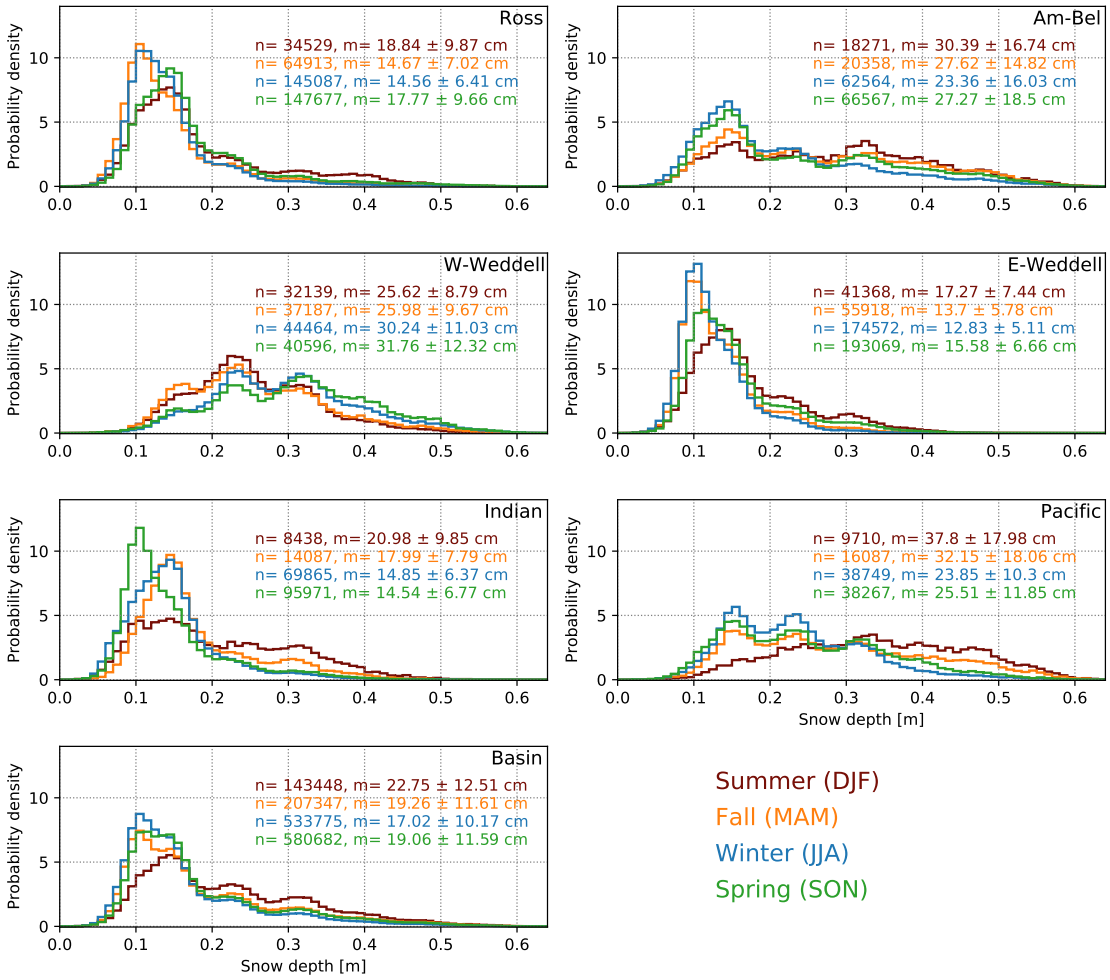

Figure 5.12: As in Fig. 5.4 but for snow depth. Bin sizes are 1 cm.

Once again, more validation data in Austral summer would be useful to better understand the seasonality observed in the CryoSat-2 returns.

5.4.4 Sea ice thickness and volume

The retrieved snow freeboards and snow depths shown above are used in Equation 5.2 to calculate the sea ice thickness. Here, first estimates of Antarctic sea ice

thickness and volume derived from CryoSat-2 from the years 2010 - 2020 are shown.

5.4.4.1 Monthly and seasonal sea ice thickness from CryoSat-2: 2010-2020

The monthly mean Antarctic sea ice thickness distributions and spatial patterns from 2010 to 2020 are given in Fig. 5.13. Basin-wide thicknesses are lowest in November (0.99 m) and largest in March (1.32 m). Monthly standard deviations range from 70 to 87 cm, while modal thickness values range between 80 and 100 cm. The winter distributions tend to be broader than other months, though all months exhibit a singular mode. The spatial pattern follows closely with that of freeboard and snow depth, with the largest thicknesses being found in the Western Weddell sector, as well as along the coast in the Am-Bel and Pacific sectors, while thinner ice tends to be found away from the coast in the Eastern Weddell, Indian, and Ross sectors. These values tend to be thicker than those observed in previous studies (e.g. Worby et al. 2008), which is discussed later in this section.

The regional and seasonal distributions are given in Fig. 5.14. The regional variability is immediately apparent, as the Pacific, Western Weddell, and Am-Bel sectors showcase a broad distribution with larger mean values and modes typically greater than 1 m, while the other regions show a narrower distribution with modes centered around or below 1 m. The largest seasonality within a region is found in the Pacific sector, where the fall and summer ice thickness is noticeably thicker than the other seasons, owing to the low extent present during these seasons. Once

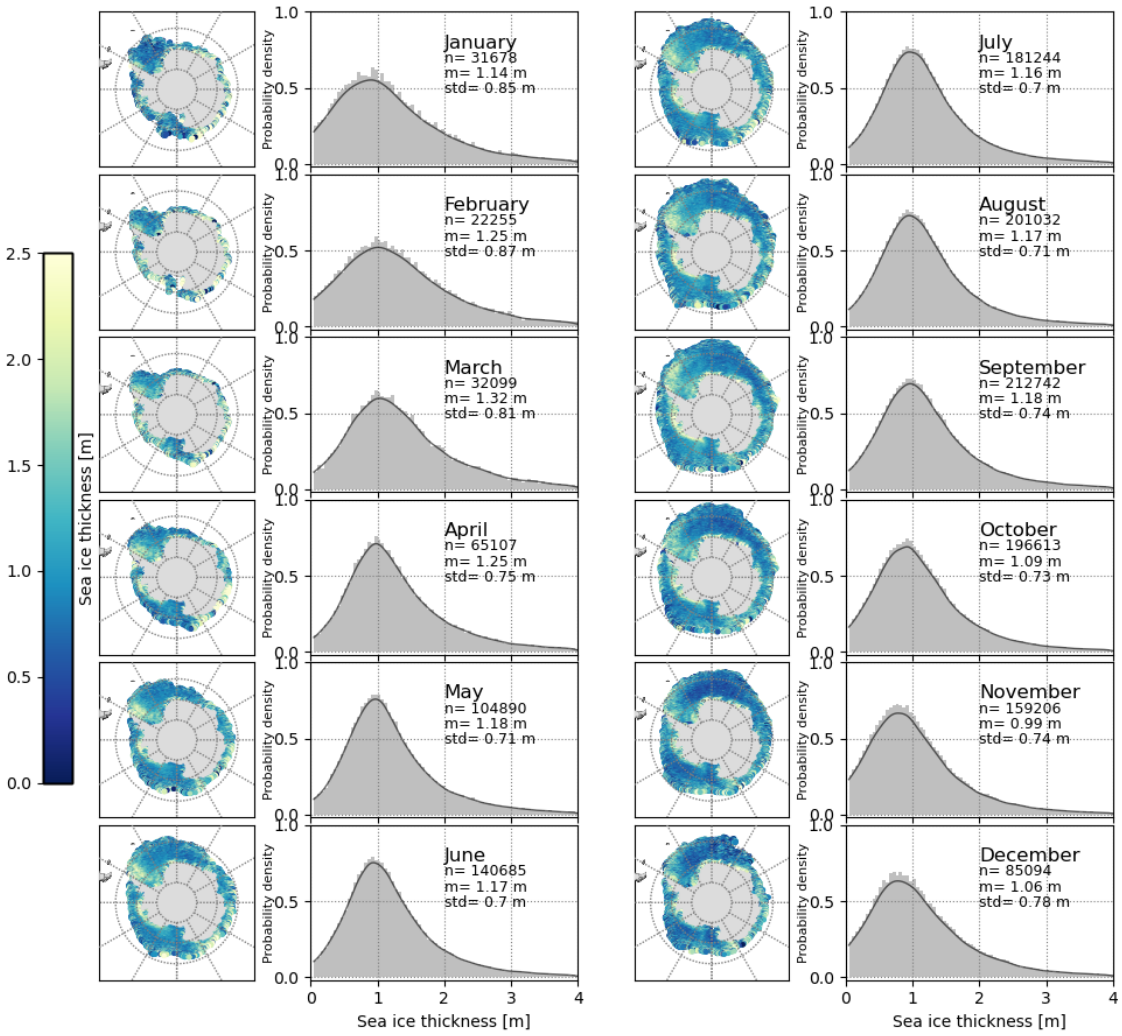

Figure 5.13: As in Fig. 5.3 but for sea ice thickness. Bin sizes are 5 cm.

again, the Western Weddell sector shows puzzling results, where the thinnest season is found to be summer. This potential anomaly follows the similar feature observed in the seasonal freeboard and snow depth distributions (Fig. 5.8 and 5.12), and could be again related to the presence of surface melt (Markus and Cavalieri, 1998). Freeboards and/or snow depths that are biased due to mis-classification of floe-type points could also lead to anomalous ice thicknesses. This region is clearly complex in terms of seasonality in snow depth, ice thickness, and potential surface melt, and

should be the focus of future study.

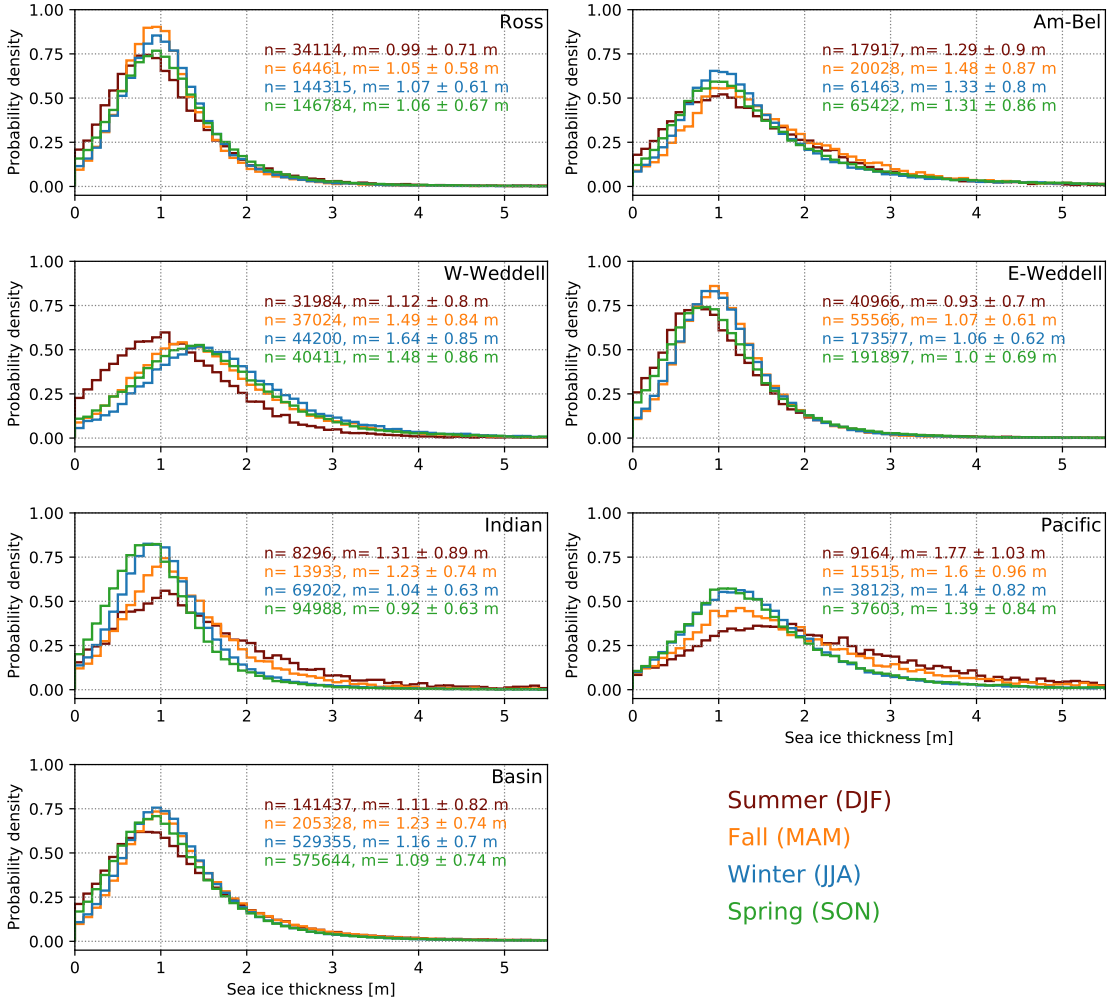

Figure 5.14: As in Fig. 5.4 but for sea ice thickness. Bin sizes are 10 cm.

Another interesting feature in the seasonal distributions is the perceived lack of seasonal variability in some regions. Some sectors showcase seasonal variation in the distributions, such as the Indian and Pacific sectors. In the Am-Bel and Ross regions, however, each season shares a very similar mode and distribution shape. This lack of seasonality contrasts what is found in Arctic sea ice, where a clear seasonal cycle exists in the thickness distributions (Petty et al., 2020b). To further explore the monthly and inter-annual variability, a full time series of Antarctic sea

ice thickness was created.

Figure 5.15 shows the monthly average sea ice thickness basin-wide (solid black line) as well as from individual sectors (thin lines) from July 2010 until October 2020. The shading represents the estimated thickness uncertainty provided in Table 5.1. When viewed in this sense, a clear seasonal cycle of thickness emerges: basin-averaged thickness increases at the beginning of the calendar year, reaching a maximum around March, before falling on average as new ice forms around the continent. This maximum corresponds to the minimum in sea ice extent (Parkinson, 2019). There is then a slight thickening at the end of Austral winter and beginning of spring, as the sea ice extent stops growing outward but basal growth continues. This thickening quickly switches to a thinning by the middle and end of spring, as basal melt begins basin-wide. The thickness only increases on average once the thinnest ice melts entirely in the beginning of summer, leaving only the thickest ice present near the continent. This cycle continues each year.

While the time series in Fig. 5.15 shows the general seasonal cycle described above, there does exist some variability in the magnitude of the mean thickness. For example, the March peaks in ice thickness vary between 1.2 and about 1.5 m on average, while the November minima also vary between $\sim$0.9 and 1.05 m. This variation can be even larger amongst individual regions.

The time series of the individual regions gives insight not just into the spatial distribution of thickness, but also highlights potential issues with the retrievals. For one, the sharp decline (and subsequent rise) in summer (fall) thickness in the Western Weddell is clearly seen each year beginning around December and appears

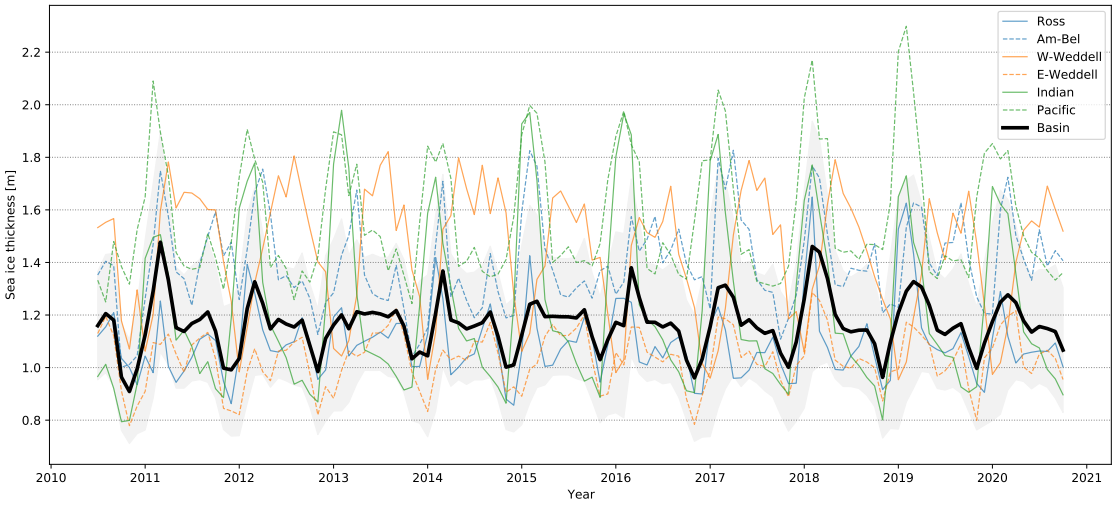

Figure 5.15: Time series of Antarctic sea ice thickness covering the entire CryoSat-2 mission 2010-2020. Dark black line represents the pan-Antarctic average, while the shading indicates the uncertainty estimate provided in Table 5.1. Thin lines show individual regions.

to show melt rates and growth rates much larger than would be expected from basal processes alone (since the areal coverage is fairly constant in this region). As stated above, it is hypothesized that snow cover melt in summer could affect the radar returns, leading to anomalously thin values. Another potential issue is seen in the Indian sector thickness time series, which records the thickest overall ice out of any region in 2013 and near the thickest in multiple years. Worby et al. (2008) found this sector to be one of the thinnest sectors in summer, contrasting what is found here. While it is true that the only ice remaining in this sector during the summer is likely thicker, it is unlikely thicker than ice in other regions and therefore could signal a difficulty in this algorithm to retrieve ice thickness near the coast in the Indian sector.

Overall, the mean thickness values shown here appear to be slightly higher than expected, especially in months of new ice growth where one would expect much of the

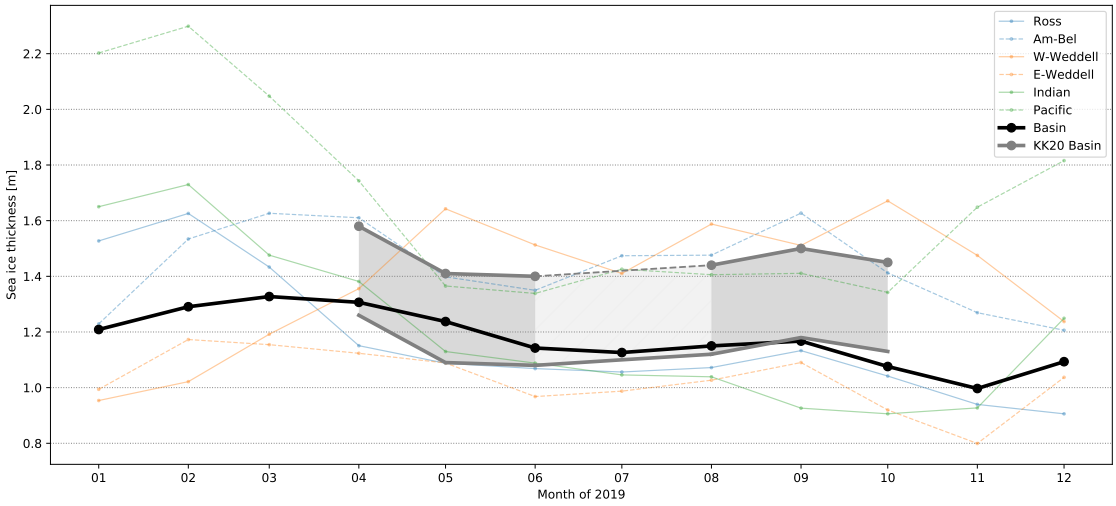

Figure 5.16: As in Fig. 5.15 but just for the year 2019. Thickness results from KK20 are added for comparison, where the top dark grey line indicates their thickness values computed, and the shading indicates the range of corrected thickness values, down to $\delta = 6cm$. Lighter grey shading shows linear interpolation for the missing month of July 2019.

ice cover to be below 1 m. Kurtz and Markus (2012) found mean values below 1 m for all seasons, with the caveat of using the zero ice freeboard assumption. Worby et al. (2008) and Maksym and Markus (2008) both found thinner annual and seasonal means from ship-based and passive microwave-based thicknesses. However, KK20 found thicknesses comparable - and even thicker than - these CryoSat-2 results, but also acknowledged that they seem high. Figure 5.16 shows the CryoSat-2 sea ice thickness time series (Fig. 5.15) zoomed in to 2019, with the added thickness values from KK20 included. KK20 includes multiple estimates of thickness to "correct" for the anomalously-thick results, which are shown here as the thick grey line (thickness from CryoSat-2 and ICESat-2 snow depth) as well as the shaded area (which covers their corrected thicknesses of $\delta = 3$ cm and $\delta = 6$ cm). No data were provided from July 2019, and therefore a simple linear interpolation is shown as the lighter

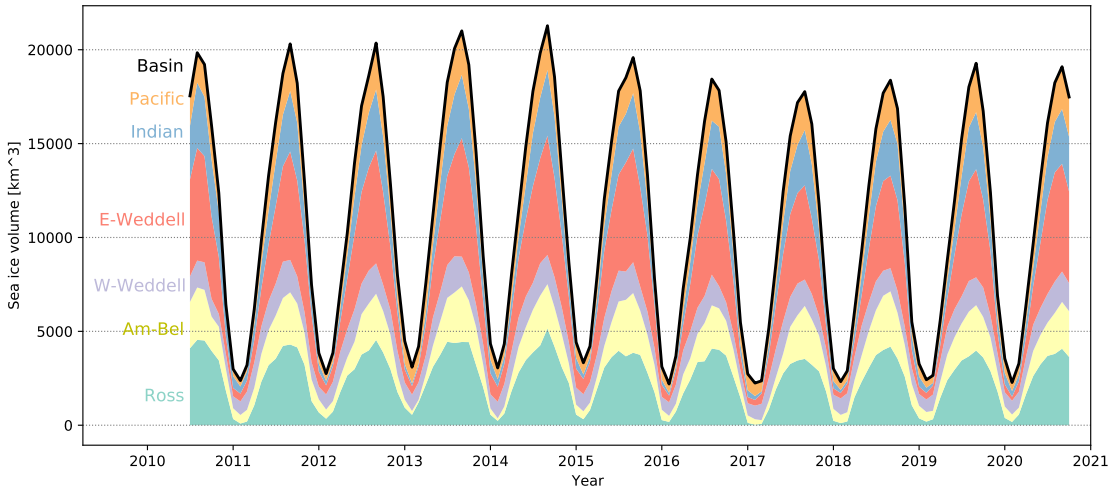

Figure 5.17: Time series of Antarctic sea ice volume covering the entire CryoSat-2 mission 2010-2020. Black line shows the pan-Antarctic volume, while the colored segments show the individual contributions from each region.

grey lines/shading. This simple comparison shows that these CryoSat-2 thickness estimates are around the same range of what was estimated by KK20, and closer to their $\delta = 6$ cm values. It is possible that the use of CryoSat-2 in both methods is leading to thicker retrieved ice thicknesses (perhaps through anomalous snow-ice interface tracking) but more work is needed to conclude this with more certainty. There is also a chance that the Antarctic sea ice thickness distribution is simply thicker than previously assumed (Williams et al., 2015), meaning that the results shown here could be closer to the true thickness values. More discussion is provided in Section 5.5.

5.4.4.2 Sea ice volume

For each month of sea ice thickness data shown above, the monthly mean sea ice volume is also computed. This is done by multiplying the sea ice areal coverage in

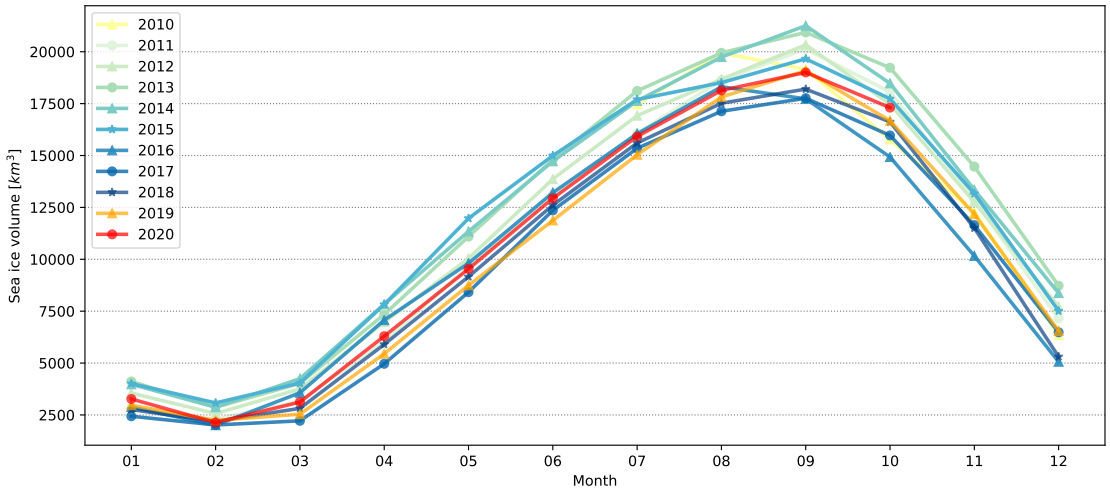

Figure 5.18: Seasonal cycle of Antarctic sea ice volume, where each line represents a different year of data. The lines connect each monthly average volume estimate (points).

the basin or region by the mean ice thickness. A time series of volume is given in Fig. 5.17, where the basin-total volume (black line) is broken down into contributions from the various sectors. The sea ice volume varies substantially within a year, ranging from less than 2500 km^3 to over 20000 km^3. The Ross and Eastern Weddell sectors contribute the largest percentage of volume in the winter and fall seasons (when area is greatest), while the Western Weddell sector tends to contribute most to the spring and summer basin-wide sea ice volume. These values compare overall to the volume estimates put forth in KK20, both in the basin-wide sense as well as in the individual regions. Monthly average volume estimates from the entire time period are included in Table 5.2.

Figure 5.18 shows the same pan-Antarctic sea ice volume results, but focusing only on the seasonal cycle where each line represents a different year of data. The cycle and magnitude of the volume results shown here are similar to those found

in Holland (2014). There is clearly more interannual variability during months of greater sea ice volume (August - October) when compared to months of less volume (January - March), which follows a similar pattern in Antarctic sea ice extent (Parkinson, 2019). Additionally, in all months, more recent years appear to have smaller volume (i.e. darker lines tend to be below lighter lines in Fig. 5.18) which would suggest a potential trend in volume (investigated further in the next section). The overall maximum in volume (September 2014) corresponds to the maximum recorded sea ice extent, while 2017 shows the lowest September volume, corresponding to the smallest maximum extent occurring that year.

5.4.5 Trends and variability in sea ice thickness and volume

5.4.5.1 Seasonal sea ice thickness trends

Given this 10+ year time series of Antarctic sea ice thickness and volume, it makes sense to investigate potential trends in the data. Figure 5.19 shows seasonal mean sea ice thicknesses from each region between 2010 and 2020, where each line represents the change over time in sea ice thickness for that particular region and season. Each line is fit with a linear least-squares regression, and the slopes (which denote the trend) are provided in Table 5.3. To determine the statistical significance of the reported trends, the p-values and q-values are reported, where the p-values are from a Wald test of the null hypothesis that the slope (trend) is zero, and the q-values indicate the False Discovery Rate (FDR) adjusted p-values following the Benjamini-Hochberg procedure (Benjamini and Hochberg, 1995). The Benjamini-

Region	Variable	Month 01	02	03	04	05	06	07	08	09	10	11	12
Ross	h_{fs} [cm]	31.2 ± 20.2	35.3 ± 22.3	27.7 ± 16.0	23.8 ± 12.1	22.7 ± 9.7	23.2 ± 10.5	23.6 ± 10.5	24.2 ± 11.0	27.2 ± 13.9	26.0 ± 13.2	24.2 ± 12.5	24.7 ± 13.0
	h_{fi} [cm]	10.8 ± 14.0	12.9 ± 15.7	10.3 ± 10.5	8.8 ± 8.5	8.5 ± 7.4	8.8 ± 8.1	9.1 ± 8.1	9.3 ± 8.0	9.9 ± 8.7	8.9 ± 8.4	7.4 ± 8.3	7.2 ± 8.8
	h_s [cm]	21.3 ± 11.6	24.5 ± 12.6	17.8 ± 10.1	14.9 ± 7.6	13.9 ± 5.6	14.2 ± 5.7	14.4 ± 6.3	15.0 ± 7.1	18.1 ± 9.9	17.8 ± 9.7	17.4 ± 9.3	18.0 ± 9.1
	h_i [m]	1.15 ± 0.78	1.33 ± 0.90	1.17 ± 0.69	1.04 ± 0.58	1.02 ± 0.56	1.05 ± 0.59	1.07 ± 0.62	1.10 ± 0.63	1.16 ± 0.67	1.07 ± 0.67	0.94 ± 0.66	0.94 ± 0.67
	$V[km^3]$	446.9	223.6	545.6	1593.5	2562.0	3241.6	3750.0	4005.9	4235.5	3824.6	2967.4	1702.7
Am-Bel	h_{fs} [cm]	37.7 ± 22.1	43.6 ± 21.3	46.4 ± 21.7	39.7 ± 21.4	36.0 ± 20.6	34.8 ± 21.8	33.6 ± 20.7	34.7 ± 23.7	38.5 ± 25.9	36.4 ± 23.1	35.2 ± 21.7	37.5 ± 22.9
	h_{fi} [cm]	11.4 ± 13.2	14.1 ± 14.5	16.0 ± 14.7	13.8 ± 12.5	12.9 ± 12.0	12.8 ± 12.4	12.4 ± 11.5	13.0 ± 12.7	13.9 ± 13.5	12.4 ± 12.4	10.6 ± 11.2	11.2 ± 13.4
	h_s [cm]	29.3 ± 16.0	33.6 ± 12.1	35.0 ± 13.1	28.6 ± 15.0	25.2 ± 14.4	23.8 ± 15.1	22.8 ± 15.0	23.5 ± 17.4	27.3 ± 19.7	26.9 ± 17.7	27.7 ± 17.8	30.1 ± 17.8
	h_i [m]	1.29 ± 0.90	1.55 ± 0.92	1.68 ± 0.93	1.52 ± 0.87	1.40 ± 0.84	1.34 ± 0.80	1.32 ± 0.79	1.34 ± 0.80	1.40 ± 0.86	1.31 ± 0.84	1.20 ± 0.85	1.23 ± 0.89
	$V[km^3]$	542.2	365.7	401.3	780.5	1195.1	1658.6	2206.5	2577.3	2666.1	2214.6	1800.1	1120.6
W-Weddell	h_{fs} [cm]	28.6 ± 11.8	29.8 ± 11.4	32.5 ± 12.1	35.0 ± 13.5	40.5 ± 15.0	40.7 ± 14.4	40.1 ± 14.3	42.4 ± 16.4	40.5 ± 16.2	41.4 ± 15.5	38.3 ± 13.8	36.1 ± 14.5
	h_{fi} [cm]	7.5 ± 8.8	8.6 ± 8.8	11.3 ± 9.3	13.3 ± 10.0	14.8 ± 10.3	14.7 ± 10.1	14.4 ± 10.2	15.1 ± 10.3	14.0 ± 10.1	13.7 ± 9.8	11.6 ± 9.5	10.1 ± 9.8
	h_s [cm]	23.2 ± 7.6	23.2 ± 7.2	23.5 ± 7.6	24.3 ± 9.2	29.5 ± 10.5	29.7 ± 9.8	29.6 ± 10.2	31.4 ± 12.7	30.8 ± 13.2	32.8 ± 12.8	31.8 ± 10.4	30.0 ± 9.4
	h_i [m]	1.01 ± 0.77	1.11 ± 0.76	1.32 ± 0.78	1.48 ± 0.83	1.64 ± 0.86	1.64 ± 0.84	1.60 ± 0.84	1.68 ± 0.85	1.55 ± 0.85	1.52 ± 0.85	1.35 ± 0.86	1.24 ± 0.86
	$V[km^3]$	735.8	790.9	981.0	1226.1	1494.5	1568.9	1550.7	1658.0	1500.9	1339.3	1096.4	957.8
E-Weddell	h_{fs} [cm]	23.7 ± 12.6	26.8 ± 12.6	25.5 ± 13.0	23.8 ± 11.4	22.1 ± 10.3	21.9 ± 9.8	22.3 ± 9.6	22.6 ± 9.7	24.8 ± 10.8	23.4 ± 10.8	21.9 ± 10.7	23.7 ± 11.3
	h_{fi} [cm]	7.3 ± 9.8	8.5 ± 9.8	9.2 ± 9.9	9.2 ± 8.2	8.8 ± 7.9	8.7 ± 7.9	8.9 ± 7.9	9.1 ± 7.9	9.2 ± 8.2	7.9 ± 8.3	6.4 ± 8.1	6.9 ± 8.5
	h_s [cm]	16.5 ± 7.7	19.3 ± 8.6	16.2 ± 6.7	14.4 ± 6.1	12.7 ± 5.0	12.6 ± 4.9	12.8 ± 5.2	13.0 ± 5.2	15.7 ± 6.5	15.6 ± 6.6	15.4 ± 7.0	17.1 ± 7.0
	h_i [m]	0.92 ± 0.72	1.05 ± 0.74	1.10 ± 0.65	1.09 ± 0.61	1.05 ± 0.59	1.04 ± 0.60	1.06 ± 0.62	1.08 ± 0.64	1.11 ± 0.69	0.99 ± 0.69	0.86 ± 0.69	0.91 ± 0.69
	$V[km^3]$	620.6	447.0	724.2	1402.6	2430.2	3595.9	4709.5	5434.0	5755.3	4849.9	3485.5	1661.9
Indian	h_{fs} [cm]	39.9 ± 19.1	42.2 ± 18.0	39.2 ± 17.9	31.0 ± 14.0	25.0 ± 11.7	24.9 ± 11.0	24.2 ± 11.2	22.8 ± 11.1	22.5 ± 10.8	21.9 ± 10.9	21.5 ± 10.9	28.1 ± 15.8
	h_{fi} [cm]	16.1 ± 15.1	16.3 ± 15.1	15.2 ± 15.0	11.1 ± 10.3	9.6 ± 9.6	9.1 ± 8.7	8.7 ± 8.7	8.2 ± 8.4	7.7 ± 8.0	7.1 ± 8.1	6.7 ± 8.4	10.2 ± 12.0
	h_s [cm]	25.7 ± 9.4	28.4 ± 8.2	26.6 ± 8.2	20.8 ± 8.4	15.3 ± 5.7	15.7 ± 6.1	15.3 ± 6.2	14.1 ± 6.6	14.6 ± 6.8	14.4 ± 6.6	14.6 ± 7.0	18.5 ± 9.1
	h_i [m]	1.66 ± 0.96	1.73 ± 0.98	1.61 ± 0.92	1.32 ± 0.77	1.13 ± 0.67	1.11 ± 0.65	1.07 ± 0.64	1.00 ± 0.61	0.96 ± 0.62	0.91 ± 0.62	0.87 ± 0.65	1.16 ± 0.81
	$V[km^3]$	480.3	251.1	259.8	693.5	1105.2	1758.9	2446.9	2860.5	3100.9	2945.6	1835.1	814.2
Pacific	h_{fs} [cm]	57.8 ± 33.5	60.8 ± 31.8	56.5 ± 30.7	50.8 ± 28.9	36.8 ± 21.7	35.3 ± 18.2	35.4 ± 17.8	34.4 ± 19.1	35.7 ± 19.2	35.1 ± 17.8	37.9 ± 21.6	45.4 ± 25.1
	h_{fi} [cm]	21.4 ± 22.6	22.8 ± 21.7	20.8 ± 20.3	18.0 ± 17.1	14.1 ± 15.4	13.2 ± 12.8	12.9 ± 12.8	12.7 ± 13.4	13.0 ± 13.1	12.5 ± 12.7	13.2 ± 14.7	16.5 ± 17.3
	h_s [cm]	41.1 ± 19.6	44.5 ± 19.6	41.8 ± 20.1	37.5 ± 19.9	24.8 ± 11.8	24.0 ± 10.5	24.3 ± 9.4	23.4 ± 10.9	24.8 ± 12.0	25.0 ± 10.7	27.4 ± 13.0	32.7 ± 14.3
	h_i [m]	1.87 ± 1.06	1.96 ± 1.09	1.84 ± 1.06	1.74 ± 0.99	1.42 ± 0.86	1.42 ± 0.83	1.42 ± 0.82	1.36 ± 0.82	1.40 ± 0.83	1.36 ± 0.82	1.41 ± 0.89	1.64 ± 0.97
	$V[km^3]$	751.7	526.2	556.0	1068.6	1307.5	1755.0	1996.9	2117.4	2206.6	2048.2	1386.7	947.0
Basin	h_{fs} [cm]	32.0 ± 20.4	34.7 ± 20.2	33.5 ± 19.3	30.1 ± 17.6	27.4 ± 15.3	26.9 ± 14.8	26.6 ± 14.2	26.8 ± 15.3	28.5 ± 16.3	27.2 ± 15.4	26.2 ± 15.3	28.9 ± 16.9
	h_{fi} [cm]	10.1 ± 13.2	11.2 ± 13.2	12.0 ± 12.3	11.1 ± 10.6	10.3 ± 9.7	10.1 ± 9.5	10.1 ± 9.4	10.2 ± 9.6	10.3 ± 9.8	9.2 ± 9.5	8.0 ± 9.4	8.7 ± 10.7
	h_s [cm]	23.6 ± 13.0	25.8 ± 12.8	23.2 ± 12.9	20.0 ± 12.4	17.6 ± 10.3	17.1 ± 9.9	16.9 ± 9.7	17.0 ± 10.7	19.1 ± 11.8	18.9 ± 11.3	19.2 ± 11.6	21.6 ± 12.1
	h_i [m]	1.14 ± 0.85	1.25 ± 0.87	1.32 ± 0.81	1.25 ± 0.75	1.18 ± 0.71	1.17 ± 0.70	1.16 ± 0.70	1.17 ± 0.71	1.18 ± 0.74	1.09 ± 0.73	0.99 ± 0.74	1.06 ± 0.78
	$V[km^3]$	3279.8	2425.7	3348.9	6569.6	9975.9	13447.7	16531.2	18579.0	19385.8	17113.3	12434.5	6921.4

Table 5.2: July 2010 - October 2020 monthly mean values and standard deviations (when applicable) of Antarctic sea ice physical properties, given regionally and basin-wide. Properties include snow freeboard (h_{fs}), ice freeboard (h_{fi}), snow depth (h_s), ice thickness (h_i), and ice volume (V).

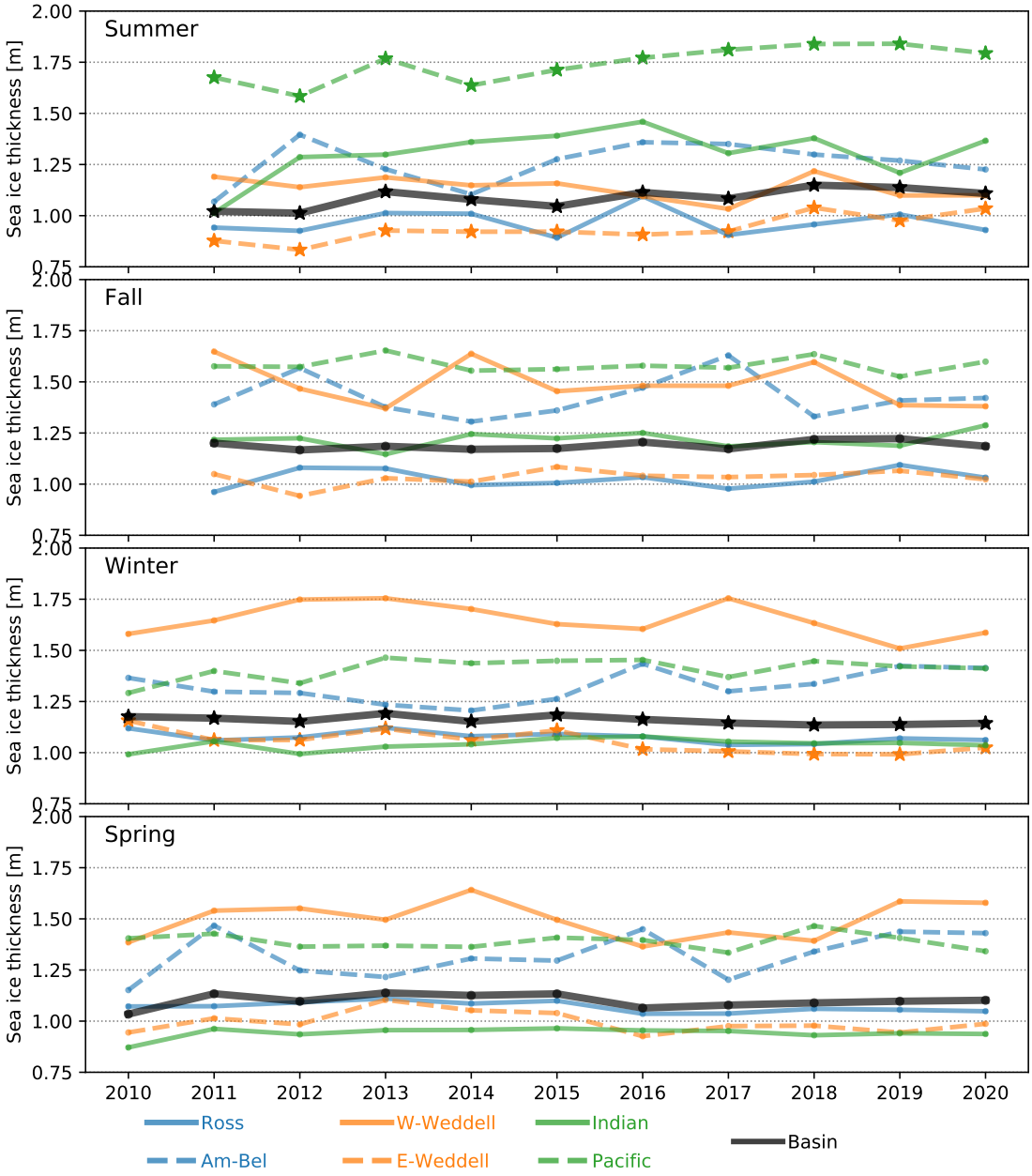

Figure 5.19: Time series of season-average sea ice thickness from 2010-2020. Each plot shows a different season, while each line represents a single region. The dark black line shows the pan-Antarctic average. Lines with stars as markers denote time series with statistically significant trends in Table 5.3.

Hochberg procedure is used with an FDR of 10% to decrease the number of false positives due to multiple tests. Bold values in Table 5.3 reject the null hypothesis that there is no trend in the data, and are statistically significant at the 97% level or better. Regions and seasons with statistically significant trends are also denoted with stars as markers for individual years in Fig. 5.19.

Statistically significant trends in ice thickness between 2010 and 2020 are found to occur only in the summer and winter seasons. The Eastern Weddell and Pacific sectors show summer thickness trends of 1.8 and 2.1 cm/yr, respectively, while basin-wide shows a statistically significant trend of 1.1 cm/yr over this period. In the winter, only the Eastern Weddell sector and basin-wide show statistically significant trends of -1.2 and -0.4 cm/year, respectively. This result suggests that there is a general thickening of summer sea ice basin-wide and a general thinning of winter sea ice basin-wide. The magnitudes of these trends are much lower than basin-wide trends observed in the Arctic (Kwok and Cunningham, 2015).

5.4.5.2 Spatial patterns of trends in sea ice thickness

To further investigate trends in sea ice thickness, trend maps were created that show the change in thickness between 2010-2020 for each 25 km grid cell basin-wide. Like in Fig. 5.19, a linear least-squares regression is applied to the time series of each grid cell, and trends are only computed if a respective grid cell contains at least four years of data. To reduce noise in the trend data, sea ice thickness maps are first smoothed with a 5x5 grid cell Gaussian kernel filter, which corresponds to an

Season		Sector Ross	Am-Bel	W. Weddell	E. Weddell	Indian	Pacific	Basin
	Ice thickness trend (cm/yr)	0.03	1.12	-0.72	**1.78**	1.69	**2.15**	**1.14**
	p (q) value	.96 (.1)	.34 (.09)	.24 (.07)	**.002 (.01)**	.24 (.06)	**.007 (.03)**	**.01 (.04)**
Summer	Ice volume trend (km^3/yr)	-24.3	-0.2	-4.9	-134.7	-46.7	13.9	-204.7
	p (q) value	.61 (.06)	.99 (.1)	.76 (.09)	.14 (.01)	.18 (.04)	.64 (.07)	.18 (.03)
	P_{MC} (%)	57	11	73	49	41	66	48
	Ice thickness trend (cm/yr)	0.24	-0.03	-1.25	0.43	0.35	-0.06	0.29
	p (q) value	.66 (.07)	.98 (.1)	.28 (.03)	.33 (.04)	.45 (.06)	.89 (.09)	.22 (.01)
Fall	Ice volume trend (km^3/yr)	-45.1	2.7	-13.0	-107.0	**-40.3**	-23.6	-225.6
	p (q) value	.31 (.09)	.93 (.1)	.18 (.06)	.16 (.04)	**.003 (.01)**	.26 (.07)	.09 (.03)
	P_{MC} (%)	21	56	75	34	5	45	14
	Ice thickness trend (cm/yr)	-0.48	1.04	-0.75	**-1.24**	0.39	0.74	**-0.37**
	p (q) value	.06 (.04)	.15 (.07)	.36 (.1)	**.005 (.01)**	.14 (.06)	.16 (.09)	**.03 (.03)**
Winter	Ice volume trend (km^3/yr)	**-74.2**	-44.0	-13.8	-18.2	**-61.0**	4.3	**-216.4**
	p (q) value	**.03 (.04)**	.12 (.06)	.36 (.07)	.67 (.09)	**.02 (.03)**	.88 (.1)	**.01 (.01)**
	P_{MC} (%)	24	61	32	49	54	40	2
	Ice thickness trend (cm/yr)	-0.44	1.48	0.27	-0.40	0.18	-0.10	-0.01
	p (q) value	.05 (.01)	.16 (.03)	.77 (.07)	.45 (.04)	.49 (.05)	.79 (.09)	.97 (.1)
Spring	Ice volume trend (km^3/yr)	-59.4	7.1	-6.1	-13.2	-39.8	9.1	-105.7
	p (q) value	.06 (.01)	.83 (.1)	.76 (.07)	.77 (.09)	.10 (.03)	.73 (.06)	.40 (.04)
	P_{MC} (%)	38	14	13	25	5	59	41

Table 5.3: Seasonal sea ice thickness and volume trends by region. Statistics of significance for each trend are given, where p- and q-values are from a Wald test of the null hypothesis (that the trend is zero) controlling for a FDR of 10%. Bold values indicate statistically significant trends at the p<.05 level (when controlling for a FDR of 10%). P_{MC} values give the percent of Monte Carlo-simulated trends with slopes greater than the observed trend, as described in Section 5.4.5.

effective size of 125x125 km (Kurtz and Markus, 2012). The seasonal trend maps are given in Fig. 5.20. One can initially see lots of variation in the trends around the continent in all seasons, however, some areas exhibit larger magnitude trends. In the summer and fall, most of the Western Weddell sector exhibits a strong thinning of over 5 cm/yr, which is closer to zero in winter and spring. In winter, there is a large area of thinning predominantly in the Eastern Weddell sea, corresponding to the statistically significant regional trend observed of -1.2 cm/yr on average (Table 5.3). As clearly seen in Fig. 5.20, the average winter thinning in the Eastern Weddell of 1.2 cm/yr is greater in some locations, with trends as large as -5 cm/yr found. On average, the summertime ice thickness trend is greater in magnitude than the other seasons. It is important to note that in these trend maps, even though many grid

cell trends are individually significant at the >95% level ($P< .05$), correcting for the impact of multiple testing and adjusting to control the FDR to 10% results in no statistically significant trends at the grid cell level.

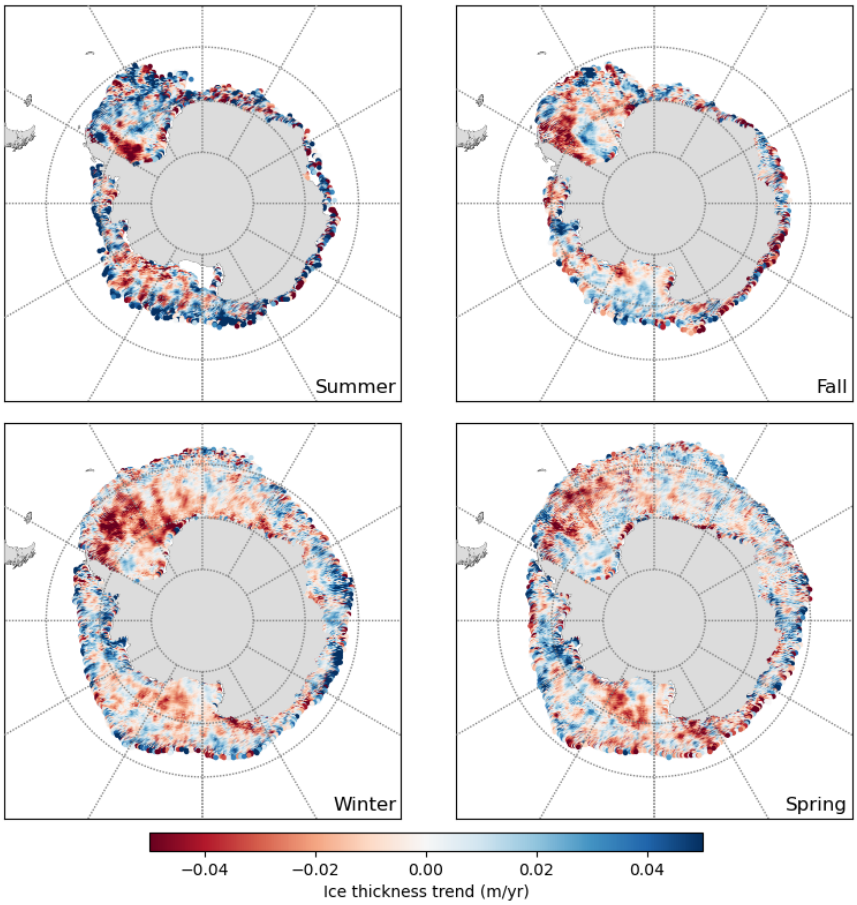

Figure 5.20: Seasonal ice thickness trend maps over the CryoSat-2 mission 2010-2020. Each grid cell value shows the slope of the regression line fit to the time series of thickness from that respective grid cell. Grid cell trends are only computed if at least four years of data exist.

5.4.5.3 Seasonal sea ice volume trends

Figure 5.21 shows the same as Fig. 5.19, but for sea ice volume instead of thickness. Much like in Fig. 5.19, most regions show little overall change over time, with the Eastern Weddell and Ross sectors showing more year-to-year variability

than other regions (likely due to their larger area). Once again, stars in Fig. 5.21 represent statistically significant trends in sea ice volume, which are provided as bold values in Table 5.3. A Benjamini-Hochberg FDR of 10% is used to remain consistent with the thickness trend results. Statistically significant trends in volume occur only in the Austral fall and winter seasons, with both recording a general thinning. The ice volume trend in the Indian Ocean sector in fall shows a thinning of around 40 km^3/yr. In the winter, statistically significant trends are found in the Ross Sea, Indian Ocean, and basin-wide, with sea ice volume trends of -74, -61, and -216 km^3/yr, respectively.

5.4.5.4 Impact of interannual variability on observed trends

While the bold values in Table 5.3 show trends that are statistically significant, they do not rule out trends that may have arisen simply due to interannual variability in the sea ice and snow density terms that make up the thickness calculation (Eqn. 5.2). If the interannual variability in the density terms is small, then higher confidence can be placed in the observed trends. If there is higher interannual variability in the density terms, however, there is a chance that the observed trends are simply due to variability in the sea ice and snow density. If that is the case, then trends with magnitudes greater than the variations due to density interannual variability should be given higher confidence than those with trends smaller than those due to interannual variability. To test this hypothesis, the procedure proposed in Kurtz and Markus (2012) is applied, which runs Monte Carlo simulations to calcu-

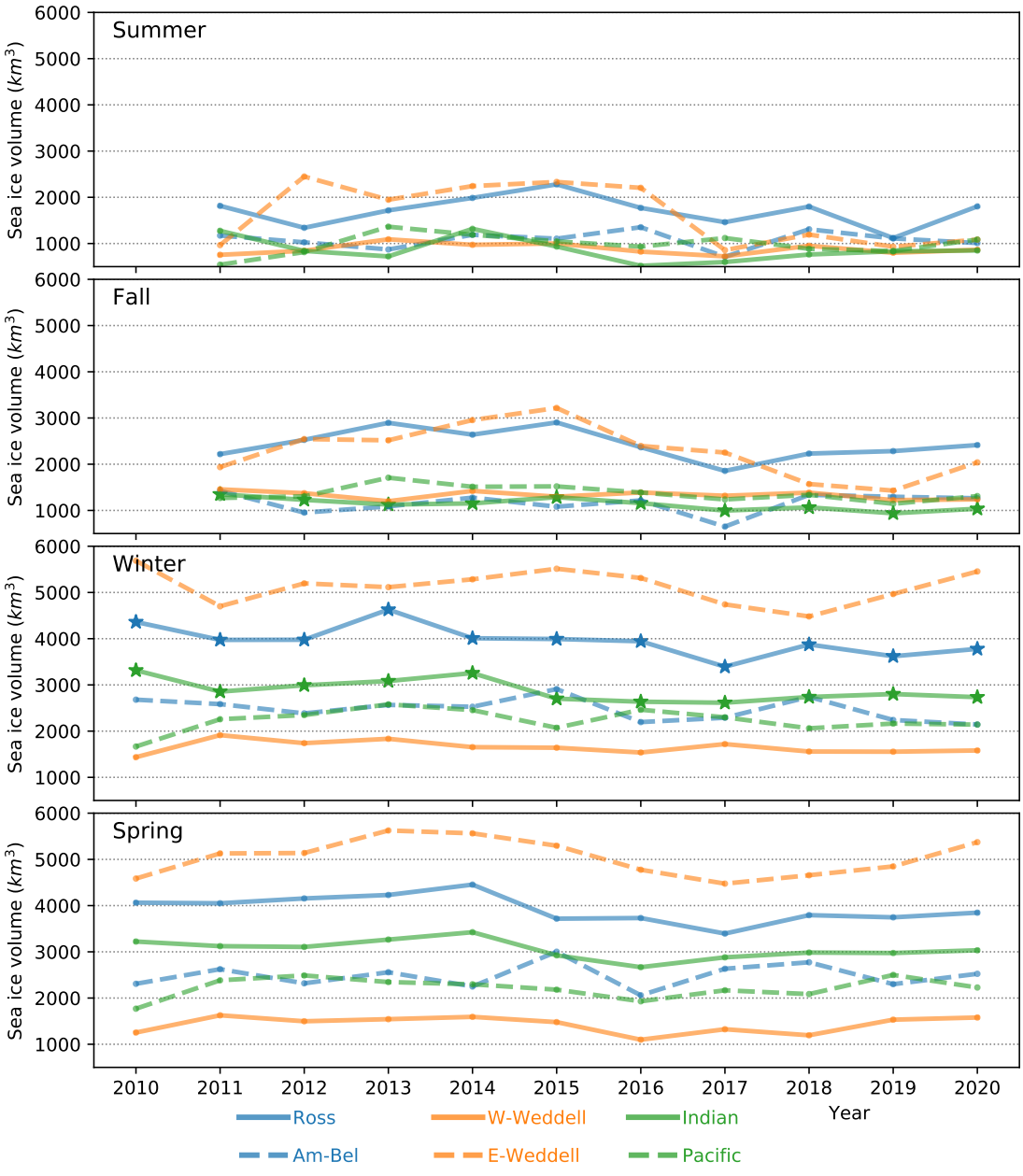

Figure 5.21: As in Fig. 5.19 but for sea ice volume.

late sea ice thickness trends assuming normally distributed interannual variabilities of sea ice and snow densities. A null hypothesis is prescribed that assumes there is no trend in the data and that any observed trend is simply due to the interannual variability in the sea ice and snow density terms. Values of 50 kg/m^3 and 20 kg/m^3 are chosen as the interannual variability of snow and sea ice, respectively. In this study, 10000 simulations were ran, with each simulation calculating a seasonal trend over the 10+ year time series with random density values picked from the assumed distributions. Then, the percentage of simulated trends with magnitudes greater than the observed trend for a given season is computed (P_{MC} in Table 5.3). Lower values of P_{MC} reject the null hypothesis and suggest higher confidence that the observed trends are not due to interannual variabilities of the density terms. Larger values of P_{MC} suggest that there is a greater chance that the observed trend is only due to the density variability.

As shown in Table 5.3, there is a >10% chance that many of the statistically significant (bold) observed trends are due to the interannual variability in sea ice density terms and not due to actual trends in sea ice thickness. However, the statistically significant negative trend in winter sea ice thickness (volume) of -0.37 cm/yr (-216 km^3/yr) also is significant at the $P_{MC} < .05$ level and suggests that the observed trend is likely not due to sea ice and snow density variability. This result provides further confidence in this observed basin-wide thinning of wintertime Antarctic sea ice. The fact that most values of P_{MC} are greater than 10% suggests that the variation in sea ice and snow density can contribute to the thickness distribution, and that more information on the seasonality and regionality of the density

terms would be helpful when estimating sea ice thickness from satellite altimetry.

5.5 Future work: Reconciling the laser-radar altimetry thickness record

With a 10+ year time series of Antarctic sea ice thickness from CryoSat-2, one can start connecting the satellite altimetry-based record of thickness that began with ICESat from 2003 - 2008 (Kurtz and Markus, 2012) and continues with ICESat-2 (2018-present). Figure 5.22 shows a full time series with thickness estimates from all three instruments (red from ICESat, black from CryoSat-2, and blue/green from ICESat-2). In Fig. 5.22, the dashed red and solid black lines indicate the thickness results from Kurtz and Markus (2012) and this work, respectively. There is a clear bias brought on by the zero ice freeboard assumption used in Kurtz and Markus (2012). To better align the time series, a dashed black line is added which shows the CryoSat-2 thickness under a zero ice freeboard assumption and a solid red line is added showing ICESat thickness calculated using the CryoSat-2 snow depth monthly climatology (Fig. 5.11). This provides two different estimates of thickness from each satellite. ICESat-2 data are shown from KK20 (green) - which include the range of values given in Fig. 5.16 and a zero ice freeboard assumption - as well as a thickness value calculated using the ATL10 freeboard data (blue) when applying the CryoSat-2 snow depth monthly climatology (solid) and a zero ice freeboard assumption (dashed).

The overall time series shows thickness values in the same general range: zero ice freeboard-derived thicknesses (h_{i-0ifb}) usually between 0.6 and 1.1 m, and snow

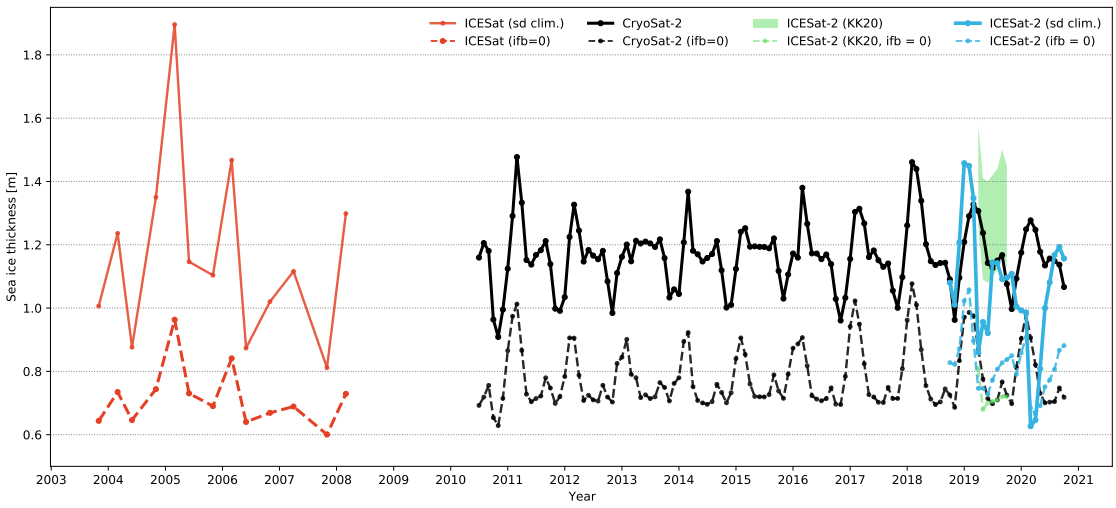

Figure 5.22: Combined Antarctic sea ice thickness time series from ICESat (Kurtz and Markus 2012, red), CryoSat-2 (this method, black), and ICESat-2 (Kacimi and Kwok 2020, green and ATL10, blue). Solid lines are computed from CryoSat-2 snow depths, while dashed lines are computed using the zero ice freeboard assumption. Monthly CryoSat-2 snow depths were used to compute CryoSat-2 thickness, while an average snow depth climatology was used to compute ICESat and ICESat-2/ATL10 thickness.

depth-derived thicknesses ($h_{i-total}$) usually between 0.8 and 1.6 m, with some outlying data points. There are, however, some dissimilarities between data sources that should be the work of future study. For one, CryoSat-2 data appear to show small interannual variability, especially in h_{i-0ifb}, while the ICESat thickness tends to vary more year-to-year. This is especially apparent in the ICESat $h_{i-total}$, where the range is much larger than is seen in CryoSat-2 and ICESat-2. There is a large discrepancy in $h_{i-total}$ from CryoSat-2 and ICESat-2 in early 2020, which was explored in the snow freeboard data in Chapter 4 and thought to be related to the initialization of the CryoSat-2 waveform model. Despite the differences, it is encouraging to see general agreement in the overall mean values of $h_{i-total}$.

The clear discrepancy between the two types of thicknesses - h_{i-0ifb} and $h_{i-total}$

- estimated here complicates the current understanding of the pan-Antarctic thickness distribution. With these measurements alone, it is tough to know which estimate technique produces the "correct" sea ice thickness estimate basin-wide. Likely, one can think of h_{i-0ifb} as a lower bound on the actual thickness, given the assumptions of the snow depth. Additionally, as mentioned in KK20, uncertainties in the satellite-derived thickness can lead to $h_{i-total}$ being treated as more of an upper bound on the actual thickness. Therefore, the "true" sea ice thickness could be somewhere between these two estimates (though some studies suggest it could be even higher; Williams et al. 2015). Reliable, independent, and widespread validation data are crucially needed to better uncover the absolute thickness distribution from Antarctic sea ice.

It is important to note that no work went into reconciling the data shown in Fig. 5.22, and many important points must first be considered before trying to relate these data statistically or with more confidence. For one, the differences in geometric sampling could have substantial impacts on the freeboard - and therefore the thickness - distributions. This effect was discussed in Chapter 4, but would be further complicated by adding in another sensor (ICESat) with a different footprint size. Also, the frequency differences between radar and laser must be taken into account when assessing the data, as the varying responses from sea ice and heterogeneous surfaces can impact the surface type classification, which can bias the freeboard retrievals (Tilling et al., 2019) and influence the thickness.

A final difficulty relates to validating measurements and comparing them to each other and to independent datasets. No temporal overlap occurred between

ICESat and CryoSat-2, which increases the difficulty in trying to reconcile the measurements. Instead, independent measurements must be used that existed for both platforms. While these independent measurements spanning ICESat and CryoSat-2 operation exist in the Arctic (e.g. the WHOI Beaufort Gyre moorings, WHOI 2018), they do not exist for Antarctic sea ice. Therefore some ICESat/CryoSat-2 comparisons should be done for the Arctic that could enhance confidence in reconciling Antarctic observations. Luckily, ICESat-2 and CryoSat-2 are currently in coincident operation. The sea ice altimetry community must utilize this important temporally-overlapping time period of two-plus years of data (and counting) to better understand the biases that may exist between the two instruments and be able to reconcile freeboard and thickness measurements between them, enabling a longer time series of Antarctic sea ice thickness.

5.6 Conclusions

In this chapter, estimates of Antarctic sea ice freeboard, snow depth on sea ice, and sea ice thickness derived from CryoSat-2 have been shown. The physical model and waveform-fitting process introduced in previous chapters was applied to all CryoSat-2 data over the Southern Ocean between July 2010 and October 2020, and results were aggregated into monthly and seasonal-averaged maps. Basin-averaged monthly ice freeboards ranged between 8 cm and 12 cm, showing good agreement with ice freeboards derived in KK20. Comparisons with P18 showed that their threshold retracking method records an ice freeboard much thicker than

this CryoSat-2 method, which suggests more confidence in the hypothesis that this physical retracker, when accounting for attenuation of the radar pulse by the snow layer, can better track the actual snow-ice interface over Antarctic sea ice than 50% threshold retrackers. This finding motivates the retrieval of snow-ice interface elevation and the estimation of snow depth from CryoSat-2.

Snow depths derived from this method showed a few centimeter high bias when compared to that from KK20, though the spatial patterns tended to match well. Monthly means range from ∼17 to 26 cm, and show stark gradients in the spatial patterns that result in multi-modal distributions. Comparisons with independent snow depth measurements from OIB Snow Radar and AWI snow buoys lacked substance, and more so highlighted difficulty with comparing point and high resolution airborne measurements to satellite data. Snow depth and freeboard results from summer months - especially in the Western Weddell sector - showed puzzling results involving thin freeboards/snow depths and irregular distributions compared to other seasons and regions. This was hypothesized to be caused by various processes observed in summer months, including surface melt (Markus and Cavalieri, 1998) and ice submergence (Haas et al., 2001), which could produce erroneous returns and potentially bias the freeboard and thickness retrievals. The lack of coincident data from any source in Austral summer limits the potential for validation, and therefore this season should surely be the subject of future work.

The retrieved freeboard and snow depth data were then combined to estimate sea ice thickness. Spatial patterns appeared as expected (similar to that from KK20 and Kurtz and Markus 2012), and had mean values ranging between 0.99 and 1.32

m monthly. These values are likely on the thick side, as one would expect thinner ice during certain months of new ice growth. The retrieved thicknesses tend to agree with - and be slightly thinner than - KK20, who also thought their thickness values were thicker than expected. Nevertheless, a time series from 2010 to 2020 was constructed that shows some interannual variability, but highlights a consistent seasonal cycle and range of values. Multiplying the retrieved thicknesses by the monthly average areal sea ice coverage provides an estimate of sea ice volume, which is given as a time series in Fig. 5.17. Basin-wide volume ranges substantially within a year between $\sim$2500 and over 20000 km^3.

Trends in sea ice thickness and volume were uncovered by linear regressions to mean values of each season and region across the 10+ year time series. Trends were found to be statistically significant if the Wald p-value statistic was less than the q-value statistic, which was calculated using the Benjamini-Hochberg method to adjust for multiple testing and to limit the FDR to 10%. A significant basin-average thickening of 1.1 cm/yr was found during Austral summer, while a basin-wide thinning of 0.4 cm/yr was found to occur in Austral winter. Similarly, a basin-wide negative trend in sea ice volume was found in the Austral winter of -216 km^3/yr. Other regions showed statistically significant positive thickness trends in summer and negative thickness and volume trends in winter. When using a Monte Carlo method to test the percentage of trends that may have occurred due to interannual variability of sea ice and snow density alone, the basin-average thinning shown in winter months was found to be significant at the $P_{MC} < .05$ level, suggesting more confidence that the trend is physically-realistic and not simply due to density

variability.

Overall, this work has shown a first attempt at producing a decade-long time series of Antarctic sea ice thickness and volume from CryoSat-2, complimenting the Antarctic sea ice thickness record that began with ICESat (Kurtz and Markus, 2012) and continues with ICESat-2 (Kacimi and Kwok, 2020). It is clear that more independent validation measurements are required to better get a sense of the "true value" of Antarctic sea ice thickness, which would help in combining estimates from these three instruments into a cohesive time series. Additionally, future work is necessary to establish biases between the instruments and reconcile thickness estimates in light of the geometric sampling and frequency-related discrepancies. The current temporal overlap between CryoSat-2 and ICESat-2 observations is invaluable for comparison and validation, and would be even more beneficial provided the CRYO2ICE campaign can be optimized for the Southern Hemisphere (Chapter 4). Reconciling these observations will lead to a better understanding of recent changes in Antarctic sea ice thickness and volume.

Chapter 6: Application to Arctic Sea Ice Retrievals

While this dissertation is primarily focused on Antarctic sea ice, this chapter briefly explores the possibility of applying the techniques developed in previous chapters to Arctic sea ice, in order to test the algorithm over different sea ice types and conditions and to make use of the prevalent ground- and aircraft-based validation data that have been collected in the Arctic.

6.1 Introduction

As discussed in Chapter 1, Arctic and Antarctic sea ice can differ substantially in their formation pathway, geographical constraints, and overall thickness and snow cover. For this work, the most notable difference is the thicker snow cover on Antarctic sea ice, which acts to complicate radar returns of the snow-ice interface by depressing the ice closer to the sea level and enabling processes such as flooding, wicking, and refreezing to occur (Ackley et al., 2020; Maksym and Jeffries, 2000; Massom et al., 2001). These processes can result in the dominant scattering surface at Ku-band frequencies originating from above the snow-ice interface (Willatt et al., 2010). This obfuscation of the snow-ice interface to radars makes collecting reliable snow depth and ice freeboard validation data over Antarctic sea ice extremely diffi-

cult, which is why few remotely-sensed datasets currently exist (Kacimi and Kwok, 2020; Paul et al., 2018). Even the largest cryosphere-focused airborne campaign ever, NASA's OIB, has no official ice freeboard or snow depth data products over Antarctic sea ice, despite flying more than 35 dedicated Antarctic sea ice flights (Kurtz et al., 2015). Analysis in the previous chapter was hindered by the lack of validation data over Antarctic sea ice, and therefore only generalized comparisons between satellite products could be made.

In the Arctic, however, a few key features benefit satellite product validation. For one, the comparatively thicker sea ice and thinner/dryer snow cover tends to allow for more widespread Ku-band penetration to the snow-ice interface as compared to Antarctic sea ice (Willatt et al., 2011, 2010). This fact instills more confidence in the Ku-band returns and allows for basin-wide ice freeboard estimation from CryoSat-2 (Kurtz et al., 2014; Kwok and Cunningham, 2015; Laxon et al., 2013; Ricker et al., 2014; Tilling et al., 2018). For the same reason, more airborne validation data on snow depth and ice freeboard exist with a higher confidence in the retrievals (Farrell et al., 2012; Kurtz and Farrell, 2011; Kurtz et al., 2013). In addition to the more "favorable" snow cover, the Arctic tends to be more easily accessible than the Antarctic, and therefore more ground-based measurements - whether from moored instruments, buoys, or field campaigns - tend to exist. Finally, the orbital inclinations of current satellite altimeters ($\sim$92°, Markus et al. 2017; Wingham et al. 2006) allows for a greater density of satellite tracks to occur over Arctic sea ice than Antarctic, allowing for greater coverage and more overall measurements. These facts make performing validation of satellite altimeter-based sea ice thickness products

easier and more reliable in the Arctic compared to the Antarctic.

In this chapter, the methods to retrieve Antarctic sea ice properties from CryoSat-2 (outlined in previous chapters) are applied to data over Arctic sea ice. This is done for a few key reasons. First, it capitalizes on the advantages outlined above, utilizing the relatively abundant validation data from which to make comparisons. Second, it allows for the testing of this algorithm over different sea ice types and locations, to evaluate its performance under different sea ice conditions. Finally, it allows for the potential to consider global sea ice freeboard and thickness measurements, and be able to relate trends observed in Antarctic sea ice to those observed in the Arctic by using the same instrument and methodology globally. This chapter will first outline the minor - though necessary - adjustments made to the retrieval process to analyze Arctic data (Section 6.2.1). Section 6.2.2 will show results and comparisons to NASA's ICESat-2. Then, this chapter will compare snow depth and ice freeboard retrievals - two parameters lacking comparisons in the previous chapter - to independent measurements from the airborne OIB campaign (Section 6.3) and the ground-based MOSAiC Expedition (Section 6.4). Then, some potential uses for a decade-long time series of CryoSat-2 snow depth data are proposed (Section 6.5). Finally, this chapter concludes with a summary of these Arctic sea ice retrievals and potential future work (Section 6.6).

6.2 CryoSat-2 retrievals in the Arctic

The CryoSat-2 retrieval algorithm outlined in Chapters 3 through 5 was applied to four months of data over Arctic sea ice: March 2017, April 2018, and March and April 2020. These months were chosen to best correspond with available comparison datasets. This section outlines small modifications made to the retrieval algorithm and briefly discusses results and comparisons to data from ICESat-2.

6.2.1 Retrieval modifications

In order to process CryoSat-2 data collected over the Arctic, some minor adjustments had to be made to the retrieval process. The first (and largest) modification was to change the initialization values used in the waveform model. For the Antarctic, a combined ICESat/ICESat-2 snow freeboard climatology was used as the initial guess for the snow depth parameter, invoking the zero ice freeboard assumption due to the lack of pan-Antarctic snow depth on sea ice information (Chapter 4; Kurtz and Markus 2012). While a similar ICESat-based climatology from Arctic sea ice could have be constructed and used in this work, it is known that a zero ice freeboard assumption is less valid in the Arctic (Maksym and Jeffries, 2000). Additionally, there are more snow depth models and reanalysis products available as compared to the Antarctic (e.g. Liston et al. 2018; Petty et al. 2018). Therefore, modeled snow depth results are instead used for the snow depth parameter initialization.

The model output used in this study is the NASA Eulerian Snow on Sea

Ice Model (NESOSIM, Petty et al. 2018). NESOSIM is a 3-D snow budget model that uses ancillary data (such as reanalysis precipitation, passive microwave sea ice concentration, and satellite-derived sea ice drift) to derive the snow depth and density throughout the accumulation season (August - April). For each CryoSat-2 floe-type waveform, a NESOSIM snow depth value is obtained corresponding to the day, latitude, and longitude of the waveform. This value is then used as an initial guess into the waveform model. The use of a model, such as NESOSIM, for parameter initialization has a number of benefits over a satellite-derived dataset. For one, the enhanced temporal coverage is far better than what can be gathered from a single altimeter. NESOSIM data are provided basin-wide at daily time steps, whereas a satellite-derived basin-scale map would require multiple weeks of data to generate and would still contain gaps in the satellite tracks that must be interpolated. Additionally, not using any ICESat-2 data in the initialization allows for completely independent comparisons, shown in Section 6.2.2. Other initialization parameters shown in Table 4.1 remain the same as shown for the Antarctic, since they have been found to represent the respective parameters on Arctic sea ice as well (Kurtz et al., 2014).

The only other modifications made relate to the map projection used and the density values assumed in the thickness calculation. All CryoSat-2 data north of 40° are processed and gridded to the 25 km NSIDC north polar stereographic grid (EPSG: 3413). The density values of snow and seawater are taken to be 320 and 1024 kg/m^3, which are the same as was used for the Antarctic but also have been used for Arctic sea ice (Kurtz et al., 2014). The sea ice density is here taken to be

900 kg/m^3, which is lower than that used for the Antarctic (917 kg/m^3). This is to account for the greater abundance of multiyear ice within the Arctic ice pack, which tends to have a lower density (Kern et al., 2015; Wadhams et al., 1992). It is acknowledged that this value is a simplification of the ice cover, and that an ice density value that varies with ice type would be more realistic. Given that this chapter is simply a feasibility study, the single value of 900 kg/m^3 is used here, while future work will incorporate an ice-type-dependant ice density value.

These density values (snow, ice, and water) are used in the calculation of thickness, following that from Chapter 5:

$$h_{i-total} = \left(\frac{\rho_w}{\rho_w - \rho_i}\right) h_{fs} + \left(\frac{\rho_s - \rho_w}{\rho_w - \rho_i}\right) h_s, \tag{6.1}$$

where $h_{i-total}$ is the ice thickness computed from the snow freeboard, h_{fs} is the snow freeboard, h_s is the snow depth, and ρ is the density of seawater (ρ_w), ice (ρ_i), and snow (ρ_s). The values for h_{fs} and h_s are found from CryoSat-2. Thickness results are shown in the next section and in comparison with MOSAiC data in Section 6.4.2.

6.2.2 Results and comparison with ICESat-2

Monthly average values for the four parameters of interest - snow freeboard, ice freeboard, snow depth, and ice thickness - are calculated for the four months of March 2017, April 2018, and March and April 2020. March 2020 is shown in Fig. 6.1 as an example month. The other months (not shown) have similar spatial

patterns to the ones observed in Fig. 6.1. Mean snow freeboard values are 36 cm (2017) and 32 cm (2020) in March and 38 cm (2018 and 2020) in April. These values parallel snow depth values, which are also lower in March (14 cm in 2017 and 12 cm in 2020) than in April (15 cm in 2018 and 16 cm in 2020). This result makes sense given the expected increase in snow accumulation from March to April (Petty et al., 2020b). Mean ice freeboard and ice thickness values are consistent across all months at around 16 cm and between 1.5 and 1.6 cm, respectively, which also makes physical sense as the sea ice growth rates tend to drop to zero between March and April (Petrich and Eicken, 2016).

The spatial pattern in the variables observed seems to be as expected, with the thickest ice north of Greenland and the Canadian Archipelago. Thinner ice is found in the Beaufort Sea and in Baffin Bay. The magnitude and pattern of sea ice thickness tends to broadly match the CPOM CryoSat-2 NRT thickness (Shepherd, 2015; Tilling et al., 2016), which is derived using the processing from Laxon et al. (2013). The most spatial variation occurs in the ice freeboard and snow depth maps, as standard deviations of the values are around 50% and 48%, respectively, of the mean values. The monthly average snow freeboard and thickness composites have standard deviations around 36% of their respective mean values.

The snow freeboard results shown above are compared against ICESat-2 snow freeboards from the same month in Fig. 6.2. Here, the ICESat-2 ATL20 data are used, which are 25 km gridded monthly mean snow freeboard values (Petty et al., 2020a). Figure 6.2 compares the monthly maps (top plots) as well as the basin-scale distribution (bottom right). One can see the similar spatial patterns in snow free-

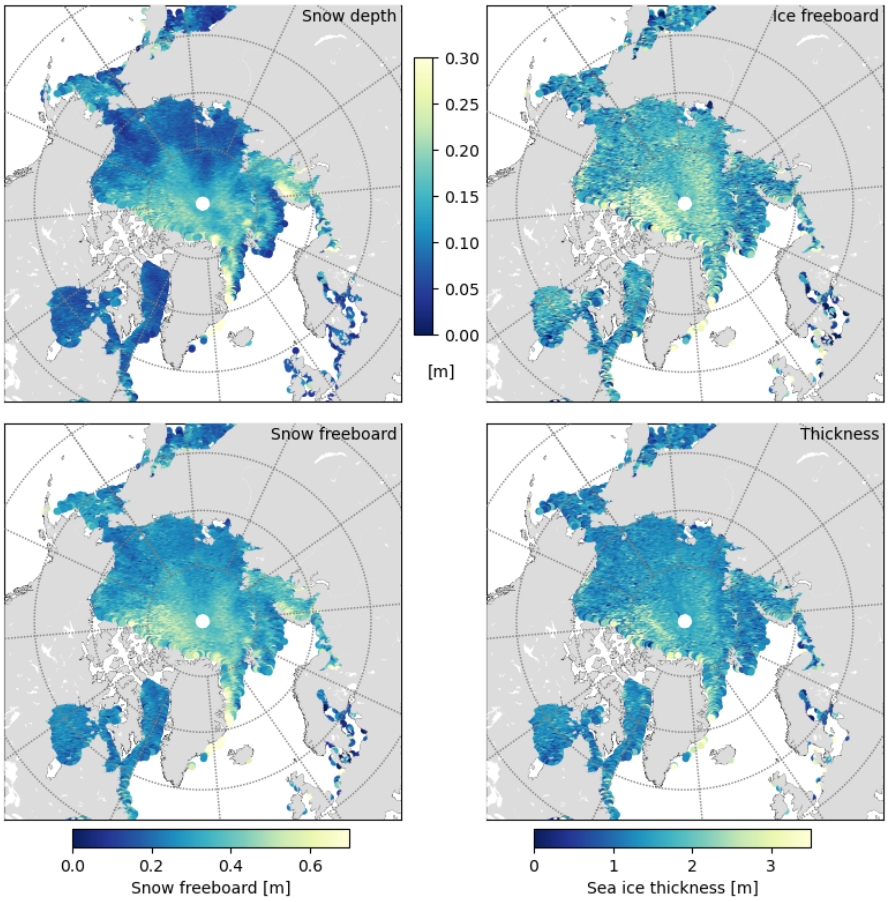

Figure 6.1: Example maps of sea ice physical properties from CryoSat-2 for the example month March 2020. They are (clockwise from top-left) snow depth, ice freeboard, sea ice thickness, and snow freeboard.

board, with both satellites showing comparable patterns of thick freeboards along the Canadian Archipelago. Similar features of thicker snow freeboards extending into the Central Arctic are also seen in both plots at around 110° E and 180° E. The thinnest snow freeboards are similarly found in the Kara Sea, the Beaufort and Chukchi Seas, and in Baffin Bay. These moderately similar patterns (r=0.55) are encouraging given the fact that this comparison is completely independent (i.e. no ICESat-2 data are used in the initialization of the CryoSat-2 model).

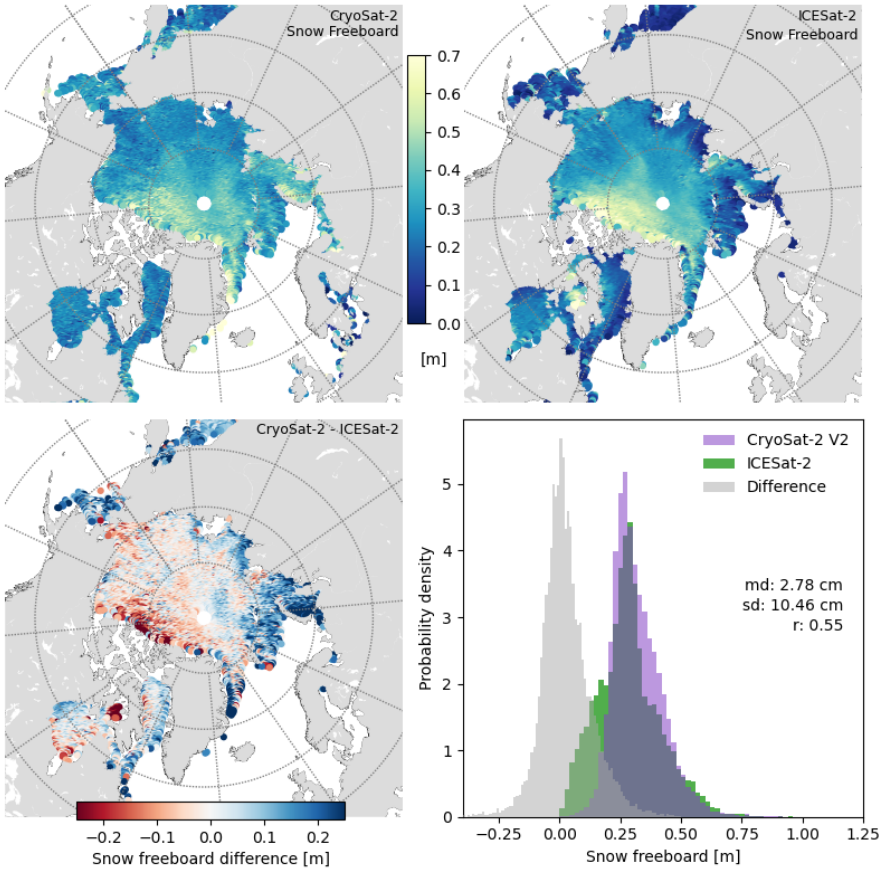

Figure 6.2: Comparison of CryoSat-2-derived snow freeboard (top left) with ICESat-2 ATL20 data (top right) from March 2020. Difference map (lower left) shows CryoSat-2 minus ICESat-2, with the distribution of differences shown as grey histogram in lower right.

Despite the similarity in the spatial patterns, there exist differences in the

magnitudes of the freeboard values. Basin-wide, ICESat-2 is about 3 cm thicker than CryoSat-2, with a standard deviation of differences over 10 cm. ICESat-2 shows a large area of snow freeboards greater than 60 cm, while CryoSat-2 shows the same area between 45 and 60 cm. The thickest freeboards from ICESat-2 located very near the coast at around 100° W are much thinner in the CryoSat-2 data. The opposite is true for regions of thinner freeboard in ICESat-2, which tend to be thinner than what is shown in CryoSat-2. This finding is similar to what was found in Chapter 4 for the Antarctic: CryoSat-2 distributions tended to be taller and narrower - recording more "average" freeboard values - while ICESat-2 was typically broader - recording more thinner and thicker values. In these Arctic distributions, CryoSat-2 is more uniform, though broader at thick values (around 40 cm) and records very few thin (<10 cm) freeboards. ICESat-2 shows a similar mode, but is broader at thin values (<25 cm), which appears to come from the peripheral seas (Fig. 6.2). It was hypothesized in Chapter 4 that the geometric sampling (i.e. footprint size) differences caused this discrepancy. Once again, an area of future work to improve this CryoSat-2 algorithm will be to try to better understand how the sampling differences between the two sensors may influence the freeboard distribution observed.

The snow freeboard comparison to ICESat-2 shown in Fig. 6.2 suggests that these CryoSat-2 snow freeboard retrievals can perform reasonably well over Arctic sea ice, capturing the general pattern seen with ICESat-2 (though not the exact magnitude). However, the real advantage of testing retrievals over Arctic sea ice comes with using validation data that are not available for Antarctic sea ice. In

the following sections, other independent data sources are used to validate the ice freeboard and snow depth retrievals from CryoSat-2.

6.3 Comparisons to airborne data: Operation IceBridge

6.3.1 OIB data

As mentioned in Chapter 1, NASA's OIB airborne campaign was the largest such cryosphere-focused mission in history. Over more than a decade, OIB made around 900 scientific flights (Merzdorf, 2020; Studinger et al., 2010), with a fair number specifically over sea ice. On these flights, a suite of instruments was used to collect information on many different sea ice characteristics. These instruments included laser scanners, nadir-pointing cameras, radars, near-infrared sensors, and others. To compare the CryoSat-2 snow depth and ice freeboard estimates to data from OIB, this study uses the Level 4 OIB Sea Ice Freeboard, Snow Depth, and Thickness Quick Look Version 1 product (Kurtz et al., 2015). This product combines laser elevation data from the ATM instrument (Studinger, 2014), radar elevation data from the OIB 2-8 GHz Snow Radar (Paden et al., 2014), and visible imagery from the Digital Mapping System (DMS) and Continuous Airborne Mapping By Optical Translator (CAMBOT) instruments (Dominguez, 2019; Studinger and Harbeck, 2019). Utilizing the difference frequencies of ATM (laser) and Snow Radar, the elevations of the air-snow and snow-ice interfaces are found using the method in Kurtz et al. (2013). The ATM data combined with imagery from DMS and CAMBOT are used to discriminate between surface types, find leads, and esti-

mate the SSH used in the freeboard calculation.

Data in the level 4 quick look product are averaged to a 40 m along-track footprint and are limited in the across-track direction to a nominal width of 14.5 m, dictated by the Snow Radar footprint (Kurtz et al., 2015). Here, OIB snow depth and ice freeboard data from a given month are gridded to 25 km and are compared with the monthly average values from CryoSat-2. This is done to reduce noise in the data through averaging, and to increase the number of comparison points (since data collected near-contemporaneously, such as on the same day, almost never overlap). OIB data from eight flights in March 2013 and seven flights from April 2018 are analyzed.

6.3.2 Results

Figure 6.3 shows a comparison between OIB Level 4 ice freeboard and CryoSat-2-derived ice freeboard from March 2017. The top plots show the CryoSat-2 monthly average freeboard map overlayed with gridded OIB ice freeboard measurements (top left), as well as a difference map for each corresponding overlapping grid cell (top right). Bottom plots show a distribution of all overlapping grid cells, as well as a distribution of the differences. Mean differences CryoSat-2 minus OIB are within -0.5 cm, with a standard deviation of differences of over 8 cm.

Similarities exist in the spatial pattern, with the western-most OIB flights (near the Beaufort Sea) recording thinner freeboards and flights north of Ellesmere Island recording the thickest freeboards - a pattern also seen in the CryoSat-2 data.

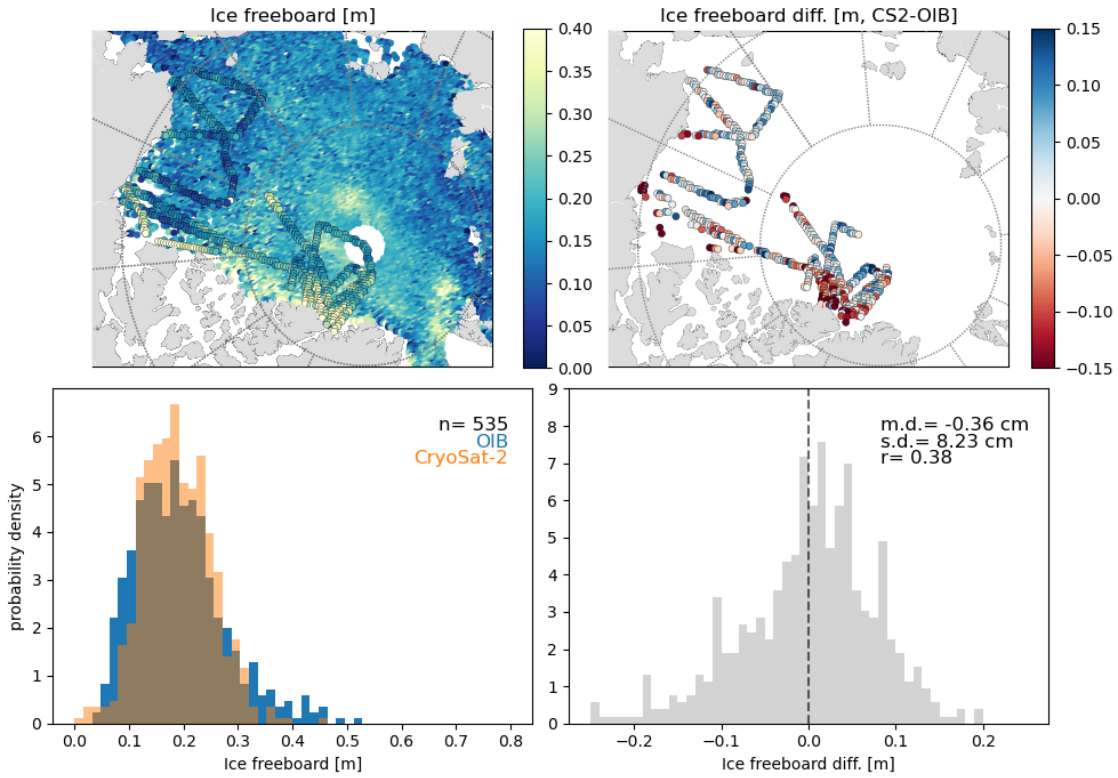

Figure 6.3: Comparison of CryoSat-2 ice freeboard with OIB for March 2017. Basin map shows CryoSat-2 data, while flight paths show OIB data. Differences are given in top right. Probability distributions (bottom) show data from just the coincident grid cells and provide the mean difference (m.d.), standard deviation of differences (s.d.) and correlation (r) as measures of agreement.

However, as was seen in the ICESat-2 comparisons, the magnitude is not captured as well by CryoSat-2 as OIB tends to record thicker ice freeboards than CryoSat-2 in areas of expected thick freeboards. This is evident in the difference map, where the largest magnitude differences seen are the large negative differences (OIB is thicker) near Ellesmere Island. Despite the magnitude differences, the distributions taken from the 525 overlapping grid cells show similar shapes, with CryoSat-2 being more slightly more symmetric and OIB being slightly more skewed-thin.

A similar result is found when comparing CryoSat-2 snow depths to that from OIB. Figure 6.4 shows the same as Fig. 6.3, but for March 2017 snow depth instead

of ice freeboard. In this comparison, the agreement is moderately better than the ice freeboard (r=0.68), though the mean difference is larger in magnitude at over -1 cm. The distribution of differences is more symmetric about zero than with ice freeboard, and the standard deviation of differences is slightly lower at around 7.75 cm. Once again, substantial differences between CryoSat-2 and OIB exist just off the coast of Ellesmere Island. However, they vary in sign over a relatively small area, which was not seen to this degree in the ice freeboard data. This could be due to increasing snow accumulation, as the various flights in this region occurred around 10 days apart. It is important to remember that the OIB data come from the respective day in which the flight occurred, while CryoSat-2 data are averaged over the entire month.

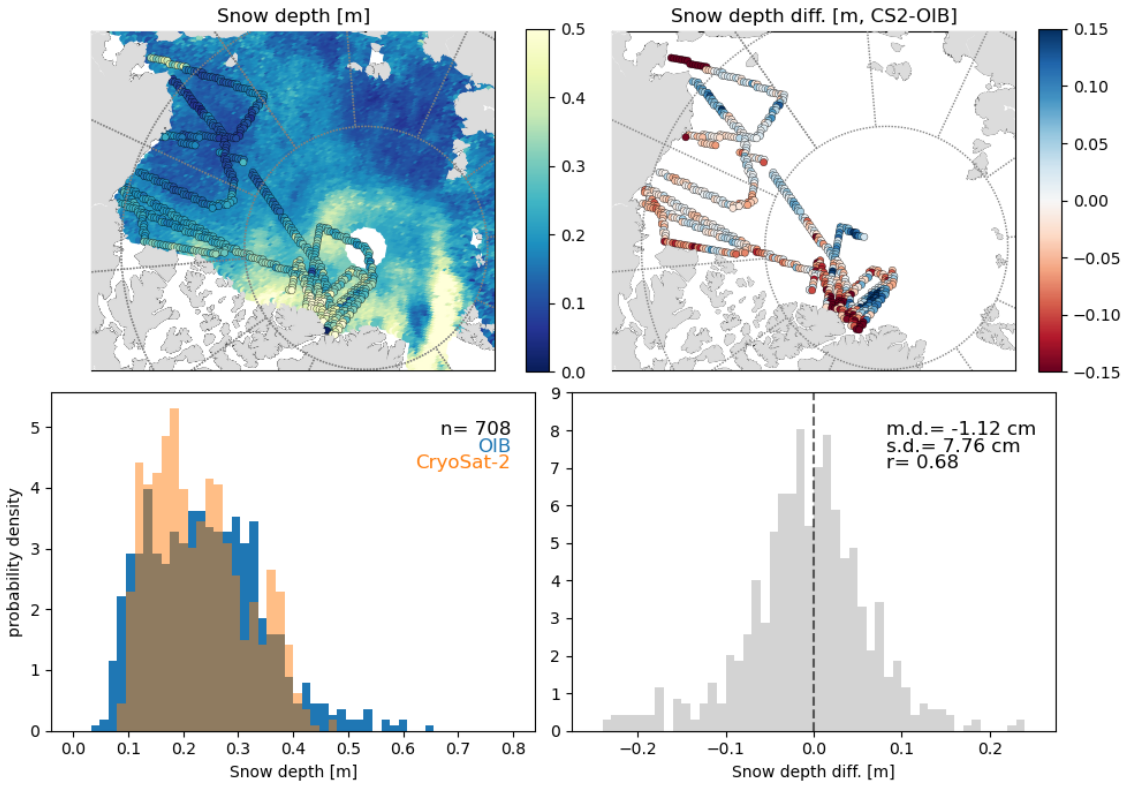

Figure 6.4: As in Fig. 6.3 but for March 2017 snow depth data.

Another interesting feature is the region of very thick snow depths in the CryoSat-2 data north of Svalbard, in which all grid cells are greater than 50 cm thick. Unfortunately, no OIB flights occurred over this region in March of 2017 to investigate if this result is physically-realistic or simply an artifact within the retrieval. Future study can look into other years and months of OIB snow depth data in the region north of Svalbard.

6.4 Comparisons to ground-based data: MOSAiC

In this section, CryoSat-2 results are compared to manual measurements collected in March and April 2020 during the MOSAiC field expedition.

6.4.1 MOSAiC data

The MOSAiC Expedition was the largest scientific polar expedition in history, lasting for more than one year and incorporating more than 300 scientists from over 20 countries. The premise of MOSAiC was to study every aspect from the ocean-ice-atmosphere system in great detail throughout an entire seasonal cycle, and was done by freezing a research vessel into the Arctic ice pack and letting it drift with the sea ice over the course of a year. The drift began in October 2019 and lasted (though broken up) until October 2020, covering 3400 km (Krumpen et al., 2020). The drift during the third leg of the expedition, which lasted from late February to June 2020, is shown in Fig. 6.5. Throughout the expedition, sea ice measurements were collected from dozens of instruments, focusing on everything from the physical

properties of the sea ice and snow cover to the microorganisms living within the sea ice. At the time of this writing, many datasets from MOSAiC are still being finalized, but will be available to the scientific community and general public in January 2023.

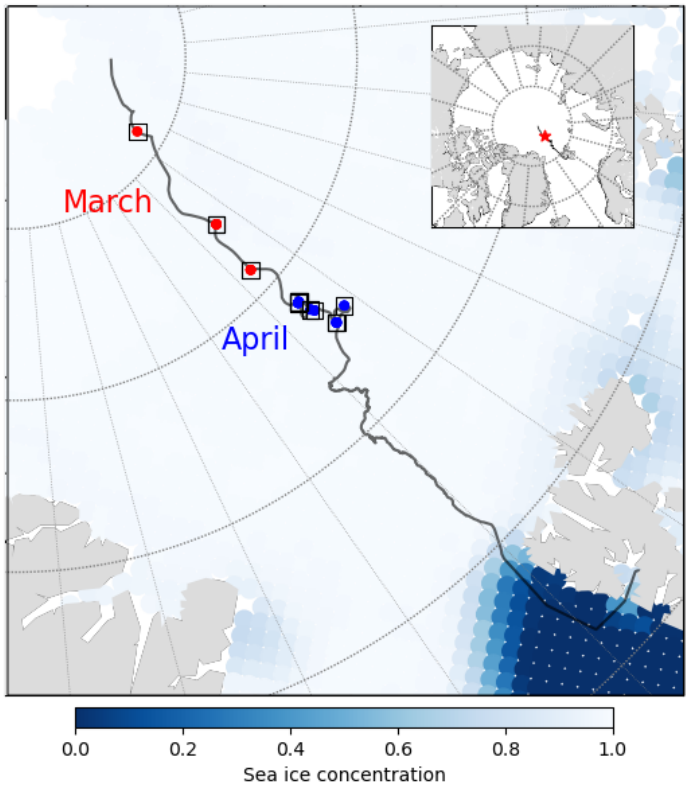

Figure 6.5: Map of the MOSAiC Leg 3 (March-June 2020) drift and ice thickness sample locations used in this study (dots). Boxes represent 25x25 km grid cells around each sample location (enlarged) from which CryoSat-2 data are collected for comparison. Map background gives the March-April 2020 average ice concentration.

For this study, manual measurements of sea ice properties collected between March 1st and April 30th, 2020 are used in comparison against CryoSat-2 data. These measurements were taken on eight different dates corresponding to 10 different sea ice coring activities, with the locations noted in Fig. 6.5. Each activity consisted of drilling individual ice cores from the same location and using the ice cores to study

Figure 6.6: The author collecting ice thickness measurements during MOSAiC. A standard thickness gauge was used in all measurements (photo by: Laura Wischnewski).

different aspects of the sea ice. Before any cores were collected, measurements of the snow depth were taken over the area using a standard ruler. After each core was drilled, a manual measurement of the ice thickness and ice draft was recorded using a thickness gauge (Fig. 6.6). From these three measurements, the snow and ice freeboard can be easily calculated. During each coring activity, anywhere from 6 to 30 ice cores were collected. Since ice thickness did not vary much over the 1 m^2 plot area, only 5 measurements from each activity are used in this analysis. A list of coring activities and average parameter values are given in Table 6.1. In two activities, no snow depth information was collected, and therefore no snow freeboard or snow depth data exist. In one activity, the ice thickness gauge was broken, and therefore the ice thickness was calculated from the retrieved ice core and no draft or freeboard data were collected.

Since the MOSAiC measurements come from only a few discrete points, it is difficult to compare these values to individual satellite overpasses. Also, creating gridded averages of the MOSAiC data and comparing them to the gridded CryoSat-2 data (as was done in the previous section) would result in too few points to draw any meaningful comparisons. Instead, a 25 km x 25 km box is taken around the average location of each MOSAiC activity date (8 in total, Fig. 6.5), and all CryoSat-2 data that are collected within that box from the same month as the MOSAiC activity are kept and used in this study. It is assumed, therefore, that each MOSAiC measurement is representative of the surrounding area. This way, distributions can be created that utilize all MOSAiC data points as well as all CryoSat-2 data that come from locations near each manual measurement. This assumption may not be entirely valid due to the way in which the MOSAiC Floe was chosen: a large, thick floe was needed to support the expedition logistics, which may not be entirely representative of the surroundings (Krumpen et al., 2020). Future work should be aimed at contextualizing the MOSAiC Floe within the rest of the Arctic sea ice cover.

6.4.2 Results

Figure 6.7 shows box and whisker plots created from all MOSAiC measurements and all CryoSat-2 data points (purple plots) that come from regions around each MOSAiC measurement. Blue plots represent MOSAiC data coming from FYI, while orange plots represent those coming from SYI. Horizontal lines indicate the

Date	$\overline{h_i}\,[m]$	$\overline{h_d}\,[m]$	$\overline{h_s}\,[m]$	$\overline{h_{fi}}\,[m]$	$\overline{h_{fs}}\,[m]$	Ice type
09 Mar	1.47	1.36	-	0.11	-	FYI
24 Mar	2.01	1.87	0.14	0.14	0.28	SYI
30 Mar	1.47	1.28	0.12	0.19	0.31	FYI
06 Apr	1.65	1.46	0.17	0.19	0.36	FYI
06 Apr	2.17	1.94	0.16	0.22	0.38	SYI
13 Apr	1.76	1.60	0.12	0.15	0.27	SYI
14 Apr	1.96	1.78	0.11	0.18	0.29	FYI
27 Apr	1.58	1.56	0.13	0.02	0.15	FYI
27 Apr	1.68	1.54	-	0.14	-	SYI
30 Apr	1.63	-	0.14	-	-	FYI

Table 6.1: Mean values of sea ice parameters collected during MOSAiC sampling activities (10 total, coming from 8 different activity dates). Measured parameters include: ice thickness (h_i), ice draft (h_d), and snow depth (h_s), which are used to compute the ice freeboard (h_{fi}) and snow freeboard (h_{fs}).

median of the measurements while solid points represent the mean values. Boxes indicate the IQR and vertical black whiskers indicate the "maximum" and "minimum" (defined as 2.698σ point) of the data. All data from March and April 2020 are combined to make Fig. 6.7.

The left plot of Fig. 6.7 shows the distributions of the snow freeboard, ice freeboard, and snow depth from CryoSat-2 and MOSAiC FYI/SYI. At first glance, it is clear that CryoSat-2 tends to be slightly thicker than the MOSAiC data across all three parameters, and that the FYI data are the thinnest of the three. The range of snow depths observed is smaller than the freeboards, with mean values from all three plots within 5 cm of each other. The range of freeboards observed from CryoSat-2 is greater than the SYI freeboards, but less than is shown from FYI. Differences observed here could come from the assumption that the MOSAiC measurements represent the surrounding region, as the locations of FYI and SYI were more so chosen to represent their respective ice types and not necessarily

the surrounding ice as a whole. Additionally, the temporal difference between the CryoSat-2 observations and the MOSAiC data of up to as much as one month could lead to the differences observed here. More work is needed to find temporally-coincident CryoSat-2 overlaps of MOSAiC measurements.

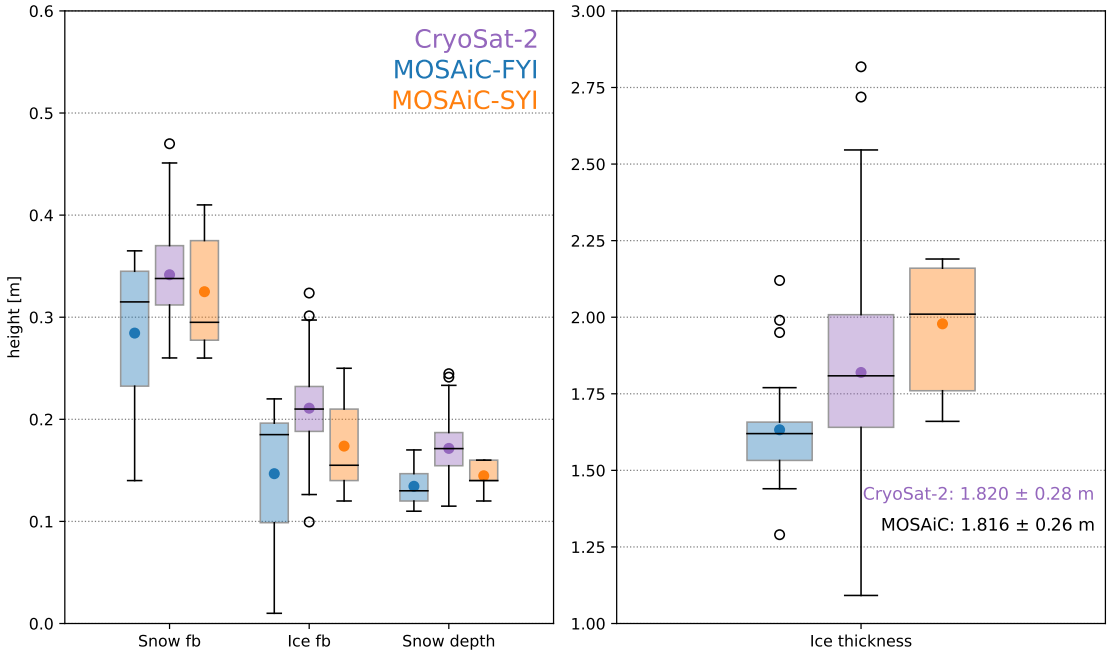

Figure 6.7: Boxplots of physical properties collected from MOSAiC FYI (blue) and SYI (orange) compared to CryoSat-2 (purple). CryoSat-2 data come from just the 25x25 km grid cells around each MOSAiC sample location. Boxes give the IQR, horizontal lines give median values, filled dots give mean values, and whiskers give min/max values. Unfilled dots show statistical outliers. Mean and standard deviation ice thickness values (right plot) are from CryoSat-2 and combined FYI/SYI MOSAiC.

The right plot of Fig. 6.7 shows the resultant thickness distributions taken from the MOSAiC measurements and computed from CryoSat-2 using the snow depth and snow freeboard values and density assumptions given in Section 6.2. The FYI mean thickness is around 1.65 m, while the mean SYI thickness is almost 2 m, which is expected for these months (Haas, 2016). When combined together, the

mean of all MOSAiC thickness measurements is 1.82 m, which is within 1 cm of the mean of all CryoSat-2 estimates collected (1.82 m). While the spread in the CryoSat-2 distribution is undoubtedly greater than the MOSAiC measurements, the standard deviations of the measurements are within 2 cm of each other. These results are encouraging, especially because the MOSAiC measurements provide a good estimate of the "ground truth" (i.e. their uncertainty is low compared to remotely-sensed thickness measurements).

This analysis of CryoSat-2-derived variables and MOSAiC measurements is exploratory and meant to be a simple comparison between ground truth measurements and the satellite retrievals. As mentioned above, MOSAiC took place over 12 months and consists of many more datasets than just manual thickness measurements. Ground-based EM surveys provide thickness data over longer transects and automated buoys were in operation that could enable ice thickness point measurements at hourly (or better) temporal resolution. Also, many helicopter-based ice thickness surveys took place that could be an important step in linking the ground-based MOSAiC measurements to those collected from satellite. Future work will surely involve more comparisons of satellite-derived data and MOSAiC observations once the data are publicly released.

6.5 Benefits of snow depth data from CryoSat-2

The CryoSat-2 retrievals developed in this dissertation for Antarctic sea ice are easily justified by the complexities involving applying typical retrieval methods

(e.g. threshold retracking methods) for Antarctic sea ice. Beyond that, the fact that there are very few CryoSat-2-derived Antarctic sea ice freeboard products also necessitates developing this new method. In the Arctic, conversely, many CryoSat-2 sea ice thickness retrieval methods currently exist that seem to do a relatively good job at estimating Arctic sea ice thickness (Spreen and Kern, 2016). Therefore, it may seem superfluous to have another CryoSat-2-based product to measure Arctic sea ice thickness. However, the benefit of this physically-based retrieval method is the potential for more representative snow depth estimates compared to other studies, as well as a potential for improvement in sea ice thickness retrievals.

Most studies involving CryoSat-2 sea ice thickness retrievals in the Arctic use a modified snow depth climatology in their thickness retrievals (Kurtz et al., 2014; Laxon et al., 2013; Ricker et al., 2014; Tilling et al., 2018) that takes the Warren et al. (1999) snow depth climatology and modifies it to reduce the snow load on FYI by some factor, usually 50% (following Kurtz and Farrell 2011). This assumed snow depth, however, is simply an estimate and does not account for the interannual variability in the snowfall that can impact the snow depth distribution and in turn, the thickness distribution (Kwok and Markus, 2018; Webster et al., 2018). It is clearly important to capture the snow depth variability in order to accurately derive the sea ice thickness. Other studies have tried to improve upon this assumption by using models of snow depth on sea ice, such as from a reanalysis-derived snow budget model like NESOSIM (Petty et al., 2018). These models tend to do a better job at capturing the interannual variability, but still are reliant upon assumptions and ancillary data to model the snow cover. More recent methods to derive snow depth

basin-wide involve utilizing the different frequencies of altimeters (like ICESat-2 and CryoSat-2) have emerged, that calculate snow depth through the differencing of the snow and ice freeboard measurements (Guerreiro et al., 2016; Kwok et al., 2020c; Lawrence et al., 2018). In Kwok et al. (2020c), they find good agreement to snow depth from reanalysis datasets, but are restricted to the time period in which both satellites are operating. Lawrence et al. (2018) also show good agreement between CryoSat-2 and AltiKa (Ka-band) derived snow depths and OIB data, but can only provide estimates up to 81.5° N due to AltiKa's orbital inclination.

Utilizing the CryoSat-2 method proposed here would allow for a decade-long time series of snow depth on sea ice, similar to what was shown in Chapter 5 for Antarctic sea ice. This snow depth time series could then be used by other retrieval methods to improve sea ice thickness estimates, either through the generation of a new snow depth climatology or through the utilization of coincident snow depth data from a given month.

One example of these CryoSat-2 snow depths improving other products' estimates is shown in Fig. 6.8. Here, sea ice draft estimates derived from CryoSat-2 thickness estimates from Kurtz et al. (2014) are compared against draft measurements in the Beaufort Sea collected from the Beaufort Gyre Exploration Project (BGEP) moorings (WHOI, 2018). These moorings are located at three locations in the Beaufort Gyre (Fig. 6.8) and take continuous draft measurements when sea ice is present. All scatter plot points represent a coincident monthly average of BGEP mooring sea ice drafts and CryoSat-2-derived sea ice drafts from the same month that are collected within 25 km of a given mooring. The black points show draft

measurements calculated from the Kurtz et al. (2014) Level 4 CryoSat-2 product generated using the "modified Warren" snow depth climatology (explained above). The orange points show the same thing, with the exception that the Cryosat-2 snow depths come from the method described here. The four months of data that were processed for this study were averaged to generate two pseudo snow depth "climatologies" (one for March and one for April), which was then used in this thickness calculation for all years of CryoSat-2 level 4 freeboard data (Kurtz et al., 2014) from March and April. This resulted in 49 monthly averaged points.

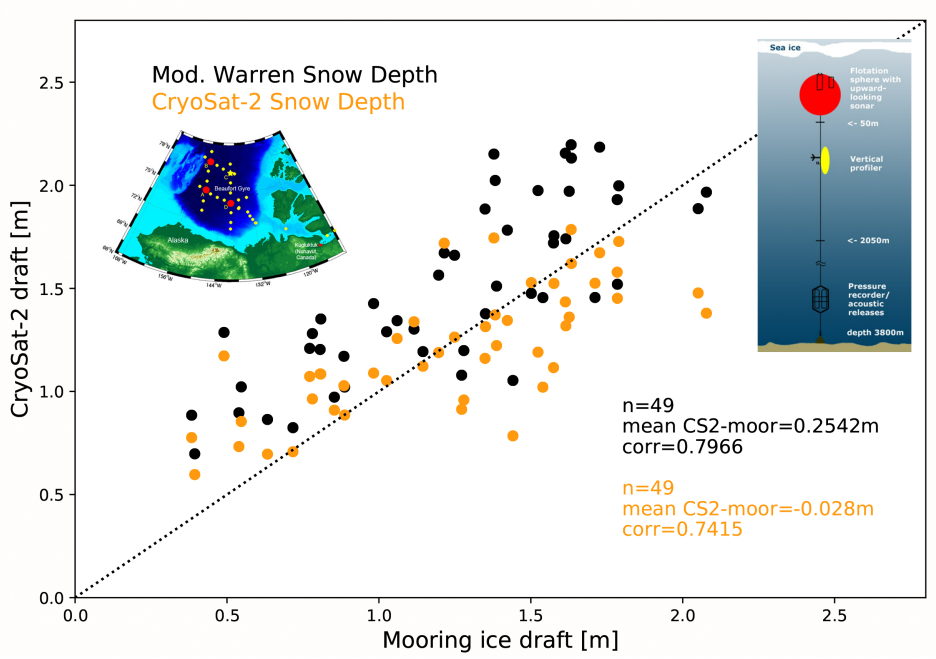

Figure 6.8: Linear regression comparing BGEP mooring ice draft to CryoSat-2 derived ice draft. Black points show monthly average drafts calculated using the modified Warren snow depth climatology, while orange points show monthly average drafts calculated used a CryoSat-2 average snow depth climatology. Red points on the map show locations of the moorings, while the diagram shows the setup of each mooring.

It is clear from Fig. 6.8 that using the CryoSat-2 snow depths derived with this CryoSat-2 method show an improvement over the modified Warren climatology

in this region. The mean difference between CryoSat-2 drafts and mooring drafts is over 25 cm when using the modified Warren climatology, though the correlation is fairly high at almost 0.80. When using the snow depth climatology derived here, the correlation stays fairly high (0.74) but the mean absolute difference drops to under 3 cm. This simple comparison shows the promise that using this CryoSat-2 snow depth information has in improving sea ice thickness estimates over currently-used methods. Of course, this is just one comparison using snow depths averaged from four individual months. Further work is needed in validating individual monthly maps and the interannual variability detected with this method. Once done, it is hoped that this CryoSat-2-derived snow depth time series could be a valuable asset for sea ice thickness estimation.

6.6 Conclusions

In this brief chapter, the CryoSat-2 retrieval algorithm originally developed for Antarctic sea ice was applied to four months of data collected over Arctic sea ice. This was done as an exercise to test if the retrievals would perform similarly under the different ice and snow conditions of the Arctic. Additionally, it done to be able to make used of more abundant airborne and ground-based measurements of snow depth on sea ice and ice freeboard.

Initial comparisons of snow freeboard over Arctic sea ice show similar spatial patterns to that from ICESat-2, which is especially encouraging considering that no ICESat-2 data were included in the CryoSat-2 model initialization. Similar to what

was seen in Chapter 4, there is still some discrepancy in the relative magnitudes of the retrieved snow freeboards between the two sensors, especially over thicker ice and snow. More work is needed to investigate the geometric sampling differences and how they may influence the freeboard distributions observed.

Ice freeboard and snow depth values retrieved from CryoSat-2 were compared against airborne measurements from OIB and ground-based measurements from the MOSAiC Expedition. Distributions of both variables matched closely with that from OIB, with the snow depth correlation matching better at r=0.68. Manual measurements from MOSAiC provided ground-truth data points, and CryoSat-2 snow depth, ice freeboard, and snow freeboard estimates were all found to have a slight thick bias compared to those from MOSAiC. Differences were hypothesized to be due to the different spatial and temporal scales of sampling, though more data from MOSAiC will be useful to build confidence in this hypothesis. When combining the CryoSat-2 snow depth and snow freeboard to calculate thickness, however, CryoSat-2 was within 1 cm of the FYI/SYI average thickness value from MOSAiC.

Finally, the potential impact of a decade long CryoSat-2 snow depth time series was discussed, with a pseudo climatology from CryoSat-2 being shown to reduce bias in sea ice draft estimates over the modified Warren climatology when compared to the BGEP moorings. These comparisons show promise that this CryoSat-2 retrieval method can be utilized over Arctic sea ice, but that more work would be useful to further improve the algorithm and better understand some of the observed differences.

Chapter 7: Conclusions and Outlook

The overall goal of this dissertation was to develop and validate a new method to retrieve Antarctic sea ice physical properties of snow freeboard and snow depth on sea ice from satellite radar altimetry, in order to enable the calculation of Antarctic sea ice thickness from space. The previous chapters describe individual components of this process, from the motivation (Chapter 2), to the initial development (Chapter 3) and verification of the snow freeboard retrievals (Chapter 4). This process was then used to estimate sea ice thickness and volume for the 10+ years of the CryoSat-2 mission (Chapter 5). Finally, the potential to be used for Arctic sea ice retrievals was discussed (Chapter 6). While individual chapter conclusions are given throughout the dissertation, this chapter summarizes these conclusions and provides an outlook for future work.

7.1 Conclusions

7.1.1 Retrieval of snow freeboard of Antarctic sea ice using waveform fitting of CryoSat-2 returns

In Chapter 3, the basis for a CryoSat-2 snow freeboard retrieval algorithm was described. This method tracks the location of the air-snow interface on each CryoSat-2 waveform by using a physical waveform model and a least-squares fitting method, in combination with the idea that scattering at Ku-band frequencies over sea ice can originate from the air-snow interface. Radar pulse scattering was included in the two-layer (snow and ice) physical model through parameterized snow and ice backscatter terms and extinction coefficients. This method was found to reasonably represent CryoSat-2 waveforms, and was used to retrieve the air-snow interface elevation and snow freeboard of Antarctic sea ice.

Comparisons of retrieved air-snow interface elevation were made using two near-coincident underflights of the CryoSat-2 orbit by OIB campaigns in 2011 and 2012. Mean differences were found to be under 2.6 cm with general agreement in the profiles, but had moderately large standard deviations of differences around 28 cm. Snow freeboards were retrieved from the CryoSat-2 data and compared against non-temporally-overlapping data from ICESat, showing general agreement in the snow freeboard spatial patterns Antarctic-wide. Finally, an initial test in retrieving snow depth on sea ice showed the possibility for retrievals in the near-coast Pacific sector, but showed unrealistically uniform snow depth patterns elsewhere around

the continent.

Despite the promise shown in the initial comparisons, it is clear that this study was a first look into the possibility of retrieving snow freeboard from CryoSat-2. At the time of publication, the lack of coincident snow freeboard retrievals hindered the ability to assess the retrievals with a high degree of confidence. With the launch of ICESat-2 soon after, a better assessment could be made (Chapter 4).

7.1.2 Assessing CryoSat-2 Antarctic snow freeboard retrievals using data from ICESat-2

The launch of ICESat-2 in October 2018 provided a continuous record of snow freeboard at both poles and a much-needed dataset for validation of the algorithm developed in Chapter 3. This chapter showcased comparisons between CryoSat-2 and ICESat-2 snow freeboards both from near-contemporaneous along-track profiles and pan-Antarctic monthly grids. First, developments were made to the retrieval algorithm that improved the physical-representation of the waveform model and reduced the potential for the optimization procedure to converge into local minima. Additionally, an uncertainty estimate was provided that aimed to characterize the uncertainties present in the waveform-fitting routine through the use of synthetic waveforms and Monte Carlo simulations.

Along-track comparisons between CryoSat-2 and ICESat-2 were made by first finding near-coincident orbital overlaps and then analyzing the snow freeboard profiles at different spatial resolutions. CryoSat-2 was found to capture the general

shape of the ICESat-2 profiles when averaged to longer (25 km) along-track segments, but the discrepancies in the footprint sizes made full-resolution comparisons difficult. When viewed as monthly averages, CryoSat-2 captured a similar distribution to ICESat-2 in most months, with the exception of the Austral fall, in which CryoSat-2 showed between 2 and 6 cm thicker freeboards on average. Other months showed mean differences closer to zero, with CryoSat-2 tending to show a narrower pan-Antarctic freeboard distribution than ICESat-2.

It became clear in this chapter that the sampling differences between CryoSat-2 and ICESat-2 - both geometric and frequency-related - may contribute to the differences in freeboard observed. While coincident data (such as that from the CRYO2ICE campaign) are useful in helping to quantify and attribute these differences, this study found that optimizing the CryoSat-2 orbit to favor overlaps in the Arctic has eliminated Antarctic sea ice overlaps and reduced the potential for future along-track comparisons. While these comparisons with ICESat-2 instill more confidence in the snow freeboard retrievals from CryoSat-2, more work is needed in addressing and quantifying inter-satellite biases.

7.1.3 Ten years of Antarctic sea ice physical properties from CryoSat-2

In Chapter 5, the CryoSat-2 algorithm described and refined in Chapters 3 and 4 is applied to the entire CryoSat-2 record from July 2010 until October 2020. In addition to snow freeboard, the ice freeboard and snow depth are also retrieved

by utilizing the snow-ice interface elevation obtained with the retrieval process. The snow and ice freeboards and snow depths are compared to other measurements from Antarctic sea ice, including that from Kacimi and Kwok (2020) as well as Paul et al. (2018). The ice freeboard comparison suggests that this physical method improves upon a 50% threshold retracking method for finding ice freeboard, while snow depth comparisons show slightly higher values in each region during 2019 when compared to Kacimi and Kwok (2020). Independent comparisons with buoy and airborne data were attempted, but in both cases the external datasets were lacking in confidence, which in turn reduced confidence in the comparisons.

The retrieved snow freeboard and snow depth data were combined with estimates of sea ice, snow, and seawater density to produce the first pan-Antarctic estimates of Antarctic sea ice thickness and volume from CryoSat-2. Mean thickness values basin-wide were found to range between 1 and 1.32 m, with results from 2019 falling within the range of values found by Kacimi and Kwok (2020). Distributions of sea ice thickness varied seasonally and regionally, with seemingly anomalous results occurring in the Western Weddell sector in Austral summer. Basin-wide sea ice volume ranged annually between about 2500 and 20000 km^3.

Using the 10+ year time series, trends in the sea ice thickness and volume were uncovered. A statistically-significant pan-Antarctic thickening of 1.1 cm/yr was found during Austral summer months, while a pan-Antarctic thinning of 0.4 cm/yr was found during Austral winter months. When accounting for the impact of potential interannual variability in the snow and sea ice density estimates on the observed trends through Monte Carlo simulations, the basin-average wintertime

thinning was found to be significant at the 98% level, suggesting high confidence that the observed trend was not due to interannual density variability.

This chapter was the culmination of the efforts outlined in the previous chapters, and resulted in useful estimates of sea ice thickness over the CryoSat-2 mission. These results can be a part of a longer altimetry-based time series of Antarctic sea ice thickness that began with ICESat in the early 2000s and continues at the time of this writing with ICESat-2. In order to reconcile the three missions, more work is needed in establishing biases and uncertainties in the respective measurements, discussed in Section 7.2.

7.1.4 Application to Arctic sea ice retrievals

While the bulk of the dissertation focused on Antarctic sea ice, Chapter 6 took an exploratory look into the potential to use this algorithm over Arctic sea ice. First, modifications were made to the retrieval method that enabled operation in the Arctic, which mainly consisted of using NESOSIM snow depths as an initialization into the model. Snow freeboard comparisons with ICESat-2 were shown, and similar results to the Antarctic were found: CryoSat-2 tended to record thicker snow freeboards on average but often would show thinner freeboards than ICESat-2 over regions known to have thick freeboards. Nevertheless, the spatial pattern matched close to ICESat-2 despite being a completely independent comparison (i.e. no ICESat-2 data were included in the initialization).

Ice freeboard and snow depth values retrieved from CryoSat-2 were compared

against independent measurements from airborne and ground-based campaigns that did not exist in the Antarctic. CryoSat-2 data showed good agreement with OIB especially in terms of snow depth, where a mean difference of around 1 cm and a correlation of 0.68 were found. While freeboard and snow depth values were thicker on average than the ground-truth data collected during the MOSAiC field campaign, the mean sea ice thickness difference was within 1 cm of the manual measurements on MOSAiC, building confidence in the thickness retrievals over Arctic sea ice.

This chapter concluded with potential benefits for an Arctic snow depth on sea ice time series. It is presented that this work could improve current Arctic thickness retrievals that rely on snow depth climatologies, and an example is given that shows better agreement with sea ice draft data from moorings when using the derived CryoSat-2 snow depths instead of the modified Warren et al. (1999) climatology.

7.2 Future work

This section outlines potential avenues for future work relating to CryoSat-2 and the retrieval methods proposed in this dissertation.

7.2.1 Arctic sea ice

As discussed in Chapter 6, one potential area of future work revolves around Arctic sea ice. The results and comparison shown come from just four months of CryoSat-2 data processed as part of a brief exploration. The entire CryoSat-2 time series could easily be processed for Arctic sea ice, since the input snow depth

initialization data from NESOSIM exist back to at least 2001 (Petty et al., 2018). This analysis would simply take time and computing resources. Once processed, the time series of snow depth on sea ice will be valuable for satellite-based sea ice thickness estimation (as shown in Chapter 6).

Additionally, the ability to compare ice freeboard estimates with other CryoSat-2 products over many years could help to uncover how well threshold retracking actually works in the Arctic, and whether or not physical retrackers can consistently do a better job at tracking the snow-ice interface. With a year's worth of ground-truth data forthcoming from MOSAiC, Arctic sea ice retrievals from CryoSat-2 could also benefit substantially by having validation opportunities available that cover the whole seasonal cycle.

Finally, having a single sea ice retrieval algorithm operating in both hemispheres provides more opportunities to relate trends in Arctic sea ice thickness to those observed in Antarctic sea ice thickness. Most products focus only on either Arctic or Antarctic sea ice, with fewer applying the same techniques to both. Using data from the same satellite and retrieval method eliminates the need for inter-satellite bias reconciliation and allows for a more straightforward way to estimate uncertainties between the poles.

7.2.2 Model and optimization improvements

As was done in Chapter 4, there is always room for improving the model and optimization approach presented here. One large future improvement could cen-

ter around the handling of surface roughness in the model. Landy et al. (2020) found that surface roughness is an important source of uncertainty often overlook in CryoSat-2 retrievals. Here, roughness is initialized with a single value and bounds are provided that should capture the range of observed sea ice roughness. However, two key changes could be made. First, the use of a static initial value for roughness could be updated to be more dynamic and change based on the region or the waveform itself. A roughness discrimination could look similar to the current surface-type discrimination, which relies on waveform characteristics to separate lead-type points from floe-type points. Second, Landy et al. (2020) found that varying roughnesses can impact the observed snow-ice interface tracking point, where the snow-ice interface point was found to be higher (i.e. at a lower waveform power level) over rough surfaces and lower (i.e. at a higher waveform power level) over smooth surfaces. Future work could look into altering the initial guess tracking point from 70% to be dynamic based on the estimated roughness of the waveform.

While most potential improvements relate to the initialization used with the waveform model, one area of future work involves removing the need for parameter initial guesses altogether. Currently, the least-squares optimization uses a local optimization approach, meaning that physically-realistic initial guesses that are close to the expected values are required. By instead utilizing a global optimization technique, the entire parameter space is searched to find the best-guess output parameters, eliminating the need for initialization parameters. A global optimization is not used currently simply due to processing constraints. This current local optimization takes around 1 second to process each CryoSat-2 waveform, while global

optimization can take over an order of magnitude longer. While it may not seem substantial for this method to take e.g. 10 seconds to fit to each CryoSat-2 waveform, processing over 10+ years of 20 Hz CryoSat-2 data can be insurmountable with current processing capabilities. As processing power becomes more readily available in cloud-based computing environments, however, a shift towards global optimization could be realized.

7.2.3 Reconciling the laser-radar altimetry record

A final potential avenue for future work involves combining sea ice thickness measurements from ICESat, CryoSat-2, and ICESat-2 to create a 17+ year time series of Antarctic sea ice thickness derived from altimetry. Though an initial plot was shown in Chapter 5 that included measurements from each of these missions, reconciling these datasets requires significantly more work than simply displaying them end-to-end.

For one, the inter-satellite biases and geometric sampling differences between the three sensors need to be fully characterized and quantified before attempting to reconcile them. As shown in Chapter 4 and in other works (e.g. Tilling et al. 2019) footprint size differences between sensors can lead to discrepancies in the observed freeboard distribution. Tilling et al. (2019) corrected for this effect in the Arctic when comparing CryoSat-2 and Envisat by using the distance between lead and floe measurements as a way to better resolve discrete surfaces from Envisat. A similar process would need to be done in the Antarctic between CryoSat-2 and ICESat-2

to better understand differences seen in the results. Without it, any geometric-related impacts on the freeboard retrievals could bias the results from one of the instruments, potentially leading to erroneous trends or jumps in the combined time series.

Additionally, in order to combine measurements, the wavelength discrepancies between satellites and their respective impacts on retrieved elevations would need to be better understood. Radar frequencies tend to interact with the sea ice surface differently than lasers, which is most prominent over mixed sea ice surfaces. In these cases, radar returns can be overwhelmed by the specular open water surface while lidar returns could either record a drop or rise in the return power depending on the roughness of the surface. Surface-type classifications, floe lengths, and SSH estimates all could be impacted by differing returns over mixed surfaces - all of which could influence the freeboard and thickness distributions. The wavelength of the instrument also determines the geophysical corrections that need to be applied to the data, which should be as consistent as possible across platforms.

As shown in Chapters 5 and 6, the choice of snow depth estimate to include in the thickness calculation is also a vital component when comparing measurements. A similar method of estimating snow depth should be applied to all sensors, or else very large differences could be seen (e.g. when comparing the zero ice freeboard assumption to the CryoSat-2 snow depth estimate, as in Fig. 5.22).

One final point to include when attempting to reconcile the laser-radar altimeter thickness time series in the Antarctic is the need for comparison with independent datasets to increase confidence in each individual dataset as well as the time

series as a whole. Few ground and airborne-based Antarctic thickness measurements currently exist, which limits the validation that can be done for each dataset. In the Arctic, this problem is slightly easier as some measurements exist that have spanned the lifetimes of ICESat and continue until today, such as the BGEP moorings (WHOI, 2018). Any work in the Antarctic will need to utilize all available ground-based data - or more likely collect new in situ data - to increase confidence and reduce uncertainty in the absolute thickness retrievals. While relative uncertainties between CryoSat-2 and ICESat-2 can be established by utilizing coincident CRYO2ICE data, the absolute errors require a more in-depth approach. Perhaps the use of sea ice models (similar to Holland 2014) could aid in the comparison between these datasets and the combination to create a harmonized time series.

It is clear that a reconciled ICESat - CryoSat-2 - ICESat-2 time series of Antarctic sea ice thickness will be important to understand how Antarctic sea ice has changed in recent years and to help determine the processes that may have driven that change. Though more work is needed to fully link these three missions together, it is the author's hope that this dissertation provides a substantial first step towards that goal.

Appendix A: Derivation of the Sea Ice Thickness Equation

Much of this dissertation involves estimating sea ice thickness from satellite altimetry using the assumption of hydrostatic balance in combination with freeboard, snow depth, and density terms. Here, the altimeter-based sea ice thickness equation using snow freeboard (i.e. Equation 5.2) is derived from basic principles.

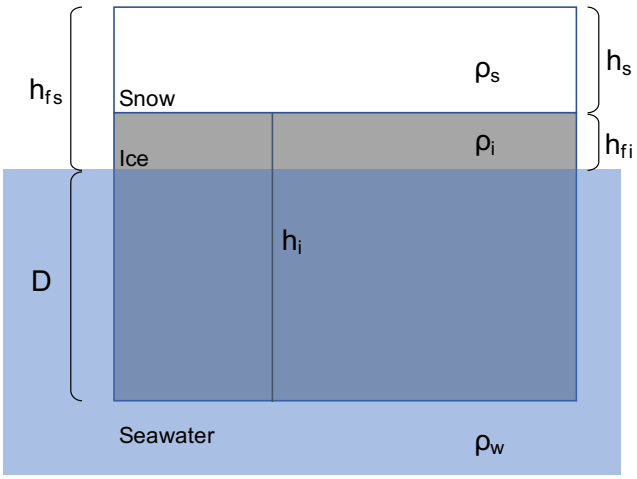

Figure A.1: A diagram of the simplified snow - ice - ocean system in hydrostatic balance, with terms used in below equations labeled.

As shown in Fig. A.1, it is clear that the sea ice thickness, h_i, is simply the sum of the sea ice draft, D, and the ice freeboard, h_{fi}, i.e.:

$$h_i = h_{fi} + D \tag{A.1}$$

However, the sea ice draft is not known when using satellite altimetry data, as conventional wavelengths do not allow for direct detection of the ice-water interface (Kwok, 2004). Instead, thickness must be calculated through the use of freeboard and snow depth estimates and the assumption of hydrostatic equilibrium.

Archimedes' Principle states that a buoyant force is exerted on an object immersed in a fluid that is equal to (and opposite in direction) the weight of the object. Therefore, for sea ice, the weight of the snow and sea ice above the water level must be equal to the buoyant force exerted by the ice below the water level, or:

$$F_{weight,fi} + F_{weight,hs} = F_{buoyant,D} \tag{A.2}$$

where F_{weight} is the force due to gravity of the snow (hs) and ice above the water line (fi) and $F_{buoyant}$ is the opposing buoyant force of ice below the water line (D). The force due to gravity (and therefore also buoyancy), F, can be given by:

$$F = \rho g V \tag{A.3}$$

where ρ is the density, g is the acceleration due to gravity, and V is the volume of a given object. Substituting A.3 into Equation A.2 gives

$$\rho_w g V_D = \rho_i g V_{fi} + \rho_s g V_{hs} \tag{A.4}$$

where ρ, g, and V are as above for seawater (w), ice (i), and snow (s). For a given

unit area, Equation A.4 can be simplified to:

$$\rho_w D = \rho_i h_i + \rho_s h_s. \tag{A.5}$$

As seen in Fig. A.1, h_{fi} is equal to h_{fs} minus h_s. Therefore, Equation A.1 can be rewritten as:

$$h_i = (h_{fs} - h_s) + D \tag{A.6}$$

Solving Equation A.6 for D and substituting into A.5 gives:

$$\rho_w(h_i - h_{fs} + h_s) = \rho_i h_i + \rho_s h_s. \tag{A.7}$$

Equation A.7 can then be rearranged to solve for h_i:

$$\rho_w h_i - \rho_w h_{fs} + \rho_w h_s = \rho_i h_i + \rho_s h_s \tag{A.7.1}$$

$$h_i(\rho_w - \rho_i) = \rho_w h_{fs} + (\rho_s - \rho_w) h_s \tag{A.7.2}$$

$$h_i = \left(\frac{\rho_w}{\rho_w - \rho_i}\right) h_{fs} + \left(\frac{\rho_s - \rho_w}{\rho_w - \rho_i}\right) h_s, \tag{A.8}$$

Equation A.8 allows for the calculation of sea ice thickness using snow freeboard. A similar process can be followed for ice freeboard, to derive Equation 5.1.

Bibliography

Aagaard, K. and Carmack, E. C. (1989). The role of sea ice and other fresh water in the Arctic circulation. *Journal of Geophysical Research*, 94(C10):14485, DOI: 10.1029/jc094ic10p14485.

Abdalati, W., Zwally, H. J., Bindschadler, R., Csatho, B., Farrell, S. L., Fricker, H. A., Harding, D., Kwok, R., Lefsky, M., Markus, T., Marshak, A., Neumann, T., Palm, S., Schutz, B., Smith, B., Spinhirne, J., and Webb, C. (2010). The ICESat-2 laser altimetry mission. *Proceedings of the IEEE*, 98(5):735–751, DOI: 10.1109/JPROC.2009.2034765.

Abdalla, S., Dinardo, S., Benveniste, J., and Janssen, P. A. (2018). Assessment of CryoSat-2 SAR mode wind and wave data. *Advances in Space Research*, 62(6):1421–1433, DOI: 10.1016/j.asr.2018.01.044.

Ackley, S. F., Perovich, D. K., Maksym, T., Weissling, B., and Xie, H. (2020). Surface flooding of Antarctic summer sea ice. *Annals of Glaciology*, 61(82):117–126, DOI: 10.1017/aog.2020.22.

Adolphs, U. (1998). Ice thickness variability, isostatic balance and potential for snow ice formation on ice floes in the south polar Pacific Ocean. *Journal of Geophysical Research: Oceans*, 103(C11):24675–24691, DOI: 10.1029/98JC02414.

Alexandrov, V., Sandven, S., Wahlin, J., and Johannessen, O. M. (2010). The relation between sea ice thickness and freeboard in the Arctic. *Cryosphere*, 4(3):373–380, DOI: 10.5194/tc-4-373-2010.

Allard, R. A., Farrell, S. L., Hebert, D. A., Johnston, W. F., Li, L., Kurtz, N. T., Phelps, M. W., Posey, P. G., Tilling, R., Ridout, A., and Wallcraft, A. J. (2018). Utilizing CryoSat-2 sea ice thickness to initialize a coupled ice-ocean modeling system. *Advances in Space Research*, 62(6):1265–1280, DOI: 10.1016/j.asr.2017.12.030.

Alley, R. B., Clark, P. U., Huybrechts, P., and Joughin, I. (2005). Ice-sheet and sea-level changes. *Science*, 310(5747):456–460, DOI: 10.1126/science.1114613.

Allison, I., Brandt, R. E., and Warren, S. G. (1993). East Antarctic sea ice: albedo, thickness distribution, and snow cover. *Journal of Geophysical Research*, 98(C7):12417–12429, DOI: 10.1029/93jc00648.

Anderson, O. B., Stenseng, L., Piccioni, G., and Knudsen, P. (2016). The DTU15MSS (Mean Sea Surface) and DTU15LAT, https://ftp.space.dtu.dk/pub/DTU15/DOCUMENTS/MSS/DTU15MSS+LAT.pdf.

Armitage, T. W. and Ridout, A. L. (2015). Arctic sea ice freeboard from AltiKa and comparison with CryoSat-2 and Operation IceBridge. *Geophysical Research Letters*, DOI: 10.1002/2015GL064823.

Arthern, R. J., Wingham, D. J., and Ridout, A. L. (2001). Controls on ERS altimeter measurements over ice sheets: Footprint-scale topography, backscatter fluctuations, and the dependence of microwave penetration depth on satellite orientation. *Journal of Geophysical Research: Atmospheres*, 106(D24):33471–33484, DOI: 10.1029/2001JD000498.

Beaven, S. G., Lockhart, G. L., Gogineni, S. P., Hossetnmostafa, A. R., Jezek, K., Gow, A. J., Perovich, D. K., Fung, A. K., and Tjuatja, S. (1995). Laboratory measurements of radar backscatter from bare and snow-covered saline ice sheets. *International Journal of Remote Sensing*, 16(5):851–876, DOI: 10.1080/01431169508954448.

Benjamini, Y. and Hochberg, Y. (1995). Controlling the false discovery rate: a practical and powerful approach to multiple testing. *Journal of the Royal Statistical Society: Series B (Methodological)*, 57(1):289–300, DOI: 10.1111/j.2517-6161.1995.tb02031.x.

Blockley, E. W. and Andrew Peterson, K. (2018). Improving Met Office seasonal predictions of Arctic sea ice using assimilation of CryoSat-2 thickness. *Cryosphere*, 12(11):3419–3438, DOI: 10.5194/tc-12-3419-2018.

Bourke, R. H. and Garrett, R. P. (1987). Sea ice thickness distribution in the Arctic Ocean. *Cold Regions Science and Technology*, 13(3):259–280, DOI: 10.1016/0165-232X(87)90007-3.

Brenner, A. C., DiMarzio, J. P., and Zwally, H. J. (2007). Precision and accuracy of satellite radar and laser altimeter data over the continental ice sheets. *IEEE Transactions on Geoscience and Remote Sensing*, 45(2):321–331, DOI: 10.1109/TGRS.2006.887172.

Brown, G. S. (1977). The average impulse response of a rough surface and its applications. *IEEE Journal of Oceanic Engineering*, 2(1):67–74, DOI: 10.1109/JOE.1977.1145328.

Budyko, M. I. (1969). The effect of solar radiation variations on the climate of the Earth. *Tellus*, 21(5):611–619, DOI: 10.3402/tellusa.v21i5.10109.

Carrère, L. and Lyard, F. (2003). Modeling the barotropic response of the global ocean to atmospheric wind and pressure forcing - Comparisons with observations. *Geophysical Research Letters*, 30(6):1275, DOI: 10.1029/2002GL016473.

Carton, J. A. (1989). Estimates of sea level in the tropical Atlantic Ocean using Geosat altimetry. *Journal of Geophysical Research*, 94(C6):8029–8039, DOI: 10.1029/JC094iC06p08029.

Cartwright, D. E. and Edden, A. C. (1973). Corrected tables of tidal harmonics. *Geophysical Journal of the Royal Astronomical Society*, 33(3):253–264, DOI: 10.1111/j.1365-246X.1973.tb03420.x.

Cavalieri, D. J., Parkinson, C. L., Gloersen, P., and Zwally, H. J. (1996). Sea ice concentrations from nimbus-7 SMMR and DMSP SSM/I-SSMIS passive microwave data, Version 1, DOI: 10.5067/8GQ8LZQVL0VL.

Cavalieri, D. J., Parkinson, C. L., and Vinnikov, K. Y. (2003). 30-Year satellite record reveals contrasting Arctic and Antarctic decadal sea ice variability. *Geophysical Research Letters*, 30(18), DOI: 10.1029/2003GL018031.

Cipollini, P. and Snaith, H. (2013). A short course on altimetry. Technical report, Cork, http://seom.esa.int/.

Comiso, J. C. (2017). Bootstrap sea ice concentrations from Nimbus-7 SMMR and DMSP SSM/I-SSMIS, version 3, DOI: 10.5067/7Q8HCCWS4I0R.

Comiso, J. C., Cavalieri, D. J., Parkinson, C. L., and Gloersen, P. (1997). Passive microwave algorithms for sea ice concentration: A comparison of two techniques. *Remote Sensing of Environment*, 60(3):357–384, DOI: 10.1016/S0034-4257(96)00220-9.

Connor, L. N., Laxon, S. W., Ridout, A. L., Krabill, W. B., and McAdoo, D. C. (2009). Comparison of Envisat radar and airborne laser altimeter measurements over Arctic sea ice. *Remote Sensing of Environment*, 113(3):563–570, DOI: 10.1016/j.rse.2008.10.015.

Costa, K. D., Kleinstein, S. H., and Hershberg, U. (2011). Biomedical model fitting and error analysis. *Science Signaling*, 4(192), DOI: 10.1126/scisignal.2001983.

Cottier, F., Steele, M., and Nilsen, F. (2016). Sea ice and Arctic Ocean oceanography. In *Sea Ice: Third Edition*, pages 197–215. Wiley Blackwell, DOI: 10.1002/9781118778371.ch7.

Curry, J. A., Schramm, J. L., and Ebert, E. E. (1995). Sea ice-albedo climate feedback mechanism. *Journal of Climate*, 8(2):240–247, DOI: 10.1175/1520-0442(1995)008<0240:SIACFM>2.0.CO;2.

Dai, A., Luo, D., Song, M., and Liu, J. (2019). Arctic amplification is caused by sea-ice loss under increasing CO 2. *Nature Communications*, 10(1):1–13, DOI: 10.1038/s41467-018-07954-9.

De Silva, L. W. A., Yamaguchi, H., and Ono, J. (2015). Ice–ocean coupled computations for sea-ice prediction to support ice navigation in Arctic sea routes. *Polar Research*, 34(1):25008, DOI: 10.3402/polar.v34.25008.

Dominguez, R. (2019). IceBridge DMS L1B geolocated and orthorectified images, version 1, DOI: 10.5067/OZ6VNOPMPRJ0.

Drinkwater, M. R., Francis, R., Ratier, G., and Wingham, D. J. (2004). The European Space Agency's Earth Explorer Mission CryoSat: Measuring variability in the cryosphere. *Annals of Glaciology*, 39:313–320, DOI: 10.3189/172756404781814663.

Ebert, E. E. and Curry, J. A. (1993). An intermediate one-dimensional thermodynamic sea ice model for investigating ice-atmosphere interactions. *Journal of Geophysical Research*, 98(6):10085, DOI: 10.1029/93jc00656.

Egbert, G. D. and Erofeeva, S. Y. (2002). Efficient inverse modeling of barotropic ocean tides. *Journal of Atmospheric and Oceanic Technology*, 19(2):183–204, DOI: 10.1175/1520-0426(2002)019<0183:EIMOBO>2.0.CO;2.

Eicken, H., Lange, M. A., and Dieckmann, G. S. (1991). Spatial variability of sea-ice properties in the northwestern Weddell Sea. *Journal of Geophysical Research*, 96(C6):10603, DOI: 10.1029/91JC00456.

EPA (2016). Climate change indicators in the United States. Technical Report April, http://www.epa.gov/climatechange/.

European Space Agency (2018). Introduction to CryoSat-2 ICESat-2 resonant orbits. Technical report, https://earth.esa.int/eogateway/missions/cryosat/cryo2ice.

European Space Agency (2019a). CryoSat-2 product handbook: Baseline D 1.1. Technical report, https://earth.esa.int/documents/10174/125272/CryoSat-Baseline-D-Product-Handbook.

European Space Agency (2019b). L1b SAR precise orbit. Baseline D, DOI: 10.5270/CR2-2cnblvi.

European Space Agency (2019c). L1b SARIn precise orbit. Baseline D, DOI: 10.5270/CR2-u3805kw.

Evans, R. J. (1972). Arctic ice dynamics: The AIDJEX project. In *Proceedings of the Annual Offshore Technology Conference*, volume 1972-May, pages II597–II602. Offshore Technology Conference, DOI: 10.4043/1683-ms.

Farrell, S. L., Kurtz, N., Connor, L. N., Elder, B. C., Leuschen, C., Markus, T., McAdoo, D. C., Panzer, B., Richter-Menge, J., and Sonntag, J. G. (2012). A first assessment of IceBridge Snow and Ice thickness data over arctic sea ice. *IEEE Transactions on Geoscience and Remote Sensing*, 50(6):2098–2111, DOI: 10.1109/TGRS.2011.2170843.

Farrell, S. L., Laxon, S. W., McAdoo, D. C., Yi, D., and Zwally, H. J. (2009). Five years of Arctic sea ice freeboard measurements from the Ice, Cloud and land Elevation Satellite. *Journal of Geophysical Research*, 114(C4):C04008, DOI: 10.1029/2008JC005074.

Fetterer, F., K, K., Meier, W., Savoie, M., and Windnagel, A. (2017). Sea ice index, DOI: 10.7265/N5K072F8.

Fons, S., Kurtz, N. T., Bagnardi, M., Petty, A. A., and Tilling, R. (2021). Assessing CryoSat-2 Antarctic snow freeboard retrievals using data from ICESat-2. *ESSOAr*, DOI: 10.1002/ESSOAR.10506473.1.

Fons, S. W. and Kurtz, N. T. (2019). Retrieval of snow freeboard of Antarctic sea ice using waveform fitting of CryoSat-2 returns. *The Cryosphere*, 13(3):861–878, DOI: 10.5194/tc-13-861-2019.

Fowler, C., Emery, W. J., and Maslanik, J. (2004). Satellite-derived evolution of arctic sea ice age: October 1978 to March 2003. *IEEE Geoscience and Remote Sensing Letters*, 1(2):71–74, DOI: 10.1109/LGRS.2004.824741.

Fox, C. and Haskell, T. G. (2001). Ocean wave speed in the Antarctic marginal ice zone. *Annals of Glaciology*, 33:350–354, DOI: 10.3189/172756401781818941.

Fromm, T., Oberdieck, C., Matz, T., and Wesche, C. (2020). Expeditions to Antarctica: ANT-Land 2019/20 Neumayer Station III, Kohnen Station, flight operations and field campaigns. Technical report, Alfred Wegener Institute, Bremerhaven, DOI: 10.2312/BzPM_0745_2020.

Galin, N., Wingham, D. J., Cullen, R., Fornari, M., Smith, W. H., and Abdalla, S. (2013). Calibration of the CryoSat-2 interferometer and measurement of across-track ocean slope. *IEEE Transactions on Geoscience and Remote Sensing*, 51(1):57–72, DOI: 10.1109/TGRS.2012.2200298.

Garcia, E. S., Sandwell, D. T., and Smith, W. H. (2014). Retracking CryoSat-2, Envisat and Jason-1 radar altimetry waveforms for improved gravity field recovery. *Geophysical Journal International*, 196(3):1402–1422, DOI: 10.1093/gji/ggt469.

Giles, K. A., Laxon, S. W., Wingham, D. J., Wallis, D. W., Krabill, W. B., Leuschen, C. J., McAdoo, D., Manizade, S. S., and Raney, R. K. (2007). Combined airborne laser and radar altimeter measurements over the Fram Strait in May 2002. *Remote Sensing of Environment*, 111(2):182–194, DOI: 10.1016/j.rse.2007.02.037.

Giles, K. A., Laxon, S. W., and Worby, A. P. (2008). Antarctic sea ice elevation from satellite radar altimetry. *Geophysical Research Letters*, 35(3):1–5, DOI: 10.1029/2007GL031572.

Giovinetto, M. B., Bromwich, D. H., and Wendler, G. (1992). Atmospheric net transport of water vapor and latent heat across 70°S. *Journal of Geophysical Research*, 97(D1):917, DOI: 10.1029/91JD02485.

Global Modeling and Assimilation Office (GMAO) (2015). MERRA-2 tavg1_2d_ocn_Nx: 2d, 1-hourly, time-averaged, single-Level, assimilation, ocean surface diagnostics V5.12.4. In *Earth Sciences Data and Information Services Center (GES DISC*. Greenbelt, MD, USA, Goddard, DOI: 10.5067/Y67YQ1L3ZZ4R.

Guerreiro, K., Fleury, S., Zakharova, E., Kouraev, A., Rémy, F., and Maisongrande, P. (2017). Comparison of CryoSat-2 and ENVISAT radar freeboard over Arctic sea ice: Toward an improved Envisat freeboard retrieval. *Cryosphere*, 11(5):2059–2073, DOI: 10.5194/tc-11-2059-2017.

Guerreiro, K., Fleury, S., Zakharova, E., Rémy, F., and Kouraev, A. (2016). Potential for estimation of snow depth on Arctic sea ice from CryoSat-2 and SARAL/AltiKa missions. *Remote Sensing of Environment*, 186:339–349, DOI: 10.1016/j.rse.2016.07.013.

Haas, C. (2016). Sea ice thickness distribution. In *Sea Ice: Third Edition*, pages 42–64. Wiley Blackwell, DOI: 10.1002/9781118778371.ch2.

Haas, C., Lobach, J., Hendricks, S., Rabenstein, L., and Pfaffling, A. (2009). Helicopter-borne measurements of sea ice thickness, using a small and lightweight, digital EM system. *Journal of Applied Geophysics*, 67(3):234–241, DOI: 10.1016/j.jappgeo.2008.05.005.

Haas, C., Thomas, D. N., and Bareiss, J. (2001). Surface properties and processes of perennial Antarctic sea ice in summer. *Journal of Glaciology*, 47(159):613–625, DOI: 10.3189/172756501781831864.

Hallikainen, M. and Winebrenner, D. P. (1992). The physical basis for sea ice remote sensing. In *Microwave Remote Sensing of Sea Ice*, pages 29–46, DOI: 10.1029/GM068p0029.

Helm, V., Humbert, A., and Miller, H. (2014). Elevation and elevation change of Greenland and Antarctica derived from CryoSat-2. *Cryosphere*, 8(4):1539–1559, DOI: 10.5194/tc-8-1539-2014.

Hendricks, S., Paul, S., and Rinne, E. (2018). ESA Sea Ice Climate Change Initiative (Sea_Ice_cci): Northern hemisphere sea ice thickness from CryoSat-2 on the satellite swath (L2P), v2.0. In *Centre for Environmental Data Analysis*, DOI: 10.5285/fbfae06e787b4fefb4b03cba2fd04bc3.

Hendricks, S., Ricker, R., and Helm, V. (2016). AWI CryoSat-2 sea ice thickness data product (v1.2) user guide. Technical report, AWI, https://epic.awi.de/id/eprint/41242/.

Hendricks, S., Stenseng, L., Helm, V., and Haas, C. (2010). Effects of surface roughness on sea ice freeboard retrieval with an airborne ku-band SAR radar altimeter. In *International Geoscience and Remote Sensing Symposium (IGARSS)*, pages 3126–3129, DOI: 10.1109/IGARSS.2010.5654350.

Holland, M. M. and Bitz, C. M. (2003). Polar amplification of climate change in coupled models. *Climate Dynamics*, 21(3-4):221–232, DOI: 10.1007/s00382-003-0332-6.

Holland, M. M., Bitz, C. M., and Tremblay, B. (2006). Future abrupt reductions in the summer Arctic sea ice. *Geophysical Research Letters*, 33(23):L23503, DOI: 10.1029/2006GL028024.

Holland, P. R. (2014). The seasonality of Antarctic sea ice trends. *Geophysical Research Letters*, 41(12):4230–4237, DOI: 10.1002/2014GL060172.

Howell, S. E. L., Tivy, A., Yackel, J. J., Else, B. G. T., and Duguay, C. R. (2008). Changing sea ice melt parameters in the Canadian Arctic Archipelago: Implications for the future presence of multiyear ice. *Journal of Geophysical Research*, 113(C9):C09030, DOI: 10.1029/2008JC004730.

Hunke, E. C. and Bitz, C. M. (2009). Age characteristics in a multidecadal Arctic sea ice simulation. *Journal of Geophysical Research*, 114(C8):C08013, DOI: 10.1029/2008JC005186.

Hunkins, K., Kristoffersen, Y., Johnson, G. L., and Heiberg, A. (1979). The Fram I Expedition. *Eos, Transactions American Geophysical Union*, 60(52):1043, DOI: 10.1029/EO060i052p01043.

IPCC (2014). *Climate change 2014: synthesis report. Contribution of working groups I, II and II to the fifth assessment report of the Intergovernmental Panel on Climate Change*. IPCC, Geneva.

Jain, M., Andersen, O. B., Dall, J., and Stenseng, L. (2015). Sea surface height determination in the Arctic using Cryosat-2 SAR data from primary peak empirical retrackers. *Advances in Space Research*, 55(1):40–50, DOI: 10.1016/j.asr.2014.09.006.

Kacimi, S. and Kwok, R. (2020). The Antarctic sea ice cover from ICESat-2 and CryoSat-2: freeboard, snow depth, and ice thickness. *The Cryosphere*, 14:4453–4474, DOI: 10.5194/tc-14-4453-2020.

Kern, S., Khvorostovsky, K., Skourup, H., Rinne, E., Parsakhoo, Z. S., Djepa, V., Wadhams, P., and Sandven, S. (2015). The impact of snow depth, snow density

and ice density on sea ice thickness retrieval from satellite radar altimetry: Results from the ESA-CCI Sea Ice ECV Project Round Robin Exercise. *Cryosphere*, 9(1):37–52, DOI: 10.5194/tc-9-37-2015.

Kern, S. and Ozsoy-Çiçek, B. (2016). Satellite remote sensing of snow depth on Antarctic sea ice: an inter-comparison of two empirical approaches. *Remote Sensing*, 8(6):450, DOI: 10.3390/rs8060450.

Kern, S., Ozsoy-Çiçek, B., and Worby, A. (2016). Antarctic sea-ice thickness retrieval from ICESat: Inter-comparison of different approaches. *Remote Sensing*, 8(7):538, DOI: 10.3390/rs8070538.

Kern, S. and Spreen, G. (2015). Uncertainties in Antarctic sea-ice thickness retrieval from ICESat. *Annals of Glaciology*, 56(69):107–119, DOI: 10.3189/2015AoG69A736.

King, J., Brady, M., and Newman, T. (2020). pySnowRadar. *IEEE TGRS [submitted]*, DOI: 10.5281/ZENODO.4071947.

Krumpen, T., Birrien, F., Kauker, F., Rackow, T., Von Albedyll, L., Angelopoulos, M., Jakob Belter, H., Bessonov, V., Damm, E., Dethloff, K., Haapala, J., Haas, C., Harris, C., Hendricks, S., Hoelemann, J., Hoppmann, M., Kaleschke, L., Karcher, M., Kolabutin, N., Lei, R., Lenz, J., Morgenstern, A., Nicolaus, M., Nixdorf, U., Petrovsky, T., Rabe, B., Rabenstein, L., Rex, M., Ricker, R., Rohde, J., Shimanchuk, E., Singha, S., Smolyanitsky, V., Sokolov, V., Stanton, T., Timofeeva, A., Tsamados, M., and Watkins, D. (2020). The MOSAiC ice floe: Sediment-laden survivor from the Siberian shelf. *Cryosphere*, 14(7):2173–2187, DOI: 10.5194/tc-14-2173-2020.

Ku, H. (1966). Notes on the use of propagation of error formulas. *J. of Research of the Bureau of National Standards*, 70C(4):263–273.

Kurtz, N., Studinger, M., Harbeck, J., Onana, V., and Yi, D. (2015). IceBridge L4 sea ice freeboard, snow depth, and thickness, version 1., DOI: 10.5067/G519SHCKWQV6.

Kurtz, N. T. and Farrell, S. L. (2011). Large-scale surveys of snow depth on Arctic sea ice from Operation IceBridge. *Geophysical Research Letters*, 38(20):20505, DOI: 10.1029/2011GL049216.

Kurtz, N. T., Farrell, S. L., Studinger, M., Galin, N., Harbeck, J. P., Lindsay, R., Onana, V. D., Panzer, B., and Sonntag, J. G. (2013). Sea ice thickness, freeboard, and snow depth products from Operation IceBridge airborne data. *Cryosphere*, 7(4):1035–1056, DOI: 10.5194/tc-7-1035-2013.

Kurtz, N. T., Galin, N., and Studinger, M. (2014). An improved CryoSat-2 sea ice freeboard retrieval algorithm through the use of waveform fitting. *Cryosphere*, 8(4):1217–1237, DOI: 10.5194/tc-8-1217-2014.

Kurtz, N. T. and Markus, T. (2012). Satellite observations of Antarctic sea ice thickness and volume. *Journal of Geophysical Research: Oceans*, 117(8):n/a–n/a, DOI: 10.1029/2012JC008141.

Kurtz, N. T., Markus, T., Cavalieri, D. J., Krabill, W., Sonntag, J. G., and Miller, J. (2008). Comparison of ICESat data with airborne laser altimeter measurements over arctic sea ice. *IEEE Transactions on Geoscience and Remote Sensing*, 46(7):1913–1924, DOI: 10.1109/TGRS.2008.916639.

Kurtz, N. T., Markus, T., Cavalieri, D. J., Sparling, L. C., Krabill, W. B., Gasiewski, A. J., and Sonntag, J. G. (2009). Estimation of sea ice thickness distributions through the combination of snow depth and satellite laser altimetry data. *Journal of Geophysical Research: Oceans*, 114(10):C10007, DOI: 10.1029/2009JC005292.

Kwok, R. (2004). ICESat observations of Arctic sea ice: A first look. *Geophysical Research Letters*, 31(16):L16401, DOI: 10.1029/2004GL020309.

Kwok, R. (2011). Satellite remote sensing of sea-ice thickness and kinematics: A review. *Journal of Glaciology*, 56(200):1129–1140, DOI: 10.3189/002214311796406167.

Kwok, R. (2014). Simulated effects of a snow layer on retrieval of CryoSat-2 sea ice freeboard. *Geophysical Research Letters*, 41(14):5014–5020, DOI: 10.1002/2014GL060993.

Kwok, R. and Cunningham, G. F. (2015). Variability of arctic sea ice thickness and volume from CryoSat-2. *Philosophical Transactions of the Royal Society A: Mathematical, Physical and Engineering Sciences*, 373(2045):20140157, DOI: 10.1098/rsta.2014.0157.

Kwok, R., Cunningham, G. F., Hancock, D. W., Ivanoff, A., and Wimert, J. T. (2020a). Icesat-2 algorithm theoretical basis document for sea ice products (atl07/atl10) release 003 Ice, Cloud, and land Elevation satellite (ICESat-2) project algorithm theoretical basis document (ATBD) for sea ice products. Technical report, DOI: 10.5067/UAZPI91070H4.

Kwok, R., Cunningham, G. F., Markus, T., Hancock, D. W., Morison, J. H., Palm, S. P., Farrell, S. L., Ivanoff, A., Wimert, J. T., and ICESat-2 Science Team, S. (2020b). ATLAS/ICESat-2 L3A sea ice height (ATL07), version 3. *NASA National Snow and Ice Data Center Distributed Active Archive Center*, DOI: 10.5067/ATLAS/ATL10.003.

Kwok, R., Cunningham, G. F., Zwally, H. J., and Yi, D. (2007). Ice, Cloud, and land Elevation Satellite (ICESat) over Arctic sea ice: Retrieval of freeboard. *Journal of Geophysical Research: Oceans*, 112(12):C12013, DOI: 10.1029/2006JC003978.

Kwok, R. and Kacimi, S. (2018). Three years of sea ice freeboard, snow depth, and ice thickness of the Weddell Sea from Operation IceBridge and CryoSat-2. *The Cryosphere*, 12(8):2789–2801, DOI: 10.5194/tc-12-2789-2018.

Kwok, R., Kacimi, S., Webster, M. A., Kurtz, N. T., and Petty, A. A. (2020c). Arctic snow depth and sea ice thickness from ICESat-2 and CryoSat-2 freeboards: a first examination. *Journal of Geophysical Research: Oceans*, 125(3):e2019JC016008, DOI: 10.1029/2019JC016008.

Kwok, R. and Maksym, T. (2014). Snow depth of the Weddell and Bellingshausen sea ice covers from IceBridge surveys in 2010 and 2011: An examination. *Journal of Geophysical Research: Oceans*, 119(7):4141–4167, DOI: 10.1002/2014JC009943.

Kwok, R. and Markus, T. (2018). Potential basin-scale estimates of Arctic snow depth with sea ice freeboards from CryoSat-2 and ICESat-2: An exploratory analysis. *Advances in Space Research*, 62(6):1243–1250, DOI: 10.1016/j.asr.2017.09.007.

Kwok, R., Markus, T., Kurtz, N. T., Petty, A. A., Neumann, T. A., Farrell, S. L., Cunningham, G. F., Hancock, D. W., Ivanoff, A., and Wimert, J. T. (2019). Surface height and sea ice freeboard of the Arctic Ocean from ICESat-2: characteristics and early resultss. *Journal of Geophysical Research: Oceans*, 124(10):6942–6959, DOI: 10.1029/2019JC015486.

Kwok, R., Pang, S. S., and Kacimi, S. (2017). Sea ice drift in the Southern Ocean: Regional patterns, variability, and trends. *Elementa*, 5, DOI: 10.1525/elementa.226.

Kwok, R. and Rothrock, D. A. (2009). Decline in Arctic sea ice thickness from submarine and ICESat records: 1958-2008. *Geophysical Research Letters*, 36(15):15501, DOI: 10.1029/2009GL039035.

Laforge, A., Fleury, S., Dinardo, S., Garnier, F., Remy, F., Benveniste, J., Bouffard, J., and Verley, J. (2020). Toward improved sea ice freeboard observation with SAR altimetry using the physical retracker SAMOSA+. *Advances in Space Research*, DOI: 10.1016/j.asr.2020.02.001.

Landy, J. C., Petty, A. A., Tsamados, M., and Stroeve, J. C. (2020). Sea ice roughness overlooked as a key source of uncertainty in CryoSat-2 Ice freeboard retrievals. *Journal of Geophysical Research: Oceans*, 125(5), DOI: 10.1029/2019JC015820.

Landy, J. C., Tsamados, M., and Scharien, R. K. (2019). A facet-based numerical model for simulating SAR altimeter echoes from heterogeneous sea ice surfaces. *IEEE Transactions on Geoscience and Remote Sensing*, 57(7):4164–4180, DOI: 10.1109/TGRS.2018.2889763.

Lawrence, I. R., Tsamados, M. C., Stroeve, J. C., Armitage, T. W., and Ridout, A. L. (2018). Estimating snow depth over Arctic sea ice from calibrated dual-frequency radar freeboards. *Cryosphere*, 12(11):3551–3564, DOI: 10.5194/tc-12-3551-2018.

Laxon, S., Peacock, H., and Smith, D. (2003). High interannual variability of sea ice thickness in the Arctic region. *Nature*, 425(6961):947–950, DOI: 10.1038/nature02050.

Laxon, S. W., Giles, K. A., Ridout, A. L., Wingham, D. J., Willatt, R., Cullen, R., Kwok, R., Schweiger, A., Zhang, J., Haas, C., Hendricks, S., Krishfield, R., Kurtz, N., Farrell, S., and Davidson, M. (2013). CryoSat-2 estimates of Arctic sea ice thickness and volume. *Geophysical Research Letters*, 40(4):732–737, DOI: 10.1002/grl.50193.

Lee, S., Im, J., Kim, J., Kim, M., Shin, M., Kim, H.-c., and Quackenbush, L. (2016). Arctic sea ice thickness estimation from CryoSat-2 satellite data using machine learning-based lead detection. *Remote Sensing*, 8(9):698, DOI: 10.3390/rs8090698.

Leuschen, C. (2010). *IceBridge snow radar L1B geolocated radar echo strength profiles*. NASA National Snow and Ice Data Center Distributed Active Archive Center, Boulder, Colorado, USA, DOI: 10.5067/FAZTWP500V70.

Leuschen, C., Gogineni, P., Rodriguez-Morales, F., Paden, J., and Allen, C. (2014). *IceBridge Ku-band radar L1B geolocated radar echo strength profiles, version 2, October–November 2011–2012*. NASA National Snow and Ice Data Center Distributed Active Archive Center, Boulder, Colorado, USA, DOI: 10.5067/D7DX7J7J5JN9.

Lewis, M., Tison, J., Weissling, B., Delille, B., Ackley, S., Brabant, F., and Xie, H. (2011). Sea ice and snow cover characteristics during the winter–spring transition in the Bellingshausen Sea: An overview of SIMBA 2007. *Deep Sea Research Part II: Topical Studies in Oceanography*, 58(9-10):1019–1038, DOI: 10.1016/J.DSR2.2010.10.027.

Li, H., Xie, H., Kern, S., Wan, W., Ozsoy, B., Ackley, S., and Hong, Y. (2018). Spatio-temporal variability of Antarctic sea-ice thickness and volume obtained from ICESat data using an innovative algorithm. *Remote Sensing of Environment*, 219:44–61, DOI: 10.1016/j.rse.2018.09.031.

Liston, G. E., Polashenski, C., Rösel, A., Itkin, P., King, J., Merkouriadi, I., and Haapala, J. (2018). A distributed snow-evolution model for sea-ice applications (snowmodel). *Journal of Geophysical Research: Oceans*, 123(5):3786–3810, DOI: 10.1002/2017JC013706.

Lyard, F., Lefevre, F., Letellier, T., and Francis, O. (2006). Modelling the global ocean tides: Modern insights from FES2004. *Ocean Dynamics*, 56(5-6):394–415, DOI: 10.1007/s10236-006-0086-x.

Maksym, T. and Jeffries, M. O. (2000). A one-dimensional percolation model of flooding and snow ice formation on Antarctic sea ice. *Journal of Geophysical Research: Oceans*, 105(C11):26313–26331, DOI: 10.1029/2000JC900130.

Maksym, T. and Markus, T. (2008). Antarctic sea ice thickness and snow-to-ice conversion from atmospheric reanalysis and passive microwave snow depth. *Journal of Geophysical Research: Oceans*, 113(2):C02S12, DOI: 10.1029/2006JC004085.

Maksym, T., Stammerjohn, S. E., Ackley, S., and Massom, R. (2012). Antarctic sea ice- A polar opposite? *Oceanography*, 25(3):140–151, DOI: 10.5670/oceanog.2012.88.

Mallett, R. D. C., Lawrence, I. R., Stroeve, J. C., Landy, J. C., and Tsamados, M. (2020). Brief communication: Conventional assumptions involving the speed of radar waves in snow introduce systematic underestimates to sea ice thickness and seasonal growth rate estimates. *The Cryosphere*, 14(1):251–260, DOI: 10.5194/tc-14-251-2020.

Markus, T. and Cavalieri, D. J. (1998). Snow depth distribution over sea ice in the southern ocean from satellite passive microwave data. In *Antarctic Sea Ice: Physical Processes, Interactions and Variability*, volume 74, pages 19–39. American Geophysical Union, DOI: 10.1029/AR074p0019.

Markus, T., Massom, R., Worby, A., Lytle, V., Kurtz, N., and Maksym, T. (2011). Freeboard, snow depth and sea-ice roughness in East Antarctica from in situ and multiple satellite data. *Annals of Glaciology*, 52(57 PART 2):242–248, DOI: 10.3189/172756411795931570.

Markus, T., Neumann, T., Martino, A., Abdalati, W., Brunt, K., Csatho, B., Farrell, S., Fricker, H., Gardner, A., Harding, D., Jasinski, M., Kwok, R., Magruder, L., Lubin, D., Luthcke, S., Morison, J., Nelson, R., Neuenschwander, A., Palm, S., Popescu, S., Shum, C., Schutz, B. E., Smith, B., Yang, Y., and Zwally, J. (2017). The Ice, Cloud, and land Elevation Satellite-2 (ICESat-2): Science requirements, concept, and implementation. *Remote Sensing of Environment*, 190:260–273, DOI: 10.1016/J.RSE.2016.12.029.

Markus, T., Stroeve, J. C., and Miller, J. (2009). Recent changes in Arctic sea ice melt onset, freezeup, and melt season length. *Journal of Geophysical Research*, 114(C12):C12024, DOI: 10.1029/2009JC005436.

Martin, T. V., Zwally, H. J., Brenner, A. C., and Bindschadler, R. A. (1983). Analysis and retracking of continental ice sheet radar altimeter waveforms. *Journal of Geophysical Research*, 88(C3):1608, DOI: 10.1029/JC088iC03p01608.

Maslanik, J. A., Fowler, C., Stroeve, J., Drobot, S., Zwally, J., Yi, D., and Emery, W. (2007). A younger, thinner Arctic ice cover: Increased potential for rapid, extensive sea-ice loss. *Geophysical Research Letters*, 34(24):L24501, DOI: 10.1029/2007GL032043.

Massom, R. A., Drinkwater, M. R., and Haas, C. (1997). Winter snow cover on sea ice in the Weddell Sea. *Journal of Geophysical Research: Oceans*, 102(C1):1101–1117, DOI: 10.1029/96JC02992.

Massom, R. A., Eicken, H., Haas, C., Jeffries, M. O., Drinkwater, M. R., Sturm, M., Worby, A. P., Wu, X., Lytle, V. I., Ushio, S., Morris, K., Reid, P. A., Warren, S. G., and Allison, I. (2001). Snow on Antarctic sea ice. *Reviews of Geophysics*, 39(3):413–445, DOI: 10.1029/2000RG000085.

Massonnet, F., Mathiot, P., Fichefet, T., Goosse, H., König Beatty, C., Vancoppenolle, M., and Lavergne, T. (2013). A model reconstruction of the Antarctic sea ice thickness and volume changes over 1980-2008 using data assimilation. *Ocean Modelling*, 64:67–75, DOI: 10.1016/j.ocemod.2013.01.003.

Mcgoogan, J. T., Miller, L. S., Brown, G. S., and Hayne, G. S. (1974). The S-193 Radar Altimeter Experiment. *Proceedings of the IEEE*, 62(6):793–803, DOI: 10.1109/PROC.1974.9519.

Meier, W. N., Fetterer, F., and Windnagel, A. (2017). Near-real-time NOAA/NSIDC climate data record of passive microwave sea ice concentration, version 1, DOI: 0.7265/N5FF3QJ6.

Meredith, M., Sommerkorn, M., Cassota, S., Derksen, C., Ekaykin, A., Hollowed, A., Kofinas, G., Mackintosh, A., Melbourne-Thomas, J., Muelbert, M., Ottersen, G., Pritchard, H., Schuur, E., Boyd, P., Hobbs, W., and Hodgson-Johnston, I. (2019). Polar regions. *IPCC Special Report on the Ocean and Cryosphere in a Changing Climate*.

Meredith, M. P. and Brandon, M. A. (2016). Oceanography and sea ice in the Southern Ocean. In *Sea Ice: Third Edition*, pages 216–238. Wiley Blackwell, DOI: 10.1002/9781118778371.ch8.

Merzdorf, J. (2020). NASA's Operation IceBridge completes eleven years of polar surveys, http://www.nasa.gov/.

Mu, L., Yang, Q., Losch, M., Losa, S. N., Ricker, R., Nerger, L., and Liang, X. (2018). Improving sea ice thickness estimates by assimilating CryoSat-2 and SMOS sea ice thickness data simultaneously. *Quarterly Journal of the Royal Meteorological Society*, 144(711):529–538, DOI: 10.1002/qj.3225.

Nandan, V., Geldsetzer, T., Yackel, J., Mahmud, M., Scharien, R., Howell, S., King, J., Ricker, R., and Else, B. (2017). Effect of snow salinity on CryoSat-2 Arctic first-year sea ice freeboard measurements. *Geophysical Research Letters*, 44(20):10,419–10,426, DOI: 10.1002/2017GL074506.

Neumann, T. A., Martino, A. J., Markus, T., Bae, S., Bock, M. R., Brenner, A. C., Brunt, K. M., Cavanaugh, J., Fernandes, S. T., Hancock, D. W., Harbeck, K., Lee, J., Kurtz, N. T., Luers, P. J., Luthcke, S. B., Magruder, L., Pennington, T. A., Ramos-Izquierdo, L., Rebold, T., Skoog, J., and Thomas, T. C. (2019). The Ice, Cloud, and Land Elevation Satellite – 2 mission: A global geolocated photon product derived from the Aadvanced Ttopographic Llaser Aaltimeter Ssystem. *Remote Sensing of Environment*, 233:111325, DOI: 10.1016/j.rse.2019.111325.

Newman, T., Farrell, S. L., Richter-Menge, J., Connor, L. N., Kurtz, N. T., Elder, B. C., and McAdoo, D. (2014). Assessment of radar-derived snow depth over Arctic sea ice. *Journal of Geophysical Research: Oceans*, 119(12):8578–8602, DOI: 10.1002/2014JC010284.

Nghiem, S. V., Rigor, I. G., Clemente-Colón, P., Neumann, G., and Li, P. P. (2016). Geophysical constraints on the Antarctic sea ice cover. *Remote Sensing of Environment*, 181:281–292, DOI: 10.1016/j.rse.2016.04.005.

Nicolaus, M., Arndt, S., Hendricks, S., Heygster, G., Hoppmann, M., Huntemann, M., Katlein, C., Langevin, D., Rossmann, L., Schwegmann, S., and König-Langlo, G. (2016). Snow depth on Antarctic sea ice from autonomous measurements. *EPIC3XXXIV SCAR Open Science Conference*, DOI:10013/epic.48489.d001.

Nicolaus, M., Hoppmann, M., Arndt, S., Hendricks, S., Katlein, C., König-Langlo, G., Nicolaus, A., Rossmann, L., Schiller, M., Schwegmann, S., Langevin, D., and Bartsch, A. (2017). Snow height and air temperature on sea ice from Snow Buoy measurements., DOI: 10.1594/PANGAEA.875638.

Nielsen, K., Stenseng, L., Andersen, O. B., Villadsen, H., and Knudsen, P. (2015). Validation of CryoSat-2 SAR mode based lake levels. *Remote Sensing of Environment*, 171:162–170, DOI: 10.1016/j.rse.2015.10.023.

NSIDC (2020). State of the sryosphere: Sea ice, https://nsidc.org/cryosphere/sotc/.

Onstott, R. G. (2011). SAR and scatterometer signatures of sea ice. In *Microwave Remote Sensing of Sea Ice*, pages 73–104. Washington, DC, USA, DOI: 10.1029/gm068p0073.

Paden, J., Li, J., Leuschen, C., Rodriguez-Morales, F., and Hale, R. (2014). IceBridge snow radar L1B geolocated radar echo strength profiles, version 2., DOI: 10.5067/FAZTWP500V70.

Parkinson, C. L. (2014). Global sea ice coverage from satellite data: Annual cycle and 35-yr trends. *Journal of Climate*, 27(24):9377–9382, DOI: 10.1175/JCLI-D-14-00605.1.

Parkinson, C. L. (2019). A 40-y record reveals gradual Antarctic sea ice increases followed by decreases at rates far exceeding the rates seen in the Arctic. *Proceedings of the National Academy of Sciences of the United States of America*, 116(29):14414–14423, DOI: 10.1073/pnas.1906556116.

Paul, S., Hendricks, S., Ricker, R., Kern, S., and Rinne, E. (2018). Empirical parametrization of envisat freeboard retrieval of arctic and antarctic sea ice based on CryoSat-2: Progress in the ESA climate change initiative. *Cryosphere*, 12(7):2437–2460, DOI: 10.5194/tc-12-2437-2018.

Payne, R. E. (1972). Albedo of the sea surface. *Journal of the Atmospheric Sciences*, 29(5):959–970, DOI: 10.1175/1520-0469(1972)029<0959:aotss>2.0.co;2.

Perovich, D. K., Andreas, E. L., Curry, J. A., Eiken, H., Fairall, C. W., Grenfell, T. C., Guest, P., Intrieri, J., Kadko, D., Lindsay, R. W., McPhee, M. G., Morison, J., Moritz, R. E., Paulson, C. A., Pegau, W. S., Persson, P., Pinkel, R., Richter-Menge, J. A., Stanton, T., Stern, H., Sturm, M., Tucker, W., and Uttal, T. (1999). Year on ice gives climate insights. *EOS, Transactions of the American Geophysical Union*, 80(41):481, DOI: 10.1029/E0080i041p00481-01.

Perovich, D. K. and Polashenski, C. (2012). Albedo evolution of seasonal Arctic sea ice. *Geophysical Research Letters*, 39(8), DOI: 10.1029/2012GL051432.

Persson, O. and Vihma, T. (2016). The atmosphere over sea ice. In *Sea Ice: Third Edition*, DOI: 10.1002/9781118778371.ch6.

Petrich, C. and Eicken, H. (2016). Overview of sea ice growth and properties. In *Sea Ice: Third Edition*, pages 1–41. Wiley Blackwell, DOI: 10.1002/9781118778371.ch1.

Petty, A., Kwok, R., Bagnardi, M., Ivanoff, A., Kurtz, N., Lee, J., Wimert, J., and Hancock, D. (2020a). ATLAS/ICESat-2 L3B daily and monthly gridded sea ice freeboard, version 1, DOI: 10.5067/ATLAS/ATL20.001.

Petty, A. A., Kurtz, N. T., Kwok, R., Markus, T., and Neumann, T. A. (2020b). Winter Arctic sea ice thickness from ICESat-2 freeboards. *Journal of Geophysical Research: Oceans*, 125(5), DOI: 10.1029/2019JC015764.

Petty, A. A., Markus, T., and Kurtz, N. T. (2017). Improving our understanding of Antarctic sea ice with NASA's Operation IceBridge and the upcoming ICESat-2 mission. *US CLIVAR Variations*, 15(3):13–18, https://ntrs.nasa.gov/archive/nasa/casi.ntrs.nasa.gov/20170008477.pdf.

Petty, A. A., Webster, M., Boisvert, L., and Markus, T. (2018). The NASA Eulerian Snow on Sea Ice Model (NESOSIM) v1.0: Initial model development and analysis. *Geoscientific Model Development*, 11(11):4577–4602, DOI: 10.5194/gmd-11-4577-2018.

Pinker, R. T., Niu, X., and Ma, Y. (2014). Solar heating of the Arctic Ocean in the context of ice-albedo feedback. *Journal of Geophysical Research: Oceans*, 119(12):8395–8409, DOI: 10.1002/2014JC010232.

Polashenski, C., Perovich, D., Richter-Menge, J., and Elder, B. (2011). Seasonal ice mass-balance buoys: Adapting tools to the changing Arctic. *Annals of Glaciology*, 52(57 PART 1):18–26, DOI: 10.3189/172756411795931516.

Ponsoni, L., Massonnet, F., Fichefet, T., Chevallier, M., and Docquier, D. (2019). On the timescales and length scales of the Arctic sea ice thickness anomalies: A study based on 14 reanalyses. *Cryosphere*, 13(2):521–543, DOI: 10.5194/tc-13-521-2019.

Price, D., Beckers, J., Ricker, R., Kurtz, N., Rack, W., Haas, C., Helm, V., Hendricks, S., Leonard, G., and Langhorne, P. J. (2015). Evaluation of CryoSat-2 derived sea-ice freeboard over fast ice in McMurdo Sound, Antarctica. *Journal of Glaciology*, 61(226):285–300, DOI: 10.3189/2015JoG14J157.

Price, D., Soltanzadeh, I., Rack, W., and Dale, E. (2019). Snow-driven uncertainty in cryosat-2-derived antarctic sea ice thickness - Insights from McMurdo sound. *Cryosphere*, 13(4):1409–1422, DOI: 10.5194/tc-13-1409-2019.

Quartly, G. D., Rinne, E., Passaro, M., Andersen, O. B., Dinardo, S., Fleury, S., Guillot, A., Hendricks, S., Kurekin, A. A., Müller, F. L., Ricker, R., Skourup, H., and Tsamados, M. (2019). Retrieving sea level and freeboard in the Arctic: A review of current radar altimetry methodologies and future perspectives. *Remote Sensing*, 11(7):881, DOI: 10.3390/RS11070881.

Raney, K. R. (1998). The delay/doppler radar altimeter. *IEEE Transactions on Geoscience and Remote Sensing*, 36(5 PART 1):1578–1588, DOI: 10.1109/36.718861.

Ray, C., Martin-Puig, C., Clarizia, M. P., Ruffini, G., Dinardo, S., Gommenginger, C., and Benveniste, J. (2015). SAR altimeter backscattered waveform model. *IEEE Transactions on Geoscience and Remote Sensing*, 53(2):911–919, DOI: 10.1109/TGRS.2014.2330423.

Reiser, F., Willmes, S., and Heinemannm, G. (2020). A new algorithm for daily sea ice lead identification in the Arctic and Antarctic winter from thermal-infrared satellite imagery. *Remote Sensing*, 12:1957, DOI: 10.3390/rs12121957.

Rex, M., Shupe, M., Dethloff, K., Sommerfeld, A., and Rabe, B. (2019). The Multidisciplinary drifting Observatory for the Study of Arctic Climate (MOSAiC). In *Geophysical Research Abstracts*, https://meetingorganizer.copernicus.org/EGU2019/EGU2019-6737.pdf.

Ricker, R., Hendricks, S., Helm, V., Skourup, H., and Davidson, M. (2014). Sensitivity of CryoSat-2 Arctic sea-ice freeboard and thickness on radar-waveform interpretation. *Cryosphere*, 8(4):1607–1622, DOI: 10.5194/tc-8-1607-2014.

Ricker, R., Hendricks, S., Perovich, D. K., Helm, V., and Gerdes, R. (2015). Impact of snow accumulation on CryoSat-2 range retrievals over Arctic sea ice: An observational approach with buoy data. *Geophysical Research Letters*, DOI: 10.1002/2015GL064081.

Rosmorduc, V., Benveniste, J., Bronner, E., Dinardo, S., Lauret, O., Maheu, C., Milagro, M., Picot, N., Ambrozio, A., Escolà, R., Garcia-Mondejar, A., Restano, M., Schrama, E., and Terra-Homem, M. (2016). Radar altimetry tutorial, http://www.altimetry.info.

Rothrock, D. A., Yu, Y., and Maykut, G. A. (1999). Thinning of the Arctic sea-ice cover. Technical Report 23, DOI: 10.1029/1999GL010863.

Sadai, S., Condron, A., DeConto, R., and Pollard, D. (2020). Future climate response to Antarctic Ice Sheet melt caused by anthropogenic warming. *Science Advances*, 6(39):eaaz1169, DOI: 10.1126/sciadv.aaz1169.

Scagliola, M. (2013). Advanced Doppler ambiguity resolution strategies for wave mode data: CryoSat footprints. Technical report, Aresys Technical Note, https://earth.esa.int/.

Schröder, D., Feltham, D. L., Tsamados, M., Ridout, A., and Tilling, R. (2019). New insight from CryoSat-2 sea ice thickness for sea ice modelling. *Cryosphere*, 13(1):125–139, DOI: 10.5194/tc-13-125-2019.

Schwegmann, S., Rinne, E., Ricker, R., Hendricks, S., and Helm, V. (2016). About the consistency between Envisat and CryoSat-2 radar freeboard retrieval over Antarctic sea ice. *The Cryosphere*, 10(4):1415–1425, DOI: 10.5194/tc-10-1415-2016.

Shepherd, A. (2015). CryoSat operational monitoring - sea ice, http://www.cpom.ucl.ac.uk/csopr/seaice.php.

Shirshov, P. and Fedorov, E. (1938). Scientific work of the drifting north polar station. *Nature*, 141(3571):629–632, DOI: 10.1038/141629a0.

Simmonds, I. (2015). Comparing and contrasting the behaviour of Arctic and Antarctic sea ice over the 35 year period 1979-2013. *Annals of Glaciology*, 56(69):18–28, DOI: 10.3189/2015AoG69A909.

Sørensen, L. S. (2016). Altimetry theory. Technical report, DTU, Leeds, http://seom.esa.int/.

Spreen, G. and Kern, S. (2016). Methods of satellite remote sensing of sea ice. In *Sea Ice*, pages 239–260. John Wiley & Sons, Ltd, Chichester, UK, DOI: 10.1002/9781118778371.ch9.

Spreen, G., Kern, S., Stammer, D., and Hansen, E. (2009). Fram Strait sea ice volume export estimated between 2003 and 2008 from satellite data. *Geophysical Research Letters*, 36(19):L19502, DOI: 10.1029/2009GL039591.

Steffen, K. and Demaria, T. (1996). Surface energy fluxes of Arctic winter sea ice in Barrow Strait. *Journal of Applied Meteorology*, 35(11):2067–2079, DOI: 10.1175/1520-0450(1996)035<2067:SEFOAW>2.0.CO;2.

Stiles, W. H. and Ulaby, F. T. (1981). Dielectric properties of snow. *Review of the Remote Sensing Laboratory*.

Stouffer, R. J., Yin, J., Gregory, J. M., Dixon, K. W., Spelman, M. J., Hurlin, W., Weaver, A. J., Eby, M., Flato, G. M., Hasumi, H., Hu, A., Jungclaus, J. H., Kamenkovich, I. V., Levermann, A., Montoya, M., Murakami, S., Nawrath, S., Oka, A., Peltier, W. R., Robitaille, D. Y., Sokolov, A., Vettoretti, G., and Weber, S. L. (2006). Investigating the cause of the response of the thermohaline circulation to past and future climage changes. *Journal of Climate*, 19(8):1365–1387, DOI: 10.1175/JCLI3689.1.

Stroeve, J., Barrett, A., Serreze, M., and Schweiger, A. (2014). Using records from submarine, aircraft and satellites to evaluate climate model simulations of Arctic sea ice thickness. *Cryosphere*, 8(5):1839–1854, DOI: 10.5194/tc-8-1839-2014.

Stroeve, J., Nandan, V., Willatt, R., Tonboe, R., Hendricks, S., Ricker, R., Mead, J., Mallett, R., Huntemann, M., Itkin, P., Schneebeli, M., Krampe, D., Spreen, G., Wilkinson, J., Matero, I., Hoppmann, M., and Tsamados, M. (2020). Surface-based Ku-and Ka-band polarimetric radar for sea ice studies. *Cryosphere*, 14(12):4405–4426, DOI: 10.5194/tc-14-4405-2020.

Studinger, M. (2014). *IceBridge ATM L2 Icessn elevation, slope, and roughness. version 2.* NASA National Snow and Ice Data Center Distributed Active Archive Center, Boulder, Colorado, USA, DOI: 10.5067/CPRXXK3F39RV.

Studinger, M. and Harbeck, J. (2019). IceBridge CAMBOT L1B geolocated images, version 2, DOI: 10.5067/B0HL940D452L.

Studinger, M., Koenig, L., Martin, S., and Sonntag, J. (2010). Operation IceBridge: Using instrumented aircraft to bridge the observational gap between ICESat and ICESat-2. In *International Geoscience and Remote Sensing Symposium (IGARSS)*, pages 1918–1919, DOI: 10.1109/IGARSS.2010.5650555.

Thomas, D. N. (2017). *Sea ice*. John Wiley & Sons, Ltd, Chichester, UK, DOI: 10.1002/9781118778371.

Tilling, R., Ridout, A., and Shepherd, A. (2019). Assessing the impact of lead and floe sampling on Arctic sea ice thickness estimates from Envisat and CryoSat-2. *Journal of Geophysical Research: Oceans*, 124(11):7473–7485, DOI: 10.1029/2019JC015232.

Tilling, R. L., Ridout, A., and Shepherd, A. (2016). Near-real-time Arctic sea ice thickness and volume from CryoSat-2. *Cryosphere*, 10(5):2003–2012, DOI: 10.5194/tc-10-2003-2016.

Tilling, R. L., Ridout, A., and Shepherd, A. (2018). Estimating Arctic sea ice thickness and volume using CryoSat-2 radar altimeter data. *Advances in Space Research*, 62(6):1203–1225, DOI: 10.1016/j.asr.2017.10.051.

Tiuri, M. E., Sihvola, A. H., Nyfors, E. G., and Hallikaiken, M. T. (1984). The complex dielectric constant of snow at microwave frequencies. *IEEE Journal of Oceanic Engineering*, DOI: 10.1109/JOE.1984.1145645.

Ulaby, F. T., Moore, R. K., and Fung, A. K. (1982). *Microwave remote sensing: active and passive. Volume II. Radar remote sensing and surface scattering and emission theory.* Artech House.

Virtanen, P., Gommers, R., Oliphant, T. E., Haberland, M., Reddy, T., Cournapeau, D., Burovski, E., Peterson, P., Weckesser, W., Bright, J., van der Walt, S. J., Brett, M., Wilson, J., Millman, K. J., Mayorov, N., Nelson, A. R., Jones, E., Kern, R., Larson, E., Carey, C. J., Polat, , Feng, Y., Moore, E. W., VanderPlas, J., Laxalde, D., Perktold, J., Cimrman, R., Henriksen, I., Quintero, E. A., Harris, C. R., Archibald, A. M., Ribeiro, A. H., Pedregosa, F., van Mulbregt, P., Vijaykumar, A., Bardelli, A. P., Rothberg, A., Hilboll, A., Kloeckner, A., Scopatz, A., Lee, A., Rokem, A., Woods, C. N., Fulton, C., Masson, C., Häggström, C., Fitzgerald, C., Nicholson, D. A., Hagen, D. R., Pasechnik, D. V., Olivetti, E., Martin, E., Wieser, E., Silva, F., Lenders, F., Wilhelm, F., Young, G., Price, G. A., Ingold, G. L., Allen, G. E., Lee, G. R., Audren, H., Probst, I., Dietrich, J. P., Silterra, J., Webber, J. T., Slavič, J., Nothman, J., Buchner, J., Kulick, J., Schönberger, J. L., de Miranda Cardoso, J. V., Reimer, J., Harrington, J., Rodríguez, J. L. C., Nunez-Iglesias, J., Kuczynski, J., Tritz, K., Thoma, M., Newville, M., Kümmerer, M., Bolingbroke, M., Tartre, M., Pak, M., Smith, N. J., Nowaczyk, N., Shebanov, N., Pavlyk, O., Brodtkorb, P. A., Lee, P., McGibbon, R. T., Feldbauer, R., Lewis, S., Tygier, S., Sievert, S., Vigna, S., Peterson, S., More, S., Pudlik, T., Oshima, T., Pingel, T. J., Robitaille, T. P., Spura, T., Jones, T. R., Cera, T., Leslie, T., Zito, T., Krauss, T., Upadhyay, U., Halchenko, Y. O., and Vázquez-Baeza, Y. (2020). SciPy 1.0: fundamental algorithms for scientific computing in Python. *Nature Methods*, 17(3):261–272, DOI: 10.1038/s41592-019-0686-2.

Wadhams, P., Tucker, W. B., Krabill, W. B., Swift, R. N., Comiso, J. C., and Davis, N. R. (1992). Relationship between sea ice freeboard and draft in the Arctic Basin, and implications for ice thickness monitoring. *Journal of Geophysical Research*, 97(C12):20325, DOI: 10.1029/92JC02014.

Warren, S. G., Rigor, I. G., Untersteiner, N., Radionov, V. F., Bryazgin, N. N., Aleksandrov, Y. I., and Colony, R. (1999). Snow depth on Arctic sea ice. *Journal of Climate*, 12(6):1814–1829, DOI: 10.1175/1520-0442(1999)012<1814:SDOASI>2.0.CO;2.

Webster, M., Gerland, S., Holland, M., Hunke, E., Kwok, R., Lecomte, O., Massom, R., Perovich, D., and Sturm, M. (2018). Snow in the changing sea-ice systems, DOI: 10.1038/s41558-018-0286-7.

Weissling, B. P. and Ackley, S. F. (2011). Antarctic sea-ice altimetry: Scale and resolution effects on derived ice thickness distribution. *Annals of Glaciology*, 52(57 PART 2):225–232, DOI: 10.3189/172756411795931679.

WHOI (2018). Mooring data – Beaufort Gyre Exploration Project (BGEP), https://www2.whoi.edu/site/beaufortgyre/data/mooring-data/.

Willatt, R., Laxon, S., Giles, K., Cullen, R., Haas, C., and Helm, V. (2011). Ku-band radar penetration into snow cover on Arctic sea ice using airborne data. *Annals of Glaciology*, 52(57 PART 2):197–205, DOI: 10.3189/172756411795931589.

Willatt, R. C., Giles, K. A., Laxon, S. W., Stone-Drake, L., and Worby, A. P. (2010). Field investigations of Ku-band radar penetration into snow cover on antarctic sea ice. *IEEE Transactions on Geoscience and Remote Sensing*, 48(1):365–372, DOI: 10.1109/TGRS.2009.2028237.

Williams, G., Maksym, T., Wilkinson, J., Kunz, C., Murphy, C., Kimball, P., and Singh, H. (2015). Thick and deformed Antarctic sea ice mapped with autonomous underwater vehicles. *Nature Geoscience*, 8(1):61–67, DOI: 10.1038/ngeo2299.

Wingham, D. J., Francis, C. R., Baker, S., Bouzinac, C., Brockley, D., Cullen, R., de Chateau-Thierry, P., Laxon, S. W., Mallow, U., Mavrocordatos, C., Phalippou, L., Ratier, G., Rey, L., Rostan, F., Viau, P., and Wallis, D. W. (2006). CryoSat: A mission to determine the fluctuations in Earth's land and marine ice fields. *Advances in Space Research*, 37(4):841–871, DOI: 10.1016/j.asr.2005.07.027.

Wingham, D. J., Phalippou, L., Mavrocordatos, C., and Wallis, D. (2004). The mean echo and echo cross product from a beamforming interferometric altimeter and their application to elevation measurement. In *IEEE Transactions on Geoscience and Remote Sensing*, volume 42, pages 2305–2323, DOI: 10.1109/TGRS.2004.834352.

Worby, A. P., Geiger, C. A., Paget, M. J., Van Woert, M. L., Ackley, S. F., and DeLiberty, T. L. (2008). Thickness distribution of Antarctic sea ice. *Journal of Geophysical Research: Oceans*, 113(5):1–14, DOI: 10.1029/2007JC004254.

Worby, A. P. and Wu, X. (1998). East Antarctic sea ice: Observations and modelling. *Annals of Glaciology*, 27:427–432, DOI: 10.3189/1998aog27-1-427-432.

Xie, H., Ackley, S. F., Yi, D., Zwally, H. J., Wagner, P., Weissling, B., Lewis, M., and Ye, K. (2011). Sea-ice thickness distribution of the Bellingshausen Sea from surface measurements and ICESat altimetry. *Deep-Sea Research Part II: Topical Studies in Oceanography*, 58(9-10):1039–1051, DOI: 10.1016/j.dsr2.2010.10.038.

Yang, J. and Neelin, J. D. (1993). Sea-ice interaction with the thermohaline circulation. *Geophysical Research Letters*, 20(3):217–220, DOI: 10.1029/92GL02920.

Yi, D., Kurtz, N., Harbeck, J., Kwok, R., Hendricks, S., and Ricker, R. (2019). Comparing coincident elevation and freeboard from IceBridge and five different CryoSat-2 retrackers. *IEEE Transactions on Geoscience and Remote Sensing*, 57(2):1219–1229, DOI: 10.1109/TGRS.2018.2865257.

Zwally, H. J., Schutz, B., Abdalati, W., Abshire, J., Bentley, C., Brenner, A., Bufton, J., Dezio, J., Hancock, D., Harding, D., Herring, T., Minster, B., Quinn, K., Palm, S., Spinhirne, J., and Thomas, R. (2002). ICESat's laser measurements

of polar ice, atmosphere, ocean, and land. *Journal of Geodynamics*, 34(3-4):405–445, DOI: 10.1016/S0264-3707(02)00042-X.

Zwally, H. J., Yi, D., Kwok, R., and Zhao, Y. (2008). ICESat measurements of sea ice freeboard and estimates of sea ice thickness in the Weddell Sea. *Journal of Geophysical Research: Oceans*, 113(2), DOI: 10.1029/2007JC004284.